6-21-2021 2:00 PM

Analysis and Differentiation of Uniform and Localized Corrosion of Cu

Roshan J. Daljeet, *The University of Western Ontario*

Supervisor: Noël, James J., *The University of Western Ontario*
Co-Supervisor: Shoesmith, David W., *The University of Western Ontario*
A thesis submitted in partial fulfillment of the requirements for the Doctor of Philosophy degree in Chemistry

Recommended Citation

Daljeet, Roshan J., "Analysis and Differentiation of Uniform and Localized Corrosion of Cu" (2021). *Electronic Thesis and Dissertation Repository*. 8036.
https://ir.lib.uwo.ca/etd/8036

Abstract

The current plan for disposal of used nuclear fuel in Canada involves sealing the waste in steel containers coated with 3 mm of copper and burying them in a deep geologic repository (DGR). The purpose of the copper coating is to provide corrosion resistance. To achieve long term containment, it is necessary that the copper layer corrodes slowly and predictably via active dissolution rather than passivating due to film formation. Film formation could allow pitting corrosion to occur in early phase repository conditions when groundwater ions such as Cl^{-}, SO_4^{2-} and HCO_3^{-} play a dominant role in influencing copper`s corrosion behaviour. The tendency of copper to undergo active dissolution was tested by immersing a piece of copper in a variety of solutions with different combinations of Cl^{-}, SO_4^{2-} and HCO_3^{-} ions at various concentrations and temperatures while observing the electrochemical behaviour. It was found that in most scenarios active dissolution was the preferred corrosion process.

While active dissolution is favoured under DGR conditions, the distribution of corrosion damage in the form of surface roughening needs to be elucidated if an acceptable corrosion allowance is to be specified. Corroded copper surfaces were examined using a combination of optical microscopy and confocal laser scanning microscopy (CLSM). Multielectrode arrays (MEA's) were designed to simulate copper surfaces.

Copper coupons were tested using galvanostatic charging or immersion in Cl^{-}-based solutions to determine the surface roughening pattern. Using this information, an oxidizing solution was designed which could buffer the potential of the system without externally controlling the potential or current. This solution also replicated the roughening damage observed in both the galvanostatic charging and immersion experiments. This created a link between accelerated and non-accelerated testing. This solution was then used to roughen the MEA electrodes. It was found that roughening of copper surfaces in Cl^{-}-based solutions proceeds via preferential dissolution of different grains. The depth of metal dissolution was increased or limited depending on the grain orientation of the reactive surfaces present in the copper. Therefore, corrosion of used fuel containers in the DGR will be limited by the grain structure of their copper coating.

Keywords: Copper, Roughening, Multielectrode Arrays, Corrosion, Nuclear Waste Disposal, Electrochemistry, Groundwater Anions, Profilometry

Summary for Lay Audiences

Nuclear power is a prominent source of energy used in many countries across the globe. However, the permanent and safe disposal of the waste generated by nuclear power plants is a requirement for nuclear energy to be considered a green source of power. Many countries have a plan for permanent disposal of the nuclear waste that involves sealing it in metal containers which are then buried 500 m underground in a deep geologic repository (DGR). The Canadian steel used fuel container (UFC) is designed with a thin copper coating to avoid fabrication issues and reduce the cost per container. However, this copper layer needs to be properly assessed to ensure it can provide the necessary corrosion resistance within a DGR, making it important to determine how damage will accumulate as corrosion occurs in a DGR environment.

To effectively study this problem, a wide variety of solutions containing groundwater species anticipated in a DGR, such as chloride, sulphate and carbonate, were tested to determine the progression of corrosion on a UFC surface. This resulted in a large database which enabled the influences of the concentration of the groundwater species, temperature and pH to be evaluated. This database indicates copper will actively corrode under DGR conditions. However, the fine details of how the corrosion damage will progress are not well understood.

A unique setup, involving microelectrode arrays fabricated on premade electronic circuit boards was utilized. The copper electrodes in these arrays were designed to be micro-sized. The microelectrode arrays were used to simulate a copper surface and specialized imaging techniques were used to create accurate 3D representations of each electrode. These 3D representations were analyzed to determine the changes in the metal surface as the copper dissolved over time. Using these 3D representations specific parameters such as the height or roughness of the copper surfaces were calculated using specialized software. This provided insight into the previously undetermined progression of corrosion as the copper dissolved over time. These insights were then used to help determine if a thin copper layer could provide the necessary corrosion resistance in conditions similar to those anticipated on the surface of a UFC buried in a DGR.

Co-Authorship Statement

This thesis includes published data in Chapter 1.

Chapter 1: Amy Ai and Nasrin Farhangi assisted with collecting the potentiodynamic measurements of copper in groundwater solutions. Dr. James Noël and Dr. David Shoesmith assisted with editing.

Chapter 2: Sina Matin assisted with initial array designs and optimization. Dr. James Noël and Dr. David Shoesmith assisted with editing.

Chapter 3: Sina Matin assisted with the photoresist selection and the photomask design. Dr. James Noël and Dr. David Shoesmith assisted with editing.

Chapter 4: Dr. James Noël and Dr. David Shoesmith assisted with editing.

Chapter 5: Dr. James Noël and Dr. David Shoesmith assisted with editing.

Chapter 6: Dr. Mengnan Guo assisted with prepared and conducting the growth of Cu_2S films for anode/cathode verification. Dr. James Noël and Dr. David Shoesmith assisted with editing.

Dedication

This thesis is dedicated to my family who have been supporting me from the start of this long journey, it is also dedicated to my loving girlfriend and adorable/crazy dog that joined me along the way. This is for you Mom, Dad, Sonya, Persis, Pat and Hobbes.

Acknowledgements

Well Jamie you get first honours. It’s been a crazy, fun, and stressful (I’m sure for the both of us) time. Over the course of my studies, you went from a research associate into my official supervisor (and full time prof), and I couldn’t have been happier about that. However, that brought along a new set of challenges for the both of us which I think we navigated well for the most part. It’s been an honour being mentored by someone so distinguished and knowledgeable in his field. It’s also been fun, your lighthearted attitude made it a lot easier for me especially in the moments where I doubted myself. I’m sure I could say more but I’ll just leave it at thanks, thanks for everything I couldn’t imagine this journey without you.

Dave, I owe you a lot. You are the reason I decided to pursue my graduate studies at Western and in corrosion. I think my first conversation with you about grad school sold me on the whole idea (and trust me that was a hard sell at the time). I think I’ll always be in awe with you just from your work mentality to the sheer amount of knowledge and patience you have with us students, so from me and anyone who forgets to say it, thank you. I don’t think I would have stayed for a PhD had it not been for the lab environment you’ve helped cultivate. But it wasn’t just the lab environment it’s the guidance, the patience, the honesty, and the great example you set for the students which makes us all want to be better at everything we do. Between you and Jamie I couldn’t have asked for a better team of supervisors.

To my family. You all have been the unfailing rock that has allowed me to push forward through the difficult times. Home may be two hours away but it never felt that far. I can’t thank you enough for the support, love and encouragement throughout my thesis. A lot has happened since I started grad school, both good and bad, but we always stand together and I wouldn’t have it any other way. Mom and Dad, thanks for all your support and love, I wouldn’t be the person I’ve grown today without you two. To Sons and Per, I can’t imagine life without you two. I also have to say I’m so proud of all you’ve accomplished while I’ve been in grad school and I’m glad I was able to attend and see you two grow as much as possible over my time in school. Thanks for always letting me be there when I could.

This is the big one, Pat. I honestly don't know where to begin, but I guess I'll say I got lucky finding you. If my degree had all been for nothing it would be worth doing regardless so I could meet you and fall in love with you. Looking back on all my time in school I wouldn't change a thing because it feels like all of it was leading up to meeting you and falling for you. I think before I met you I wasn't really myself and I thank you for letting me always be 100% me even when it can be inconvenient and tough. Even when I doubt myself, I know you'll be there to pick me up and love me unconditionally. I really can't imagine my life if you weren't in it. I'm so grateful we've had the chance to grow alongside each other. Now I think there's only one remaining step left for us…

The Laylo household has been my home away from home and I can't stress enough how important that has been to me. Much like me the Laylo family has a great love of food and cheesy jokes and we have bonded over the years. I've spent a lot of time at the household sharing lots of laughs and great meals. I've always felt accepted for who I am with the Laylos and that means a lot to me, the support and love they have given me has been monumental. In short there's no other way to put it other than I consider you all family.

Lastly, I can't forget the crazy crew that is the Shoesmith/Noël lab. You all have been amazing. The daily support from this group and the continuing support from past members has been tremendous. No one tells you when you get into grad school you make some friends for life. So, thanks to all the past and present members you've truly made the entire experience what it is and I'm incredibly honoured to be a part of your lives moving forward past school.

This research was funded under the Collaborative Research and Development Grant (CRDPJ507465e16) agreement between the Natural Sciences and Engineering Research Council of Canada (NSERC, Ottawa) and the Nuclear Waste Management Organization (NWMO, Toronto).

Contents

List of Figures

List of Tables

List of Symbols, Abbreviations and Acronyms

Symbols

a_x	Activity of species X
E^o	Standard reaction potential
$E_A{}^o$	Anodic standard reaction potential
$E_C{}^o$	Cathodic standard reaction potential
E_1	Passivation potential
E_b	Breakdown potential
E_{corr}	Corrosion potential
E^e	Equilibrium potential
E_{rp}	Re-passivation potential
F	Faraday constant
ΔG^o	Change in Gibbs free energy at the standard state
I_a/i_a	Anodic reaction current/rate
I_c/i_c	Cathodic reaction current/rate
I_{corr}	Corrosion current
n	number of electrons
S_a	Arithmetical mean deviation of the assessed surface
S_q	Root mean square deviation from the assessed surface
S_z	Maximum height of surface
S_v	Maximum surface valley depth
S_p	Maximum surface peak height
S_{sk}	Skewness of the assessed surface
S_{ku}	Kurtosis of the assessed surface

Abbreviations and Acronyms

AM	As-made
A/P	Active dissolution/Passivity

CC	Charging current
CE	Counter electrode
CLSM	Confocal laser scanning microscopy
CV	Cyclic voltammetry
DGR	Deep geologic repository
EBL	Electron beam lithography
EDX	Energy dispersive x-ray spectroscopy
FE-SEM	Field emission scanning electron microscopy
G1, G2, G3	Generation 1,2 and 3 of multielectrode arrays
I1, I2, I3	Iteration 1, 2, and 3 of generation 3 multielectrode arrays
iPa	Isopropyl alcohol
ME	Microelectrode
MEA	Multielectrode array
MIBK	Methyl isobutyl ketone
MMA	Multichannel multielectrode analyzer
NMP	Non-measured point
NWMO	Nuclear waste management organization
PCB	Printed circuit board
PEB	Post exposure bake
PMMA	Poly methyl methacrylate
RE	Reference electrode
RH	Relative humidity
RPM	Revolutions per minute
RT	Room temperature
SCE	Saturated calomel electrode
SEM	Scanning electron microscopy
SECM	Scanning electrochemical microscopy
SHE	Standard hydrogen electrode

SKB	Svensk Kärnbränslehantering AB
UFC	Used fuel container
UME	Ultramicroelectrode
UV	Ultra violet
VP	Variable pressure
WE	Working electrode
ZRA	Zero resistance ammeter

1. Introduction and Literature Review

1.1 Project Background

1.1.1 The Deep Geologic Repository and Nuclear Power

Nuclear energy is an emission-free energy source that accounts for approximately 15% of Canada's, and over 50% of Ontario's, overall electricity production.[1] A single nuclear fuel bundle can power 100 homes for an entire year.[1] Nuclear power however, is not without its drawbacks. The fuel waste it produces is highly radioactive and dangerous to the environment if mismanaged. If nuclear energy is to remain a sustainable energy source it is necessary to safely manage and eventually disposed of the waste. The current plan for Canadian nuclear waste disposal is to seal the used nuclear fuel in metal containers and dispose of them in a deep geologic repository (DGR), approximately 500 metres below ground.[2] After the used fuel containers (UFCs) are placed in the DGR it will be backfilled with bentonite clay to seal the containers in place, as illustrated in Figure 1.1. This method of placement ensures a self-sealing slow-transport medium for radionuclides if a UFC should eventually fail.

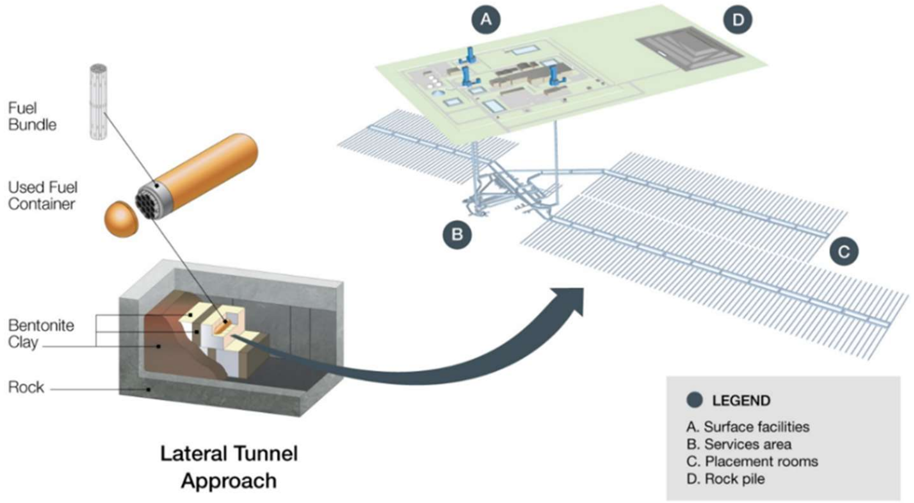

Figure 1.1. A schematic representation of a Canadian DGR[7]

The current UFC design consists of a carbon steel vessel coated with a thin (~ 3 mm) electrodeposited Cu layer with a cold spray Cu coating applied to cover the final closure weld. The Nuclear Waste Management Organization (NWMO) has shown that fabricating the containers in this manner drastically reduces their weight and cost compared to the previous design, which used a separate Cu shell with a thickness of 25 mm.[3]

Once the containers are emplaced and the DGR is backfilled with bentonite and sealed, the conditions the UFCs will be exposed to will slowly and constantly evolve over a period of hundreds of thousands of years. The environment around the container will change in composition and temperature, most notably over the relatively early period of emplacement. Thus, it is important to consider a variety of exposure conditions and corrosion possibilities. The near-field conditions are especially important since they dictate the corrosive species in the environment at the UFC surface.

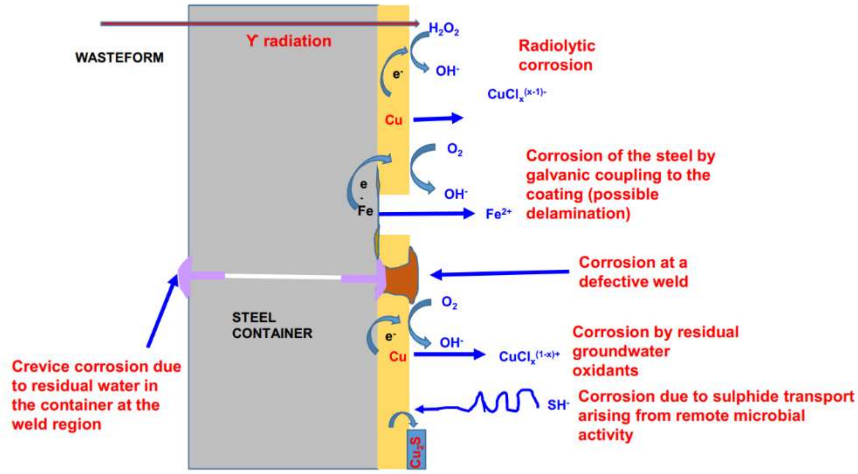

Figure 1.2. Possible corrosion processes at the Cu/bentonite interface in a DGR[8]

Figure 1.2 illustrates the various corrosion processes that can occur at the Cu/bentonite interface. After emplacement the UFC will have a high surface temperature that will decrease as radioactivity emitted by the wasteform decays. If pitting, a form of localised corrosion, is to occur the Cu surface must be passive, which can only occur in the presence of oxidants. Since the main oxidants (dissolved O_2 and radiolytic oxidants) are only present during the early emplacement period, pitting is only possible during this period. The concentration of the oxidants in the groundwater or the bentonite porewater will change over time as they are consumed by reactions with minerals and organic material in the clay. The exact timeline of changes in temperature and composition is uncertain since it will depend on the design and location of the DGR. Recent studies suggest that the O_2 could be entirely depleted within a few months, compared to the original prediction of many years.[4,5,6] This means many of the reactions shown in Figure 1.2 can only occur for short amounts of time due to their dependence on O_2.

The Cu/bentonite interface is expected to evolve through a sequence of exposure periods after emplacement, although their duration, separation and relative importance is only qualitatively known: (1) an aerated period with no condensed H_2O on the Cu surface; (2) a period when the Cu is exposed to aerated and irradiated vapour in equilibrium with a condensed H_2O layer on the Cu surface; (3) a period when a fully saturated, potentially oxidizing aqueous layer is present on the surface and (4) an aqueous anoxic period after available O_2 has been consumed.[7] Throughout these exposure periods the temperature of the container surface will decrease from ~90°C to 70°C, eventually reaching <~20°C after ~10^5 years.[8] In the anticipated repository environment the Cu coating is expected to undergo uniform corrosion.[9] However, the lack of data available to help predict the conditions at the UFC surface, especially in the early oxidizing period, means the possibility of localized corrosion, in the form of pitting, cannot presently be ruled out. Since the Cu coating of the UFC is thin, a measure of the nature and extent of damage to the Cu coating must be determined if the long-term integrity of the UFC is to be assured.

Minimal damage to the UFC Cu coating is expected in exposure period 1 since the environment will be dry. Above 85% relative humidity (RH) in the near-field UFC environment the amount of water condensed onto a metal surface is sufficient to support corrosion, although the specific number of condensed monolayers of H_2O will vary from metal to metal.[10] In period 2, the RH will be constantly changing as the container temperature changes, with a RH> 85% required for corrosion damage to occur.[7] This can be considered the critical RH value for Cu corrosion in a DGR. If this RH is exceeded while oxic conditions prevail in period 3, pitting could be possible, and a probabilistic assessment of pitting damage would be required. However, pitting can only occur if the oxic conditions lead to passivity. Also, the composition of the pore water in the bentonite clay will play a key role in determining whether passivity is possible. This pore water will contain Cl^-, HCO_3^- and SO_4^{2-} and their relative concentrations are expected to determine whether passivation is possible.[11] If it can be demonstrated that pitting will not occur present conservative calculations yield a maximum penetration depth of 1.2 mm over 10^6 years.[12]

1.1.2 Pitting of Copper in a DGR Scenario

In a DGR there are four main factors that can potentially influence pitting. These factors are pore water composition, temperature, H_2O radiolysis and the presence of surface deposits.[9] The most influential features of the pore water are the anions (HCO_3^-, Cl^-, SO_4^{2-}) and the pH. Current knowledge of pH and anion effects suggest that increasing [HCO_3^-] and pH will support passivation while increasing [Cl^-] and [SO_4^{2-}] could either cause passive film breakdown and the onset of pitting or, in the case of Cl^-, total film breakdown and active dissolution.[9] From these studies it is clear that Cu passivation will depend on both the presence of an oxidant and the groundwater composition. Based on early Cu pipeline studies, Cl^- causes local film breakdown and pitting, with SO_4^{2-} exhibiting an even more pronounced effect than Cl^- in comparable conditions. However, results from study to study have proven inconsistent.[9] According to these studies, at low $[Cl^-]$ and low $[SO_4^{2-}]$ both anions can cause pitting, while at low $[Cl^-]$ and high $[SO_4^{2-}]$ the $[Cl^-]$ counteracts the influence of $[SO_4^{2-}]$ on pitting. When $[Cl^-]$ is higher than $[SO_4^{2-}]$ the Cl^- is thought to be mostly responsible for pitting.[9] HCO_3^- has little effect at low concentrations, but when increased it promotes surface passivation. Even though passivation is a prerequisite for pitting, HCO_3^- can inhibit film breakdown by shifting the breakdown potential to more positive potentials allowing passivity to be maintained.[9] An increase in temperature has been shown to promote active dissolution rather than passivity, although published evidence is sparse.[9]

These studies show there is much uncertainty around the possibility for passivation, which could lead to pitting. The studies also show that the possibility for passivation is determined by pH, the relative concentration of groundwater anions and, possibly, temperature. This makes it important to know the conditions and composition of the pore water, which will contact the UFC surface. Originally the groundwater pH was predicted to be between 7.0 and 8.0, but this range has since been refined to 7.5-8.2.[11] The ion concentration ranges investigated in this thesis were 0.1 M-5 M Cl^-, 0.005 M-0.1 M SO_4^{2-} and 0.0001 M-0.01 M for HCO_3^-.[11]

1.1.3 Thesis Goals

Provided the oxidizing conditions defining exposure period 3 are achieved at the container surface, it is important to determine whether passivity could be established, since this is a prerequisite for the occurrence of pitting. Since the pore water conditions at the container surface are uncertain, the first goal of this thesis was to investigate whether Cu would undergo active dissolution, and hence be immune to pitting, or experience passive film formation, and hence be potentially susceptible to pitting (this is termed the active/passive (A/P) behaviour). Analyses were performed in a wide range of environments, which encompassed a variety of possible pore water conditions. This was determined by investigating the behaviour of Cu in a series of unary, binary, and ternary solutions containing various concentrations of Cl^-, SO_4^{2-}, and HCO_3^- at various pH values and temperatures. Many results from other studies have shown that it is likely that if the $[Cl^-]$ is high then active dissolution will be favoured. Ochoa et al., studied O_2-free Cu in groundwater solutions using sheets of copper that were ground to 200-600 grit and coated with epoxy to expose only a 1 cm^2 area.[13] They found that Cl^- promoted active dissolution along with increased temperature, while SO_4^{2-} promoted passive film formation as temperature increased. They also noted that HCO_3^- promoted passive film formation, with pitting in some cases. Li et al. also studied Cu immersed in ammonium sulphate solutions and found that Cu_2O formation was promoted by SO_4^{2-}.[14] Kong et al. analyzed the effect of temperature on Cu corrosion in a high-level nuclear waste environment.[15] They found that an increase in temperature promoted passive film breakdown, therefore supporting active dissolution. This information, found in Chapter 2, was required as a basis for the research described in Chapters 3-6 regarding the study of active dissolution or the evaluation of pitting probability.

The study of active dissolution was the focus of the remainder of this thesis. Chapter 3 explores the fabrication process for multielectrode arrays (MEAs) capable of housing up to 100 electrodes. Different iterations of MEAs and the evolution towards printed circuit board (PCB) MEAs were explored. Different coatings and electronic component combinations were tested to optimize the setup for the MEAs. Multiple optimizations were performed to determine the ideal method of fabricating PCB MEAs. MEAs in this section were analyzed using scanning electron microscopy and optical microscopy.

The experiments described in Chapter 4 were performed to analyze the corrosion damage that a 1 M NaCl solution could produce in accelerated conditions. Acceleration was attempted by galvanostatically charging Cu in O_2-limited solutions and analyzing the corrosion depth and the extent of surface roughening resulting from different charging rates using optical microscopy and confocal laser scanning microscopy (CLSM).

The experiments described in Chapter 5 were performed to determine if the corrosion depth and resulting surface roughening (indicated by surface topography) produced by galvanostatically charging Cu in 1 M NaCl could be replicated by immersing Cu in 1 M NaCl for up to 1 day. Analyses in this chapter were performed using optical microscopy and CLSM. Alternative oxidant solutions were also explored to determine if a valid link could be established between accelerated testing (charging) and non-accelerated testing (immersion) experiments.

In Chapter 6 the information from the previous chapters was used to determine the ideal experimental conditions for the PCB MEAs, as well as to analyze the effect of coatings on corrosion depth and the resulting surface topography. Immersion time and the effect of multiple immersions on corrosive roughening and depth were examined using alternative oxidation solutions to corrode PCB MEAs. The effect of electrode size on surface roughening via active dissolution using the PCB MEAs was also examined to determine if individual anodes/cathodes could be isolated on a single electrode surface.

1.2 Electrochemistry and Corrosion

1.2.1 Corrosion Reactions and Electrochemistry

Natural processes that proceed spontaneously require a negative change in free energy (ΔG). ΔG^o, the free energy change at the standard state in electrochemical terms, is defined by equation [1.1], where n is the number of electrons transferred, F is the Faraday constant (96,485 C/mol) and E^o is the standard reaction potential. E^o is defined in equation [1.2] as the sum of E_A^o and E_C^o, the anodic and cathodic standard reaction potentials.

$$\Delta G^o = -nFE^o \quad [1.1]$$

$$E^o = E_A^o + E_C^o \quad [1.2]$$

Therefore, we can express and determine the thermodynamics of an electrochemical reaction at the standard potential under standard conditions evaluated against the Standard Hydrogen Electrode (SHE). However, most reactions occur under non-standard conditions due to the influence of temperature and the activities of the species involved, as written for the general reaction [1.3],

$$aA + bB \leftrightarrows cC + dD \quad [1.3]$$

in which a, b, c and d are the stoichiometric coefficients.

The Nernst equation for reaction [1.3] can be used to calculate the equilibrium potential (E^e) at a non-standard state as shown in [1.4],

$$E^e = E^o - \frac{RT}{nF}\ln\frac{(a_D)^d\,(a_C)^c}{(a_A)^a(a_B)^b} \quad [1.4]$$

where T is the temperature in K, R is the gas constant (8.314 J/K· mol), and a_x is the activity of species X. Commonly the Nernst equation is written with concentrations rather than activities.

Aqueous corrosion of a material (usually a metal) involves coupled redox reactions, in which an anodic electrochemical half-reaction (oxidation of a metal), reaction [1.5] in which M represents a metal species that is oxidized into a soluble species (M^+), is coupled to a cathodic electrochemical half reaction (reduction), reaction [1.6] where Ox is a generalized oxidizing species (commonly water, protons or dissolved O_2) that is reduced to the generalized reduced species, Red.

$$M \leftrightarrow M^{n+} + ne^- \qquad [1.5]$$

$$Ox + ne^- \leftrightarrow Red \qquad [1.6]$$

$$M + Ox \rightarrow M^{n+} + Red \qquad [1.7]$$

Reactions [1.5] and [1.6] are coupled half reactions occurring together on the metal surface to yield the overall corrosion reaction [1.7].

1.2.2 Corrosion Potential (E_{corr})

The corrosion potential (E_{corr}) is a potential measured at open circuit on a corroding material that is unique to the system. Since it is measured at open circuit no control over the potential or current is exerted during this measurement. At E_{corr} the rate (current) for the metal dissolution half reaction (i_a) is equal in magnitude and opposite in sign to the rate (current) for the oxidant reduction half reaction (i_c). This is because each half reaction is polarized away from its equilibrium potential leading to overpotentials for both reactions which generate a positive current for the anodic reaction (I_A) and a negative current for the cathodic reaction (I_C). The equal and opposite currents of both half reactions comprising the corroding system also indicates that at E_{corr} a mass balance is achieved, therefore an equal amount of material is being oxidized and reduced simultaneously. The measured current at E_{corr} is referred to as the corrosion current (I_{corr}) which can only be achieved at E_{corr}, as depicted in Figure 1.3.[16,17,18] .

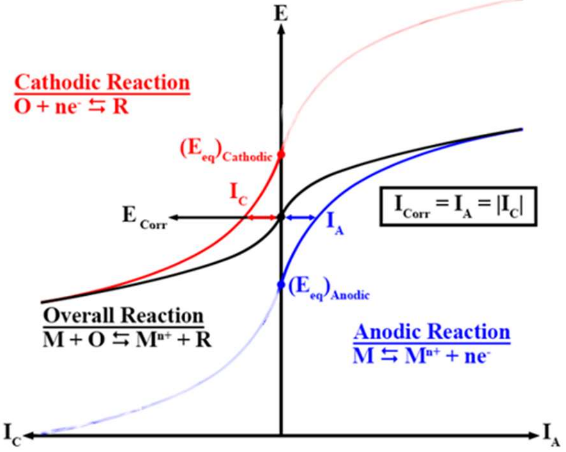

Figure 1.3. A diagram showing the coupling of anodic and cathodic half reactions to determine the corrosion potential and current.[16,17]

1.2.3 Potentiodynamic Polarization

In potentiodynamic polarization a potential scan at a constant rate is applied to an electrode and the current response measured as a function of potential. Figure 1.4 shows a schematic anodic polarization curve in which the potential is scanned in the positive direction. This schematic shows the three main regions commonly observed on a metal that can achieve passivity over a particular potential range. The first region, the active region is denoted by A, and B. In this region the metal dissolution current density increases exponentially as the potential is increased. Once the potential increases beyond B, the current decreases as oxide film formation begins and the rate of metal dissolution decreases; i.e., the metal undergoes an active-to-passive transition, which is complete when the potential reaches C. In region D the metal is passive and the current becomes independent of potential and dependent on the film properties (i.e., thickness, number of point defects, chemical dissolution rate). However in region E, termed the transpassive region, the current increases again. This increase can be due to the oxidation of H_2O to O_2 and/or the oxidation of cations in the oxide to higher more soluble oxidation states.

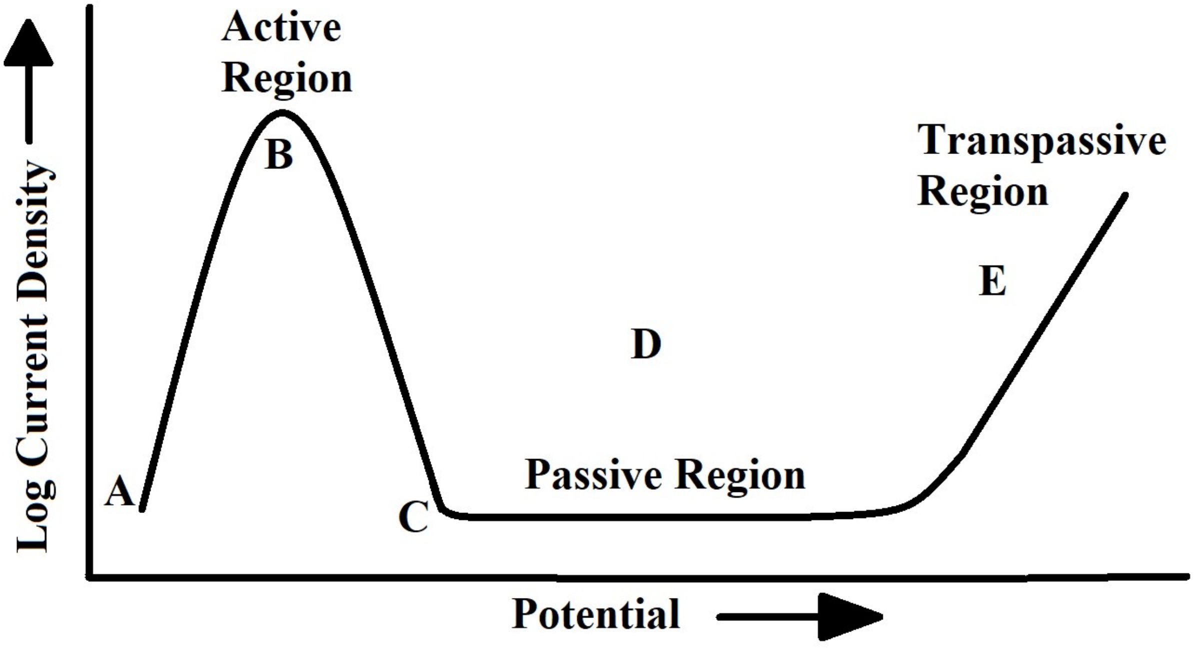

Figure 1.4. A schematic anodic polarization curve with important regions labelled A-E

A common polarization technique is cyclic voltammetry (CV), which involves applying a potential and scanning it from a designated potential (usually E_{corr} for corrosion experiments) to a specific value and back again, while measuring the current response. When the potential is scanned forward (towards more positive potentials) the features illustrated in Figure 4 are commonly observed on metals, which can form a passive film. When the scan is reversed (scanned towards more negative potentials) the state of the electrode will determine the current observed. If the metal is passive (i.e., the potential is reversed in region D), the current will remain low until a potential is reached at which the film can be electrochemically reduced, when a negative current would be observed. If the potential on the forward scan was reversed at a value in the active region, the current can retrace the values recorded on the forward scan as the current for the metal dissolution reaction decreases with decreasing potential. The potential range scanned depends on the specific reactions being investigated. A low scan rate is commonly used to allow the system to maintain a rate close to steady-state throughout the scan, thus allowing slower reactions to occur.[19] This is particularly important for oxide film growth, since growth will be accelerated at higher scan rates and the film properties will not reflect those of a naturally grown passive film.

1.2.4 Galvanostatic Polarization

In galvanostatic experiments the applied current is controlled and the potential response measured. Since the current is a measure of the reaction rate, galvanostatic experiments control this rate. The integrated value of the applied current over the time yields the charge (Q) consumed. Galvanodynamic experiments allow the rate to be changed in a controlled manner as an experiment is being performed. This allows changes in charging rate or total charge to be evaluated. Multiple charge/discharge cycles are commonly referred to as galvanodynamic cycling. Galvanodynamic experiments are also used to simulate scenarios in which a reactant is consumed over time, charging/discharging frequently occurs or the reaction rate frequently changes. Galvanostatic polarization (also commonly referred to as galvanostatic charging) offers the advantage of holding the current supplied at a specific value, allowing constant current scenarios to be more readily established.[20] In this manner the overall reaction rate can be controlled and the total amount of corrosion calculated.

1.3 Analysis Instruments and their Associated Techniques

1.3.1 Optical Microscopy

Optical microscopy was performed with a Zeiss microscope with confocal capabilities. This microscope is fitted with various objective lenses: 5×, 10×, 20× and 50×. The 10× and 20× magnifications each have 2 lens' that change the focal length, allowing for analysis of tall samples. The microscope changes between confocal and optical analysis by passing light through a reflector cube. The main advantage to using this microscope is the precise stage control it has in the x, y and z directions. While precise control in the x and y dimensions is common, the important feature is the control in the z-direction allowing for z-stack imaging in both optical and confocal analyses.

1.3.2 Z-stack Imaging

Z-stack imaging is a method of optical imaging in which images are taken at different z-values (heights) for a sample at a defined (x,y) position. Either a feature or an entire surface is analyzed with z-stack imaging. Images are taken between two points. These two points are the most over-focused (maximum) point and the most under-focused (minimum) point at a chosen magnification. The images are then compiled together and edited. The editing method removes all the unfocused sections in each image, while retaining all the in-focus sections. The resulting image is completely in focus and all of the topographical features between the maximum and minimum points are clearly visible.

1.3.3 Scanning Electron Microscopy (SEM)

SEM uses a focused beam of electrons accelerated at a designated voltage in a vacuum to scan a conductive surface. Electrons are generated at the top of the column at the electron source, as shown in Figure 1.5. The acceleration is performed by the anode, which is positively-charged. The condenser lens converges the electron beam, which is then rastered across the surface by the scanning coils and the returning electrons are used to create an image.[21] A lower raster rate results in a more accurate image. The size of the beam can be controlled by an aperture in addition to the objective lens, which also converges the beam as it is rastered. The image is produced when the desired electrons reach the detector. Secondary electrons, backscattered electrons and characteristic X-rays all require different detectors due to the angle they are ejected from the sample and their energy when they reach the detector.

Multiple different types of energy and electrons are emitted as a result of the electron beam interacting with a conductive surface, as shown in Figure 1.6. Backscattered electrons are primary electrons ejected from the solid sample at an angle above 90°, which is the product of a small energy exchange from elastic scattering.[22] Therefore, backscattered electrons have energies close to the primary beam, which makes them distinguishable from secondary electrons. Backscattered electrons typically help elucidate the variation in chemical composition through contrast in brightness of the image. Backscattered electrons also originate from much deeper in the sample compared to secondary electrons as shown in Figure 1.6.

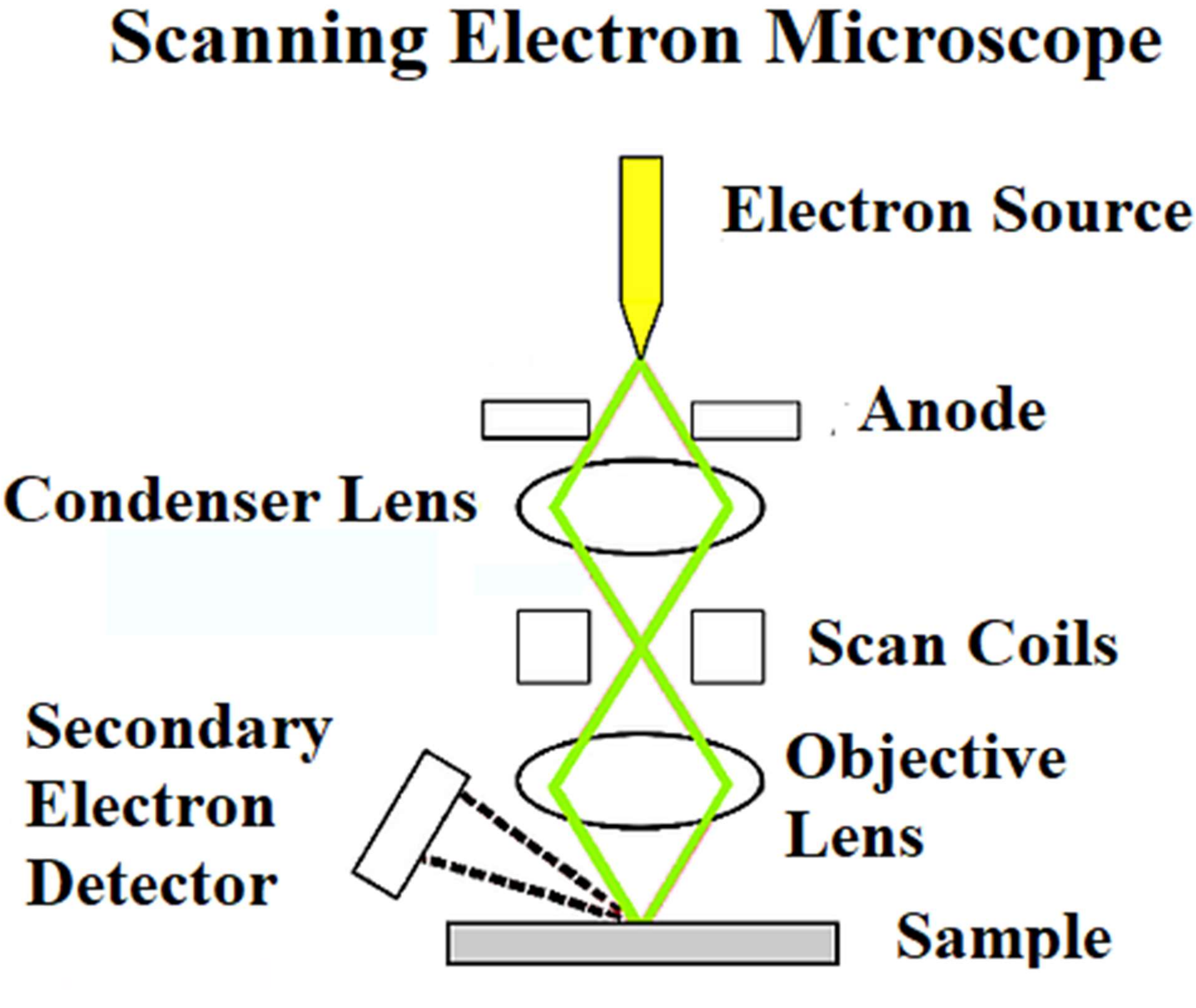

Figure 1.5. A schematic illustration of basic SEM components[23]

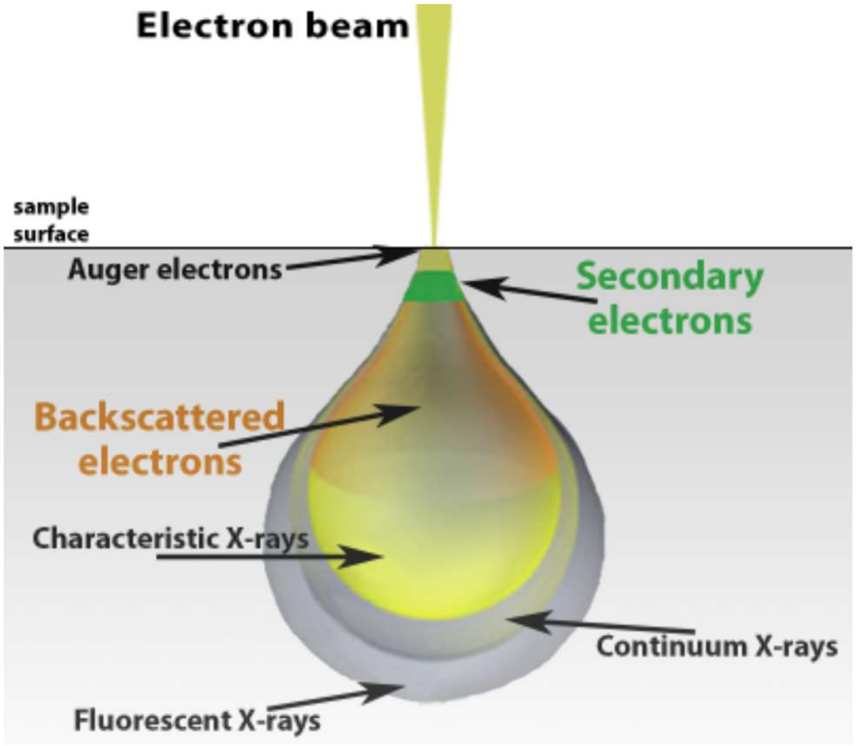

Figure 1.6. A schematic diagram of electron beam interactions with a sample surface during scanning electron microscopy[24]

Typically, secondary electrons are measured using the detector in the instrument to create images. Secondary electrons are valence or conduction electrons weakly bonded to the nucleus of the material and are a result of inelastic scattering in which a small portion of their gained energy is used to escape from an atom. The electrons are inelastically scattered as they escape the material and lose their kinetic energy in the process, meaning they originate from very small depths (< 2 nm) below the surface.[22] Secondary electrons, compared to backscattered electrons, give topographical contrast information rather than chemical composition.

Characteristic X-rays are generated when a primary electron collides with an inner-shell electron of an atom. This requires more energy to excite the inner-shell electron, and therefore a higher energy photon is emitted as the characteristic X-ray.[22] These require a separate detector to analyze, these X-rays are the basis for the technique energy-dispersive X-ray spectroscopy, which gives an accurate elemental composition of the sample surface. It is common using this method to generate elemental maps, which can be overlaid on a SEM image to correlate elemental composition to different features on the sample surface.

Non-conductive materials (such as organic surfaces) cannot be accurately imaged using SEM because the electron beam will charge the material rather than eject electrons.[21] The electronic charge built up on the non-conducting surface deflects the electrons back to the detector and obscures the image. The accumulation of surface charge on a specimen can be circumvented by using a variable pressure (VP) SEM, which introduces specified amounts of gas into the chamber. The gas molecules are ionized in the chamber and the resulting ions can neutralize the charge built up on the specimen surface, which allows a non-conductive sample to be analyzed.

1.3.4 Confocal Laser Scanning Microscopy (CLSM)

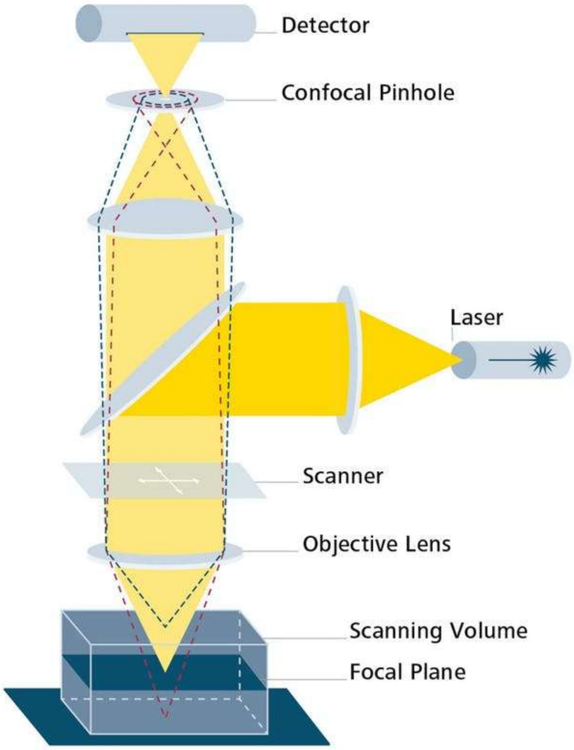

Figure 1.7. A schematic diagram illustrating a typical CLSM light path[25]

CLSM is a technique commonly used in conjunction with optical imaging. CLSM uses a light source, typically a laser, to project light through an objective lens onto a sample surface. The projected light is then reflected by the sample surface and passes through a pinhole on its way to a photodetector illustrated by Figure 1.7. The detector pinhole is calibrated to only detect light intensity in a designated range, which encompasses in-focus light rays. A stepper motor is often used to control stage movement in the x, y and z- directions and focus the laser in a designated area. The laser used in this thesis had a wavelength of 405 nm. Based on return intensity and location of the reflected light the sample topography can be determined in the x, y and z-planes by reconstructing a 3D image of the analyzed location. It is important to note that a 3D reconstructed image is comprised of a series of line profiles. Typically, a CLSM image is produced using the z-stack imaging method in order to obtain accurate sample height information, which allows a 3D reconstructed image of the imaged area to be produced and analyzed via confocal analysis software (Confomap® in this thesis).

1.3.5 Roughness Analysis

The CLSM analysis suite (Confomap®) has many tools to analyze the data collected by the Zeiss microscope. The optimal method for roughness analysis is conducted in three steps. Throughout the entire analysis process a set of roughness parameters is generated in a table format (called a roughness parameter table) before and after each operation to ensure data are not being over-manipulated. First, images have outliers and noise removed using the remove outliers function. This operation is performed to remove false height data that often appears as single large peaks or pits on the surface. These false data are produced by over-/under-focusing (this is reflected in the S_z parameter, section 1.3.6) and are usually the product of light being reflected at an odd angle (peaks) or being trapped (pits). The second operation (levelling) levels the surface based on an average baseline created from the average height values of the surface. This operation is not always necessary but, for larger coupons, it helps to negate slopes either introduced by the grinding/polishing process or due to an uneven base/sample holder. Typically, smaller samples do not need to be levelled. The third operation generates a series of profiles and/or 3D reconstructed images to verify and supplement the roughness parameter values. A series of profiles and the 3D reconstructed images help visualize sample topography. A series of profiles can correspond to individual vertical or horizontal lines of measurement across the surface, these values can be sorted by the pixel count in the image and their corresponding pixel row or column.

3D reconstructed images were the main method adopted to analyze surface topography or any unique surface features/patterns in this thesis. If any aspects of the 3D reconstructed image were unclear the optical image used to produce the 3D reconstructed image was consulted to verify the data integrity.

1.3.6 Roughness Parameter Definitions

There are 7 roughness parameter measurements generated using Confomap® that can evaluate the roughness of a sample.[26] These values are S_q, S_{sk}, S_{ku}, S_p, S_v, S_z, S_a.

S_a, S_q and S_z are the main parameters used to determine roughness.[26] S_a is the arithmetical mean deviation of the absolute values of the surface profiles and is the most commonly used parameter to define the average roughness. S_a is not heavily skewed by outlier peaks or valleys since the values are absolute. S_q is the counterpart to S_a; and defined as the root mean square deviation of the surface profiles and places more emphasis on larger height values than S_a. S_z is defined as the total height of the sample. S_z is calculated by taking the absolute value of the lowest point on the sample and adding it to the highest point on the sample; the minima and maxima are labelled as S_v and S_p respectively. This makes S_z the absolute sum of two of the listed roughness parameters.

S_{sk} and S_{ku} are descriptive parameters that describe the shape or nature of the roughness.[26] S_{sk} represents skewness, which is defined as the quotient of the mean cube ordinate and the cubed value of S_q. S_{sk} values describe whether the surface is above or below the measured mean line of the surface. The skewness values are analyzed relative to 0 and to each other. A negative skewness value indicates the surface is mostly above the mean line while a positive skewness dictates the surface is mostly below the mean line. S_{ku} is the kurtosis of the surface profiles. This is the mean quartic value of the surface profiles. Kurtosis describes the shape of the surface and differentiates between spiky and bumpy surfaces. Kurtosis is also a relative value. A high Kurtosis value indicates a spiky surface, while a low value indicates a bumpy surface, however unlike S_{sk}, Kurtosis is not measured relative to 0 and has to be standardized. S_{sk} and S_{ku} are useful values, but they must be standardized per data set or the values will only indicate a trend if there is no prior knowledge of the sample. Due to the lack of a standardization procedure and the availability of the 3D reconstructed images S_{sk} and S_{ku} were not used in analyses in this thesis.

1.3.7 Profile Versus Surface Analysis

Roughness parameters can be generated for the entire surface or for a single profile (horizontal or vertical line of data pixels). Profiles and surface roughness parameters can be differentiated in the Confomap® software based on the capital letter before the subscripted letter in the roughness parameters table. The letter S is designated for whole surface analyses and the letter R is designated for single profiles. A profile yields more detailed information for a single slice of the collected image, while a surface analysis gives an overview of the entire collected image. However, profiles can have values that differ greatly from those in the surface analysis, since there is a reduced averaging effect due to the lower number of data points recorded in a profile. Profiles are most useful when analyzing local height differences or determining the S_z value of a specific feature. Surface analyses are used in this thesis since the general trends for an entire surface were of primary interest.

1.3.8 Multichannel Microelectrode Analyzer (MMA)

The MMA is a configurable galvanostat/potentiostat that has 100 controllable and measurable connections grouped into 5 cables with 20 connections, which are subdivided into two smaller cables with 10 connections each.[27] Each set of 10 connections can be outfitted with an electrometer for measuring potential or a zero resistance ammeter (ZRA) allowing current measurements.

The MMA has been used in many applications such as measuring sensor arrays, impedance analyses, catalyst investigation, and most prominently corrosion studies.[27] With a large number of connections, which can be controlled or used to make measurements, many experimental configurations are possible, including their use for multielectrode arrays (MEAs), in which micro-sized electrodes in close proximity can be used. These microelectrodes (MEs) can be galvanically coupled to simulate a macroscopic surface as demonstrated by Hampel et al, who used stainless steel MEAs with the MMA, in conjunction with scanning electrochemical microscopy to detect localized corrosion.[28] Another common application of the MMA is high throughput testing due to its large number of connections. Chambers et al. performed high throughput testing of various corrosion inhibitors using 50 individual cells containing 2 different wire electrodes (using a total of 100 connections).[29] In this study, they measured currents at each electrode with the individual wire electrodes polarized at different potentials to test the corrosion inhibitor solutions. Droplet studies are also common using the MMA, in which the effect of droplet size, composition and shape can be studied. Muster et al. used a MEA consisting of Zn wire electrodes and deposited droplets of various volumes to study the effect of size and droplet shape on the electrochemistry.[30]

It is evident that the large number of connections, with the ability to measure/control them gives the MMA compatibility with a wide variety of experiment setups.

The final configuration for measurements using the MMA involved connecting each of the main ribbon cables into the circuit board adapter described below in 1.3.9. The adapter consolidates these connections and groups them into an output cable which connects to the centre of the circuit board adapter as seen in Figure 1.9. The output cable then connects to a MEA which is a smaller circuit board. The electrodes on the MEA were covered and immersed in solution using the tank cell as described below in 1.3.11.

A typical snapshot of the MMA data output for one measurement interval is shown in Figure 1.8. Each square represents a single electrode. The arrangement of the squares is customizable and arranged to replicate the actual array shape. In this case it is designed to replicate a circuit board MEA that is described later in Chapters 3 and 6. The colour of a square indicates the relative magnitude of the current and the sign of the measured current based on the colour legend shown below the output grid. According to the colour legend, cathodes are represented by blue and green which correspond to large negative currents. Yellow and white squares indicate neutral or almost neutral currents which correspond to small negative or positive currents very close to or equal to zero. Red, pink and purple squares indicate anodes which correspond to large positive currents. Black squares are omitted from the measurement process indicating blank areas in the MEA.

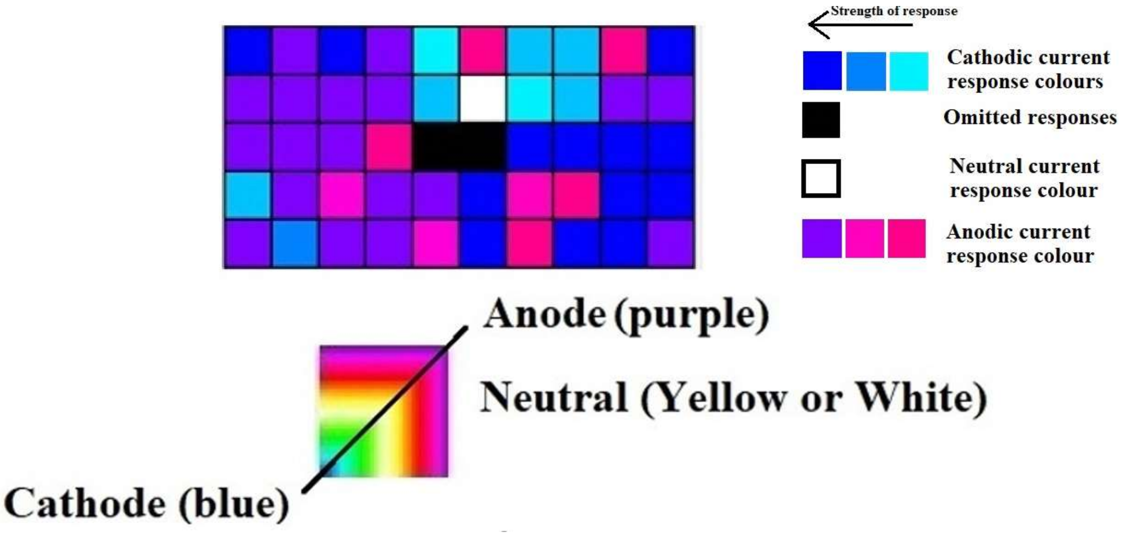

Figure 1.8. An example data output frame from a single measurement interval on the MMA

1.3.9 Circuit Board Adapter

The circuit board adapter was designed and built by the UWO chemistry machine shop to reduce cable clutter caused by the MMA ribbon cables. The board has 5 pairs of 34-pin ribbon cable connectors around its outer edge and one 50 pin connector in the centre used to connect to the MEA as shown in Figure 1.9. Each of the headers within the 5 pairs of connectors on the circuit board adapter is specifically configured to connect with either an “odd” or “even” cable from one of the 5 main ribbon cables connected to the MMA. This is because the wiring is different between the odd- and even-labelled cables. Each of the 10 connections of the odd and even numbered cables are paired within by an individual trace that runs between each pair of connectors on the circuit board adapter that leads to the 50-pin connector. Therefore, each of the 5 main MMA ribbon cables has its subdivided cables measuring inputs paired together. This design effectively limits the MMA measuring capacity to 50 electrodes. The rationale for this design was to reduce clutter and pair the connections to simultaneously measure current and potential with a single connection on the 50-pin ribbon cable.

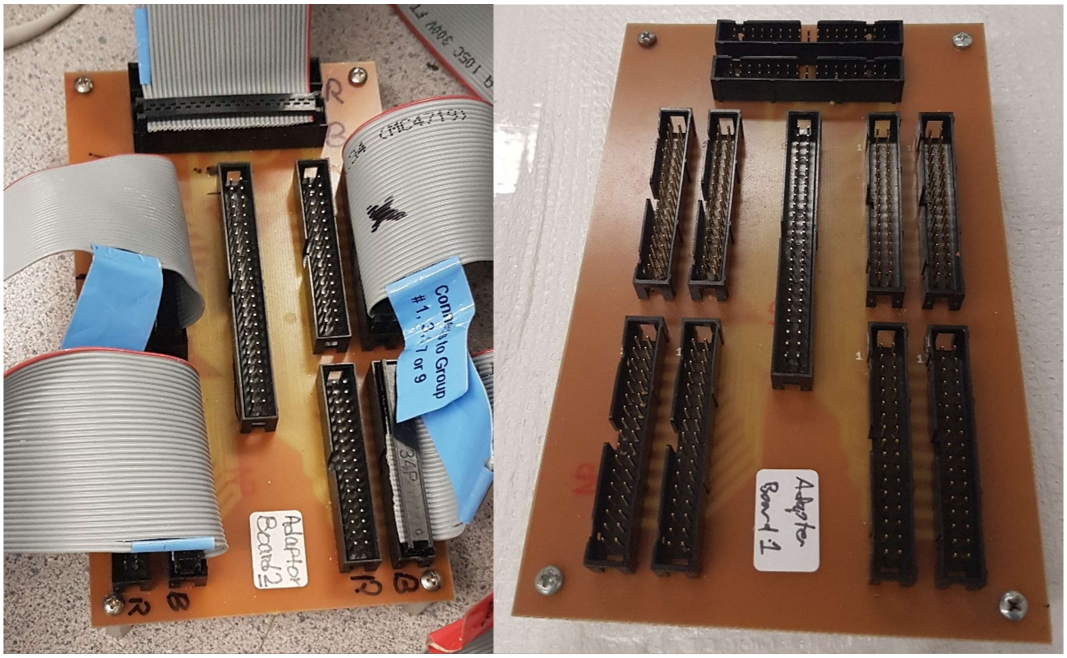

Figure 1.9. The circuit board adapter designed for use with the MMA. On the right is the unplugged board, on the left the board is set up using a cable configuration for an experiment without the 50-pin connector for the sample in the centre

1.3.10 Microcell

Due to the size of the MEAs and MEs used in this thesis the cell used to hold solution was designed to limit the amount of solution exposed to the total area of the MEA. Additionally, a small electrode surface area to solution volume ratio decreases the chance of rapid reagent depletion, as opposed to a cell with a large ratio where reagent depletion is common. A cell was made by trimming a borosilicate glass O-ring joint with a Viton® O-ring. A specialized clamp with a Viton® O-ring was used to pressure seal the glass joint over the electrodes of the printed circuit board (PCB) MEAs to prevent solution loss, Figure 1.10. The main disadvantage to this cell was the inability to fit a standard SCE reference electrode inside along with a counter electrode. Also, gas sparging risked splashing solution out of the cell and onto the 50-pin ribbon cable connections.

Figure 1.10. The assembled microcell clamped onto an array sealed with an O-ring and the pressure applied by the clamp. An additional smaller cell can be seen to the left

1.3.11 Tank Cell

The tank cell was designed to overcome the space limitations of the microcell. The tank cell was made by fusing a standard 250 mL beaker to the top of the microcell. The larger beaker on top was fitted with a butyl stopper wrapped in Teflon® tape with holes drilled in the top to accommodate a reference electrode, counter electrode and sparging tube as shown in Figure 1.11. The sparging tube was placed deep enough in the cell to promote solution convection in the narrow microcell portion of the cell. This design still exposes the MEA electrodes to the same volume of solution as in the microcell, but resolves the two key issues that made the microcell less practical (the lack of convection and the inability to house a reference electrode). This design also retains the pressure sealing clamp and O-ring used with the microcell, which now seals the tank cell to the MEA.

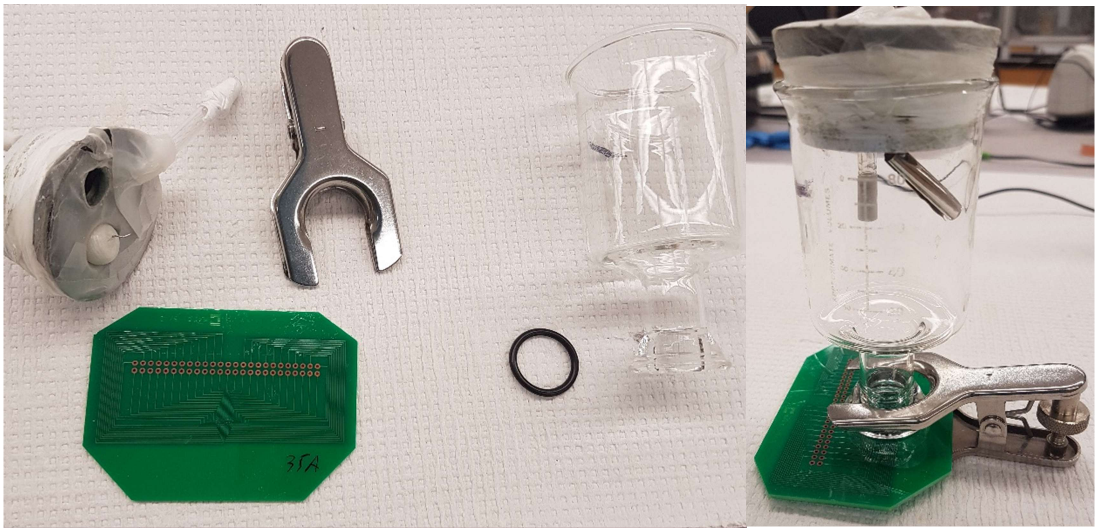

Figure 1.11. The disassembled tank cell setup (left) and the assembled version on the sample without a reference electrode (right)

1.3.12 Corrosion Potential Measurements

Corrosion potential (E_{corr}) (open circuit potential (OCP)) measurements on the MMA are performed slightly differently compared those performed with a conventional multistat/potentiostat/galvanostat and a three-electrode electrochemical cell. This is due to the design of the MMA hardware, which causes the potential measurement to directly influence the current measurement rather than being independent if they use the same cable or are measured in sequence.[27] Therefore, performing these measurements simultaneously for each individual electrode creates unreliable readings. Consequently, for the purposes of this thesis only current was measured across individual electrodes and the overall potential was monitored using a SCE (saturated calomel electrode) to avoid the issue with unreliable readings. This means that all cables that could measure potential were disconnected. No CE (counter electrode) was used since the potential was not controlled for these measurements and a glass joint with a frit to prevent contamination of CE reaction products could not be feasibly fit into the tank cell. The current measured in these experiments is the current relative to the surrounding electrodes and groups of electrodes (intraelectrode and interelectrode current respectively) since the current passes through adjacent electrodes to complete the circuit rather than a counter electrode.[27] It is possible electrodes in the MEAs can galvanically couple based on surface features. Measurements were also made in Ar-sparged solution to promote convection and remove O_2.

1.4 Fabrication Techniques

1.4.1 Spin coating

Spin coating is a technique used to apply thin layers of polymers or photoresists onto a substrate.[31] The coating process evenly distributes a suspension or solution using centrifugal force.[31] Spin coating is performed by depositing a small amount of polymer in a suspension on the centre of the chosen substrate while it is stationary. The substrate is then spun slowly to evenly spread the suspension, after which the speed is increased to remove excess polymer and create a uniform, thin layer. After the desired layer thickness is achieved, the spin speed is decreased until the spin has fully stopped to prevent the sample from falling off the mount. The thickness of the layer is determined by the spin speed and compound itself. Most compounds come with manuals that include calibration curves to determine thickness values on ideal substrates. The speed at which a substrate can be spun depends on its size and shape. Samples are held on a mount, commonly referred to as a chuck, with a hole in its centre that connects to a vacuum system. Samples are centred over the vacuum portion of the chuck and suctioned in place. The vacuum suction is the only force holding the sample in place.

1.4.2 Electron Beam Lithography (EBL)

Electron beam lithography uses a focused beam of electrons to scan or trace a particular pattern over an electron-sensitive film, otherwise known as a resist. When the beam is scanned over the resist the crosslinking process is initiated. This is referred to as “exposing” a resist. This process is similar to how photography uses light to initiate photochemical reactions to produce an image on a film surface. Depending on the type of the resist, exposure will solubilize or cure (harden) the resist allowing sections of it to be easily removed via a chemical developer. EBL is popular due to its very high resolution, which allows it to produce patterns in the nm range with a high degree of accuracy. Since the electrons are stable in vacuum and samples often require imaging prior to EBL, systems are created using attachments that modify electron microscopes, such as SEM systems, to give them the ability to perform EBL.[32] The primary flaw with these combined systems is that during the imaging phase with SEM it is highly possible to accidentally expose the substrate before proper EBL tracing if there is no previous knowledge of the sample.[32] Therefore, performing EBL involves first quickly taking a SEM image at a low voltage and beam intensity to avoid exposing the resist. Then a pattern is created and overlaid using the surface image to map to the specific areas where exposure is desired. The appropriate dose rate before exposing the resist is calculated after creating the pattern to ensure that the film is not over-exposed, which would make it brittle.[32] After the calculation, EBL can be performed with an automated system or by manually inputting the coordinates determined in the imaging phase to move the beam to the appropriate areas.

1.4.3 Photomask and Mask Aligner (Photolithography)

A photomask is an opaque series of silica plates fused together that contain holes or transparencies arranged in a unique pattern etched into one of the layers that is designed to allow or block light for photolithography.[33] The pattern design itself is dependent on the type of photoresist used.[33] Photomasks are designed to aid in exposing photoresists to a light source; the masks used in Western's Nanofabrication Facility are set to be used with 365 nm UV light. A mask aligner is often used in conjunction with the photomask to ensure that exposure occurs at the desired area of the sample. The mask aligner is used after the sample has had a photoresist applied and has been soft baked to remove the tackiness from the resist (refer to the Chapter 3 for more information). The mask aligner uses a vacuum system to hold the photomask and sample in place with a moveable stage below the sample. The stage movement is used to align the photomask pattern with the sample. The alignment is checked using optical microscopy. While the sample is being aligned, the mask and the sample are at "separation pressure", which is a manually calibrated value that is defined as the force required to put the sample and photomask almost into contact. Once alignment is finished "contact pressure" can be applied, which is a higher, manually chosen pressure that is chosen to ensure contact between the sample and the photomask. At either contact or separation pressure the sample can be exposed using the attached, calibrated UV source with a monochromator (a full spectrum Hg lamp). Any exposure cycles required for the sample were manually performed.

1.5 Metal Structure and its Effects on Reactivity

1.5.1 Metal Grains

The metallic Cu crystal has a face-centred cubic (fcc) unit cell. All crystalline metals are composed of grains with distinct surface planes. The orientation and direction of these surface planes or exposed surfaces can be described using Miller indices. Miller indices for fcc lattices are described using a 3-coordinate cubic Cartesian system such as (*hkl)* where xyz values are the reciprocals of *hkl*, respectively, and *hkl* are integers. Planes which are parallel or sometime perpendicular to each other, such as (100) and (001), are considered to be equivalent, any values of *hkl* that are parallel to the planes defined as the origin are considered to be equivalent to zero resulting in a x, y or z value of 0.[34]

Cu has three main grain orientations: (111), (100) and (110). Grain faces can have different surface energies and some grain faces are known to react at different rates compared to others. An example of this is Si wafers which are standardized to be cut at the (100) or (111) planes. The (111) plane for Si wafers is known to etch slower compared to other planes which allows more predictability when fabricating micro- or nanostructures using this face. A schematic depicting the 3 main grain faces of Cu is shown in

Figure 1.12. Areas at which dissimilar grains meet are known as grain boundaries which can also have differing reactivities compared to the grains depending on the stress in the boundary.

If surface energy is related to reactivity or surface stress it can be reasoned that exposed planes with higher surface energies will react faster than those with lower surface energies. According to previous studies the (111) plane has the least, and the (110) plane the most, surface energy making reactivity or corrosion more likely on the (110) oriented face.[35] Corrosion would be expected to proceed via preferential grain dissolution. However, the grain size is also a factor when considering the relative reactivity of grains.

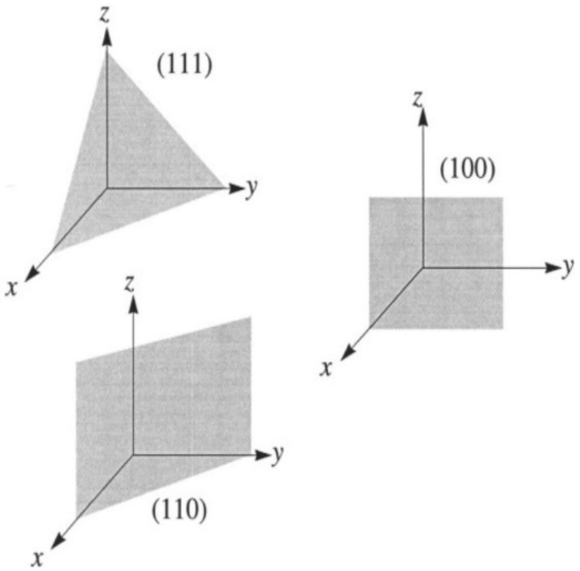

Figure 1.12. A schematic depiction of the 3 main grain faces of Cu using a 3-coordinate cubic Cartesian coordinate system[34]

1.5.2 Studies Involving the Reactivity of Copper Crystal Planes

While it is possible surface energy can be a limiting factor in determining grain reactivity, many studies have shown that Cu grains have varied reactivity depending on the exposure conditions. The dissolution kinetics of Cu grains in Cl^--based solutions has yet to be studied, but there are many studies which can provide some helpful insight into what to expect if preferential grain dissolution occurs.

If surface energies are the only factor to consider then the studies by Setty and Mayanna and Vitos et al. provide insight into grain dissolution rates.[35,36] Setty and Mayanna studied the effect of adding halide ions to dilute H_2SO_4 on the dissolution rate of individual grain types of Cu. It was found that the (110) plane dissolved the fastest and the (111) plane the slowest when Cl^- was added. The trend was the same when no Cl^- ions were added.[36] The study performed by Vitos et al., which calculated the surface energies of different planes for various metals also indicated that the (110) plane for Cu had the highest, while the (111) plane had the lowest, surface energy.[35] If surface energy is indicative of reactivity then these two studies yield similar conclusions regarding Cu crystal plane reactivity.

Sheshadri and Nandeesh studied the enhanced reactivity of the (110) plane compared to the (100) and (111) planes. An inhibitor was used to prevent corrosion of Cu single crystal planes in 0.1 M H_2SO_4. Even with an inhibitor present the (110) plane was found to dissolve faster than the (100) plane, which in turn dissolved slightly faster than the (111) plane.[37] However, this study also introduced another factor to consider which is the surface adsorption of species to specific planes. It was concluded that the inhibition of the dissolution was due to surface adsorption of the inhibitor. Other studies investigated the reaction rates of different Cu crystal planes and primarily examined the surface coverage of reactive species onto specific planes to determine the reactivity. A good example of this is the research by Vvedenskii et al. who analyzed the kinetics of formation of Cu oxides on Cu single crystals. As part of the oxide formation process the Cu crystals first adsorbed OH^- on to the surface with the Cu (111) crystal having the highest percent coverage by OH^- while the Cu (110) had the lowest which is opposite to the previously predicted trends.[38] However, the adsorption is dependent on the reactive species as shown by a study performed by Mayanna, in which the adsorption of I^- to single Cu crystal planes in H_2SO_4 was examined.[39] In this study it was determined that Cu (110) had the highest, while Cu (111) had the lowest, surface coverage, consistent with the trends described in other studies.[35,36,37,39]

There are many studies in which Cu single crystals are used as electrodes/catalysts for organic reduction reactions. For example, Cu single crystals have been used in the reduction of CO into other organic products such as ethylene. In these studies it has been demonstrated that certain crystal planes have better reactant adsorption and that different planes are selective for different anions/cations depending on their size. Huang et al. studied Cu (100) and Cu (111) crystals which have similar surface energies and found that Cu (100) is slightly more reactive as a result of its surface structure and has a higher CO coverage when reducing CO to ethylene.[40] Koper and coworkers have also studied the use of Cu single crystals to reduce CO to various products, primarily using Cu (100) and Cu (111) crystals. These studies show that Cu (100) is more likely to reduce CO and the Cu (100) crystal also accommodates larger ions compared to the Cu (111) crystal.[41,42]

The last consideration alongside surface energy and reactant adsorption for grain reactivity is the surface structures on individual grains such as terraces divided by steps. While the reactivity of these features is not widely studied for Cu crystals it is generally regarded that steps are more reactive than terraces. Koper et al. studied CO reduction on Cu (100) crystals and found that reactions occurred exclusively on terraces rather than steps, likely due to the instability and limited reactive surface area of a step.[43] Overall, studies on crystal orientations have shown, that despite the many factors to consider, it is likely that the Cu (110) plane will dissolve preferentially followed by Cu (100) and Cu (111). However, the surface adsorption of the species must be considered as well as the surface features present on individual grains along with the grain sizes which could limit reactive space. If the grain size is small enough it could reduce the gap in dissolution rates if corrosion of Cu proceeds through the adsorption of Cl^- or O-species onto the reactive surface.

1.6 Previous Literature

1.6.1 Array Overview

Multielectrode arrays, commonly referred to as MEAs, consist of small electrodes arranged in a two-dimensional pattern with a specialized interface designed to connect to a measurement instrument of choice. MEAs can vary in size, pattern and function. MEAs are commonly used to simulate bulk surfaces or perform high throughput measurements. MEAs are mostly used in biological studies, specifically to analyze neural activity or cell signals. MEAs allow for accurate identification of activity of cell cultures, propagation of neural signals and networking multiple neurons compared to single electrodes.[44] These advantages are largely due to high spatial resolution, and the biocompatibility of the MEA substrates. This is a constantly advancing field, with the majority of the published work utilizing MEAs involving biological analysis and modification of MEAs to optimize the analysis. In biological studies the MEAs interface directly with the measured tissue, and therefore the flexibility of the MEA substrate is extremely important. The placement of the MEA is shown in two configurations in Figure 1.13: active and passive, though these terms have a different meaning from the typical corrosion standpoint. Passive arrays measure the voltage of the sensing pad in reference to the inactive parts of a living cell. Active arrays are the natural progression from passive arrays because they use a transistor to amplify the sensing pad and multiplex each cell, which reduces the total number of wires and increases the spatial resolution.[44] Three criteria stand out when designing MEAs for biological purposes: conformability, transparency and biocompatibility. [44] Conformability increases the surface area of the living cell that can interact with the MEA. Transparency allows optical microscopy to be performed in tandem with voltage or current measurements. Biocompatibility increases the stability of the array and lengthens the maximum possible exposure for an experiment.

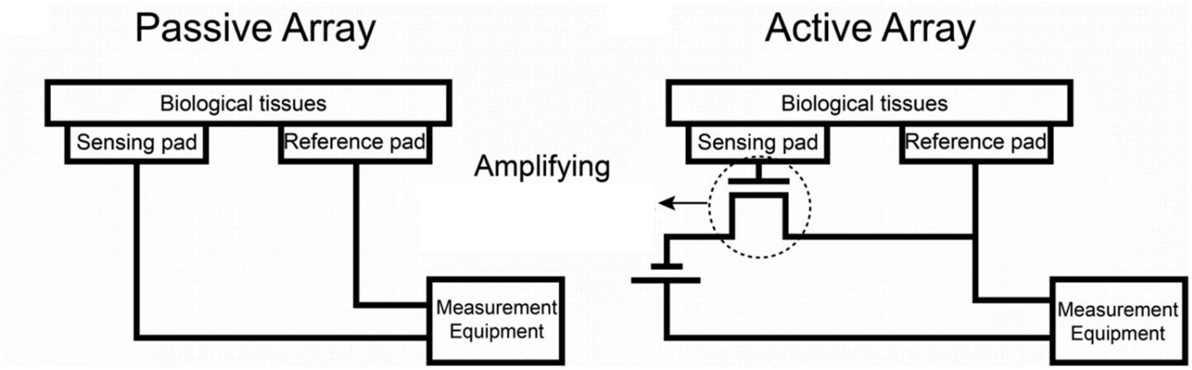

Figure 1.13. A schematic illustration of the difference between active and passive configurations for biological MEAs[44]

MEAs in corrosion studies can be a powerful tool; however, compared to biological applications, only a few researchers have used MEAs to analyze corrosion. This is mainly because MEAs are much more difficult to optimize when used in corrosion analyses. MEAs for corrosion analysis are typically exposed to harsher environments than biological samples. Solutions used for corrosion analysis often contain many different anions and are often acidic or basic to promote anodic metal dissolution or passivation. These conditions can negatively affect the MEA substrate, which makes protective layer and substrate selection difficult. When designing MEAs for corrosion analyses there are some similarities to the principles used to design MEAs for biological analyses. Three broad criteria are considered for corrosion MEA production: solution compatibility, crevicing and transparency. Solution compatibility refers to the stability of the MEA substrate and electrodes in a test solution. The substrate should be unaffected or react slowly with the test solution compared to the electrodes. Crevicing requires that the formation of crevices between the electrode and protective polymer layers be avoided or readily accounted for during data treatment. Transparency refers to the ability to see and analyze electrodes in the MEA after or during exposure to the test solution. It is possible to design an in-situ method for corrosion analysis using a MEA, but it would require either using very little solution or a specialized microscope. Even with the proper design it would be very difficult to monitor multiple small electrodes simultaneously while maintaining a stable test environment. To avoid these issues sensor electrodes could be used to detect ions and/or monitor pH. These sensor electrodes could be placed near a corroding surface to monitor the conditions in-situ.

In addition to the criteria and considerations being slightly different when using MEAs for biological versus corrosion analyses, it is important to differentiate the MEA type/function. Biological MEAs are sensor MEAs used to study the tissue not the electrodes in the MEA. Therefore, for sensor MEAs the state of the electrodes after fabrication is less important providing a voltage or current measurement can be made. In this thesis the MEAs studied are the active sample and are referred to as consumable MEAs. Therefore, any faulty or pre-corroded electrodes are not useful and can negatively affect the electrochemical measurement of adjacent electrodes.

1.6.2 Neuroscience Applications

In neuroscience, sensor MEAs are popular because traditional detection methods for neuroactive substances are cumbersome, time-consuming, energy-consuming and expensive.[45] These advantages are true for corrosion applications as well. MEAs are used to analyze neuroactive substances such as dopamine, which can be over- or under-produced in the case of a neurological disease. It is important to monitor real-time dopamine release because its distribution to different active tissues and the amount released per vesicle can vary greatly.[45] The release of neurotransmitters is also a quick process, which is easily tracked due to the high spatial/temporal resolution offered by MEAs. The large number of microelectrodes that can fit in a MEA overcomes the disadvantages of conventional electrodes for measuring in vivo substances such as low detection sensitivity and the possibility of destroying test subjects.[45]

Voltammetry is recognized as one of the most effective methods for measuring neurotransmitters.[46] Different modifications can be made to the MEA electrodes to improve various performance aspects. Nafion selectively measures neurotransmitters, while Au nano particles can enhance electron transfer between the neurotransmitter and the working electrode.[45] Typically MEAs are used for neuroelectrical research rather than neurochemical research.[47] Most commonly MEAs are used for high throughput work such as cell screening or drug discovery. They are also used for cell analysis to determine activity parameters like neurotransmitter release and activity potential.[48] Another focus of neuroscience MEA work is determining the relationship between neuroelectrical and neurochemical activity, which is performed by monitoring fluctuations of neurotransmitters in response to electrical stimulation in various regions of the brain.

Polypyrrole and graphene are the two widely used biocompatible modifiers to help increase electrical sensitivity and charge transfer abilities of the MEA. Additionally, MEAs have their size and dimensions modified such as the 4-channel intracortical MEA made on a flexible glassy-carbon substrate produced by Castagnola et al., which allowed analysis at four different depths of tissue to obtain electrophysicological parameters and neurotransmitter release times simultaneously from single cells.[49] The main advantage of these MEAs is the ability to use flexible substrates and coatings on the electrodes to enhance sensitivity and charge transfer since the measured response of the electrodes is more important than the state of the electrodes.

1.6.3 Corrosion Applications

Unlike sensor MEAs, corrosion MEAs are consumable MEAs with a focus on the state of the MEA electrodes in addition to the measured electrode responses in order to correlate the electrochemical behaviour to the physical state of the electrodes. Since the physical state of the electrodes is important, electrode size is usually chosen based on the available, compatible measurement and fabrication techniques. Therefore, depending on the study electrodes can range from macro to ultramicro sizes. Depending on the spacing and size of the electrodes, a MEA can simulate a bulk surface or a series of individual electrodes. Microelectrodes (MEs) or ultramicroelectrodes (UMEs) could possibly allow the isolation and identification of anodic and cathodic events on the reactive surface. Since MEA electrodes tend to be smaller, this makes them ideal for studying localized corrosion.

MEs and UMEs are often analyzed by surface profiling or SECM (scanning electrochemical microscopy), which can measure local topography and reactivity, respectively. An early example of this kind of study was conducted by Lister and Pinhero using 304 stainless steel; however, at the time, they noted the state and exact size of the electrodes pre- and post-experimentation was not known.[50] While Lister and Pinhero's work was conducted 15 years ago, it illustrates the need for MEA optimization and proper design, which they noted as required developments.

A good example of innovation in MEA design is embedded metal electrodes in a curved substrate to simulate a bent piece of piping as shown in Figure 1.14. Usually, consumable MEAs have trouble simulating curved or bent surfaces depending on the metal and substrate. This is because the electrodes can be hard to place into a bent substrate and physical pre-treatment of electrodes in these positions can be difficult due to the inflexible substrates. This unique array was devised by Si et al. who aimed to study the electrochemical behaviour of bent piping.[51]

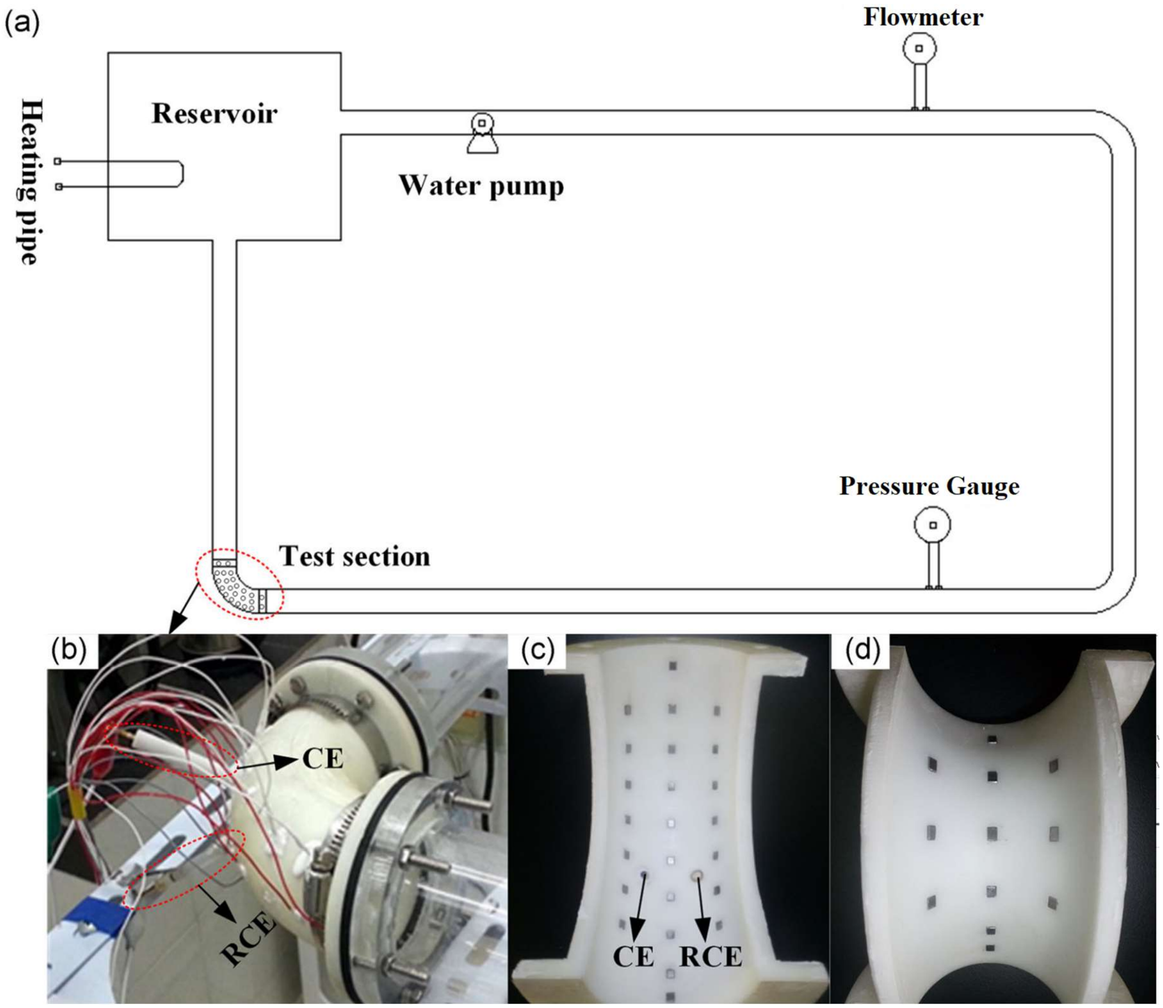

Figure 1.14. The bent array created by Si et al.: a) shows the loop system the array is designed to simulate; b) shows the assembled array; c) and d) show the distribution of electrodes[51]

The most recently published review of the applications of MEAs in corrosion science by Budiansky et al. highlights a number of applications for MEAs.[52] Lunt et al. initiated crevice corrosion by using a small stainless steel MEA fitted into an epoxy insert with a spot for an attached crevice former as shown in Figure 1.15.[53] In this example, the MEA simulates a bulk surface and crevice initiation can be tracked across the surface by the electrochemical response from individual electrodes. Another important corrosion application for MEAs is the tracking of corrosion spreading in concrete. This was studied by Torres-Acosta and Sagues who used simulated concrete porewater, and a MEA that contained two metals that were commonly embedded in concrete.[54] This avoided the major issue of attempting to analyze two independent metals inside concrete.

More recently, King et al. used MEAs to study how limited solution affects the coupling current and potential distribution between dissimilar metals.[55] In their experiment they produced droplets of solution by controlling the relative humidity of the experimental environment and deposited these droplets onto a stainless steel MEA. The MEA design was simple compared to the previous examples, involving a straight line of electrodes, as shown in Figure 1.16. These applications illustrate specific advantages of MEAs but the more general use of MEAs has, to date, been limited by the difficulty in optimizing the design.

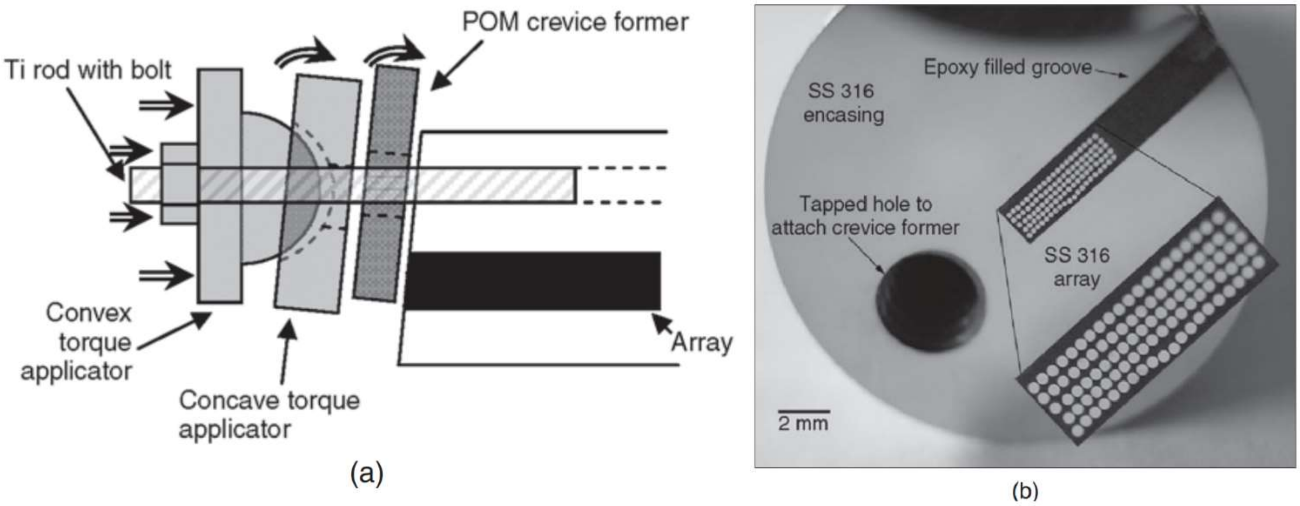

Figure 1.15. A schematic (A) and planar (B) view of an array used for crevice analysis with all the necessary components[53]

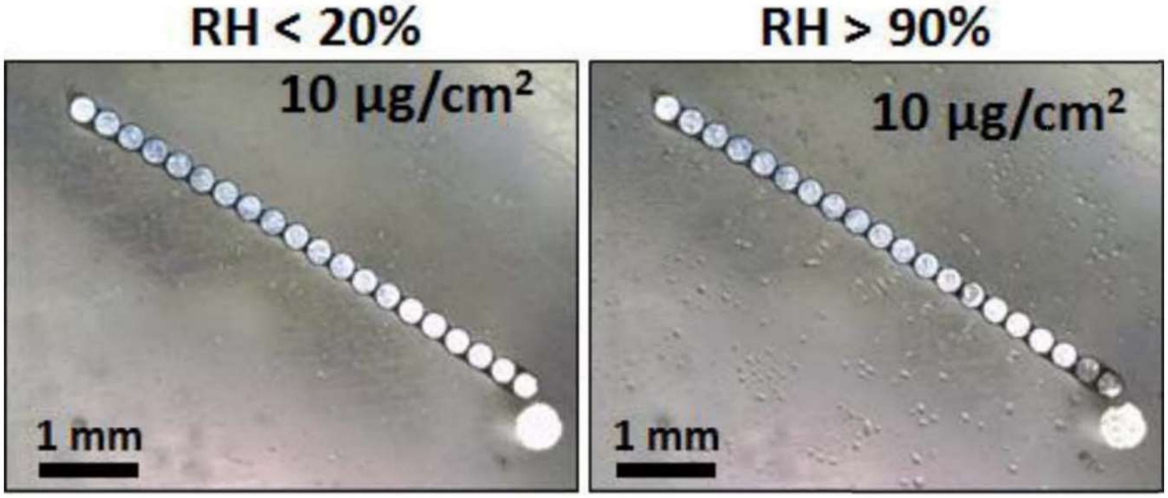

Figure 1.16. A magnified view of the stainless steel array used for droplet studies at two different RHs[55]

1.6.4 Typical Array Sizes

Sensor MEAs generally employ MEs and UMEs. [44] This is because the MEA electrodes themselves are not being analyzed and very stable metals can be chosen for their fabrication. Depending on the required size of MEs or UMEs and the limitations imposed by the fabrication process smaller electrodes can be achieved through either using nanofabrication methods on larger electrodes, such as photolithography, or inkjet printing. [44] Corrosion MEAs can use large electrodes such as 150 µm Cu wires in a 5 x 20 grid as shown in Cong et al.[56] Yang et al. show that steel electrodes can even be as large as 1-1.2 mm.[57] However, more recently Rafla et al. managed to create MEAs with 20 MEs using stainless steel electrodes with diameters of 250 µm.[58]

1.6.5 Previous Related Studies

Within the last 10 years the Scully group has published a series of papers using MEAs to study corrosion problems.[52,53,55,56,58,59,60,61] Recent papers have mainly been studies on stainless steel or Mg alloys with only one study on Cu electrodes.[56]

The first notable corrosion MEA innovation in the Scully group was performed by Bland, in which Al electrodes were embedded into a Mg matrix. The spacing and number of Al electrodes were controlled and varied depending on the sample, as shown in Figure 1.17.[59] This is a unique example where the substrate and the MEA electrodes are dissimilar metals. The purpose of this MEA was to study the effect of intermetallic Al particles in Mg-Al alloys. This study also used optical Z-stacking to determine the topography of various electrodes. Compared to CLSM, the resolution using this method is limited.

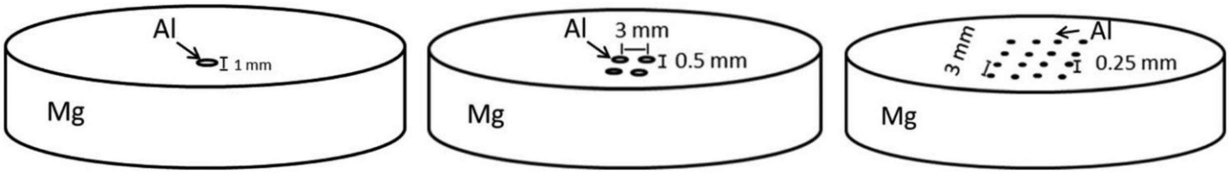

Figure 1.17. Schematic diagram of MEAs where Mg is the substrate and the Al electrodes are used to simulate intermetallic particles in various patterns, sizes and distribution[59]

Subsequently, Bland et al. used a MEA designed to mimic weld zones interacting in a divided weld.[60] The MEA consisted of different electrodes lined up in order to mimic the different weld regions in proximity to each other. This resulted in a line MEA which simulated these sections, as shown in Figure 1.18.

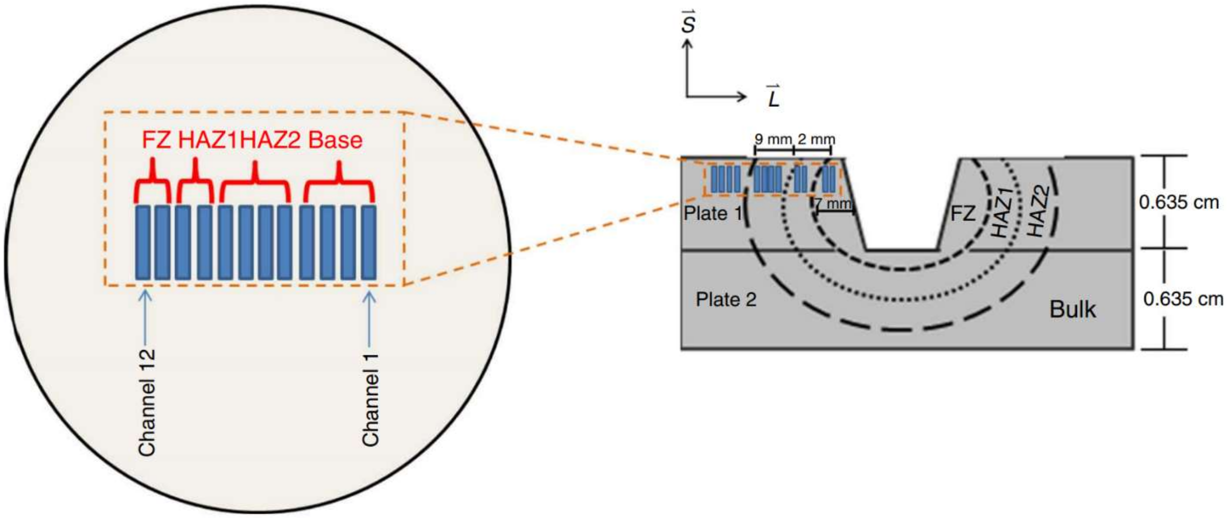

Figure 1.18. Schematic illustration of the weld zone (right) and how the regions are represented in the MEA line array (left)[60]

King et al. deposited solution droplets onto an MEA in a controlled relative humidity (RH) environment conducted in a humidity chamber in order to control the deposition of various amounts of saltwater droplets onto the MEA. The experimental setup, Figure 1.19, shows a complicated system that includes a camera to record optical images of the electrodes when exposed to various RH.[55] In this study, some of the line MEAs contained both Mg and an Al alloy in order to study how the Mg acts as a sacrificial anode to cathodically protect the Al alloy.

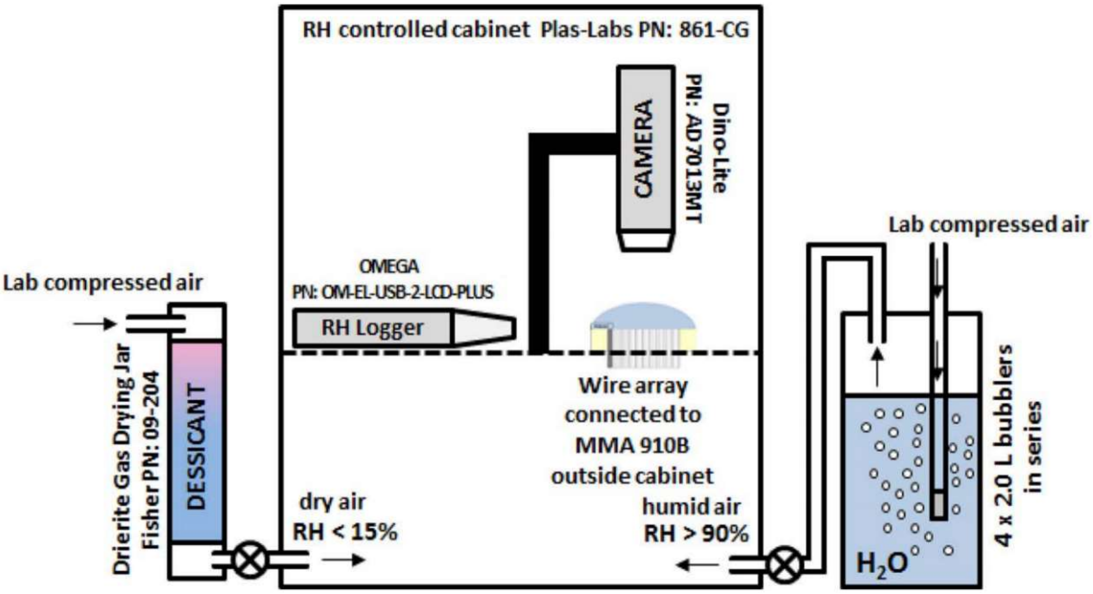

Figure 1.19. Schematic illustration of the experimental setup used by King et al. to monitor droplets on a line array using controlled relative humidity [55]

A notable design innovation is a MEA cast in epoxy, in which the electrode in the middle was a larger reference/counter electrode, as shown in Figure 1.20.[58] This study also controlled the RH to condense small amounts of liquid onto the MEA for testing. Hurley and Scully studied the radial and lateral spreading of corrosion on rebar in concrete.[61] However, in this study no MEA schematic was included, but the MEAs built were described as 5 x 20 arrays made with 250 µm diameter wires of various metals to simulate different scenarios in concrete.

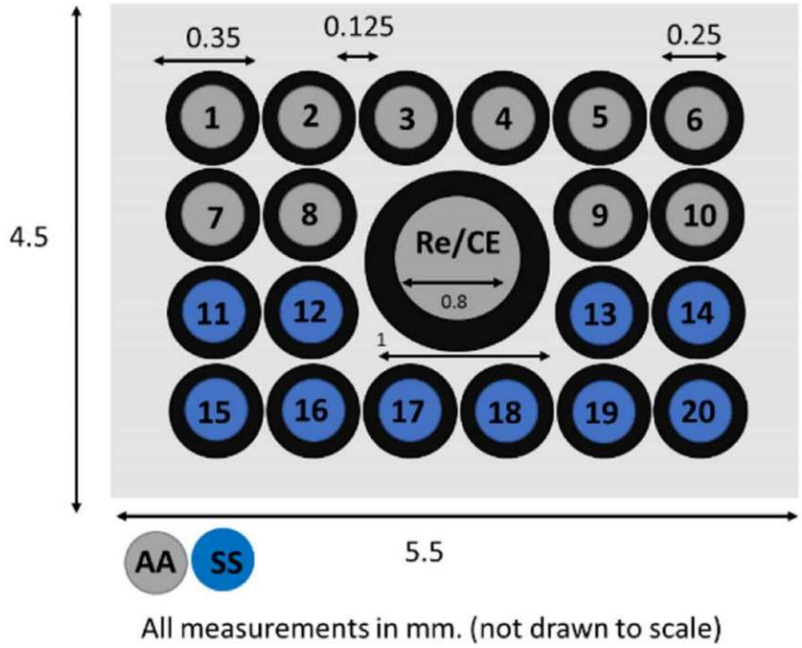

Figure 1.20. Schematic MEA design with an embedded RE/CE and two different metals and controlled spacing[58]

Of most relevance to this thesis, Cong et al. used MEAs to study the pitting of Cu in potable water.[56] Their MEAs were fabricated by casting 100, 150 µm Cu wires in a 5 x 20 rectangle in epoxy with 30 µm separation distance in both the x and y directions. The study concluded that in chlorinated water chlorine reduction is the dominant cathodic reaction, that high [HCO_3^-] promoted passivity of Cu, and that the MEA allowed accurate testing of low conductivity solutions. The results contained no measure of the surface roughness and surface topography resulting from corrosion. It can be noted that the use of Cu MEAs for corrosion studies, specifically roughness determination via surface analysis, and examination of local anodes/cathodes and their attributes (size, spatial arrangement and persistence) during uniform corrosion have not been investigated and a considerable effort will be required to optimize the use of MEAs.

The analysis of corroded Cu roughness is limited in the literature. Often studies only take a passing glance at the surface topography of Cu after corrosion to look at the resulting microstructures. Most of the resources pertaining to this subject are not directly relatable to studying Cu surface topography in conditions such as the ones used in this thesis.

There are some studies that can offer some insight pertaining to what to expect. Hu et al. studied the effect of Cu surface roughness on corrosion in simulated ground water for a possible nuclear waste repository in Beishan, China.[62] However, the focus of this study was on how the roughness produced by grinding during sample preparation affected the corrosion surface morphology. Scanning electrochemical microscopy (SECM) and SEM were used to study different scratches on the surface, which contained different surface morphologies. Martinez-Lombardia et al. studied Cu in the active state using a 5 mM NaCl solution at E_{corr}.[63] Analysis in this study was performed using SECM. They found that Cu dissolved preferentially based on individual grain orientation, as well as the orientation of adjacent grains in the material. However, no topographical measurements were recorded. A study that involved some height measurement of a roughened surface was conducted by Lee et al.[64] In this study they assembled a PCB-like substrate manually by electrodepositing Cu onto a Cu substrate, roughening the electrodeposited layer and then applying a solder mask. In this study the electrodeposited Cu was annealed and then etched using a combination of formic acid and HCl, which was the main method of roughening the surface. They determined that despite most of the Cu having micro-grains, protrusions of larger grains could exist. These protrusions were up to 2.6 μm higher than the rest of the surface and up to ~6-8 μm in width.

These studies all use SECM and more commonly SEM as the chosen method for imaging corroded Cu surfaces. Despite this, there are very little height analyses of the surface features on corroded Cu, most analyses being preliminary or qualitative rather than quantitative. These studies offer a good idea of what to expect of roughened Cu surfaces, but they do not provide the fine details needed to accurately describe or predict the roughening trends for Cu.

1.7 References

---

1. Davis, M.; Ahiduzzaman, M.; Kumar, A. Mapping Canadian Energy Flow from Primary Fuel to End Use. *Energ. Convers. Manage.* **2018,** 156, 178-191.

2. *Moving Towards Partnership: Triennial Report 2017 to 2019;* Technical Report; NWMO, Toronto, Canada, 2020.

3. Crowe, R.; Birch, K.; Freire-Canosa, J.; Chen, J.; Dolye, D.; Garisto, F.; Gierszewski, P.; Gobien, M.; Boyle, C.; Hunt, N.; Hirschorn, S.; Jensen, M.; Keech, P.; Kennell-Morrison, L.; Kremer, E.; Medri, C.; Mielcarek, M.; Murchison, A.; Parmenter, A.; Sykes, E.; Yang, T. *Technical Program for Long-Term Management of Canada's Used Nuclear Fuel- Annual Report 2016;* NWMO-TR-2017-01; NWMO: Toronto, Canada, 2017.

4. Muller, H.R.; Garitte, B.; Vogt, T.; Kohler, S.; Sakaki, T.; Weber, H.; Spillmann, T.; Her- ¨ trich, M.; Becker, J.K.; Giroud, N.; Cloet, V.; Diomidis, N.; Vietor, T. Implementation of the Full-Scale Emplacement (FE) Experiment at the Mont Terri Rock Laboratory. *Swiss J. Geosci*. **2017**, 110 (1), 287–306.

5. Giroud, N.; Tomonaga, Y.; Wersin, P.; Briggs, S.; King, F.; Vogt, T.; Diomidis, N. On the Fate of Oxygen in a Spent Fuel Emplacement Drift in Opalinus Clay. *Appl. Geochem.* **2018,** 97, 270–278.

6. Tomonaga, Y.; Giroud, N.; Brennwald, M.S.; Horstmann, E.; Diomidis, N.; Kipfer, R.; Wersin, P. On-Line Monitoring of the Gas Composition in the Full-Scale Emplacement Experiment at Mont Terri (Switzerland). *Appl. Geochem.* **2019**, 100, 234–243.

7. Ibrahim, B.; Zagidulin, D.; Behazin, M.; Ramamurthy, S.; Wren, J.C.; Shoesmith, D.W. The Corrosion of Copper in Irradiated and Unirradiated Humid Air. *Corros. Sci.* **2018,** 141, 53-62.

8. Standish, T.; Chen, J.; Jacklin, R.; Jakupi, P.; Ramamurthy, S.; Zagidulin, D.; Keech, P.; Shoesmith, D.W. Corrosion of Copper-Coated Steel High Level Nuclear Waste Containers Under Permanent Disposal Conditions. *Electrochim. Acta.* **2016,** *211*, 331-342.

9. King, F; Lilja, C. *Localised corrosion of copper canisters in bentonite pore water;* TR-13-27; SKB: Stockholm, Sweden, 2013.

10. Schweitzer, P.A. *Fundamentals of Corrosion: Mechanisms, causes, and preventative methods*. CRC Press, Boca Raton, FL, 2010, pp 27-29.

11. Qin, Z.; Daljeet, R.; Ai, M.; Farhangi, N.; Noël, J. J.; Shoesmith D. W.; King F.; Keech, P. The Active/Passive Conditions for Copper Corrosion under Nuclear Waste Repository Environment. *Corros. Eng. Sci. Techn.* **2017,** 52, 45-49.

12. Hall, D.S.; Behazin, M.; Binns, W.J.; Keech, P.G. An Evaluation of Corrosion Processes Affecting Copper-Coated Nuclear Waste Containers in a Deep Geological Repository. *Prog. Mater. Sci.* **2021,** 118, 100766.

13. Ochoa, M.; Rodriguez, M.A.; Farina, S.B. Corrosion of High Purity Copper in Solutions Containing NaCl, Na_2SO_4, and $NAHCO_3$ at Different Temperatures. *Proc. Mat. Sci.* **2015,** 9, 460-468.

14. Li, K.; Chen, Z.; Li, J.; Sun, X.; Xu, F.; Xu, L. Corrosion Mechanism of Copper Immersed in Ammonium Sulfate Solution. *Mater. Corros.* **2018,** 69, 1597-1608.

15. Kong, D.; Dong, C.; Xiao, K.; Li, X. Effect of Temperature on Copper Corrosion in High-level Nuclear Waste Environment. *T. Nonferr. Metal. Soc.* **2017,** 27, 1431-1438.

16. Turnbull, J.P. The Influence of Radiolytically Produced Nitric Acid on the Corrosion Resistance of Copper-Coated Used Nuclear Fuel Containers. Ph.D. Dissertation, University of Western Ontario, London, ON, 2020.

17. Bard, A.J.; Faulkner, L.R. *Electrochemical Methods: Fundamentals and Applications.* 2nd ed. John Wiley & Sons, Inc.: New York, 2001; p 231.

18. Stansbury, E.E; Buchanan, R.A. *Fundamentals of Electrochemical Corrosion*. ASM International; Materials Park, OH, 2000, pp 146-160.

19. Kelly, R.G.; Scully, J.R.; Shoesmith, D.W.; Buchheit, R.G. *Electrochemical Techniques in Corrosion Science and Engineering*. Marcel Dekker, Inc. New York, NY, 2002, p 9-124.

20. Marcus, P.; Mansfeld, F. *Analytical Methods in Corrosion Science and Engineering.* 1st ed. CRC Press: Boca Raton, 2006; p 450.

21. Zhou, W.; Apkarian, R.; Wang, Z.L.; Joy, D. *Fundamentals of Scanning Electron Microscopy (SEM). In Scanning Microscopy for Nanotechnology;* Springer, 2006; pp 1-40.

22. Egerton, R.F. *Physical Principles of Electron Microscopy.* Springer Science + Business Media Inc.: New York, 2005; pp 131-142.

23. ThermoFisher Scientific- What is SEM? Scanning Electron Microscopy Explained. https://www.thermofisher.com/blog/microscopy/what-is-sem-scanning-electron-microscopy-explained.html (accessed Mar 1, 2021).

---

24. Nanoscience Instruments- Scanning Electron Microscopy. https://www.nanoscience.com/techniques/scanning-electron-microscopy.html (accessed Nov 11, 2020).

25. Confocal Microscopy ZEISS LSM 900 for Materials. https://www.zeiss.com/microscopy/int/products/confocal-microscopes/lsm-900-for-materials-non-contact-surface-topography-in-3d.html (accessed Mar 3, 2021)

26. Leach, R. K. *Good Practice Guide No.37: The measurement of Surface Texture using Stylus Instruments.* 1st ed. National Physical Laboratory: Middlesex; pp 16-25.

27. Scribner Associates Inc. MMA Model 900/910. http://www.scribner.com/products/model-900-910/ (accessed Sept 1, 2020)

28. Hampel, M.; Schenderlein, M.; Schary, C.; Dimper, M.; Ozcan, O. Efficient Detection of Localized Corrosion Processes on Stainless Steel by Means of Scanning Electrochemical Microscopy (SECM) using a Multi-electrode Approach. *Electrochem. Commun.* **2019,** 101, 52-55.

29. Chambers, B.D.; Taylor, S.R.; Kendig, M.W. Rapid Discovery of Corrosion Inhibitors and Synergistic Combinations Using High-Throughput Screening Methods. *Corrosion.* **2005,** 61, 480-489.

30. Muster, T.H.; Bradbury, A.; Trinchi, A.; Cole, I.S.; Markley, T.; Lau, D.; Dligatch, S.; Bendavid, A.; Martin, P. The Atmospheric Corrosion of Zinc: The Effects of Salt Concentration, Droplet Size and Droplet Shape. *Electrochim. Acta.* **2011,** 56, 1866-1873.

31. Pujar, P.; Gandla, S.; Gupta, D.; Kim, S.; Kim, M. Trends in Low-Temperature Combustion Derived Thin Films for Solution-Processed Electronics. *Adv. Electron. Mater.* **2020,** 6, 2000464.

32. Rahman, F.; Carbaugh, D.J.; Wright, J.T.; Rajan, P.; Pandya, S.G.; Kaya, S. A Review of Polymethyl Methacrylate (PMMA) as a Versatile Lithograhpic Resist- With Emphasis on UV Exposure. *Microelectron. Eng.* **2020,** 224, 111238-111250.

33. del Barrio, J.; Sánchez-Somolinos, C. Light to Shape the Future: From Photolithography to 4D Printing. *Adv. Opt. Mater.* **2019,** 7, 1900598.

34. Reed, M.L.; Fedder, G.K.; Micro Mechanical Systems. In Handbook of Sensors and Actuators, Vol. 6; ScienceDirect, 1998; pp 13-61.

35. Vitos, L; Ruban, A.V.; Skriver, H.L.; Kollár, J. The Surface Energy of Metals. *Surf. Sci.* **1998,** 411, 186-202.

36. Mayanna, S.M.; Setty, T.H.V. Effect of Halide Ions on the Dissolution of Copper Single Crystal Planes in Dilute Sulphuric Acid. *Corros. Sci.* **1974,** 14, 691-699.

37. Nandeesh, L.S.; Sheshadri, B.S. Inhibitory Effect of 2-mercapto pyrimidine on Corrosion of Copper Single Crystal Planes in 0.1 M H_2SO_4. *Proc. Indian. Acad. Sci (Chem. Sci.)* **1991,** 103, 763-775.

38. Vvedenskii, A.; Grushevskaya, S.; Ganzha, S.; Eliseev, D.; Abakumova, L.I. Copper Oxides: Kinetics of Formation and Semiconducting Properties. Part II. Copper Single Crystals. *J. Solid. State. Electr.* **2014,** 18, 3437-3451.

39. Mayanna, S.M. Adsorption Isotherm of Iodide Ions on Copper Single Crystal Planes in Sulfuric Acid. *J. Electrochem. Soc.* **1975,** 122, 251-252.

40. Huang, Y.; Handoko, A.D.; Hirunsit, P.; Yeo, B.S. Electrochemical Reduction of CO_2 using Copper Single-Crystal Surfaces: Effects of CO^* Coverage on the Selective Formation of Ethylene. *ACS. Catal.* **2017,** 7, 1749-1756.

41. Pérez-Gallent, E.; Marcandalli, G.; Figueiredo, M.C.; Calle-Vallejo, F.; Koper, M.T.M. Structure- and Potential-Dependent Cation Effects on CO Reduction at Copper Single-Crystal Electrodes. *J. Am. Chem. Soc.* **2017,** 139, 16412-16419.

42. Schouten, K.J.P.; Qin, Z.; Pérez-Gallent, E.; Koper, M.T.M. Two Pathways for the Formation of Ethylene in CO Reduction on Single-Crystal Copper Electrodes. *J. Am. Chem. Soc.* **2012,** 134, 9864-9867.

43. Schouten, K.J.P.; Pérez-Gallent, E.; Koper, M.T.M. Structure Sensitivity of the Electrochemical Reduction of Carbon Monoxide on Copper Single Crystals. *ACS. Catal.* **2013,** 3, 1292-1295.

44. Lee, W.; Someya, T. Emerging Trends in Flexible Active Multielectrode Arrays. *Chem. Mater.* **2019,** 31, 6347-6358.

45. He, C.; Tao, M.; Zhang, C.; He, Y.; Xu, W.; Lie, Y.; Zhu, W. Microelectrode-Based Electrochemical Sensing Technology for in Vivo Detection of Dopamine: Recent Developments and Future Prospects. *Crit. Rev. Anal. Chem.* **2020,** 2-10.

46. Kissinger, P.T.; Hart. J.B.; Adams, R.N. Voltammetry in Brain Tissue-A New Neurophysiological Measurement. *Brain. Res.* **1973,** 55, 209-213.

47. Zhang, S.; Song, Y.; Wang, M.; Zhang, Z.; Fan, X.; Song, X.; Zhuang, P.; Yue, F.; Chan, P.; Cai, X. A Silicon Based Implantable Microelectrode Array for Electrophysiological and

---

Dopamine Recording from Cortex to Striatum in the Non-human Primate Brain. *Biosens. Bioelectron.* **2016,** 85, 53-61.

48. Ino, K.; Shiku, H.; Matsue, T. Bioelectrochemical Applications of Microelectrode Arrays in Cell Analysis and Engingeering. *Curr. Opin. Electrochem.* **2017,** 5, 146-151.

49. Castagnola, E.; Vahidi, N.M.; Nimbalkar, S.; Rudraraju, S.; Thielk, M.; Zucchini, E.; Cea, C.; Carli, S.; Gentner, T.Q.; Ricci, D.; Fadiga, L.; Kassengne, S. *In Vivo* Dopamine Detection and Single Unit Recordings Using Intracortical Glassy Carbon Microelectrode Arrays. *MRS. Advances.* **2018,** 3, 1629-1634.

50. Lister, T.E.; Pinhero, P.J. Microelectrode Array Microscopy: Investigation of Dynamic Behaviour of Localized Corrosion at Type 304 Stainless Steel Surfaces. *Anal. Chem.* **2005,** 77, 2601-2607.

51. Si, X.; Si, H.; Li, M.; Zhang, R.; Zhou, K. Investigation of Corrosion Behaviour at Elbow by Array Electrode and Computational Fluid Dynamics Simulation. *Mater. Corros.* **2020,** 71, 1637-1650.

52. Budiansky, N.D.; Bocher, F.; Cong, H.; Hurley, M.F.; Scully, J.R. Use of Coupled Multi-electrode Arrays to Advance the Understanding of Selected Corrosion Phenomena. *Corros. Sci.* **2007,** 63, 537-554.

53. Lunt, T.T.; Brusamarello, V.; Scully, J.R.; Hudson, J.L. Interactions among Localized Corrosion Sites Investigated with Electrode Arrays. *Electrochem. Solid. St.* **2000,** 3, 271-274.

54. Torres-Acosta, A.A.; Sagues, A.A. Concrete Cover Cracking with Localized Corrosion of Reinforcing Steel. *Amer. Conc. I.* **2000,** SP-192, 591-611.

55. King, A.D.; Lee, J.S.; Scully, J.R. Galvanic Couple Current and Potential Distribution between a Mg Electrode and 2024-T351 under Droplets Analyzed by Microelectrode Arrays. *J. Electrochem. Soc.* **2015,** 162, C12-C23.

56. Cong, H.; Budiansky, N.D.; Michels, H.T.; Scully, J.R. Use of Coupled Electrode Arrays to Elucidate Copper Pitting as a Function of Potable Water Chemistry. *ECS. Transcations.* **2007,** 3, 531-544.

57. Yang, L.; Sridhar, N.; Brossia, C. S.; Dunn, D.S. Evaluation of the Coupled Multielectrode Array Sensor as a Real-time Corrosion Monitor. *Corros. Sci.* **2005,** 47, 1794-1809.

58. Rafla, V.N.; Khullar, P.; Kelly. R.G.; Scully, J.R. Coupled Multi-electrode Array with a Sintered Ag/AgCl Counter/Reference Electrode to Investigate AA7050-T7451 and Type 316

Stainless Steel Galvanic Couple under Atmospheric Conditions. *J. Electrochem. Soc.* **2018,** 165-C562-C572.

59. Bland, L.G.; Birbilis, N.; Scully, J.R. Exploring the Effects of Intermetallic Particle Size and Spacing on the Corrosion of Mg-Al Alloys using Model Electrodes. *J. Electrochem. Soc.* **2016,** 163, C895-C906.

60. Bland, L.G.; Rincon Troconis, B.C.; Santucci Jr, R.J.; Fitz-Gerald, J.M.; Scully, J.R. Metallurgical and Electrochemical Characterization of the Corrosion of a Mg-Al-Zn Alloy AZ31B-H24 Tungsten Inert Gas Weld: Galvanic Corrosion Between Weld Zones. *Corros. Sci.* **2016,** 72, 1226-1242.

61. Hurley, M.F.; Scully, J.R. Lateral and Radial Corrosion Propagation Behaviour of 9-21% Cr and 18% Cr + 2.8% Mo Stainless Steel Reinforcing Materials in Simulated Concrete Environments. *Mater. Corros.* **2013,** 64, 752-763.

62. Hu, M.; Zhang, W.; Shang, X.; Wen, J.; Zhao, Z.; Qiao, B.; Kong, D.; Dong, C. Effect of Surface Roughness on Copper Corrosion in Simulated Beishan Groundwater, China. *Int. J. Electrochem. Sci.* **2020,** 15, 2961-2972.

63. Martinez-Lombardia, E.; Gonzalez-Garcia, Y.; Lapiere, L.; De Graewe, I.; Verbeken, K.; Kesten, L.; Marcuse, P.; Terryn, H. Scanning Electrochemical Microscopy to Study the Effect of Crystallographic Orientation on the Electrochemical Activity of Pure Copper. *Electrochim. Acta.* **2014,** 116, 89-96.

64. Lee, C.; Lin, P.; Yang, C.; Ho, C. Significantly Improving the Etching Characteristics of Electroplated Cu Films Through Microstructure Modification. *Surf. Coat. Tech.* **2020,** 386, 125471.

2. The Determination of Cu Tendency Towards Active Dissolution versus Passive Film Formation in DGR and Near-DGR Environments

2.1 The Behaviour of Copper

2.1.1 Active Behaviour versus Passivity

Pitting is a stochastic process and can only occur in potential-pH regions where the metal is passive, i.e. a region within which the stable phase is an oxide. Passive film formation is described as when the corrosion product is formed on the corroding surface and blocks the metal dissolution reaction. Corrosion can be inhibited by the formation of either thin or thick films, although the term passivity is generally used to describe thin, highly resistive, adherent, and chemically inert oxide films. If the metal dissolves and exceeds its solubility product and is then precipitated on the corroding surface, the film is referred to as a corrosion product deposit, not a passive film. Cu can grow thin films which exhibit passivity.

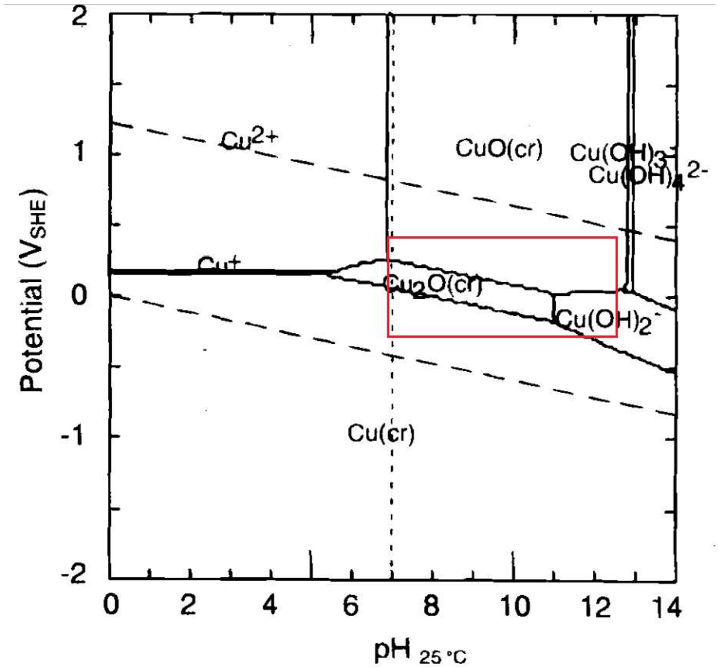

Figure 2.1. A Pourbaix diagram of Cu with a concentration of 10^{-6} mol/kg in pure water at 25°C [1]

Pourbaix (potential-pH) diagrams provide a thermodynamic summary of the stable phase(s) that should be formed in a range of conditions at a fixed temperature. These figures are constructed from the Nernst relationships of the possible half reactions involved and the solubility and complexation constants for dissolved metallic species. An example of the Pourbaix diagram for the Cu/H_2O system at 25°C with a Cu concentration of 10^{-6} mol/kg is shown in Figure 2.1.[1] The diagonal dashed lines indicate the stability region of water. When the potential of the system is above the upper dashed line O_2 is stable in solution and H_2O would be oxidized into O_2. When the potential of the system is below the lower dashed line H_2O is unstable and would be reduced to H_2. When the potential of the system is between the dashed lines H_2O is stable. The stability of Cu and various oxide/hydroxide phases and dissolved metal cations can then be defined based on the position of the lines for individual reactions compared to these two lines for the stability of H_2O. Regions within which metal is the stable phase are referred to as immune regions within which corrosion will not occur. A main feature of Figure 2.1 is that it shows that the stability region for Cu lies within the stability region for H_2O indicating that Cu would be stable in anoxic conditions. However, if dissolved O_2 is present either dissolved metal cations or oxide phases would be stable depending on the pH.

If the stable state is a dissolved metal cation then the region is defined as corrosive, and active behaviour, involving metal, would be expected. If the stable state is an oxide or hydroxide then the region is referred to as passive, and the metal could be protected from corrosion depending on the physical properties of the film. Examples of all these regions can be seen in Figure 2.1. According to Figure 2.1 we can identify general regions in which Cu will be passive or active. The red box drawn on Figure 2.1 shows the pH and potential range to be analyzed in this chapter, which is based on estimated DGR conditions and natural limits.[6] In this region passive film formation is thermodynamically possible (coverage by the oxides Cu_2O and CuO). It is important to probe whether this is truly a passive region. At low pH, Cu should be active or immune depending on the system potential. At very basic pH values within the range studied, the formation of $Cu(OH)_x^{(x-2)-}$ becomes possible. While Pourbaix diagrams are instructive, they refer only to a very specific set of conditions based on thermodynamics while passivity is dominated by kinetics. The locations of the boundaries between regions will change with temperature, the concentration of the dissolved metal ion, the anion concentrations, and the anion type.

2.1.2 Localized Corrosion

Localized corrosion can occur when passive films breakdown at discrete sites.[2] While most of the surface remains passive, these breakdown sites corrode actively, leading to metal dissolution in small areas. These sites, known as pits, can experience very high penetration rates since the underlying surface becomes exposed to solution and dissolution can occur rapidly. Localized corrosion requires a spatial separation between anodic and cathodic sites on the surface and is accompanied by the rapid development of aggressive acidic conditions at anodic locations. The acidic conditions are a product of cation hydrolysis which is balanced by the transport of anions into the pit to balance the positive charge produced by the H^+ ions. The pit will continue to grow while this aggressive solution chemistry is maintained. If the pit is disrupted and the aggressive chemistry lost, the oxide can regrow, leading to re-passivation of the corroded area.

2.2 Experimental Procedure

2.2.1 The Three-Electrode Electrochemical Cell

All cyclic voltammetry (CV) experiments were conducted in a three-electrode glass cell with a water jacket for heating. The counter electrode was cut from a Pt mesh and housed in a separate cell compartment connected to the main body of the cell through a glass frit. The reference electrode was a saturated calomel electrode (SCE, 0.244 V vs SHE) connected to the cell by an arm with a Luggin capillary and glass frit.[3] The working electrode was a bare rod fabricated from Cu provided by Svensk Kärnbränslehantering AB, Solna, Sweden. The rod was 20 cm in height (0.75 cm x 0.75 cm in length and width) and was sealed in the cell using a butyl stopper wrapped in Teflon tape. This design avoids the formation of crevices by not setting the electrode in an epoxy resin. The solution temperature was controlled by pumping water from a reservoir monitored by a thermostat through the cell water jacket. All experiments were performed in a grounded Faraday cage to avoid interference from external electrical noise. A 1480 Solartron multistat was used to control applied potentials and to measure current responses. Corrware software was used to control the multistat, output the data and interpret the results.

2.2.2 Preparation and Maintenance of the Working Electrode

The Cu surface to be submerged (submersion area) and an area of 0.25-0.5 cm above the submersion line were wet polished with a series of SiC papers (p200 grit to p1200 grit). The electrode was then rinsed with Type 1 water (18.2 MΩ·cm) and dried in a stream of Ar. After each CV, the working electrode was repolished using p1200 grit SiC paper unless large defects were observed, then the SiC grit size was adjusted as necessary. The rod was then placed into the Ar-sparged solution and cathodically cleaned, first at -1.5 V(SCE), and then at -1.15 V(SCE) for 1 minute each.

2.2.3 Solution Preparation

All solutions were prepared using Type 1 water and reagent grade NaCl, Na_2SO_4 or $NaHCO_3$. All dilute $NaHCO_3$ solutions were prepared by additions from a stock solution of 1 M $NaHCO_3$ using a micropipette. The solutions in the cell were Ar-sparged for at least 1 hour, and if necessary, the pH was adjusted by adding NaOH. Ar-sparging was continued throughout all experiments (from 25°C to 80°C).

2.2.4 Cyclic Voltammetry Experiments

After cathodic cleaning, E_{corr} was monitored for 30 minutes to allow a steady state to be established. The potential was then scanned to more positive values until the current reached 100 µA at which point the scan was reversed and continued until the current returned to zero. When the temperature was adjusted to a higher value, the solution was allowed to stabilize for 15-30 min under Ar-sparging before starting an experiment. The re-polished electrode was placed into the solution 5-10 minutes prior to this stabilization period. The standard scan rate of 10 mV/min (0.167 mV/s) was used in all experiments.

Table 2.1. Solution compositions used[12]

System	$[Cl^-]$ (mol/L)	$[SO_4^{2-}]$ (mol/L)	$[HCO_3^-]$ (mol/L)
Unary	0.001 ~ 5.0	–	–
	–	0.001 ~ 0.1	–
Binary	0.001 ~ 5.0	0.01	–
	–	0.01	0.0001 ~ 0.01
	0.01	0.001 ~ 0.1	–
	0.01	–	0.0001 ~ 0.01
	0.1	–	0.0001 ~ 0.0005
Ternary	0.1	0.01	0.0001 ~ 0.0005

The active/passive (A/P) behaviour was determined as a function of pH, ion concentration and temperature. Since pH and temperature are easily varied, CVs were performed for a range of anion concentrations. Solutions with multiple anions had one or two fixed anion concentrations and one varying anion concentration. The range of anion concentrations investigated is shown in Table 2.1, with various solution concentrations chosen within each range. The number of individual concentrations investigated depended on the size of the range to be tested for that anion.

2.3 Determination of Copper Behaviour

2.3.1 Cyclic Voltammetry

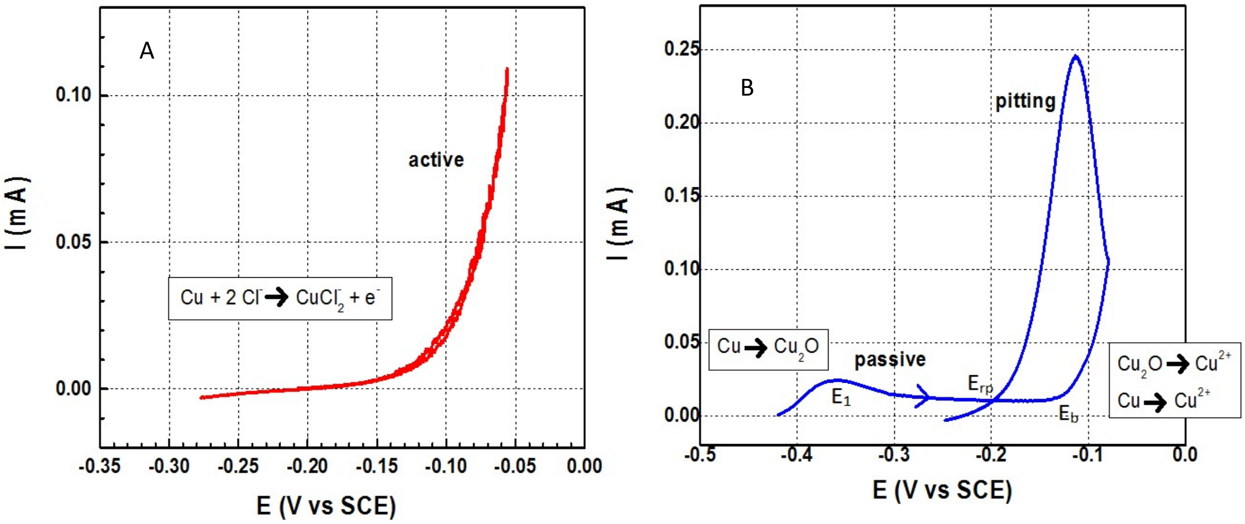

Figure 2.2. Example CVs that illustrate active behaviour (A) and passive behaviour (B) with important potential values noted[3]

Whether or not active or passive behaviour is possible is determined from key potential values observed in the CV. If the metal is active, the current increases as the potential is increased from E_{corr} in the positive direction. However, if passivity is possible the current will eventually decrease again as an oxide is formed. It should be noted that passivity is a pre-requisite for pitting, but its occurrence does not always lead to pitting.

Whether the system exhibits active dissolution or passive film formation is shown by changes in behaviour as the potential increases or decreases in a CV. Figure 2.2A, shows a response indicating active dissolution when the current rises steeply with increasing potential, and retraces this pattern on the reverse scan, indicating that the surface reactivity has not changed due to the formation of a passive film. By contrast, Figure 2.2B shows the current response indicating passive film formation. The current increases with potential until it eventually achieves a maximum around -0.35 V(SCE) on the forward scan before decreasing due to the formation of a passive Cu_2O film around -0.3 V(SCE). It should be noted that the passive film formed in this region may partially or completely cover the surface, but this cannot be determined from the CV.

Three distinct potentials define the Cu behaviour in the CV in Figure 2.2B. (i) At E_1, the passivation potential, a peak current is observed; (ii) after decreasing to an almost constant value as the potential is increased, due to the formation of a passive film, the current begins to increase rapidly again, at a potential E_b, indicating the breakdown of the film and the recurrence of metal dissolution at local sites. E_b represents the potential at which Cu_2O is oxidized to soluble Cu^{2+} leading to perforation of the passive film and the possibility of pitting. (iii) When the potential is reversed the current first continues to increase as acidic conditions develop within the breakdown site accelerating metal dissolution. Eventually, the current decreases until it reaches E_{rp}, the re-passivation potential, at which point the current decreases to a value less than the current recorded on the forward scan. This indicates the metal dissolution within the pits has decreased to such an extent that the passive film can regrow, and further pitting is prevented.

The schematic scans in Figure 2.2 show very distinct differences between active and passive behaviour, though it is often much harder to differentiate them. With respect to the DGR, active dissolution is the preferred behaviour for Cu since it is considered predictably dependent on the available oxidant and leads to uniform damage from which a corrosion rate can be derived. Passive film formation with the possibility of pitting could incite failure mechanisms in the DGR due to its unpredictability and lead to penetration of the Cu if re-passivation does not occur. It is also important to note that in Figure 2.2 the reactions listed are for a general Cl^- unary solution. The more complicated behaviour expected in more complex solutions is discussed below.

2.3.2 The Influence of Temperature

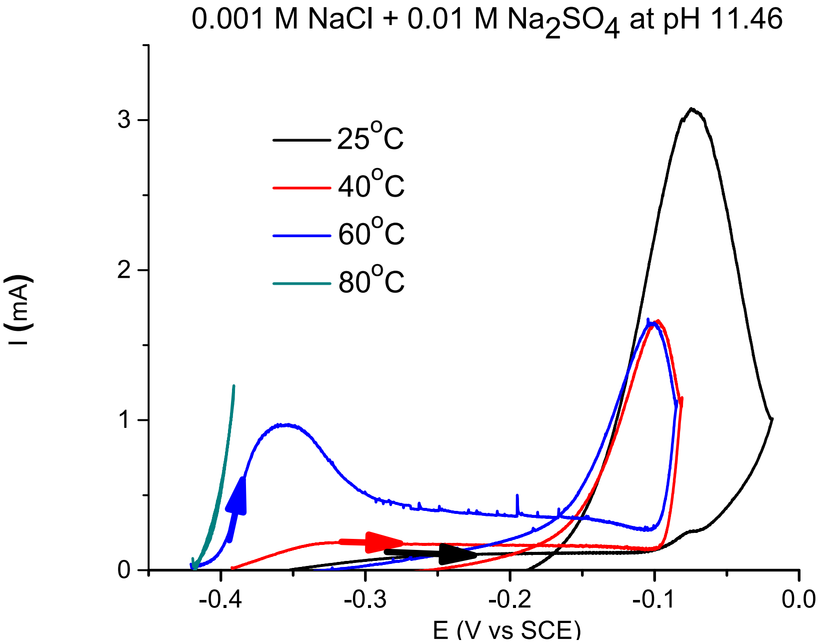

Figure 2.3. A set of potential scans organized by temperature in a solution containing $Cl^-$and SO_4^{2-} at pH 11.46, coloured arrows indicate the direction of the forward scan (Data provided by Amy Ai)

Figure 2.3 shows a series of CVs recorded in a Cl^-/SO_4^{2-} solution with a pH of 11.46 and at different temperatures. At 25°C in pH 11.46 solution, passive behaviour is favoured, indicated by the low, potential-independent current at low potentials. As the temperature increases an active region develops, as indicated by the growth of a current peak in the potential region of -0.4 V(SCE) to -0.3 V(SCE). At 60°C a very distinct active region is observed although passivity is established as the potential is increased. At 80°C only active dissolution is observed. At all temperatures for which passivity is established, a film breakdown leading to the current hysteresis indicative of pitting, is observed. This set of scans demonstrates a transition from passive to active behaviour as the temperature increases, but a transition temperature can only be partially resolved. To define this transition (i.e, the active/passive (A/P) boundary) more sharply, a larger number of temperatures would have to be investigated. It should be noted, however, that the CV is reversed once the current on the forward scan reaches 100 μA. It is possible that a current peak and the onset of passivity would be observed at 80°C if the current was not limited in this manner. This limit is arbitrarily chosen with a single caveat in mind. It is selected because under natural corrosion conditions, a corrosion current greater than this value is extremely unlikely and therefore potentials associated with those currents would never be achieved.

2.3.3 The influence of pH

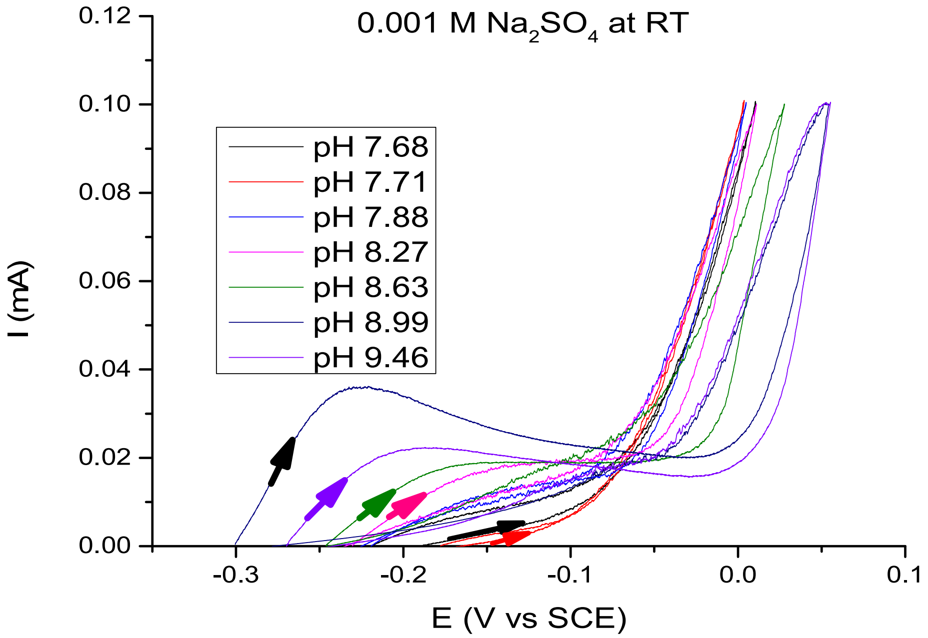

Figure 2.4. A set of potential scans organized by pH in solutions containing 0.001 M SO_4^{2-} at 25°C, coloured arrows indicate the direction of the forward scan

Figure 2.4 shows a series of scans recorded as a function of pH at a constant temperature in a dilute SO_4^{2-} solution. Since the pH anticipated inside a DGR is 7.5-8.2, scans were performed over a wide pH range encompassing these values. When the solution pH is below 8, active behaviour is observed although the current in the potential range -0.25 V(SCE) to -0.1 V(SCE) is low and increases slowly suggesting some inhibition of metal dissolution. As the pH increases, an active to passive transition develops between -0.25 V (SCE) and -0.15 V(SCE), showing that partial passivation is achieved at these higher pH values. For pH values at or above 8.27, the sudden increase in current on the forward scan at potentials more positive than E_1 is followed by a hysteresis loop on the backward scan, showing film breakdown occurs.

It is possible to identify the key potentials (E_1, E_{rp}, E_b) by examining many of these scans. While some scans clearly indicate active or passive behaviour, some are not so clearly defined, indicating a general range for the A/P border, and therefore a clear separation between active and passive behaviour cannot be confidently determined.

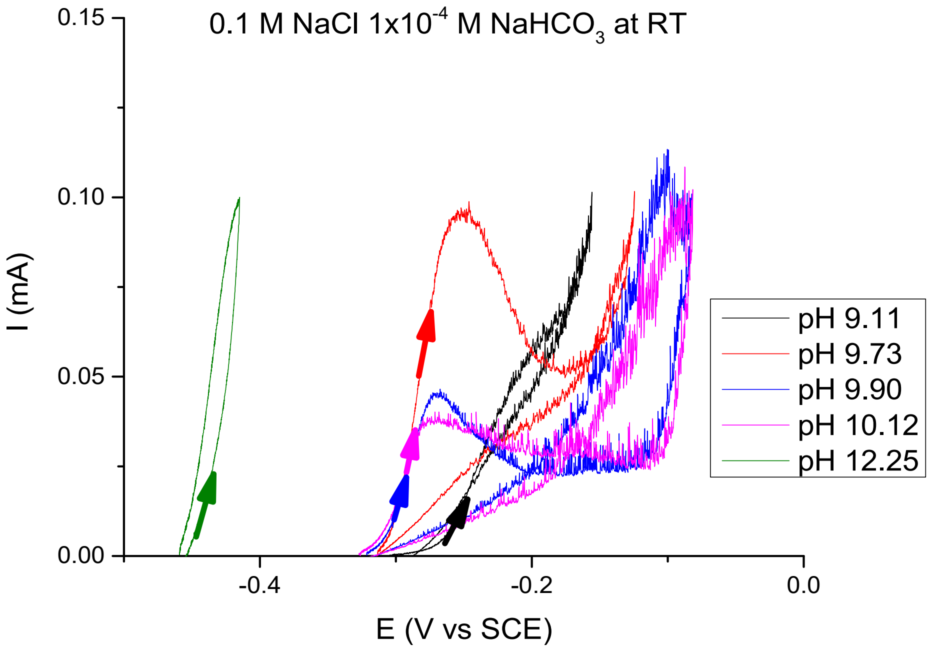

Figure 2.5. A set of potential scans ordered by pH for a 0.1 M Cl^- + 1x10^{-4} M HCO_3^- solution at 25°C, coloured arrows indicate the direction of the forward scan

Figure 2.5 shows a series of CVs in which the distinction between active and passive behaviour is unclear. This figure shows CVs performed in a 0.1 M Cl^- solution containing a small [HCO_3^-]. In the red CV, recorded at pH 9.73, an active region is observed in the potential range of -0.3 V to -0.2 V indicating an active to passive transition. The subsequent passive region only covers a narrow potential range with E_b occurring at ~ -0.15 V. Since the current for $E > E_b$ is reversible it is not clear whether passivity leading to pitting occurred. This type of behaviour is classified as active, mainly due to the reverse scan behaviour which shows no evidence of an E_{rp} value, although it could also be classified as passive. At pH 9.11 the behaviour is ambiguous. However, since no E_b or E_{rp} value is observed the behaviour is classified as active. At pH 9.90 and 10.12 the behaviour can be classified as passive since a clear active-to-passive transition, passive region and E_b and E_{rp} values are observed.

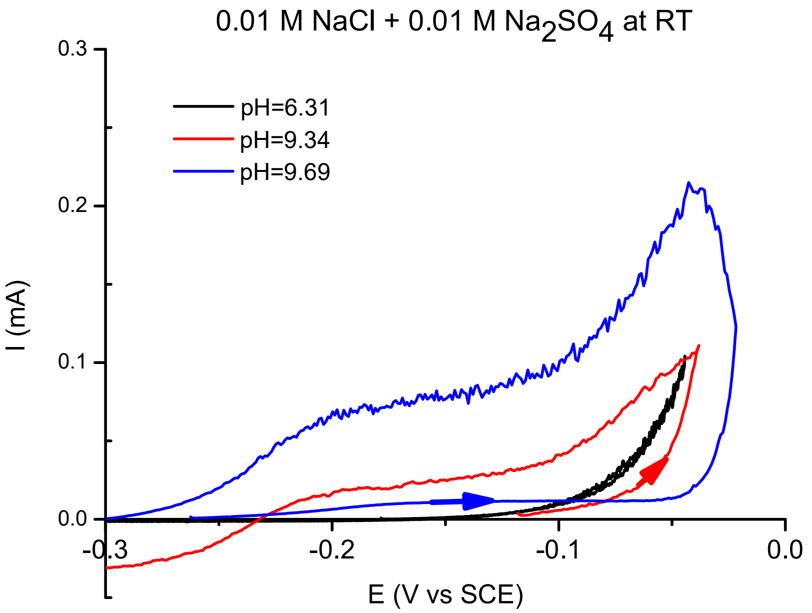

Figure 2.6. A set of potential scans ordered by pH for 0.01 M Cl^- + 0.01 M SO_4^{2-} solutions at 25°C, forward scans indicated by coloured arrows (Data provided by Amy Ai)

Figure 2.6 shows CVs recorded in a dilute solution of Cl^- and SO_4^{2-}. At pH 6.31 active behaviour is observed since the current on the reverse scan is the same as on the forward scan, indicating no suppression of metal dissolution by the formation of a passivating film. At both pH 9.34 and 9.69 well-defined breakdown potentials (E_b) are observed at positive potentials, preceded by a flat slowly increasing current region. The current for these scans is much higher on the reverse scan than on the forward scan, with the behaviour clearly indicating that passivity followed by film breakdown did occur on the forward scan. The higher currents, which only slowly decay and an E_{rp} value below the initial E value are clear indications that pitting did initiate. However, it should be noted that no optical analysis was performed on the Cu to confirm this.

2.3.4 Converting the Results into Active/Passive Maps

Based on the criteria established in the previous section, maps can be constructed which indicate whether active or passive behaviour can be expected. An A/P map is a compilation of the active/passive behaviour observed in a solution of a given composition and a specific temperature as a function of either concentration or pH. The A/P maps consolidate the effects of temperature and pH to establish rough boundaries between possibly passive and active behaviour.

Figure 2.7 (A to D) shows the A/P maps for various [Cl^-] for a range of temperatures. The data shows Cu is active at low pH for all [Cl^-] irrespective of temperature. Figure 2.7A and 7B show that at low temperatures, passivity can be established at higher pH values if the [Cl^-] is low enough. At 60°C, Figure 2.7C shows the possibility of passivity is confined to a small pH range between 10 and 11. The transition back into a region where Cu actively dissolves at any potential at high pH can be attributed to an increased Cu solubility at pH values more alkaline than that of the minimum solubility at intermediate pH values. This is consistent with the expectations based on the Pourbaix diagram displayed in Figure 2.1.

At 80°C, only active dissolution is observed for all pH and temperature conditions. Figure 2.7 shows that Cl^- causes Cu to undergo active dissolution over the whole potential range scanned except when the [Cl^-] is low and intermediate to high pH prevails. At intermediate pH, the oxide solubility (Cu_2O) decreases and passivity becomes possible.[4] As the temperature increases, there are fewer combinations of [Cl^-] and pH for which passivity can be established, and at 80°C only active dissolution is observed. This can be attributed to the ability of Cl^- to stabilize the Cu^+ state in the solution by complexation, thereby allowing the metal dissolution reaction to occur more readily[5],

$$Cu + 2Cl^- \rightarrow CuCl_2^- + e^- \qquad [2.1]$$

and at high [Cl^-][6]

$$CuCl_2^- + Cl^- \rightarrow CuCl_3^{2-} \qquad [2.2]$$

Figure 2.7 (E to H) shows the A/P maps for solutions with various [SO_4^{2-}] as a function of temperature. Figure 2.7E and Figure 2.7F show that passivity is possible at low temperatures, moderate [SO_4^{2-}] and basic pH values. Figure 2.7E, 7F and 7G show that at high enough [SO_4^{2-}] and temperature, passivity is favoured irrespective of pH. As the temperature increases active behaviour becomes progressively more likely, although passivity is still observed at 80°C at higher [SO_4^{2-}] and pH. Overall SO_4^{2-} solutions can promote passive film formation on Cu at moderate to high concentrations especially when the pH is at or above 9. These results are supported by the data gathered by Duthil et al., which suggest that, in SO_4^{2-}-dominated solutions, passivity leading to pitting is a strong possibility and that, unlike Cl^-, SO_4^{2-} promotes pitting when present at equivalent concentrations.[7] However, SO_4^{2-} does not form stable complexes with Cu^+ or Cu^{2+}, which would accelerate active metal dissolution. Consequently, pH is the key influence on CuO and Cu_2O film formation except at higher [SO_4^{2-}]. Whether or not SO_4^{2-} supports active dissolution or passivity for Cu is difficult to define, especially with respect to the DGR.[7,8] This is further complicated when Cl^- is present with SO_4^{2-}, because Cl^- appears to be the dominant anion and enforces active behaviour.

The pH in binary systems containing SO_4^{2-} and HCO_3^- is buffered by HCO_3^-/CO_3^{2-} which supports passivity and possibly pitting as indicated by the passive dominated plots shown in Figure 2.8 (A to D). HCO_3^- was found to be an important contributor to passive film formation with increasing concentrations by maintaining pH at alkaline values.[9,10] However, when Cl^- is present with HCO_3^-, passivity is only prevalent at high pH, while a combination of higher temperature and the presence of Cl^- promotes more situations where active dissolution occurs as seen in Figure 2.8 (E to H).

Figure 2.9 shows the behaviour observed in the ternary system containing all three anions. This set of conditions is the most relevant to the DGR. In this Cl^--dominated solution, passivity is only observed at low temperature and alkaline pH values. It was found that overall, when the solution temperature is increased, or the pH value is decreased, active dissolution becomes dominant. This suggests that complexation of Cu^+ by Cl^- determines whether the Cu actively dissolves or passivates in solutions that contain comparatively low SO_4^{2-} and HCO_3^- concentrations.

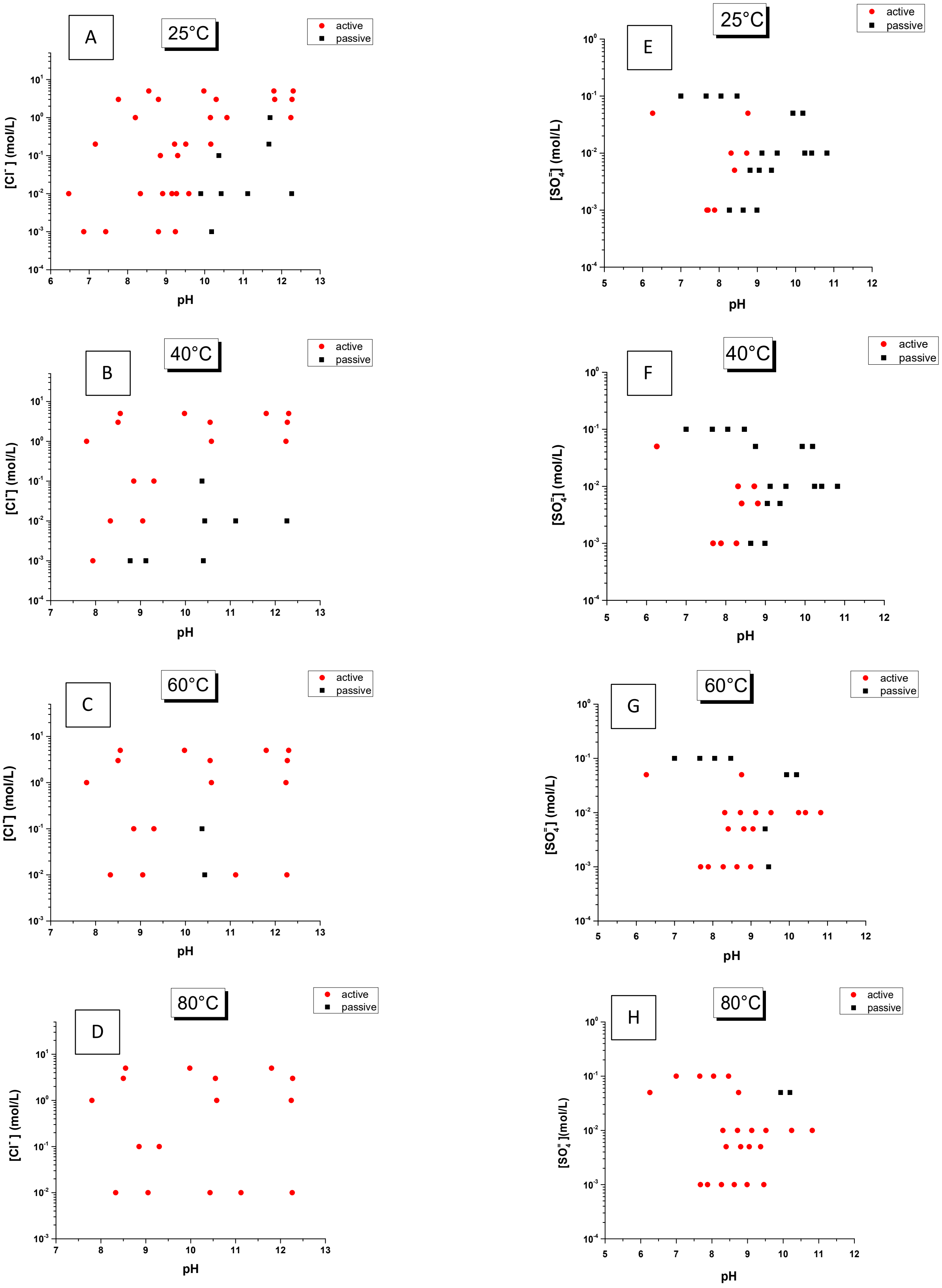

Figure 2.7. A/P maps for [X] M Cl^- solutions at 25ºC (A), 40ºC (B), 60ºC (C) and 80ºC (D) (left column) and A/P maps for [X] M SO_4^{2-} solutions at 25ºC (E), 40ºC (F), 60ºC (G) and 80ºC (H) (right column)

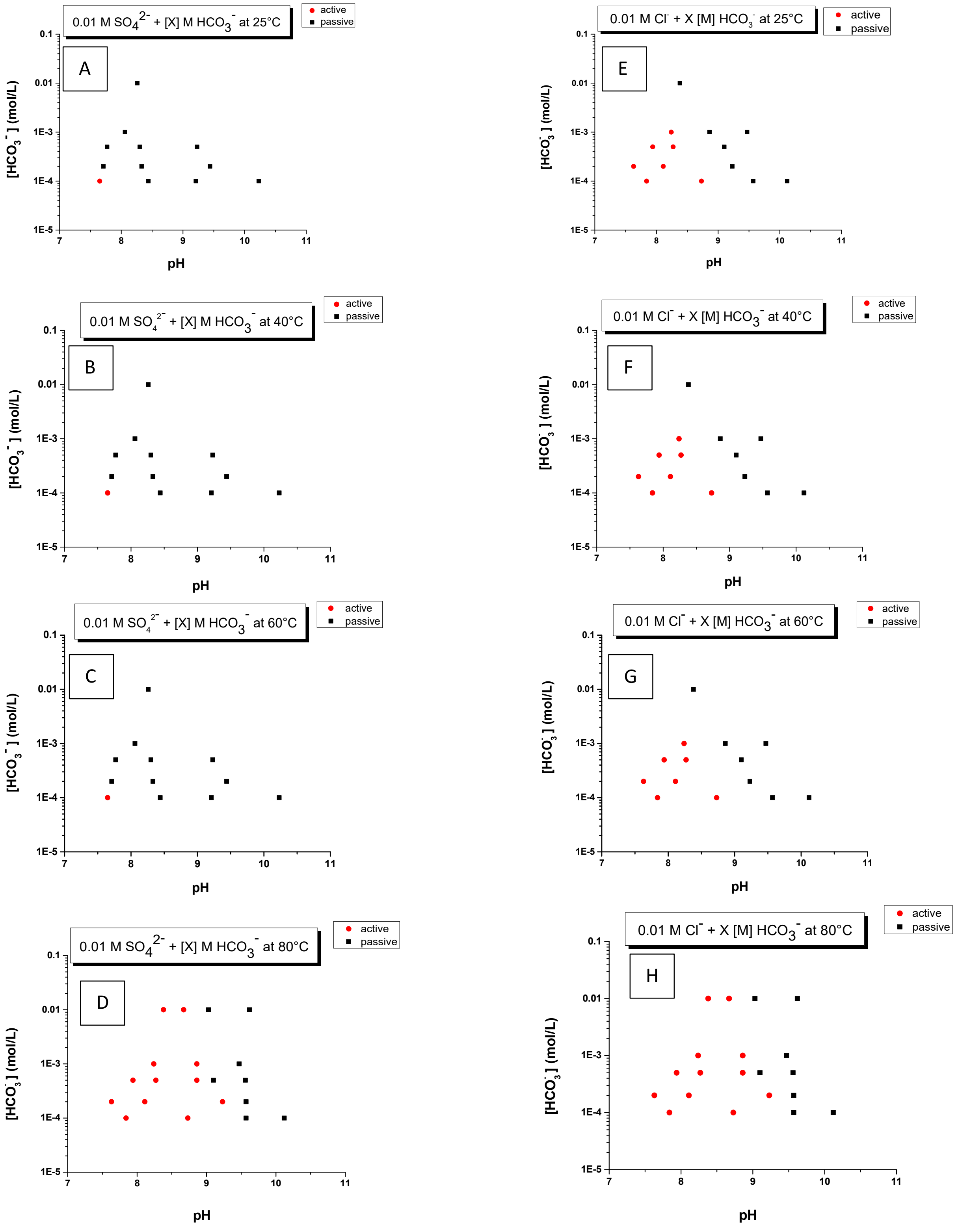

Figure 2.8. A/P maps for 0.01 M SO_4^{2-} +[X] M HCO_3^- solutions at 25ºC (A), 40ºC (B), 60ºC (C) and 80ºC (D) (left) and A/P maps for 0.01M Cl^- + [X] M HCO_3^- solutions at 25ºC (E), 40ºC (F), 60ºC (G) and 80ºC (H) (right)

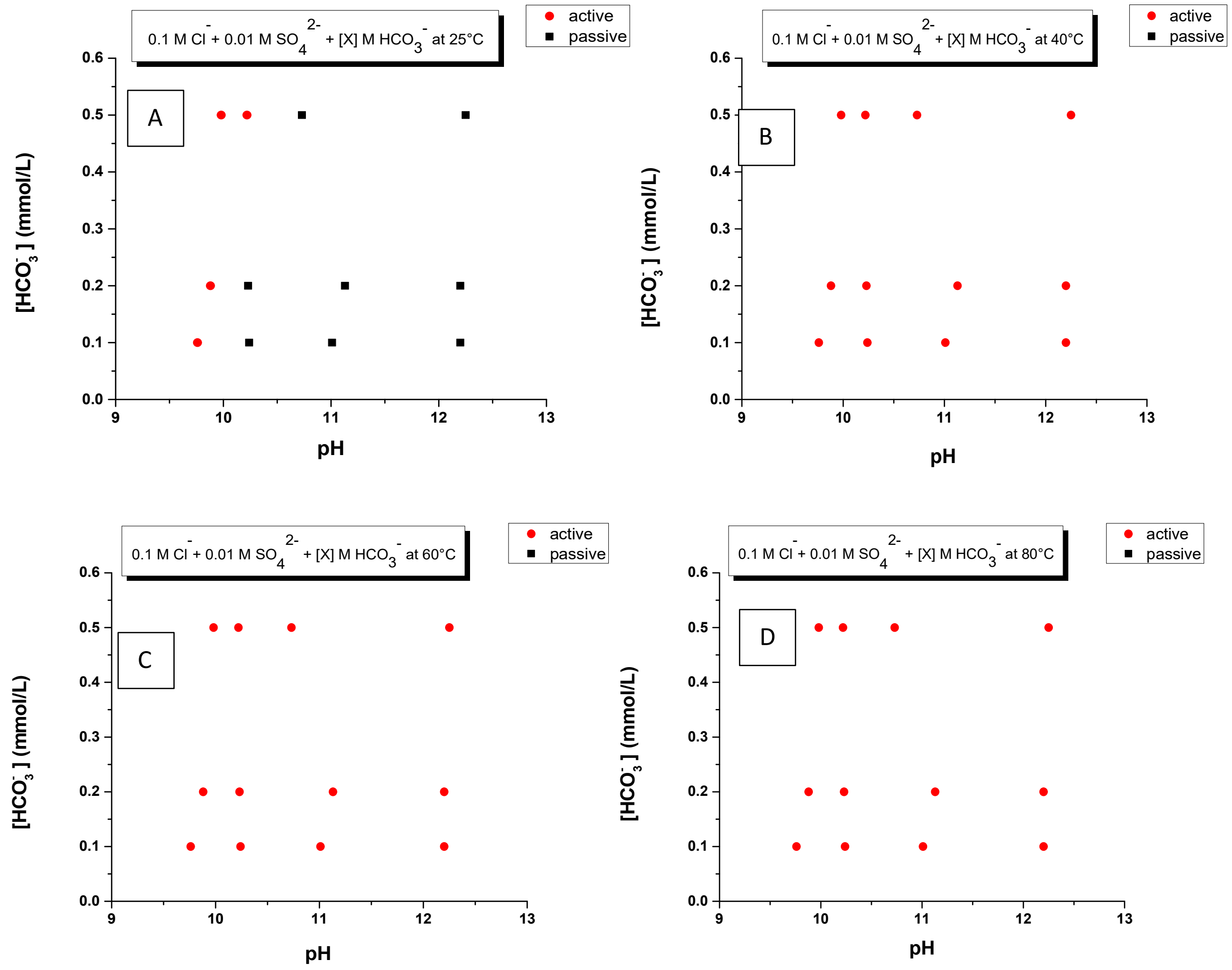

Figure 2.9. A/P maps for solutions containing 0.1 M Cl^-+ 0.01 M SO_4^{2-} + [X] M HCO_3^- at 25°C (A), 40°C (B), 60°C (C) and 80°C (D)

2.3.5 Drawing Active/Passive Boundaries

A/P boundary maps provide a visualization of the ranges where active dissolution and passive film formation can occur, for the three key parameters, temperature, pH and ion concentration. By including the range of conditions anticipated in a DGR on the same plot, a clear picture as to whether passivity, and hence possibly pitting, could occur, can be obtained. Boundaries are drawn by first taking the closest set of horizontal A/P points and averaging the distance between them. This was performed for each concentration on an A/P map and the resulting points were then connected by a smooth line. Since the amount of data is limited these lines do not show the uncertainties involved in defining the boundaries. In addition, A/P boundary maps are only drawn for the pH region slightly above the expected DGR conditions, since extremely alkaline conditions will not occur in a DGR environment. The low pH region is also not included in the

A/P boundary maps since active dissolution is guaranteed by the enhanced solubility of ions and the instability of Cu oxides. The shaded areas included in the Figure 2.10 and Figure 2.11 maps show the range of DGR conditions anticipated, based on the values in Table 2.2.

Table 2.2. Predicted near-field pore water chemistry.[6]

Temperature	pH	$[Cl^-]$ (mol/L)	$[SO_4^{2-}]$ (mol/L)	$[CO_3]_{tot}$ (mol/L)
< 100°C	7.5-8.2	0.01-6.5	0.005-0.025	0.0002-0.001

Figure 2.10A shows that, for the $[Cl^-]$ range expected in a DGR, only active dissolution would be expected since this anion promotes dissolution. For the anticipated $[SO_4^{2-}]$ range, active behaviour would be expected but the proximity of the DGR conditions to the A/P boundaries, especially at lower temperatures as shown Figure 2.10B, is very small making the influence of SO_4^{2-} unclear.

Figure 2.11A shows the influence of increasing $[Cl^-]$ on the A/P boundaries measured in a dilute SO_4^{2-} solution. As the $[Cl^-]$ is increased, the boundaries shift away from the anticipated DGR conditions, confirming that active conditions are promoted in Cl^- solutions, as expected based on Figure 2.10A. Figure 2.11B shows that if the $[Cl^-]$ is low, Cu remains active but the A/P boundary approaches the anticipated DGR conditions as the $[SO_4^{2-}]$ increases and the pH decreases. In both these cases an increase in temperature generally favours active conditions.

Figure 2.11C and 11D show the influence of small total carbonate concentrations ($[CO_3]_{tot}$) on dilute and moderately concentrated Cl^- solutions, respectively. As with SO_4^{2-} solutions, the presence of Cl^- guarantees that active conditions are maintained although the distance of the A/P boundaries from the DGR conditions is greater at higher $[Cl^-]$. Figure 2.11E shows the influence of $[CO_3]_{tot}$ in a dilute SO_4^{2-} solution. In this case, in the absence of Cl^-, the DGR conditions are clearly in the passive region over the full range of pH and temperature, indicating that these conditions could support pitting when passivity is established.

Figure 2.12 shows the behaviour observed in a realistic DGR environment with moderate $[Cl^-]$ and $[SO_4^{2-}]$ close to the expected value. The expected conditions are shown to be well into the region of active behaviour and only slightly influenced by the possible variability in groundwater $[CO_3]_{tot}$. Since, in general, increases in temperature reinforce active conditions, and

[Cl⁻] are likely to be higher rather than lower, these results indicate that active conditions will be maintained in a DGR, and that passivity leading possibly to pitting will not occur.

One final important feature to note is the very distinct differences between all the A/P boundaries shown in Figure 2.10, Figure 2.11, and Figure 2.12. The binary anion solutions show that even if the two same anions are used, the boundaries are highly dependent on concentration, since no two sets of boundaries are similar. This leads to the conclusion that this analysis is required on a case-by-case basis for specific DGR sites as well as for variances in local DGR environments that could affect the clay composition, resulting in a pH or anion concentration change. Depending on the components of the groundwater at a given site additional anions that could affect the behaviour of the Cu could be analyzed in quaternary or higher order solutions along with real groundwater analysis to help validate these results.

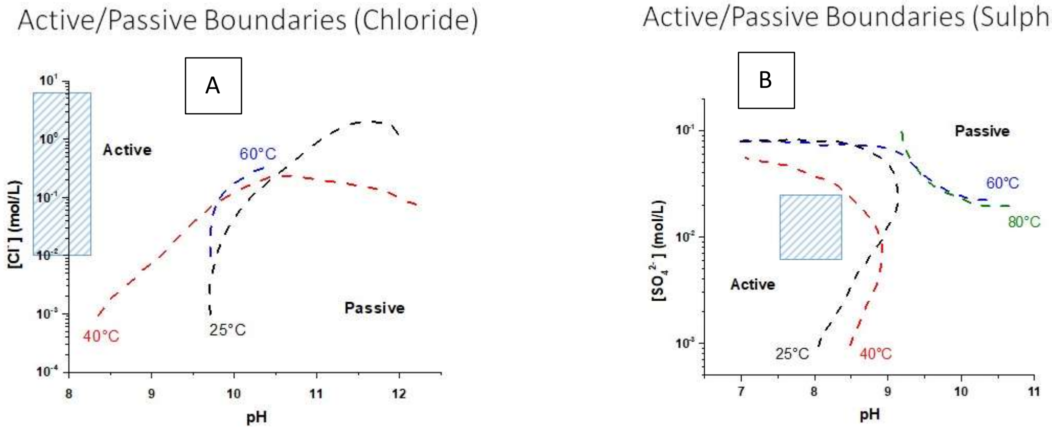

Figure 2.10. A/P boundaries for all unary anion solutions tested. The shaded areas represent the range of conditions expected in the DGR[12]

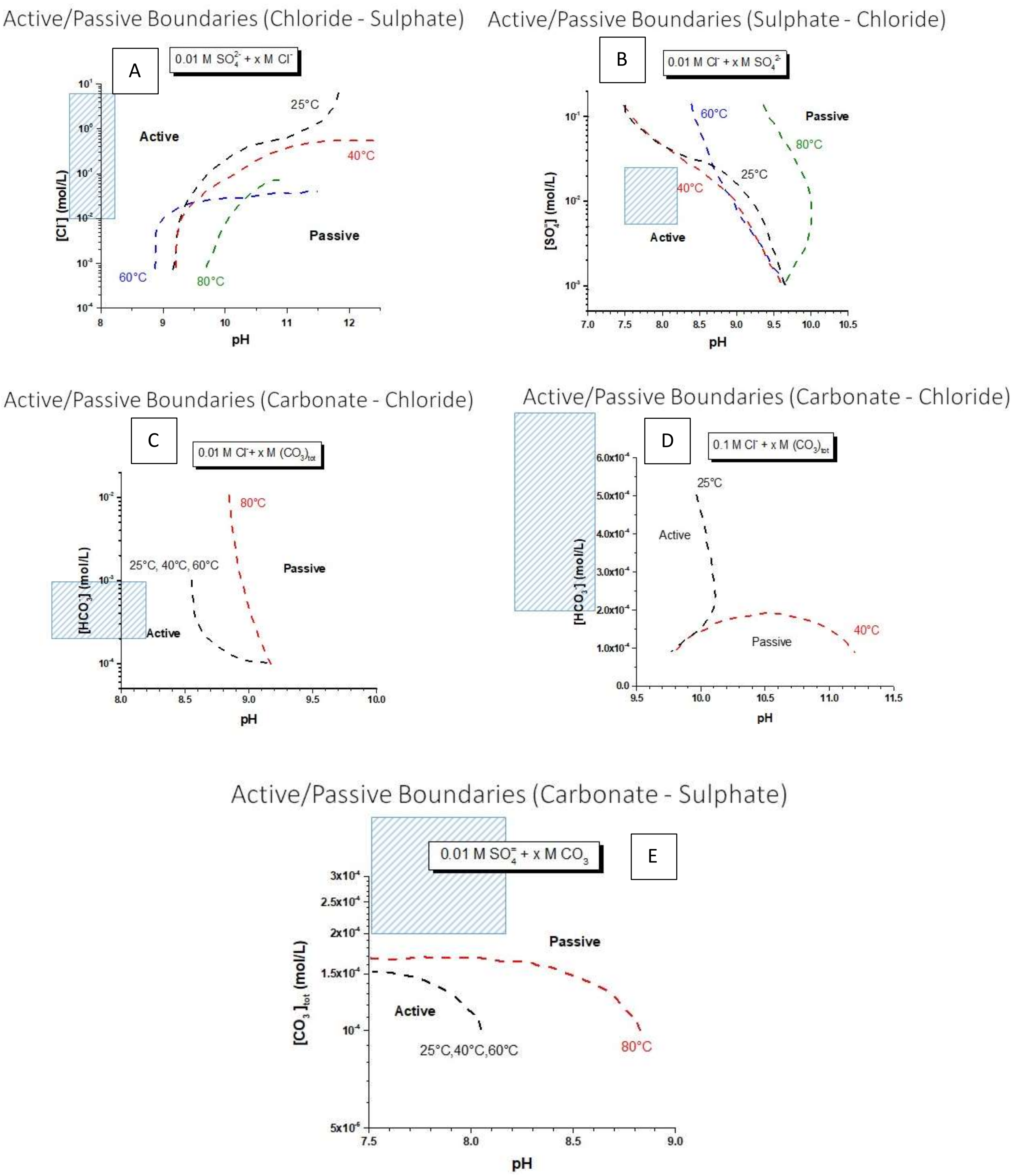

Figure 2.11. A/P boundaries for all binary anion solutions tested. The shaded areas represent the range of conditions expected in the DGR[12]

2.3.6 Determination of Sensitivity to Pitting

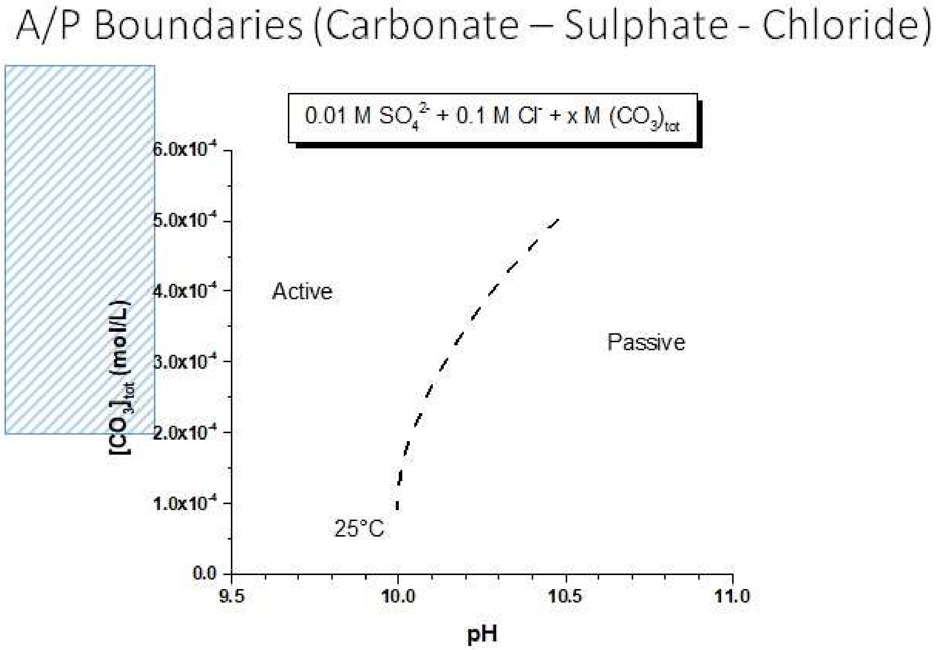

Figure 2.12. A/P boundary for the ternary anion solution tested. The shaded areas represent the range of conditions expected in the DGR[12]

From the analyses in previous sections, it was determined that the DGR is very likely to support active dissolution during the early stages of container emplacement in the DGR when O_2 remains present. While passivity is a pre-requisite its presence does not guarantee that pitting will occur. To determine the susceptibility of Cu to pitting in a specific exposure environment it is necessary to compare the relative values of the corrosion potential, E_{corr}, the film breakdown potential, E_b, and the re-passivation potential, E_{rp}. If $E_{corr} \geq E_{rp}$, Cu will be susceptible to pitting. If $E_{corr} < E_b$, then pitting is unlikely to occur with the probability increasing the closer E_b is to E_{corr}. Figure 2.2B shows a scan in which both E_b and E_{rp} are greater than E_{corr} when pitting should not occur spontaneously, despite the observation that a passive state can be achieved by polarizing the Cu surface to potentials above E_{corr}. Figure 2.13A and B show these potential values measured in SO_4^{2-} solution containing small amounts of $(CO_3)_{tot}$, for which the A/P boundary map in Figure 2.11E showed could sustain passivity. These values show that, over this pH range $E_{corr} < E_b$ and film breakdown would not be expected. However, since $E_{rp} < E_{corr}$, if pitting did initiate then re-passivation would not occur and pitting would continue. While outside the pH conditions expected in a DGR, the potential values recorded at pH 10.25 show that, while passivity would occur, E_{corr} is significantly lower than E_b and E_{rp} indicating that the passive condition should be stable.

While Figure 2.11E shows that the solution analyzed in Figure 2.13 will lead to passivity at pH values above 8 and potentials above -0.25 V(SCE), these conditions are outside the range of the expected DGR conditions shown in Table 2.2. Figure 2.13 also demonstrates how narrow the separation between the key potentials can be. Since these potentials will have statistically distributed values, and the possibility that some locations could pit remains in $SO_4^{2-}/(CO_3)_{tot}$-dominated environments.[11]

This analysis provides a good starting point for the direction further studies should take if the DGR conditions were deemed able to support passivity. It would be necessary to measure the key potential values to determine the statistical probability that pitting could occur. However, given the anticipated environment, the focus should be on active dissolution.

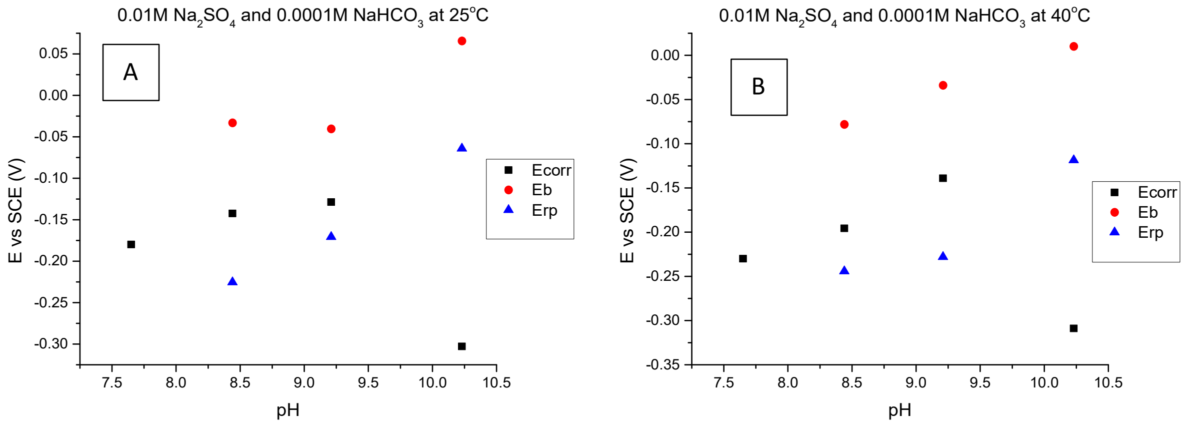

Figure 2.13. Potential vs pH plots for a solution containing 0.01 M SO_4^{2-} + $1x10^{-4}$ M HCO_3^- at low temperatures

2.3.7 Revised Considerations Regarding Active/Passive Analysis

The goal of the analysis presented is to establish a what potential groundwater compositions support active or passive conditions. While active conditions are preferred within a DGR, due to their higher predictability, passive surfaces would reduce corrosion rates if pitting was avoided. Based on the analyses in this chapter, most of the solution combinations studied, especially the most important solution (ternary), the DGR should support active dissolution with the probability of passive film formation being remote.

Cl^- has been determined to promote active dissolution by stabilizing Cu^+ by complexation as indicated by [2.1] and [2.2]. The behaviour of SO_4^{2-} is more ambiguous. While it may promote active dissolution, its behaviour is largely pH dependent since it does not significantly complex soluble Cu species. $(CO_3)_{tot}$ is a well known pH buffer that also promotes passive film formation, and since the A/P boundary maps encompass the pH region in which $(CO_3)_{tot}$ buffers, an accurate assessment of its influence on active/passive behaviour has been obtained.[10,] This is fully supported through the analysis of the ternary solution A/P map, in which the only temperature for which a boundary is observed is at 25°C and only for > pH 10, a pH range that is extremely unlikely in groundwater solutions. However, the A/P boundaries determined have limited accuracy with a better definition requiring the accumulation of more data.

2.4 Summary and Conclusions

CVs were performed in a range of solutions containing various combinations of ground water ions ($[Cl^-]$, $[SO_4^{2-}]$, $[(CO_3)_{tot}]$), pH values and temperatures to determine whether passivity of the Cu surface could be achieved, since it is a prerequisite for pitting. The criterion for passivity was an observable active to passive transition in the CVs. Based on these observations, Cu was defined as either active or passive in that particular environment. A series of A/P maps were constructed, based on these measurements. These maps showed that active conditions were promoted by low pH values (< 7.5), high temperatures and high $[Cl^-]$. Passive conditions were promoted by high $[(CO_3)_{tot}]$ and $[SO_4^{2-}]$, provided that the $[Cl^-]$ was absent from the solution. Comparison of A/P maps to the expected conditions in a DGR showed passivation was only probable in binary SO_4^{2-} solutions containing low $[(CO_3)_{tot}]$. Groundwaters with such compositions are not anticipated and experiments in the pore water solution containing all three anions, designed to simulate a DGR environment, show that active conditions are expected at all temperatures. Boundary lines drawn give a good approximation of regions of activity and passivity for Cu but can be improved with further analysis to fill in some of the larger interval gaps. The boundary lines follow no exact trend, suggesting that this analysis should be performed on a case-by-case basis for the ground water compositions for potential a DGR site.[12]

2.5 References

---

1. Beverskog, B.; Puigdomenech, I. Revised Pourbaix Diagrams for Copper at 25 to 300°C. *J. Electrochem. Soc.* **1997,** 144, 3476-3483.

2. Kelly, R.G.; Scully, J.R.; Shoesmith, D.W.; Buchheit, R.G. *Electrochemical Techniques in Corrosion Science and Engineering*. Marcel Dekker, Inc. New York, NY, 2002, p 9-124.

3. Lide, D. R. *CRC Handbook of Chemistry and Physics.* 1st ed. CRC Press: Boca Raton, 2005; pp 8-24.

4. Palmer, D.A. Solubility Measurements of Crystalline Cu_2O in Aqueous Solution as a Function of Temperature and pH. *J. Solution. Chem,* **2011,** 40, 1067-1093.

5. Arjmand, F.; Adriaens, A. Influence of pH and Chloride Concentration on the Corrosion Behavior of Unalloyed Copper in NaCl Solution: A Comparative Study Between the Micro and Macro Scales. *Materials,* **2012,** 5, 2439-2464.

6. King, F. *Corrosion of copper in alkaline chloride environments;* TR-02-25; SKB: Stockholm, Sweden, 2002.

7. Duthil, J.P.; Mankowksi, G.; Giusti, A. The Synergetic Effect of Chloride and Sulphate on Pitting Corrosion of Copper. *Corros. Sci.* **1996,** 38*,* 1839-1849.

8. Mankowski, G.; Duthil, J.P.; Giusti, A. The Pit Morphology on Copper in Chloride- and Sulphate-Containing Solutions. *Corros. Sci.* **1997,** 39, 27-42.

9. Edwards, M.; Rehrin, J.; Meyer, T. Inorganic Anions and Copper Pitting. *Corrosion,* **1994,** 50, 366-372.

10. Cong, H.; Michels, H.T.; Scully, J.R. Passivity and Pit Stability Behavior of Copper as a Function of Selected Water Chemistry Variables. *J. Electrochem. Soc.* **2009,** 156, C16-C27.

11. Milošev, I.; Metikoš-Huković, M.; Drogowksa, M.; Ménard, H.; Brossard, L. Breakdown of Passive Film on Copper in Bicarbonate Solutions Containing Sulfate Ions. *J. Electrochem. Soc.* **1992,** 139*,* 2409-2418.

12. Qin, Z.; Daljeet, R.; Ai, M.; Farhangi, N.; Noël, J. J.; Shoesmith D. W.; King F.; Keech, P. The Active/Passive Conditions for Copper Corrosion under Nuclear Waste Repository Environment. *Corros. Eng. Sci. Techn.* **2017,** 52, 45-49.

3. Mapping Individual Anodes and Cathodes using the Multichannel Microelectrode Analyzer

3.1 An In-depth Look at the MMA and MEAs

3.1.1 MMA and MEA Basics

MEAs consist of many electrodes arranged in a pattern. Electrodes in a MEA are often measured individually or in groups depending on the potentiostat/galvanostat and the wiring. These arrays can be used to conduct either a high throughput of simultaneous measurements or to perform a bulk surface simulation.[1] There are two main types of MEAs: sensory MEAs and consumable MEAs. Depending on the type and design different problems can be probed. For example, a consumable MEA consisting of more than 10 electrodes could be used to more reliably determine the A/P boundaries measured in Chapter 2, since multiple measurements can be performed simultaneously to create a distribution of values for a designated set of conditions.

Optimizing an MEA design can be difficult because the number of connections is determined by the potentiostat/galvanostat. A single potentiostat or even a multistat would offer minimal connections (1-8) with lots of cabling issues. The MMA offers up to 100 connections with simpler cabling. The instrument has 5 base connectors which connect to specially designed ribbon cables that are split into 2 and each has 10 measurable connections. Current measurements are made using zero resistance ammeters (ZRAs) with maximum measurable values of 1 μA or 100 μA and measurement accuracy in the nA range. In the event of faulty or unused connections in each group individual connections can be omitted.

A main advantage of using a MEA is the high spatial and temporal resolution across a large quantity of electrodes.[2] Another advantage is the ability to easily change the MEA design between sets of fabricated arrays to troubleshoot issues encountered during experimentation.[3] An ideal MEA in terms of this thesis was customizable and reliably reproduced with 50-100 electrodes.

Fabricating MEAs to yield reproducible measurements can be very difficult. The main method for achieving maximum reproducibility was streamlining the fabrication process. Streamlined production of the MEAs created more possibilities for adaptation of the MEA design between generations (groups of MEAs produced in the same batch).

MEA fabrication in this thesis was streamlined by using frames with a single type of connector interface which narrowed down the possible MEA components. A commonly shared sample-instrument interface allowed MEAs to be easily connected to and measured by the MMA. Another advantage offered by streamlined MEA fabrication was that the cost per experiment was decreased significantly with each MEA costing as little as $12-30.

It is important to note that the MEAs in this thesis use microelectrodes (MEs) because the fabrication of ultramicroelectrodes (UMEs) could not be achieved. UMEs are classified as having a diameter or critical dimension of less than 25 μm.[4] However, the MEs used in the final generation of MEA's range from circular to square either 50 μm in diameter or 175 μm x 175 μm, respectively. Therefore, the analysis techniques used were chosen to accommodate ME analysis.

Our MEAs were created with three major criteria in mind:1) MEA production needed to be streamlined with a universal frame; 2) a dedicated experimental setup needed to be designed; and 3) MEs or UMEs (if possible) were preferred.

3.1.2 Limitations of the MEAs

MEAs are ideal for statistical ME analysis and high throughput experiments.[5] The electrochemical behaviour of the electrodes in a MEA varies based on distance between adjacent electrodes.[6] The ratio between the interelectrode distance and the electrode diameter (or critical dimension) controls if the electrodes behave individually or simulate a single surface. As the ratio increases the electrode diffusion layers and potential fields overlap less which decreases their influence on each other. If the ratio, for disk-shaped electrodes, is greater than 30 then the electrodes are considered to act individually.[6] These MEA fabrication criteria pertain to pre-experimental preparation. When corrosion and chemical reactions are taken into consideration new problems arise.

The first problem, common to corrosion studies, is the presence of crevices. Crevices can occur in areas containing limited solution volumes between the electrode and an occluding layer. In these occluded areas corrosion damage can occur. The most common method of eliminating or minimizing crevice effects is to apply a coating to the electrodes. Three types of coating were investigated to eliminate crevices: nail polish, Miccroshield (referred to as Microshield), and

Epofix. These coatings were selected due to availability, cure times and stability. Coating viscosity, thickness, cure time, adhesion and cold flow can negatively impact its application. These coating properties and their effects on the coating stability were analyzed and taken into consideration as tests were conducted to ensure a viable layer was adhered to the electrode surface.

Another limitation considered was electrode size with respect to the current response. Isolating individual anodic and cathodic events has only been considered since the size of electrode required to sustain a single event is unknown.[7] One possibility is that the two activities are inseparable, but this has not been demonstrated at E_{corr}. Therefore, the electrode size needed to explore the separation of anodic/cathodic activity on a single electrode surface is unknown. This posed a problem for MEA fabrication and analysis, since some techniques did not have the speed, accuracy, or sensitivity for corrosion analysis on small anodes/cathodes. Another issue was ensuring the preservation of the corrosion products during analysis.

3.1.3 MEA Components

The MEAs in this thesis were broken down into the following key components: the electrode material, the substrate, the coating, and the instrument connector. Various production and analysis trials were performed to determine the optimal parts for each component. Each component has multiple characteristics that were considered in these trials. The MEAs in this thesis used either high purity (99.9%) Cu wires or electrodeposited Cu etched into lines (referred to as traces or pads) as the electrode material.

The following aspects of the substrate were considered: the space for electrodes; the physical/chemical properties; the compatibility with connections; and the compatibility with various coatings. These aspects were sorted into spatial characteristics (electrode space and compatible connections) and material characteristics (physical/chemical properties and coating compatibility). The spatial characteristics were controlled by the fabrication process, which involved the manufacturer's processing (performed by an external vendor) and substrate processing (performed by the researcher). The amount of substrate processing was reduced by providing the electronics vendor with a custom design. A substrate provided by a vendor had high reproducibility since all the components were machine-made to the designated specifications. The vendor also had a variety of choices for electrode and substrate materials, which allowed for design flexibility. A universal connector-interface adapter was designed for the MMA interface that could support up to 100 connections. These three factors made the MEA easy to use, low cost, and fast to produce. Since a wide variety of materials with various spatial characteristics were available in pre-made electronic components, such components provided an optimal source of test substrates for MEA fabrication.

A coating was applied to the MEA substrate to seal the electrodes in place and eliminate any possible crevices. The coating was also used to reduce electrode size. The following aspects of the coating were considered during selection: its stability in target environments; its curing procedure; its viscosity or cold flow prior to curing; the removal process; its cured thickness; and the ease of applying a uniform layer. These considerations were split into chemical properties of the coating (stability and removal) and mechanical properties (curing, thickness, uniformity).

The chemical properties were the first aspects tested. First, the stability of the coating was tested, which determined its viability and if it required re-application after an experiment. If the coating passed the stability test, its approximate thickness after curing was examined by various methods. Lastly, the best method to apply the coating uniformly was determined. Examination after curing was especially important since small defects could form across the surface during this step. Defect elimination required either chemical processes (thinners) or mechanical methods (shaking or vacuum pumping).

The last component considered in MEA fabrication was the instrument connector. A lot of electronic components have similar connections; therefore, an adapter was selected based on the maximum number of expected connections.

The MMA ribbon cables were either fitted into a male or female rectangular connector or the single connectors were arranged into a pattern to reduce the number of cables needed. The adapter was also selected to accommodate 50 connections.

3.2 MEA Generations

3.2.1 The First Generation of MEAs (G1)

Figure 3.1. A profile view of a blank rectangular 50 pin male header

The first premade electronic component chosen for MEA fabrication was a rectangular male header with female sockets, shown in Figure 3.1. It was able to accommodate 50 electrodes, had male connections which easily interfaced with a female counterpart or individual pin connections using crimp sockets, and female sockets that were able to accommodate Cu wire electrodes. These headers are made from plastic with gold brushed contacts and are stable in near-neutral environments. The substrate was coated with an epoxy to improve its stability in acidic or basic environments.

The coatings tested with this substrate were nail polish and Epofix (a clear resin). The coatings were used to seal the electrodes and prevent crevices.

Nail polish (Sally Hansen brand, original formulation no longer listed) was chosen to coat the Cu wires after polishing and to seal the electrodes in the sockets to eliminate any possible crevices. Nail polish is a hydrophobic compound, considered stable in Cl^- environments.[8] Nail polish was easily applied and then removed with acetone. It has a relatively low cure time (a few minutes in air), which is proportional to the thickness of the applied layer. Thick layers were achieved by multiple successive applications. The thickness and uniformity were controlled by the application method. Nail polish as a barrier is well recognized and known to be stable after solvent evaporation.[8] No additional mechanical processing was required for nail polish.

Epofix was chosen to coat Cu electrodes after the application of nail polish. Electrodes were made with Goodfellow Cu wire (99.9% purity) with a diameter of 0.5 mm. These were hand ground to p1200 grit prior to insertion into the MEA which was subsequently ground to p1200 grit. The connector to the instrument was a 50-pin ribbon cable with two male ends. Epofix prevented the nail polish from cold flowing and solution from creeping up the substrate to the connector. Epofix is more rigid than nail polish, hydrophobic and stable in neutral and basic solutions. Unlike nail polish, Epofix was removed by grinding/polishing or fracturing. Its thickness was determined by the amount poured into a curing mold and by the extent of subsequent polishing. Epofix was cured at room temperature overnight or in an oven at slightly elevated temperatures (~50°C).[9]

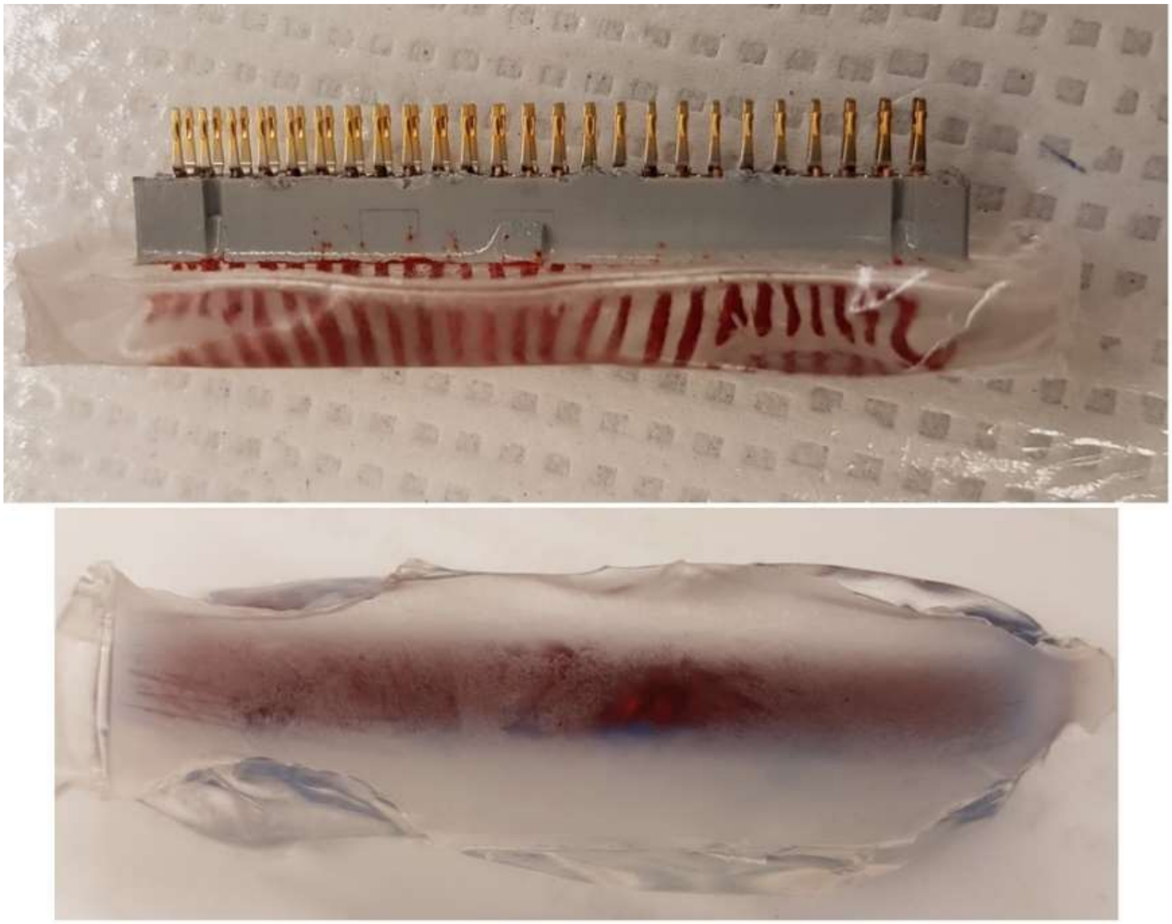

Figure 3.2. A Generation 1 MEA with nail polish coated electrodes sealed with Epofix

Prior to application Epofix was mixed with its hardener and the air bubbles formed were eliminated by thorough mixing. Typically, Epofix was applied in excess and then polished away to expose the electrodes and adjust the thickness. Figure 3.2 shows a thick layer of Epofix before polishing to p1200 grit.

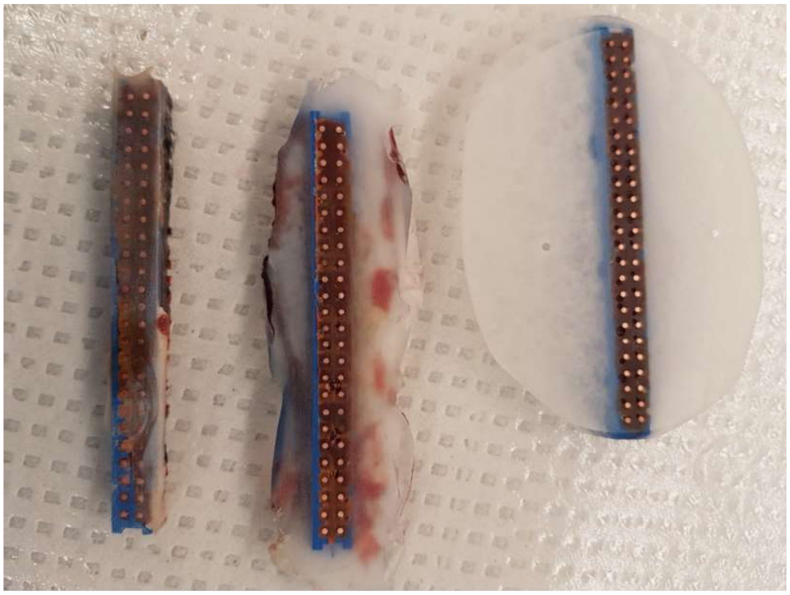

Figure 3.3. Progressive optimization of Epofix on G1 electrodes from the earliest version (left) to the final version (right)

Figure 3.3 shows multiple G1 MEAs with increasing amounts of cured Epofix from left to right. The left sample with minimal Epofix had many issues such as solution penetration to the connections and corrosion of the contacts above the gold brushed areas. The excess Epofix in the final sample (right) is referred to as "wings" which help the MEA sit at the solution interface without immersing the connections.

Figure 3.4. A generation 1 MEA and the interfacing male ribbon cable with the connection highlighted with a red circle

Figure 3.4 shows the gap between the interface cable and the MEA circled in red. The gap was painted with nail polish or taped over to prevent exposure to solution. The Epofix wings were designed to replace the sealant/tape.

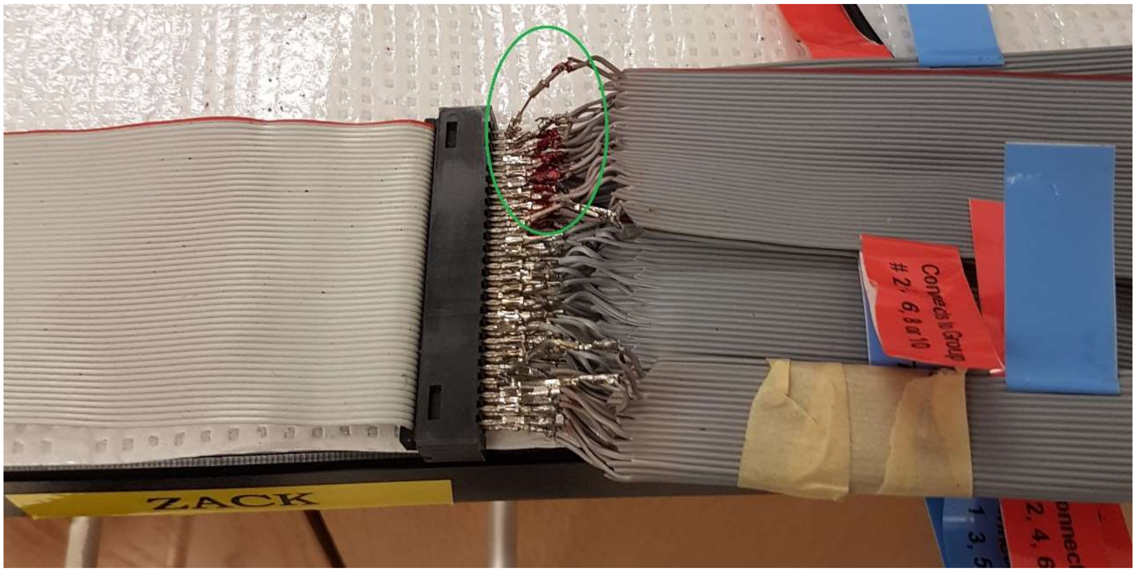

Figure 3.5. The sample-interface ribbon cable interfaced with the loose array of MMA connections. The red areas, circled in green, are coated in Microshield so that they are held in place and electrically isolated from each other

The individual MMA connections were attached to the 50-pin interface cable with crimp connectors, which provide a female connection. The crimp connectors were soldered on and then bound together in some areas with Microshield, circled in green in Figure 3.5. Microshield, is a organic polymer containing toluene, tetrahydrofuran and propylene oxide (the exact formulation or repeating unit is not listed by the manufacturer).[10] Microshield is stable in neutral environments, and in acidic environments it delaminates rather than dissolves. A thick layer can withstand up to 1 day of immersion in acidic solutions. Microshield is applied in a methyl ethyl ketone suspension and easily removed using acetone or other organic solvents. The thickness was controlled with an organic thinner (acetone) or through multiple applications.[10] The suspension dries in 1-2 minutes and must be applied quickly. Microshield layers contain no bubbles and the uniformity depends on the application method. Due to its optimal mechanical properties, and easy application and removal, Microshield was used on the interface crimp connectors.

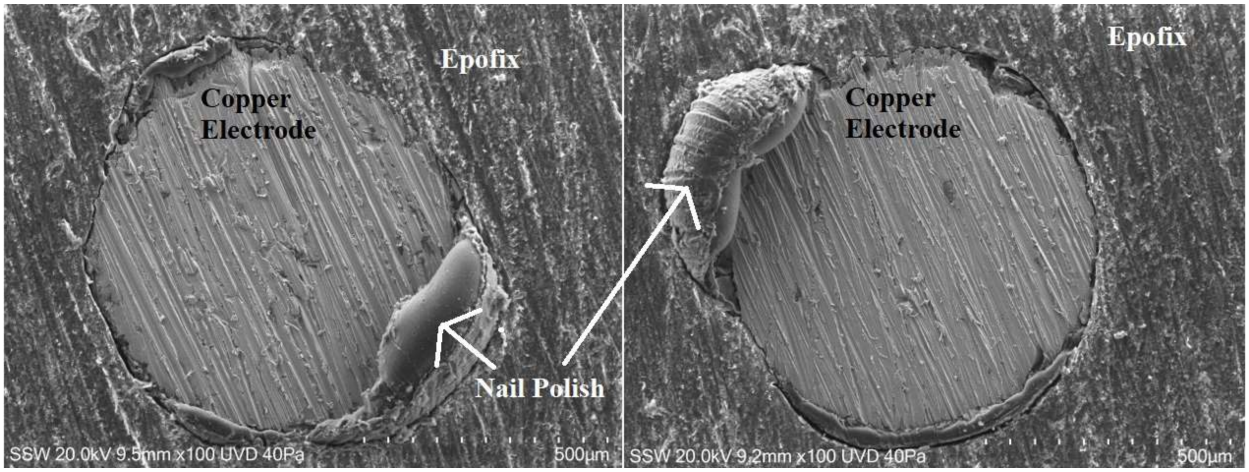

Figure 3.6. SEM images of electrodes from a generation 1 MEA polished to p360 grit

All optical images of the generation 1 (G1) MEAs show no significant differences. Therefore, optical imaging was discontinued in favour of SEM after analyzing a few G1 MEAs. The electrodes in a G1 MEA were polished/ground to between p360 and p1200 grit. In Figure 3.6 two electrodes finished at p360 grit are shown. These images indicate that the electrodes are not completely flush with the Epofix, nail polish or substrate. These images also show that the nail polish was displaced, likely during electrode emplacement, and partially covers the electrode. When the electrodes are polished to p1200 grit this partial coverage is removed, as seen in Figure 3.7. However, the observable gaps between the electrode, nail polish and substrate could act as crevices. Therefore, nail polish was not suitable for sealing the G1 MEAs.

It was determined that this coating combination was not suitable due to the possibility of the nail polish occluding the electrodes and the observable gaps between nail polish and Epofix. While a more suitable coating combination or method to reduce the number of crevices could have been found, it would have greatly increased the fabrication time. Based on these results, a MEA setup that required only one coating and had more distance between the solution and connectors was preferred.

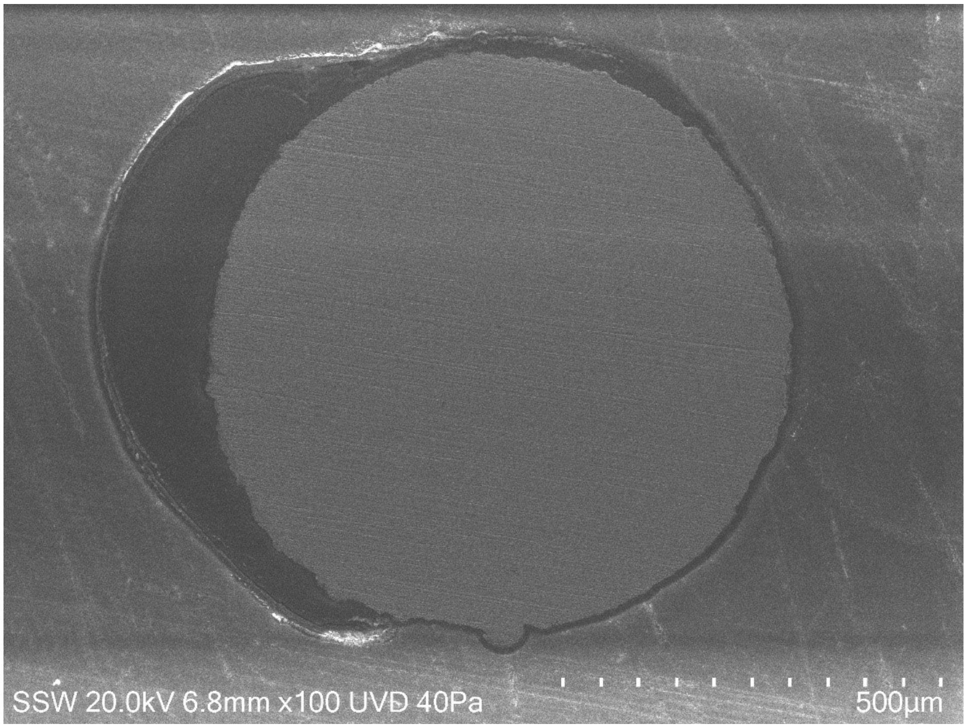

Figure 3.7. A SEM image of an electrode from a generation 1 MEA polished to p1200 grit, partial shadowing is affecting the contrast of the image, which is common for SEMs when interacting with organic layers that can charge

3.2.2 The Second Generation of MEAs (G2)

The second premade electronic component used in MEA fabrication was a rectangular FR4 board with etched Cu traces, similar to a base circuit board. FR4 is a fiber epoxy laminate which consists of a woven fabric of continuous glass cloth filaments laminated with an epoxy resin binder.[11,12] A layer of Cu (about 35 µm thick) is bound to FR4 and then etched to form traces for connections (electrodes).[12] The FR4 board had more space for electrodes than the G1 header; however, it was limited to 50 electrodes like the G1 header due to the spacing of the traces. The main spatial advantage of the FR4 board was that any connector interface was easily soldered onto it. This created more options for the instrument interface placement and provided more separation between the electrodes and instrument interfaces.

The FR4 board is very durable and stable in both acidic and basic environments. The instrument interface was placed far from the solution interface to avoid degradation. The electrodes were flush with the board, eliminating the risk of crevicing. The electrodes and traces required a coating to limit solution exposure. The disadvantage was there were 25 Cu traces on each side of the board, so the distance of electrodes widthwise was controlled by the thickness of the board. The FR4 board was also intended to be reusable, with potentially hundreds of uses per board depending on its condition after experimentation and maintenance.

The coating chosen for this setup was Microshield which can be quickly applied and removed. Microshield was also designed for harsh environments such as HF.[10] The exposed Cu area could also be modified by removing and re-applying Microshield between experiments which also refreshed the durability of the coating and allowed for precise electrode grinding. The stability of FR4 to grinding was unknown. Therefore, the condition of the board was monitored after each grinding session via SEM or a quick visual scan.

The instrument interface was a 50-pin male header soldered to the FR4 board. A male/female ribbon cable, as opposed to a double male ribbon cable, was used to connect the MEA (female end of the ribbon cable) to the instrument (male end of the ribbon cable), via the individual connections coated in Microshield.

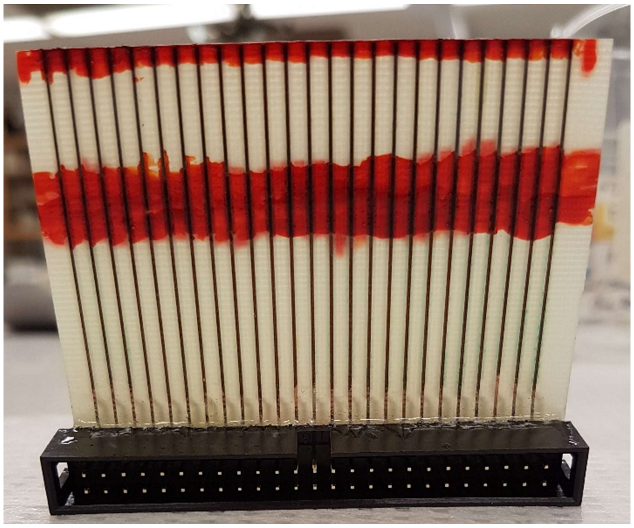

Figure 3.8. A second generation MEA coated with Microshield to limit the amount of Cu exposed to solution

As observed for G1 MEAs, optical imaging did not help identify any major flaws in the G2 MEAs. Therefore, SEM was the preferred imaging method. Figure 3.8 shows a typical electrode with Microshield applied to the top and bottom to create a rectangular exposed area. The

Microshield was also applied to the bottom edge to prevent any accidental electrical coupling of electrodes on opposite sides of the board.

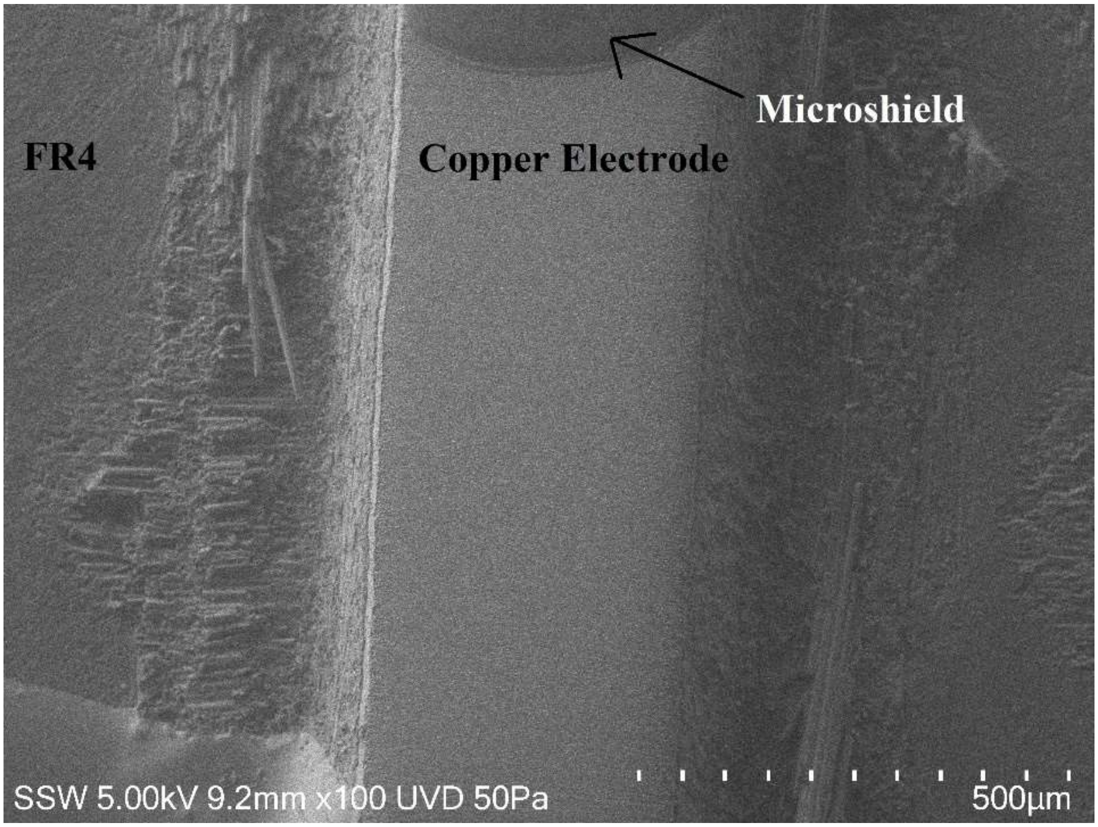

Figure 3.9. A G2 electrode after 1 day of submersion in 1 M NaCl

Figure 3.9 shows an SEM image taken after 24 hours of submersion in a 1 M NaCl solution. In this image there is no identifiable damage on the Cu electrode. However, the FR4 is slightly scratched due to grinding. The traces were hand ground to limit the damage to the Si board, though after repeated polishes up to p1200 grit with Si-C paper the FR4 board began to show some degradation.

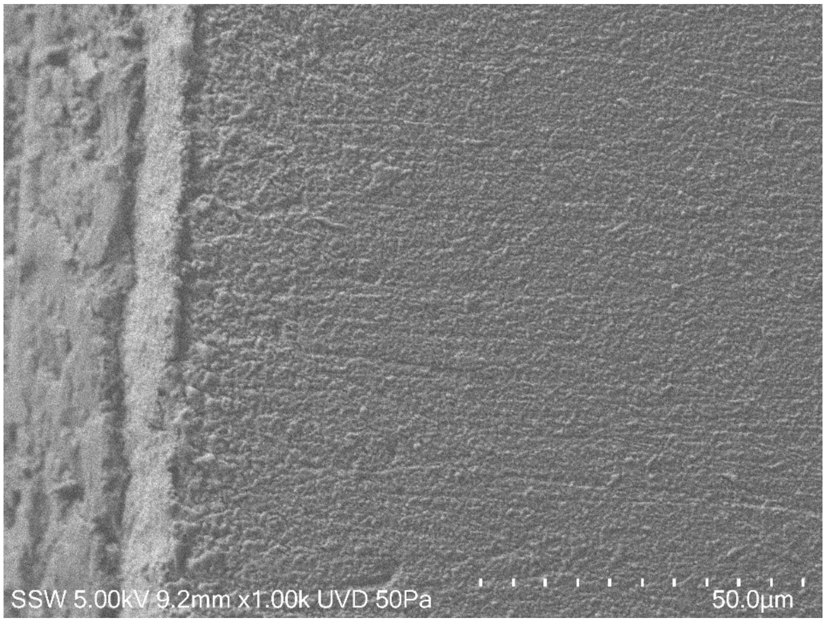

Figure 3.10. A magnified view of the Cu-FR4 board interface of the G2 electrode after 1 day of submersion in 1 M NaCl

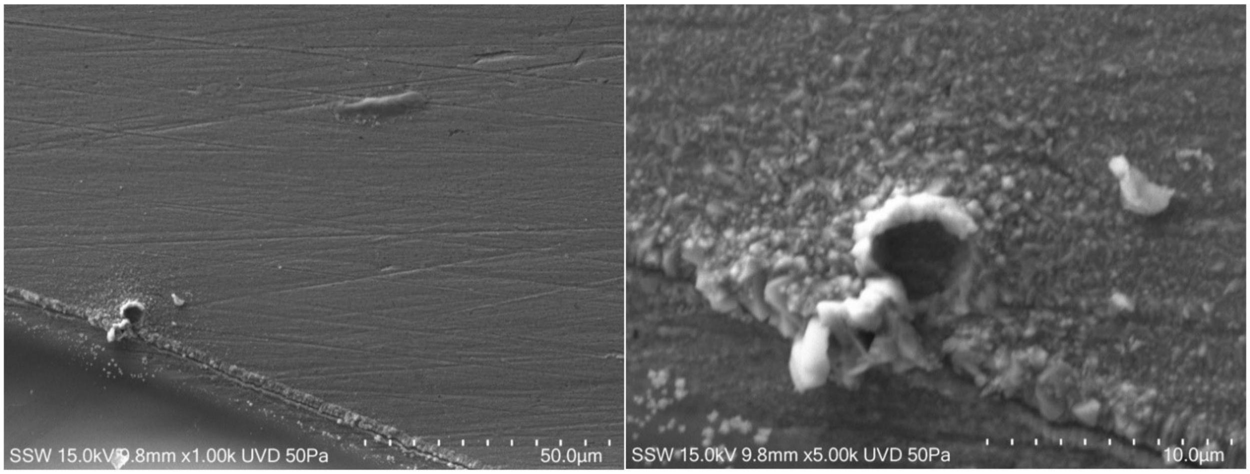

Figure 3.11. Two SEM images of varying magnifications of a pit-like defect at the Microshield-Cu interface after 1 day of submersion in 1 M NaCl

Figure 3.9 shows that the Cu trace electrodes appear to be less flush to the FR4 substrate than visual inspection indicates which means crevices could form between the Cu and FR4. However, examination of the interface in Figure 3.10 reveals only a small height difference between the Cu and FR4. Possible crevice formation was prevented by applying Microshield to the sides of the electrodes. A slower curing coating would have been more suitable, since Microshield is difficult to apply precisely since it cures quickly. Another issue is shown in Figure 3.11, where there is corrosion damage at the Microshield-Cu interface similar to pitting. While this is the only identified occurrence of such damage it represents a threat. Overall, the FR4 boards were good substrates, but required a slower curing coating in order to be utilized to their full potential. All submersions using 1 M NaCl with these G2 MEAs did not produce any significant corrosion damage. Therefore, isolation of individual anodes/cathodes could not be attempted, and no roughening pattern was discerned.

3.2.3 The Third Generation of MEAs (G3)

The third and final generation of MEAs built on the idea of FR4 boards by using premade printed circuit boards (PCB's) as the electronic component. The spatial characteristics are similar to G2 MEAs because PCBs are FR4 boards usually coated with a solder mask. The solder mask (a green coloured epoxy) exposes a small area of the traces, which act as the electrodes. The traces lead to an integrated set of female connectors that are plated with silver or gold to prevent oxidation in air. PCB manufacturing has the advantage of machine processing the FR4 PCBs within well-defined error margins which leads to high reproducibility. Manufacturers often take custom designs; therefore, batches of the same PCB can be produced. The PCB design could be altered between batches of PCBs. The main spatial flaw of the PCBs is that, to maximize space efficiency, the number of trace electrodes that could be drawn to the female connectors was limited to 48, due to trace spacing, connector location, and the chosen pattern. Therefore, the two middle electrodes of the third row of a 5 × 10 rectangle are isolated, since traces cannot be drawn there. The material characteristics of FR4 are constantly being studied through various mechanical tests and simulations which is exemplified by the work performed by Azam et al and Liakat et al.[11,12] Contrary to the physical properties the chemical properties of FR4 are much less studied. The solder mask is an exception which is stable in most environments except for prolonged exposure in strong acids or bases. The solder mask could be supplemented with an extra coating to further reduce electrodes to sizes that were not achievable by the manufacturer. Electrodes had minimum sizes of ~152 μm × ~152 μm as designated by the manufacturer, Camptech II Circuits in Markham, Ontario.

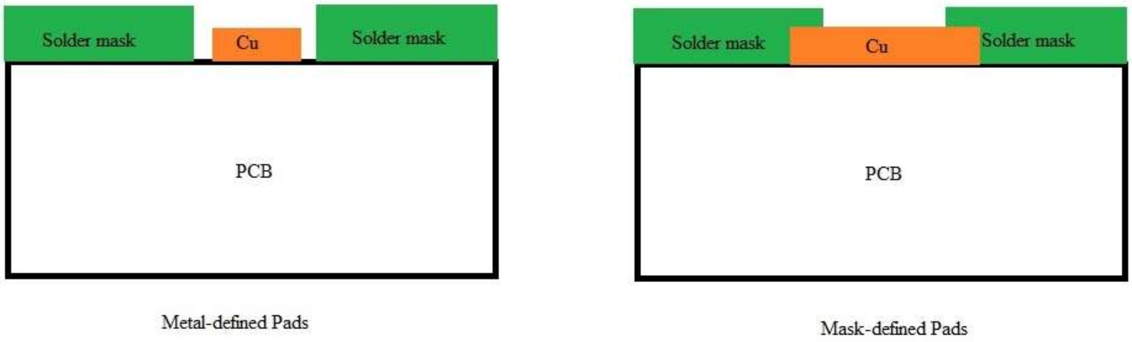

Figure 3.12. A schematic diagram of metal-defined versus mask-defined pad openings for PCBs

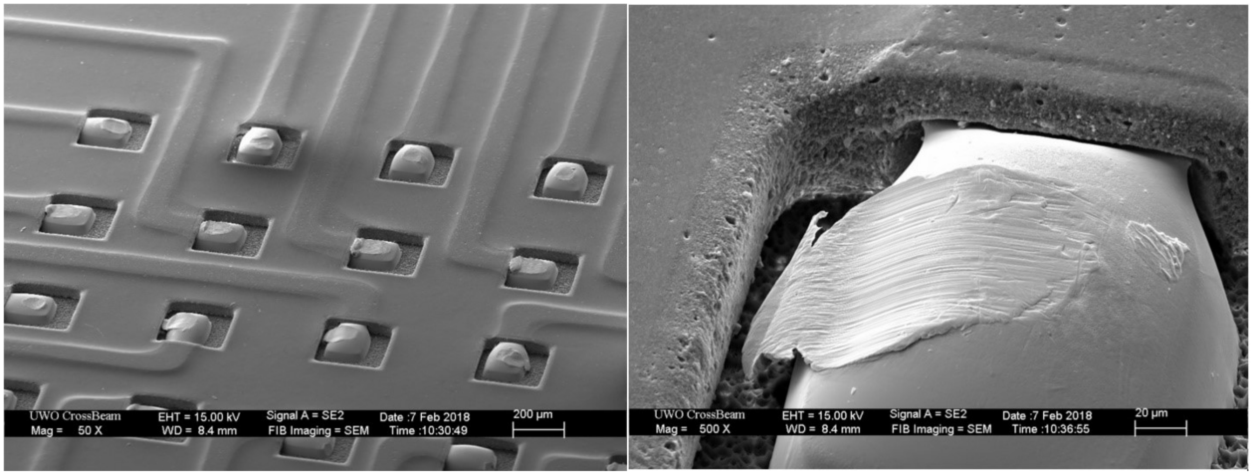

Figure 3.13. A SEM image of a fresh I1 (iteration 1) PCB MEA and a SEM image of a single electrode showing possible crevice areas and scratching due to packaging

The opening in the solder mask which exposed the electrode can be classified two ways: metal-defined or mask-defined, which is highlighted in Figure 3.12. Metal-defined electrodes have a clearance area around the electrode, therefore the mask opening is larger than the electrode size, and upon close inspection of Figure 3.13 the trace can be seen emerging from the solder mask. The openings on mask-defined electrodes are smaller than the electrode size, causing the mask to be tightly adhered to the outer portion of the electrode while only exposing the centre. Mask-defined electrodes were preferable due to the lower probability of crevice corrosion and a structure that promoted application of a coating.

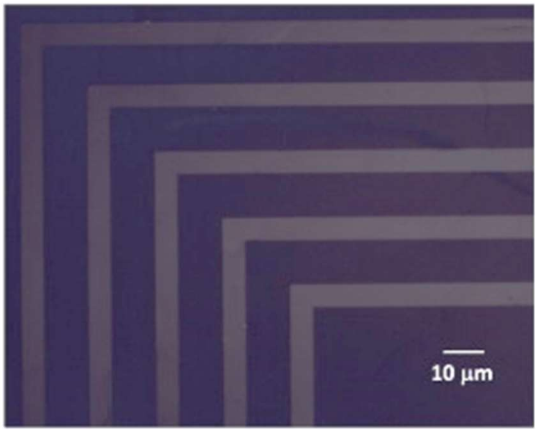

Figure 3.14. A high resolution PMMA coating in a line pattern made using photolithography on a silicon substrate[14]

The coating selected for G3 MEAs was a photoresist. Photoresists are polymers commonly used in nano/microfabrication techniques. This is due to their unique chemistry, which can be modified by functionalizing them with labile bonds or cleavable units, which makes them much sought after for lithography and 3D printing.[13] Photoresists can be accurately applied in thin layers with relative ease. Many examples of photoresists show very precise patterning using lithographic techniques, down to nanometer resolution with controlled thickness's as shown in Figure 3.14.[14]

The initial photoresist used was PMMA (poly-methylmethacrylate), with its structure shown in Figure 3.15. PMMA is a well known and commonly used polymer that is classified as a positive photoresist. Photoresists are applied to a surface, then cured using electron beams or specific wavelengths of light, and then washed with an organic solvent called a developer to remove uncured material. Positive photoresists are classified as materials where the curing makes the exposed photoresist soluble to the developer. Negative photoresists harden when exposed to light, therefore any unexposed material is soluble to the developer.

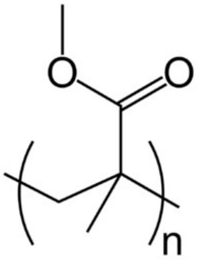

Figure 3.15. The repeating chemical unit for PMMA where n=the number of repeat units

To expose PMMA, a method called electron beam lithography (EBL) was used. EBL scans a focused electron beam over a designated area to draw a pattern on a resist. The EBL system found in Western's Nanofabrication Facility is a NPGS system paired with a Leo/Zeiss 1530 FE-SEM. With this system, patterns could be drawn with nanometer resolution; however, the process is time consuming. The process could not be automated without first scanning the PCB and setting up manual position markers, which was a long and consequently costly process for 48 individual electrodes.

When PMMA is exposed to the electron beam it becomes soluble in the developer; however, if the beam is not concentrated enough or the exposure time is too fast the resist will become partially soluble, leading to partial openings or rugged edges. The electron dose (D) required to define a designated area (A), is equivalent to the beam current (I) multiplied by the exposure time (t). This can be summarized by $DA = It$. Exposure areas were chosen quickly and at low beam currents during SEM to avoid exposing the resist in unwanted areas which would have caused holes or defects in the coating.

EBL can create openings of various shapes and sizes. Typically, each ~50 μm diameter circle took between 10-50 s to produce depending on the beam current. Increasing the beam current resulted in less accurate shapes but faster processing while decreasing the beam current risked underexposure with longer exposure times, therefore increasing the cost of coating each PCB. The failure rate of opening a hole in the PMMA, especially on uncommon substrates like PCBs is high, and is compounded by the fact that coatings can only be checked for success post-development with little to no possibility of fixing the PMMA layer without fully removing it.

PMMA is stable in a wide range of near-neutral aqueous solutions. It is considered a basic polymer and adheres best to acidic surfaces, however in both basic and acidic solution it has poor adhesion onto surfaces, and therefore prefers neutral solutions.[15,16] Therefore, it can be reasoned that PMMA also does not adhere as well to neutral or basic surfaces. When cured, PMMA has poor scratch resistance and can delaminate/degrade in strong acids/bases.

A major issue with photoresists, especially PMMA, is that they are extremely difficult to analyze with traditional techniques like SEM. During SEM the PMMA layer on the PCB charges and simultaneously degrades at moderate beam intensities or accelerating voltages. Performing SEM at reduced intensities effectively reduces the detail of the images and consequently the viability of the technique. Variable pressure SEMs (VP-SEM) elucidate finer structures up to a limit, beyond which images were consistently marred by shadowing and low resolution. Sample charging and degradation in regular SEM could have be avoided by adding another supplementary coating, however the removal of such a coating was problematic, therefore VP-SEM was a more appealing solution. It was determined that the best way to analyze the PCB MEAs was with a combination of optical and physical techniques. The method used optical analysis to provide preliminary analysis of the MEA while physical techniques such as profilometry provided roughness parameters and supplemented the optical information with height values and defect detection.

3.3 G3 Optimization

3.3.1 Working with Coatings

There were multiple factors to consider when choosing a photoresist, since they use complex or specific chemistry. The most important factor to consider was the stability of the photoresist in acidic or basic environments. The DGR is estimated to be slightly basic or at-neutral pH, but some of the testing environments tended towards acidic values, especially when roughness analysis or individual anode/cathode isolation was attempted.

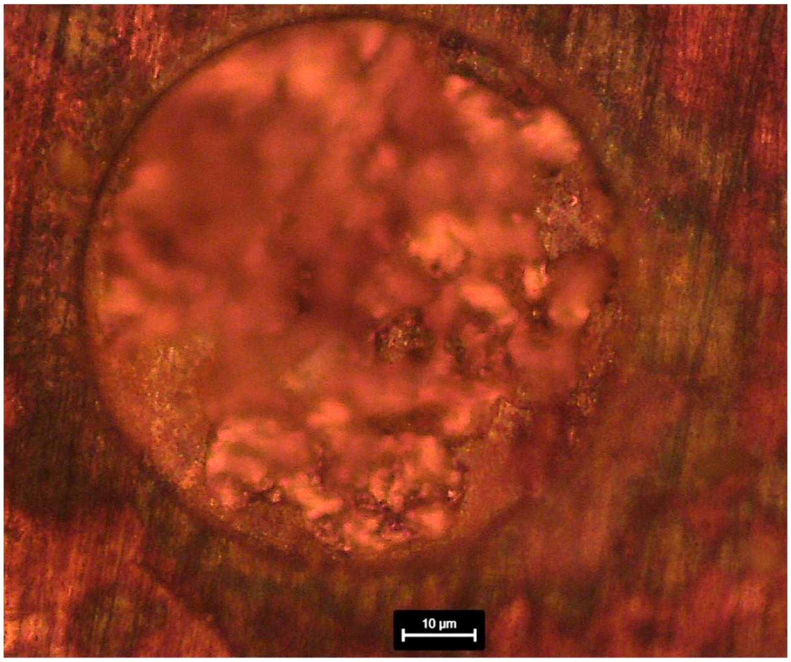

Figure 3.16. An optical image of a PMMA coated electrode immersed in 1 M NaCl for approximately 1 day. The discolouration and lack of optical focus around the edges of the electrode indicate solution leakage below the PMMA surface

PMMA has good physical stability when cured, but it is not chemically stable in solutions with pH near or below 6 and above 8, as shown in Figure 3.16. The electrode shown has a diameter of ~75 µm. In this image some of the PMMA layer has delaminated after 1 day of submersion in an as-made (AM) pH 1 M NaCl solution. The delamination is denoted by the discolouration around the electrode edges, suggesting corrosion has occurred, and the lack of focus around the ring implies the PMMA was no longer adhered to the Cu. Delamination also allows liquid to seep into or reach below the PMMA layer, consequently making it easily removed. If the solution reached below the PMMA layer during the experiment crevice corrosion would be possible on the affected electrodes.

PMMA, like many thin layer photoresists, is often spin-coated onto substrates. Ideal substrates are very flat and free of impurities, which are qualities that cannot be ensured with PCBs. This means the ideal revolutions per minute (rpm) and method of spin coating for PCBs is not well-documented or known. Spin coating involves applying a small quantity of the photoresist in a suspension onto the substrate followed by a short, slow spin (known as spread) to evenly apply the photoresist. The spread is followed by a longer, faster spin to thin out the polymer, the excess polymer is spun off into a collection pan. Near the end of the spin, the speed is slowly ramped down to avoid having the substrate fall off the holder and shift the spun layer. To ensure spin coating goes as smoothly as possible, PCBs were sprayed with an electronics cleaner called 4050A Safety Wash II (a combination of 1,1,1,2-tetrafluoroethane, propan-2-ol and methyl-2-pentane) made by MG Chemicals (to remove dust and impurities), rinsed with DI water and then etched quickly in dilute HNO_3 in order to remove debris from the surface. This process also slightly etched and roughened the Cu electrodes which increased the resist adhesion to the surface.

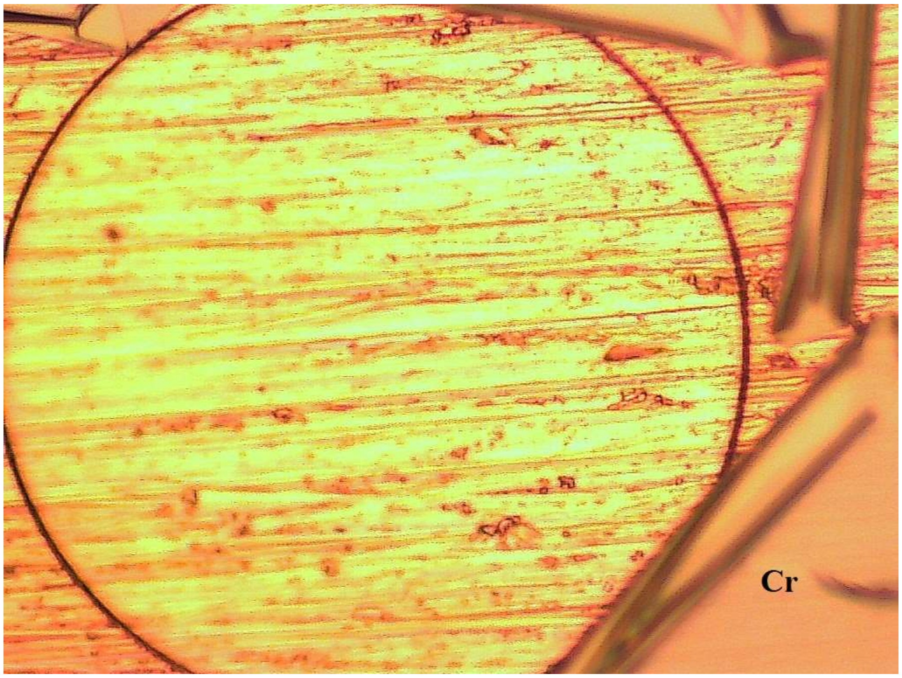

Figure 3.17. An optical image of a 100 μm diameter electrode with Cr infused into the PMMA layer after a HNO_3 dip

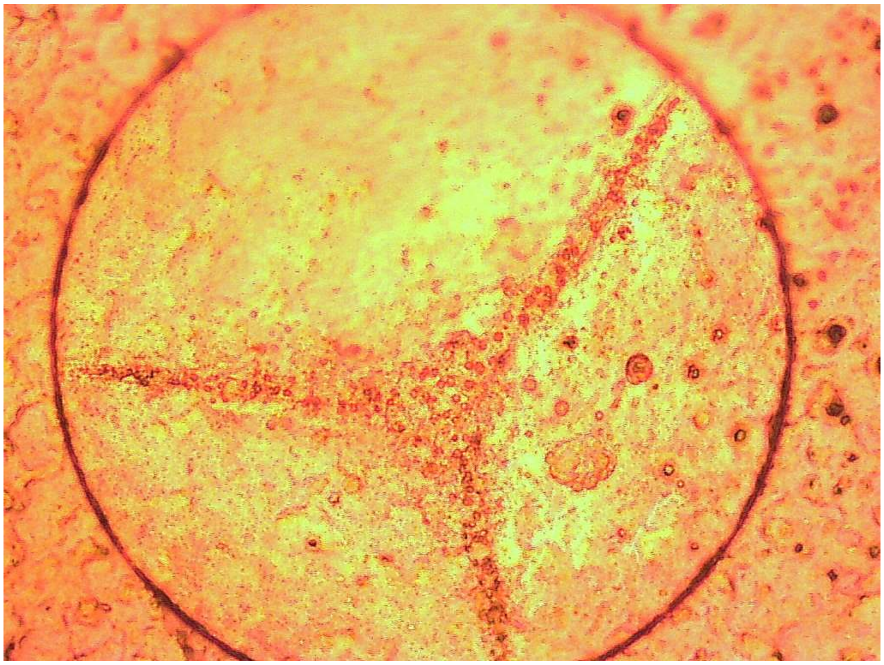

Figure 3.18. An optical image of a 100 μm diameter electrode after Cr removal and developer wash, with a major defect on the surface as a result of PMMA-developer interaction or Cr removal

In order to perform EBL on a photoresist-coated substrate, it was first coated with an additional (~3 nm) layer of Cr to prevent charging and increase visibility in the SEM. This coating was performed with a magnetron sputtering system that was calibrated to apply a thin, even coat of Cr in a vacuum environment. The application of this coat was harmless, but the removal posed an issue for the electrodes. The removal required a strong acid (HNO_3), which normally was applied for a matter of seconds, however it appears that the Cr could infuse into the PMMA during removal, especially around the contacts and electrodes. This infusion could be removed with prolonged exposure to the acid at the cost of greatly damaging the electrodes. In Figure 3.17 the Cr infused into the PMMA is labelled. Cr infusion is indicative of a higher, out-of-focus grey layer with very straight edges. This optical image shows that it was possible for Cr to remain infused in the PMMA after prolonged exposure in acid. If the Cr remained in the PMMA it was possible for it to deposit onto the electrode and render it unusable for experiments. Figure 3.18 shows that despite the successful removal of Cr (no out-of-focus upper grey layer is present) the electrode was severely damaged prior to experimentation, likely by the developer wash, rendering it useless. The developer is a solvent or solvent mixture that removes uncured, soluble polymer. A developer wash often consists of a couple cycles of short submersions in the developer. These negative effects imposed by the application of the Cr layer commonly affected the electrode surface, which decreased the viability of the PMMA layer.

The production and application of photoresist layers was performed in many steps with each having a small degree of variability that could have affected the performance of the layer. Examples of these steps are the transportation of the PCB after spin coating, Cr coating the PMMA layer, HNO_3 etching the electrodes and washing the PCB with DI water prior to spin coating. Variability was introduced in these steps by processes such as PMMA cold flow after spin coating, electrode oxidation after PCB washing and Cr infusion into PMMA during its removal step. There are also controllable parameters within these steps that can create variability. Examples of these parameters are exposure length during EBL, exposure during SEM mapping prior to EBL, and the number of developing cycles performed. During developer wash it was possible that the remaining Cr or acid saturated PMMA (from Cr removal) reacted with the developer and damaged the electrodes, similar to the damage in Figure 3.18. All of these variable processes led to a 75-80% success rate of electrodes. This was not ideal for simulating bulk surfaces, especially when the electrodes were excluded due to processing damage rather than an oxide film which can be rationally accounted for.

Two steps which had unpredictable behaviour were placing the undeveloped photoresist in a vacuum environment and heat treating the PCBs after cleaning. Photoresists can have air bubbles that are incorporated into the layers during the spin coating. It was possible to see incorporated air bubbles in thinner photoresists but thinner layers were more negatively affected by these bubbles compared to thicker photoresist layers.

During Cr coating, the PMMA was uncured and undeveloped. The Cr coating was performed at very low pressures and during the air removal from the sputtering chamber air bubbles could erupt and disrupt the photoresist. It was possible to avoid air bubbles by spinning a second photoresist layer after partially curing the first layer. Heating procedures for a photoresist are normally written in the chemical data sheet, but have been designed for ideal substrates.[17] Appropriate heating times and temperatures can sometimes be estimated based on substrate similarity: however, this is not an accurate method. There are no known heating curves for photoresists on PCBs. As a result, heating and vacuum effects were tracked to determine their influences on the application and viability of the photoresists.

Similar to heating curves, a thickness curve can be found in the chemical manual. This curve is constructed using ideal substrates to determine photoresist thickness as a function of rpm and time. Once again, these curves are not applicable for a PCB since it deviates from an ideal substrate in its size, shape, and roughness. The ideal spin time and speed for a PCB could not be predicted, due to the well the electrodes sit in formed by the solder mask. Therefore, to track the effect of spin speed, the photoresist properties were observed after spin coating and after development. During spin coating two possible behaviours emerged due to the wells where the electrodes were located. The first was that the coating over the solder mask was extremely thin while the wells were full. The second was that the photoresist piled around the edges of the wells with uneven filling and a thick coating over the solder mask. Between these two outcomes the former was preferable and more commonly occurred. Thickness was verified using profilometry before and after the photoresist layer was applied. Due the substrate size high spin speeds, which are often preferred, were not viable since the probability of the PCB falling off the holder and shifting the coating was greatly increased. If the PCB did fall off the holder a re-spin or re-application of the photoresist was required. Therefore, it was important to track the effect of spin speed along with heating and vacuum effects due to the unusual size, shape and roughness of the PCBs compared to the ideal substrate used to construct the chemical manuals for the photoresists.

3.3.2 Designing the Final MEA

The PCBs went through three iterations before a fully functioning MEA was obtained. Each iteration used about 20-30 test PCBs and most did not make it past photoresist developing. Therefore, there were limited samples for analysis during optimization that highlighted the specific challenges that will be discussed. The fabrication of 50 µm diameter circular electrodes were attempted for the majority of the fabricated MEAs.

The first iteration of boards (I1) had a rectangular shape and were the only iteration to have the metal-defined pads shown in Figure 3.13. This was detrimental because there was a clear opening to the Cu trace, with the risk of crevice corrosion. There was no feasible method available to fill the wells and make them flush with the solder masking. Therefore, the G3 I1 PCBs were abandoned before any photoresist application due to the high probability of crevice corrosion.

The second iteration (I2) of PCB MEAs used mask-defined pads to greatly reduce the possibility of Cu traces undergoing crevice corrosion. However, this introduced the possibility of crevice corrosion between the electrode and solder mask. The dimensions of the PCB were 8.9 cm x 6.3 cm, and the dimensions of the MEA were 5695 µm x 2664 µm. Electrodes in the MEA are ~620 µm apart in the x-direction and 647 µm apart in the y-direction. The electrodes were ~ 174 µm x 174 µm making the ratio of the interelectrode distance to the critical electrode dimension is 3.6-3.7. This ratio indicates that the electrodes were able to electrochemically influence each other and act as a single surface rather than react individually. Most of the I2 PCBs were coated with PMMA, however as previously mentioned there were a lot of production and analytical flaws and I2 was deemed unsuccessful. Issues such as electrode damage prior to experimentation and photoresist delamination were prevalent with I2 PCBs. The fabrication time for I2 MEAs was also very long. This was because EBL could take up to 4 to 5 hours for a single sample. The length of fabrication, low electrode success rate (~75%) and high cost per sample led to the exploration of alternative methods and materials.

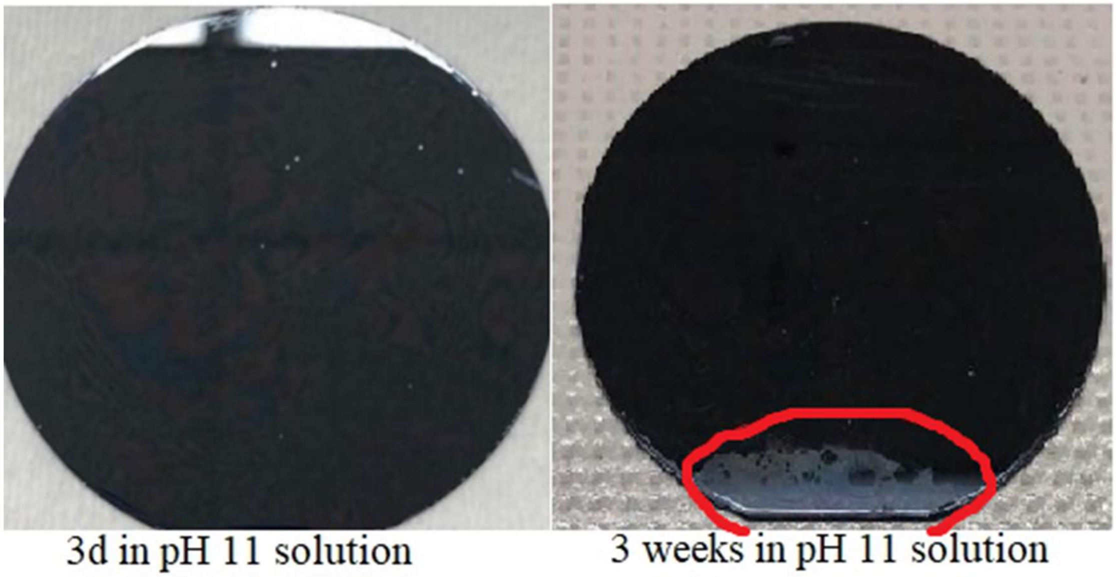

Figure 3.19. A comparison of a Su8-coated Si wafer after different lengths of exposure in basic solution. Delaminating areas are circled in red

A new photoresist, Su8-3005 (Su8) supplied by Kayaku Microchem, was selected to replace PMMA. Su8 is a combination of two phenol formaldehyde polymers and cyclopentanone. Su8 is listed as being stable in acidic and basic solutions. The Su8 was spin coated onto a Si wafer and submerged in in pH 11 1 M NaOH to test its stability and delamination mechanism. The results of the stability test are shown in Figure 3.19, indicating an ideal Su8 layer is stable for up to weeks with minor delamination. Su8, unlike PMMA, is a negative photoresist, therefore the areas that were exposed to a specific wavelength of UV-light were cured rather than broken down. A photomask was used block the UV light over the areas where the Su8 was opened to reveal the electrodes.

A photomask is a glass substrate that is patterned to block out light in a specific design (the MEA) when properly aligned over the sample. Photomask placement was performed using a mask aligner. The photomask was placed over a sample, aligned optically and sealed in place using a N_2 stream for suction. After sealing, UV exposure was performed, after which the sample was removed and developed. It should be noted that photomask patterns are unique and cannot be modified after the photomask is made. Therefore, to change the size of the openings in the Su8 that reveal the electrode area a different photomask must be used.

Figure 3.20. A comparison of an I2 board (left) and I1 board (right). The cut edges of the preliminary I2 samples are circled in red. The cell setup remains unchanged by these differences

In order to properly use the mask aligner, slightly smaller PCBs were required. To achieve this, the PCB edges were cut to create the shape shown in Figure 3.20. The solder mask on PCBs is rigid and creates a lot of debris when cut. Precise cuts were difficult without contaminating the surface. A few I2 PCBs were coated with Su8 after cutting and seemed successful, but ultimately it was more convenient and safer to alter the size of the manufactured substrate to better work with the mask aligner.

The third and current iteration of PCBs (I3) were modified by making the mask-defined electrode opening as small as the manufacturer allowed. Electrodes were ~145 µm x ~132 µm. As a consequence of the electrode size the MEA size was slightly reduced to 5641 µm x 2620 µm and the electrode spacing was reduced to 624 µm in the y-direction and 642 µm in the x-direction. This changed the ratio of interelectrode distance to the critical electrode dimension to 4.4-4.5. The I3 PCBs also had their dimensions changed to match the cut I2 samples so they could fit properly in the mask aligner. Similar to previous generations and iterations, Su8 on a non-ideal substrate like PCBs is relatively unexplored and required optimization.

Su8 provides excellent protection but is notoriously difficult to work with. Once cured, Su8 is not intended to be removed. Su8 adhesion is excellent but is easily hampered by surface moisture. The label "3005" designates that spin coating on an ideal substrate at 3000 rpm will result in a 5 μm thick layer.[17] Curing Su8 poses a challenge since it only achieves its maximum protection within a certain range of UV exposure time, which is dependent on thickness and dosage. If Su8 is under-cured it is easily rubbed off and has a gel-like texture; if it is over-cured it becomes brittle and cracks easily.

The fabrication of Su8-coated PCBs can be broken down into multiple steps. The first is a dilute HNO_3 etch (~ 1:3 70% HNO_3:DI water) which was achieved by placing a droplet of acidic solution over the MEA portion of the PCB. The etching was performed for a couple minutes to roughen the electrodes and remove debris to increase Su8 adhesion. After etching, the sample was rinsed in tap water and dried with a stream of N_2. Then the PCBs were placed into a vacuum oven for at least 30 minutes at 95°C to remove excess moisture. This temperature did not promote oxidation of the PCB electrodes. Prior to spin coating, the PCBs were removed from the oven and cooled to room temperature in an aluminum foil tray. After cooling the PCBs were spin coated individually.

Spin coating was performed as follows. A PCB was placed on the chuck and aligned. A test spin was performed to make sure the sample did not displace during rotation and then the area around the MEA was covered with the Su8 emulsion. Once the MEA was covered in the emulsion a spread spin (slow) was performed followed by a primary spin (fast).

Table 3.1 contains the spin procedures used for each MEA which includes the spread spin, the main spin, the final spin, their associated speeds and times, the time to change the speeds (ramp time) and the length of each spin. The disadvantage of using high rpm (above 2000) was that the PCB was easily displaced and the disadvantage to using a low rpm (<500) was that the spun coating could be uneven. It was discovered that multiple successive spins did not deform or modify any Su8 structures formed, such as spires or piles. These defects could only be removed by removing the entire Su8 layer. The samples towards the bottom of Table 3.1 had a higher success rate, especially once a slower primary spin step was adopted in conjunction with the addition of thinner.

After spin coating, the sample was placed into the vacuum oven under vacuum at the desired temperature for a designated amount of time. The first heating step, referred to as soft baking, removed excess solvent and dried the resist. The soft bake rigidified the Su8 layer, preventing adhesion to the photomask. After the soft bake, the sample was cooled in air before alignment in the mask aligner, followed by UV exposure. The curing was performed at separation pressure. This was when the photomask was barely touching the photoresist, as opposed to contact pressure where a higher amount of pressure was applied to ensure contact between the resist and photomask. The suction pressure in the mask aligner was applied using a N_2 stream.

Table 3.2 lists the parameters for all the performed curing cycles including the time, intervals and rest time in between cycles. It was found that curing in intervals was beneficial to reduce overheating the Su8, which led to cracking and delamination. To avoid this, a small amount of time between each interval was designated for cooling. The ideal cure time was found to be 40 s, in 10 s intervals, with 90 s of rest between intervals. Curing at separation pressure was found to be more viable than contact pressure. Contact pressure sometimes caused the Su8, which could be tacky after the soft bake, to adhere to the photomask and consequently delaminate. After removal from the mask aligner, the sample was placed in the vacuum oven for a post-exposure bake (PEB). The PEB was required to either crosslink the photoresist or finish the photoreaction initiated during the UV exposure. The sample was then air-cooled before developing in a mixture of MIBK/iPa. A single developing cycle consisted of a long wash followed by a shorter wash with fresh developer. The short wash was 10-25% of the length of the long wash. After each cycle, the sample was gently dried with an air stream and carefully wiped with a small microfiber cloth.

Table 3.3 outlines the developing cycle optimizations. It was found the optimal total development length was between 210 s and 240 s. Low washing times did not fully remove soluble Su8, while long washing times removed too much Su8 or damaged the Cu.

Table 3.1. Notable samples and their associated spin coating parameters with rpm and time values

Sample	Spread (rpm, time (s))	Spin step (rpm, time (s))	Ramp down time (s)	Final speed (rpm,time (s))	Total time (s)	Additional
CBsu8-15	500, 5	2000, 35	2	500, 8	45	N/A
CBsu8-21	500, 5	2000, 35	2	500, 8	45	N/A
CBsu8-22	500, 5	2000, 35	2	500, 8	45	N/A
CBsu8-23	500, 5	2000, 35	2	500, 8	45	N/A
CBsu8-24	500, 5	2000, 35	2	500, 8	45	N/A
CBsu8-28	500, 5	2000, 35	2	500, 8	45	N/A
CBsu8-30	500, 5	2000, 35	2	500, 8	45	N/A
CBsu8-26	500, 5	2000, 35	2	500, 8	45	N/A
CBsu8-27	500, 5	2000, 35	2	500, 8	45	N/A
CBsu8-29	500, 5	2000, 35	2	500, 8	45	N/A
CBsu8-28b	500, 5	2000, 35	2	500, 8	45	N/A
CBsu8-50b	500, 5	2000, 35	2	500, 8	45	N/A
CBsu8-50C	500, 5	2000, 35	2	500, 8	45	N/A
CBsu8-50D	500, 5	2000, 35	2	500, 8	45	N/A
CBsu8-50E	500, 5	2000, 35	2	500, 8	45	N/A
CBsu8-40A	500, 5	1500, 35	2	500, 8	45	N/A
CBsu8-40B	500, 5	1750, 35	2	500, 8	45	N/A
CBsu8-35A	500, 5	1750, 35	2	500, 8	45	N/A
CBsu8-40C	400, 5	1900, 35	2	500, 8	45	N/A
CBsu8-38A	500, 5	1750, 35	2	500, 8	45	N/A
CBsu8-40D	500, 5	1980, 35	2	500, 8	45	N/A
CBsu8-40E	500, 5	800, 40	N/A	N/A	40	1-2 thinner drops
CBsu8-40F	500, 5	800, 40	N/A	N/A	40	1-2 thinner drops +re-spin
CBsu8-40G	500, 5	800, 40	N/A	N/A	40	1-2 thinner drops +re-spin
CBsu8-40H	500, 5	800, 40	N/A	N/A	40	1-2 thinner drops +re-spin
CBsu8-40I	500, 5	800, 40	N/A	N/A	40	1-2 thinner drops +re-spin
CBsu8-40J	500, 5	800, 40	N/A	N/A	40	1-2 thinner drops +re-spin
CBsu8-40K	500, 5	800, 40	N/A	N/A	40	1-2 thinner drops +re-spin

Table 3.2. Notable samples and the UV curing times, sets and rest times

Sample	Exposure Length (s)	Interval (time (s) x sets)	Rest (min)
CBsu8-15	15	N/A	N/A
CBsu8-21	21	N/A	N/A
CBsu8-22	22	N/A	N/A
CBsu8-23	23	N/A	N/A
CBsu8-24	24	N/A	N/A
CBsu8-28	28	N/A	N/A
CBsu8-30	30	N/A	N/A
CBsu8-26	26	N/A	N/A
CBsu8-27	27	N/A	N/A
CBsu8-29	29	N/A	N/A
CBsu8-28b	28	N/A	N/A
CBsu8-50b	50	10 x 5	1
CBsu8-50C	50	10 x 5	1.25
CBsu8-50D	40	10 x 4	1.5
CBsu8-50E	50	10 x 5	1.5
CBsu8-40A	40	10 x 4	1.5
CBsu8-40B	40	10 x 4	1.5
CBsu8-35A	35	(10 x 3) + 5	1.5
CBsu8-40C	40	10 x4	1.5
CBsu8-38A	38	(10 x 3) + 8	1.5
CBsu8-40D	40	10 x 4	1.5
CBsu8-40E	40	10 x 4	1.5
CBsu8-40F	40	10 x 4	1.5
CBsu8-40G	40	10 x 4	1.5
CBsu8-40H	40	10 x 4	1.5
CBsu8-40I	40	10 x 4	1.5
CBsu8-40J	40	10 x 4	1.5
CBsu8-40K	40	10 x 4	1.5

Table 3.3. Notable samples and the developing cycle times and amounts

Sample	Long develop time (s)	Short develop time (s)	Cycles
CBsu8-15	165	15	1
CBsu8-21	165	15	1
CBsu8-22	165	15	1
CBsu8-23	165	15	1
CBsu8-24	165	15	1
CBsu8-28	165	15	1
CBsu8-30	165	15	1
CBsu8-26	90	15	1
CBsu8-27	90	15	1
CBsu8-29	90	15	1
CBsu8-28b	90	15	1
CBsu8-50b	35 + 60	15	2
CBsu8-50C	N/A	N/A	2
CBsu8-50D	N/A	N/A	2
CBsu8-50E	N/A	N/A	2
CBsu8-40A	N/A	N/A	2
CBsu8-40B	N/A	N/A	2
CBsu8-35A	N/A	N/A	3
CBsu8-40C	210	30	2
CBsu8-38A	210	30	2
CBsu8-40D	210	30	1
CBsu8-40E	210	30	2
CBsu8-40F	210	30	1
CBsu8-40G	210	30	1
CBsu8-40H	210	30	1
CBsu8-40I	210	30	1
CBsu8-40J	210	30	1
CBsu8-40K	240	30	1

Table 3.4. Notable samples and the soft bake (first bake) parameters and the post exposure bake (second bake) parameters

Sample	Soft bake (°C)	Soft bake time (min)	Post exposure bake (PEB) (°C)	PEB time (min)
CBsu8-15	65 –>95	30 + 30 ramp + 30	95	60
CBsu8-21	65 –>95	30 + 30 ramp + 30	95	60
CBsu8-22	65 –>95	30 + 30 ramp + 30	95	60
CBsu8-23	65 –>95	30 + 30 ramp + 30	95	60
CBsu8-24	65 –>95	30 + 30 ramp + 30	95	60
CBsu8-28	65 –>95	30 + 30 ramp + 30	95	60
CBsu8-30	65 –>95	30 + 30 ramp + 30	95	60
CBsu8-26	65 –>95	30 + 30 ramp + 30	95	60
CBsu8-27	65 –>95	30 + 30 ramp + 30	95	60
CBsu8-29	65	120	65	180
CBsu8-28b	65	120	65	180
CBsu8-50b	70 (vac)	120	70 –>80 (vac)	120
CBsu8-50C	65 (vac)	120 + 60 after 2nd spin	65 (vac)	150
CBsu8-50D	65 (vac)	120 + 60 after 2nd spin	65 (vac)	150
CBsu8-50E	65 (vac)	120	65 (vac)	150
CBsu8-40A	65 (vac)	120	65 (vac)	150
CBsu8-40B	65 (vac)	120	65 (vac)	150
CBsu8-35A	65 (vac)	120	65 (vac)	150
CBsu8-40C	65 (vac)	120	65 (vac)	150
CBsu8-38A	65 (vac)	90	65 (vac)	90
CBsu8-40D	65 (vac)	180	65 (vac)	90
CBsu8-40E	95	20	95	25
CBsu8-40F	95	20	95	20
CBsu8-40G	95	20	95	30
CBsu8-40H	95	20	95	30
CBsu8-40I	95	20	95	35
CBsu8-40J	95	20	95	40
CBsu8-40K	95	20	95	40

The last step in the optimization of the fabrication process was heating. Heating occurred intermittently throughout the fabrication process. According to the Su8 manual, heating should be performed twice. With an ideal sample the soft bake should be performed at 95°C after spin coating for a short amount of time (~5 minutes). The PEB is ideally performed immediately after UV curing, first at 65°C for 1 minute then at 95°C for 1-5 minutes. These heating steps are important since they affect the curing process of the photoresist and consequently the rigidity of the layer. Table 3.4 shows how drastically different the timing of the soft bake and the PEB was for non-ideal substrates compared to ideal substrates. Some of the heating steps were attempted in vacuum to minimize oxidation of the partially exposed Cu pads after UV curing. The effect of the vacuum on the Su8 layer seemed to be inconsistent. Sometimes aeration produced no visible electrode damage, whereas sometimes the vacuum environment decreased or increased the adhesion of exposed Su8 which prevented it from being removed during development. Placing an uncured photoresist in a vacuum environment is uncommon. This is because the impact of the vacuum on the Su8 layer is unknown. It is possible that the vacuum either ruptured any small air bubbles in the layer (causing delamination) or pulled the photoresist tighter and increased adhesion in developer-soluble regions. Time is a valuable parameter with regard to vacuum exposure. It is unclear if the vacuum pressure disrupted the photoresist while reaching the desired pressure or during the time it was under the desired pressure. Despite the need for exploring the effects of vacuum, Table 3.4 shows the ideal parameters were aerated soft bakes at 95°C for 20 minutes and aerated PEBs at 95°C. An optimal time was not found for PEBs though the results indicated that usually a longer PEB was better.

3.3.3 Issues Preventing a 100% Success Rate in Producing MEAs

There were four common issues with the G3 I3 MEAs and their fabrication method that led to a less than 100% success rate in their production. Sorting out these issues was crucial to achieving a functional MEA capable of testing roughness at $E_{corr.}$

The foremost issue, as previously noted, was that optical analytical techniques were difficult to employ on the Su8-coated PCBs. SEM was particularly difficult, due to charging of the organic Su8 layer. While this could be negated by applying a conductive metal layer, this was not practical since the etch to remove the metal could damage the electrodes. Therefore, the only practical application time would have been after an experiment, which would not allow any comparative data from before the experiment to be collected. Another common option was to use a variable pressure SEM (VP-SEM) which introduces air into the chamber at low pressures (up to a 200 Pa) which helps ground the charge that accumulated on the Su8 surface. However, the variable pressure (VP) mode in the SEM was performed at a cost of resolution and the inability to accurately collect EDX spectra if necessary. In VP mode images taken typically had a noticeable shadowing effect that occluded part of the image as shown in Figure 3.21.

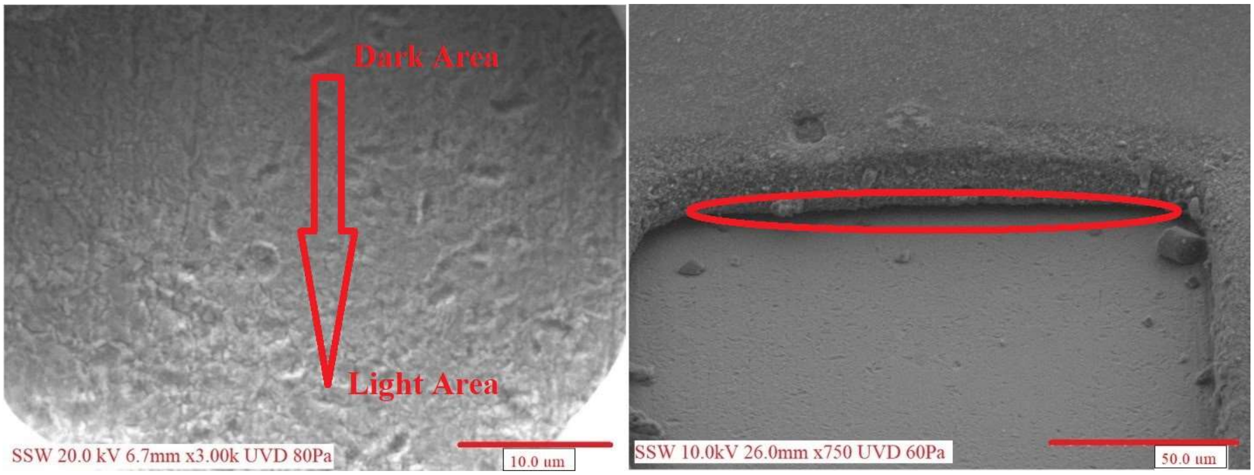

Figure 3.21. SEM images taken at different magnifications and pressures highlighting the shadowing effect for both coated (left image) and uncoated (right image) electrodes. The arrow on the coated electrode image (left) indicates the shadowing gradient while for the uncoated electrode image (right) the shadowed area is circled in red

The most effective method of analysis was to combine optical microscopy and confocal laser scanning microscopy (CLSM or confocal). This combination was able to collect valuable visual data, elucidate fine structures on the electrode surfaces, and perform roughness analysis. An additional benefit was that both techniques could be performed on the same instrument. Optical microscopy easily identified major faults in the sample, such as oxide films or deposits on the electrodes. CLSM uses a laser with a 405 nm wavelength to raster the surface and the returned light is collected and turned into height data. The height data from CLSM was used to elucidate the structure of the coated electrodes and generate roughness data. A CLSM scan for a single electrode could use step sizes of less than 100 nm, but this created extremely large data files which required lots of processing time and computing power. Therefore, larger step sizes were used, as will be discussed in Chapter 6. The CLSM data was used to generate reconstructed 3D images of each electrode for verification and elucidation of the optical images. Since both techniques are non-destructive, they were performed before and after experimentation.

The second prominent issue was O_2 exposure during MEA fabrication. Fabrication had many heating steps. At elevated temperatures it was possible to accelerate the formation of Cu_2O/CuO on the electrodes. Oxide formation on electrodes could have disrupted the Su8 layer or decreased its adhesion depending on the amount of oxide.

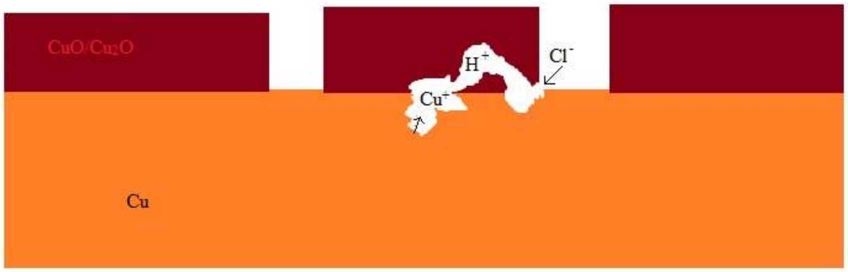

Figure 3.22. A schematic depiction of oxide penetration leading to crevice corrosion in Cu samples

The reactivity of the oxides in groundwater solutions could have changed the electrode behaviour. If the oxides were not fully dissolved, crevices could have formed due to partial surface occlusion. Crevice corrosion can lead to undetectable penetration in the limited space as shown in Figure 3.22. It was also possible for small gaps between Su8 and the Cu to grow oxides and push the Su8 upward causing delamination. The oxide production could also consume the Cu from the coating interface and cause delamination. Either way the result of such a case would look like Figure 3.23, where there was a large amount of oxide, but the mechanism of delamination is unclear. Regardless of the mechanism, the presence of large amounts of oxide had a negative impact on fabrication and testing. The presence of O_2 was unavoidable but it was limited.

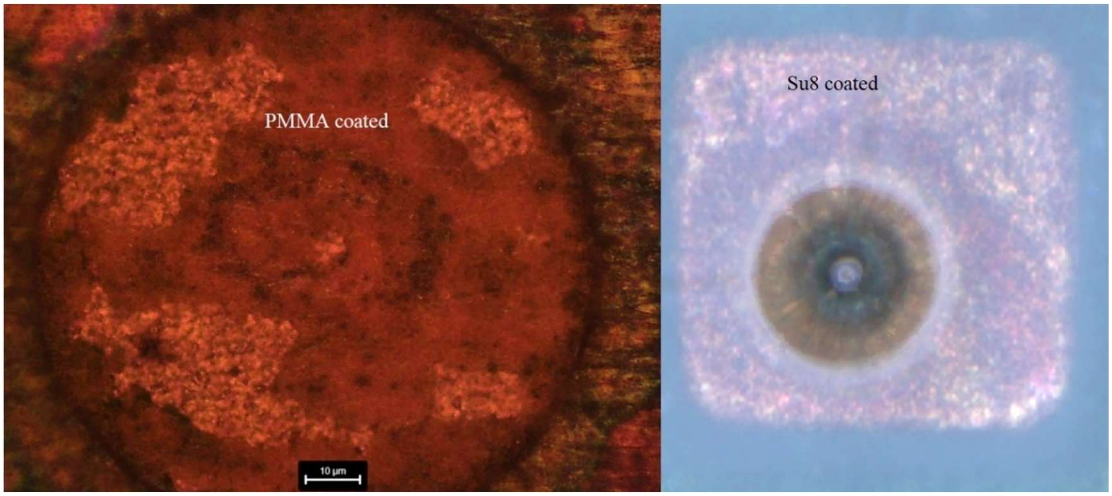

Figure 3.23. PMMA-coated (left) and Su8-coated (right) electrodes experiencing delamination (identifiable by the discoloration on the outer ring of the electrodes)

Alternatively, it was also possible during fabrication that the coating simply did not adhere properly to the Cu. The reasons for this are difficult to determine. It could have been due to a local viscosity issue during spinning, that the Cu surface was too rough, or the presence of residual moisture on the Cu.

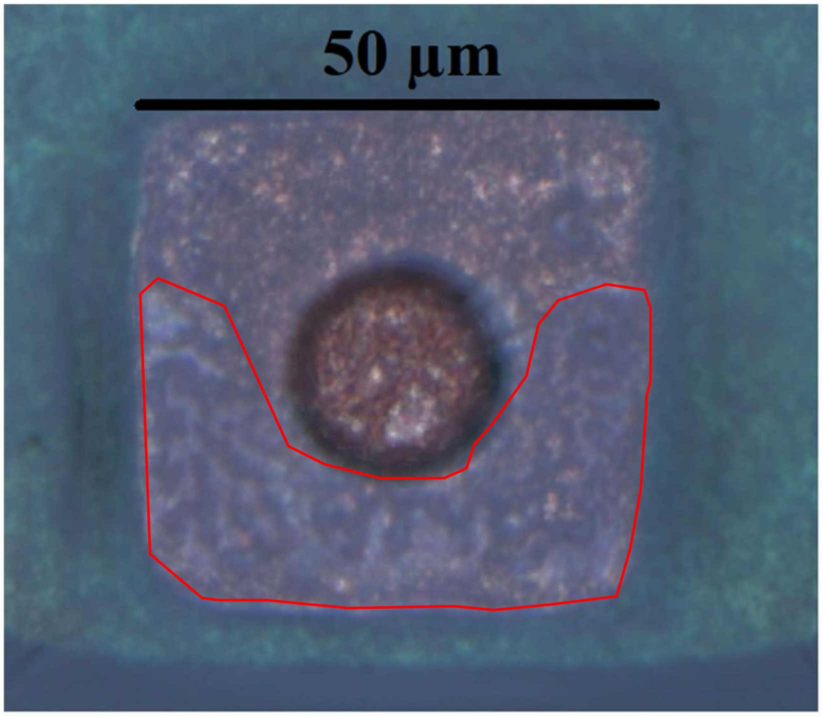

Figure 3.24. A Su8-coated Cu pad with a 50 µm diameter electrode that is experiencing filigree delamination, highlighted in red

As a consequence, electrodes could exhibit unpredictable delamination that created a filigree-type pattern on the Su8. Figure 3.24 shows an optical image of filigree delamination. This was a worry because crevice corrosion could have been initiated in these channels. However, it was unlikely that the pressure required to force solution into these pockets was achieved. It is likely that these channels were connected to the bulk solution by lateral corrosion across the Cu-Su8 interface which also avoided crevicing. However, the extent of damage was not accurately detectable visually or electrochemically.

One of the most impactful fabrication steps was spin coating. As previously noted, repeated spins of the same Su8 layer did not change the surface structure even with the addition of more Su8. If the spin went poorly, the sample could form thick pillars of Su8 at the centre of the electrodes. These pillars disrupted the UV-curing and persisted after development. This is shown in a partial profile scan accompanied by a 3D reconstructed image and optical image in Figure 3.25. Figure 3.25A is the 3D reconstruction of the area designated by the blue square in Figure 3.25B. The 3D reconstruction was used to examine the electrode shape. The yellow portion in the centre of Figure 3.25A is higher than the outer portions of the electrode (blue) which confirms Su8 is adhered to the surface. Figure 3.25B shows that the tip of the Su8 pillar appears as a bright spot at the centre of the electrode in optical images. Figure 3.25C is generated from the area of the electrode indicated by the red line in Figure 3.25B. This profile confirms the radius, shape and height of the Su8 pillar, the area highlighted in orange represents the edge of the electrode to just past the centre of the electrode. The smoothness of the profile also suggests this dome is Su8 since Cu would have a rougher profile. Overall, these images indicate a Su8 pillar persisted through a day of immersion in 1 M NaCl. It was found that the easiest method to avoid these pillars was to add a few drops Su8 thinner to the Su8 emulsion prior to spin coating.

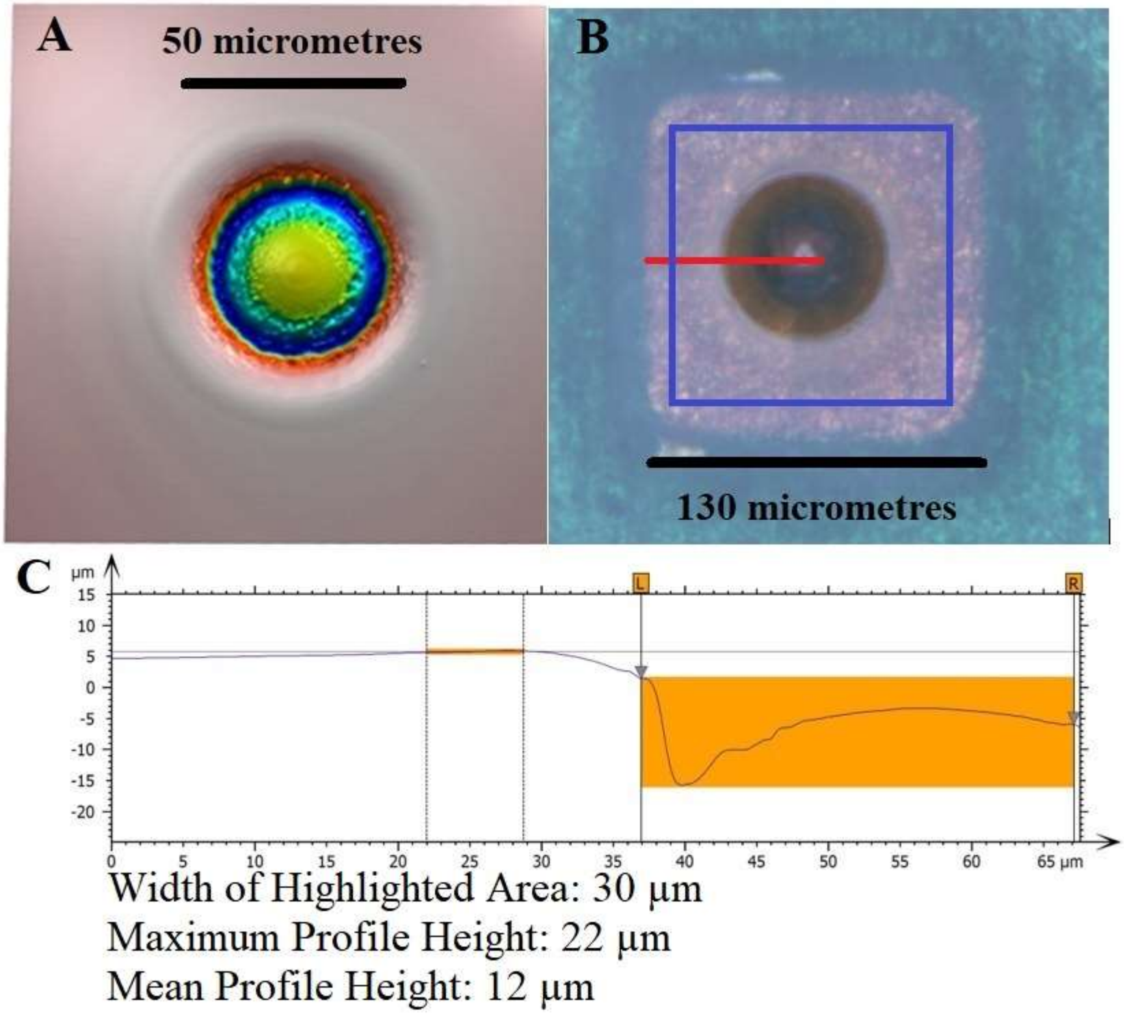

Figure 3.25. A 3D reconstructed image (A), optical image (B) and partial profile (C) of a Su8-coated electrode with a Su8 pillar blocking the electrode surface

The well height of a typical Su8-coated electrode was measured using CLSM, and also verified with a manual profilometer. The typical electrode well height found during preliminary analysis was between ~20-25 µm from the top of the Su8 to the electrode surface. Figure 3.26 shows SEM images of an uncoated PCB. These images highlight two different gap measurements between the solder mask and the Cu electrode. The first measurement is the gap between the upper portion of the solder mask and the Cu which has an average value of 16.35 µm. The second measurement is the gap between the lower portion of the solder mask and the Cu which has an average value of 2.86 µm. The difference of the two sections yielded an average solder mask thickness of 13.49 µm. Therefore, if the typical well height averaged between ~20-25 µm the Su8 is added ~ 4-9 µm on top of the solder mask. Therefore, spin coating on a non-ideal substrate at lower speeds can create a 5-10 µm thick layer of Su8 which is up to 200% thicker than spin coating on an ideal substrate. Pillars as seen could account for ~10 µm of extra thickness over the Cu electrodes. The addition of thinner reduced the viscosity of the Su8 and eliminated the presence of pillars. A very small amount of thinner was added directly over the MEA to achieve this. Since the thinner was not pre-mixed, its effects were local. If the thinner was not dropped directly over the MEA area its effectiveness was greatly reduced. Excess thinner completely removed the Su8 from the PCB. Air bubbles were also eliminated by the addition of thinner. Therefore, the addition of the thinner prior to spin coating eliminated a major problem during the fabrication process.

With three of the major MEA issues resolved one major problem remained. This was the testing environment. Solutions containing groundwater ions did not promote enough Cu dissolution to obtain a roughening trend without delaminating the Su8. Therefore, alternative solutions were explored. These solutions will be discussed in Chapter 5. First verification of Cu roughening was performed by accelerated testing to determine if it was possible to roughen Cu in a controlled manner and is described in Chapter 4.

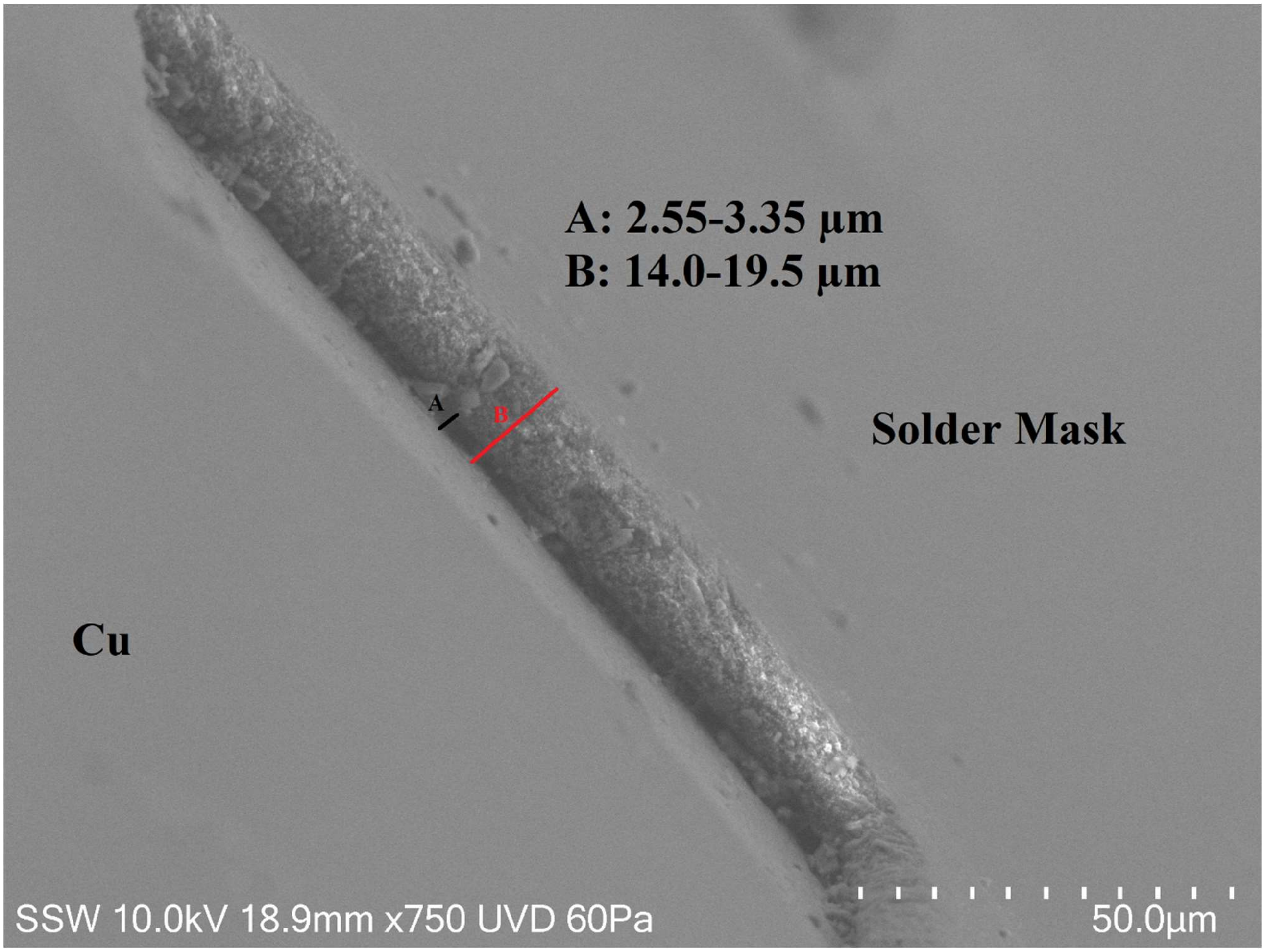

Figure 3.26. An SEM image taken at a 79° tilt highlighting the gap between the solder mask and Cu pads for a G3 I3 PCB. (A) represents the distance between the Cu and the bottom of the solder mask. (B) represents the distance between the Cu and the top of the solder mask. The range of measured values for A and B have been listed near the top of the image

3.4 References

---

1. Budiansky, N.D.; Bocher, F.; Cong, H.; Hurley, M.F.; Scully, J.R. Use of Coupled Multi-electrode Arrays to Advance the Understanding of Selected Corrosion Phenomena. *Corros. Sci.* **2007,** 63, 537-554.

2. Raina, S.; Kang, W.P.; Davidson, J.L.; Huang, J.H. High Temporal Resolution Bio-Sensing using Nitrogen-Incorporated Nanodiamond Ultra-Microelectrode Array by Fast Scan Cyclic Voltammetry. *ECS. Trans.* 45, 55-62.

3. Vogel, Y.B.; Molina, A.; Gonzalez, J.; Ciampi, S. Microelectrode Arrays with Active-Area Geometries Defined by Spatial Light Modulation. *Electrochim. Acta.* **2020,** 356, 136849-136858.

4. Aydin, V.K.; Şen, M. A Facile Method for Fabricating Carbon Fiber-Based Gold Ultramicroelectrodes with Different Shapes using Flame Etching and Electrochemical Deposition. *J. Electroanal. Chem.* **2017,** 799, 525-530.

5. He, C.; Tao, M.; Zhang, C.; He, Y.; Xu, W.; Lie, Y.; Zhu, W. Microelectrode-Based Electrochemical Sensing Technology for in Vivo Detection of Dopamine: Recent Developments and Future Prospects. *Crit. Rev. Anal. Chem.* **2020,** 2-10.

6. Xie, X.; Berner, Z.; Albers, J.; Stüben, D. Electrochemical Behavior and Analytical Performance of an Iridium-Based Ultramicroelectrode Array (UMEA) Sensor. *Microchim. Acta.* **2005,** 150, 137-145.

7. Chalhoub, C.; François, R.; Carcasses, M. Effect of Cathode-Anode Distance and Electrical Resistivity on Macrocell Corrosion Currents and Cathodic Response in Cases of Chloride Induced Corrosion in Reinforced Concrete Structures. *Constr. Build. Mater.* **2020,** 245, 118337-118352.

8. Satarpai, T.; Siripinyanond, A. Alternative Patterning Methods for Paper-based Analytyical Devices using Nail Polish as a Hydrophobic Reagent. *Anal. Sci.* **2018,** 34, 605-611.

9. *Epofix Embedding Resin;* MSDS No. 1232-A/1232-R; Electron Microscopy Sciences: Hatfield, Pa, April 13, 2020.

10. *Miccroshield;* MSDS No. 17022-AA/17022-AB; Structure Probe Inc: West Chester, Pa, October 3, 2016.

11. Liakat, M.; Khonsari, M.M. Analysis and Life Prediction of a Composite Laminate Under Cyclic Loading. *Compos. Part. B-Eng.* **2016,** 84, 98-108.

---

12. Azam, S.A.; Fragoso, A. Experimental and Numerical Simulation Study of the Vibration Properties of Thin Copper Films Bonded to FR4 Composite. *Appl. Sci.* **2020,** 10, 5197-5211.

13. Gräfe, D.; Walden, S.L.; Blinco, J.; Wegener, M.; Blasco, E.; Barner-Kowollik, C. It's in the Fine Print: Erasable Three-Dimensional Laser-Printed Micro- and Nanostructures. *Angew. Chem. Int. Ed.* **2020,** 59, 6330-6340.

14. Rahman, F.; Carbaugh, D.J.; Wright, J.T.; Rajan, P.; Pandya, S.G.; Kaya, S. A Review of Polymethyl Methacrylate (PMMA) as a Versatile Lithograhpic Resist- With Emphasis on UV Exposure. *Microelectron. Eng.* **2020,** 224, 111238-111250.

15. McCafferty, E. Lewis Acid/Lewis Base Effects in Corrosion and polymer Adhesion at Aluminum Surfaces. *J. Electrochem. Soc.* **2003,** 150, B342-B347.

16. Zhu, H.; Dhopatkar, N.; Dhinojwala, A. Effect of Acid-Base Interactions on Conformation of Adsorbed polymer Chains. *ACS. Macro. Lett.* **2016,** 5, 45-49.

17. *Su-8 3000 Permanent Negative Epoxy Photoresist;* MSDS SU-8 3000 Technical Data Sheet; Kayaku Advanced Materials: Westborough, Ma, July 2020.

4. Galvanostatically Charging Copper and Its Effect on the Corrosion Damage Pattern

4.1 The Rationale for Galvanostatically Charging Copper

4.1.1 DGR Conditions versus Experimental Conditions

In the deep geologic repository (DGR), the conditions the used fuel containers (UFCs) will be exposed to will change gradually over time. Despite the constant evolution of the repository conditions, they are bound by natural limitations. It is extremely unlikely that the repository redox condition will be able to support corrosion potentials (E_{corr}) > -0.1 V(SCE) which could lead to rapid dissolution of Cu.[1] The change in conditions is a relatively slow process since it will occur over many thousands of years.[2]

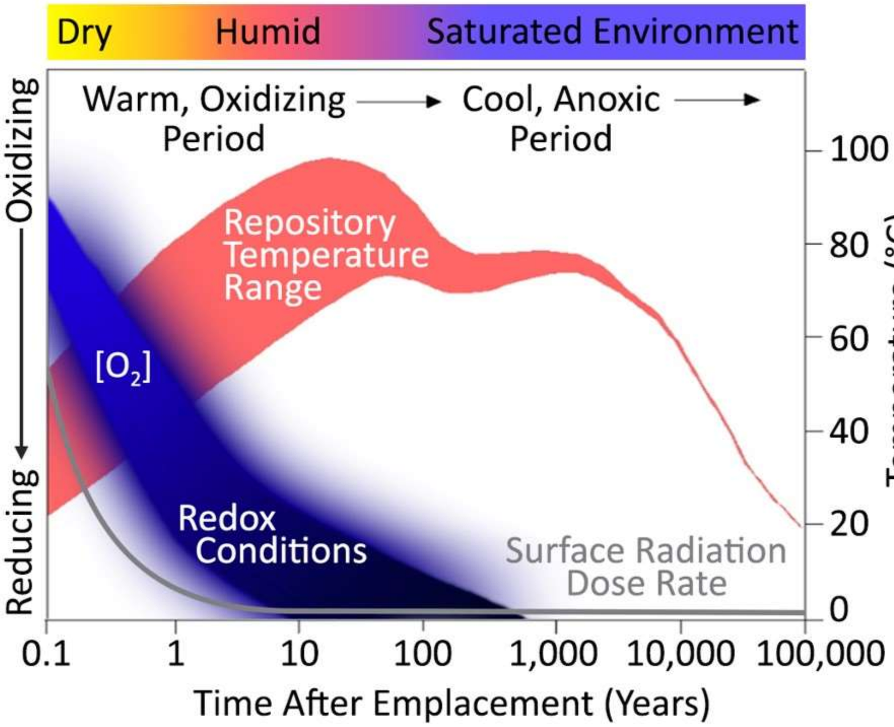

Figure 4.1. Schematic illustration of the evolution of conditions anticipated within a Canadian DGR[2]

As seen in Figure 4.1 the repository conditions are not yet fully defined. The evolution of redox conditions and the surface radiation dose rate are illustrative with the rate of consumption of O_2 likely to be much faster than shown.[3,4,5,6] This plot also shows that containers in the middle of the repository will remain at a higher temperature for longer than those on the edges due to the heat from neighboring containers. The experiments described in this chapter use conditions that approach or exceed the natural limitations of the DGR, to ensure conservative results.

4.1.2 What Information Can be Obtained by Performing Galvanostatic Charging

Galvanostatic experiments are useful to accelerate Cu corrosion to produce measurable damage on a laboratory time scale. In a galvanostatic experiment a constant current (CC) is applied and the potential response measured. Over the course of an experiment it is expected, based on the active dissolution scans in Chapter 2, that the potential response of Cu will tend towards 0 mV(SCE). However, unlike the experiments in Chapter 2, there is no limiting current value and therefore it is possible that a steady-state can be achieved or a film will form on the surface with enough time or high enough applied current. These experiments can be used to determine the steady-state potential that can be achieved during Cu charging in simulated groundwater solutions as well as the effect of constant current (CC) on the damage morphology.

Galvanostatic experiments can be conducted by varying the total experimental time or the total charge applied. The experiments in this chapter were designed by varying the CC to achieve a designated total charge, given by the CC multiplied by the duration of the experiment. The total charge consumed can be considered as simulating the consumption of a known amount of O_2 under DGR conditions. Since the electrochemical reactions for the Cu-Cl system were known, a mass loss calculation was performed using Faraday’s law to determine the total amount of material consumed.[7] This calculation was performed because it was more accurate than measuring the mass loss due to dissolution using an analytical balance. After the mass loss was calculated, the volume of Cu dissolved was calculated using the density of the material. The main goal of this work was to determine the influence of applied current and how the consumption of a specific amount of O_2, simulated by the injection of an equivalent amount of electrochemical charge influenced the Cu corrosion pattern and whether the CC used changes the corrosion morphology.

4.2 Materials

All galvanostatic charging experiments were conducted with a 1 cm x 1 cm x 1 cm electrode (referred to as a coupon) cut from a bulk block of wrought Cu supplied by Svensk Kärnbränslehantering AB (SKB). The Cu contained >99.99% Cu, <5 ppm O and 30-100 ppm P, designated as O_2-free and P-doped Cu.[8]

4.3 Experimental Procedure

A standard procedure was used in experiments. A tapped hole was machined into the Cu coupon, allowing for insertion of a steel rod prior to mounting the coupon in Epofix epoxy to avoid exposure of steel to the solution. After curing, the sample surface was prepared using a series of SiC grinding papers up to p1200 grit. The sample was then rinsed in type-1 water with a resistivity of 18.2 MΩ.cm. prepared using a Barnstead Nanopure (Thermoscientific) water purification system, and quickly dried in a stream of Ar. The coupon was then quickly transferred into the anaerobic chamber to avoid air oxidation.

If the coupon was to be used immediately in a benchtop experiment, it was placed in the cell and secured. Experiments were conducted in a 1 L glass electrochemical cell with a special inlet on the bottom to allow a circular sample to be placed upright in the cell and sealed by a Teflon screw cap and Viton O-ring. This allowed the steel rod attached to the coupon to protrude from the cell while the epoxy and O-ring prevented solution leakage. The remainder of the cell openings were covered with parafilm and the solution was sparged with Ar for the duration of the experiment if it was a benchtop experiment, whereas experiments conducted in the anaerobic chamber with an Ar atmosphere were stagnant. Sparging with Ar creates an O_2-limited environment containing < 0.5 ppm O_2 initially and < 0.3 ppm beyond 30 minutes.[9]

Benchtop experiments were initiated by sealing the coupon, then quickly filling the cell with solution while Ar sparging. Coupons were placed as far as possible from the sparging tube to prevent the attachment of gas bubbles to the coupon surface. Cell openings were then covered with parafilm for the duration of the experiment. When the experiment was finished the cell was emptied and rinsed with type-1 water before the sample was removed and also rinsed with type-1 water before being dried in a steady stream of Ar, and then stored in the anaerobic chamber until surface analysis was performed. Samples were transported to analytical equipment using a vacuum box to prevent O_2 reacting with any corrosion products formed during the experiment.

Potentials were measured against a SCE reference electrode (Accumet) using a single channel on an eight-channel Solartron 1480 multistat on the benchtop or a Solartron 1287A potentiostat in the anaerobic chamber. The SCE was calibrated versus a master SCE reference

(+241 mV vs saturated hydrogen electrode (SHE)) maintained for this purpose.[10] Before and after an experiment the SCE reference electrode was checked for 20 minutes to see if it measured within ± 5 mV of the master SCE in saturated KCl solution. This verification was especially important for the experiments conducted in the anaerobic chamber since it was possible that placing the SCE in the transfer chamber (where O_2 is pumped out and replaced with Ar to remove impurities) could dry out the solution inside the reference electrode. A Pt mesh was used as the counter electrode. Experiments were performed at a specified CC for the designated duration to achieve the same amount of total charge in each experiment.

The 75 μA CC experiments were performed in a modified beaker due to a break in the standard 1 L cell that could not be fixed in a timely manner. The modified beaker had a small glass joint fused to the bottom such that an upright facing electrode could be attached using an O-ring and clamp. Unlike a traditional glass cell, the counter electrode was not separated by a glass frit due to the size of the cell relative to that of the counter electrode. This allowed reduction products to form on the CE surface. The modified beaker was sealed using a shaved butyl rubber stopper with holes drilled through it to accommodate the various glass inserts and electrodes. The stopper was wrapped in Teflon tape and then coated with Miccroshield (an epoxy) on the bottom face to prevent solution from splashing directly onto the stopper.

Before and after each experiment the Cu coupon was mapped using optical microscopy at 50× magnification to determine if there were any surface features that should be noted. Each optical scan was followed by CLSM scans at 5 different points on the surface that were determined to be representative of the different topographies seen during the optical mapping. Each CLSM scan was used to determine and verify the surface topography. Each set of CLSM data was input into Confomap (the CLSM processing software) and 3D reconstructed images were generated along with roughness parameters to help gauge the roughness of different spots on the surface.

4.4 Galvanostatic Parameter Determination

Once sealed, the DGR will contain a limited inventory of O_2, which will be depleted by various reactions besides container corrosion: oxidation of tunnel steel support structures; the oxidation of minerals (such as pyrite) and microbial reactions.[4,5,6,11,12] The galvanostatic experiments described in this chapter were performed in groundwater ion salt solutions to simulate the consumption of a specific amount of O_2 at a potential close to the expected corrosion potential (E_{corr}), and to determine the corrosion morphology. The consumption of a specific amount of O_2 can be expressed as a charge using Faraday's law of electrolysis [4.1][8],

$$m = \frac{MQ}{Fn_e} \tag{4.1}$$

where m is the mass of dissolved Cu, M is the molar mass, Q is the associated charge, F is Faraday's constant, and n_e is the number of electrons associated with the reaction. For this calculation the predominant reaction was taken to be the two-electron oxidation of Cu.

$$Cu_{(s)} \rightarrow Cu^{2+}{}_{(aq)} + 2e^{-} \tag{4.2}$$

A penetration depth of 10 μm was arbitrarily chosen. This depth was considered to be a large enough dissolution volume to generate surface roughness for analysis on the samples used in this chapter. To calculate Q for the specified penetration depth of 10 μm, a molar mass (M) of Cu was used (63.55 g/mol) with $n_e = 2$ (determined from [4.2]), and the mass calculated using the dimensions of the electrode and the intended penetration depth. The dimensions of the reactive surface of the coupon were 5 mm x 5 mm. Assuming uniform dissolution the lost volume would be 0.25 mm^3. This target lost volume was multiplied by the density of copper (0.00896 g/mm^3) to obtain a mass loss of 0.00224 g, which yields a charge of 6.8 C.

Since Q = It, the duration of an experiment can then be calculated for a specified CC (I). CC values of 1000 μA, 500 μA, 250 μA and 75 μA were chosen with corresponding experimental times of 1.89 h, 3.77 h, 7.56 h and 25.10 h, respectively. The anaerobic chamber experiments were performed with CCs of 1000 μA, 500 μA, and 250 μA. A 1 M NaCl solution was used in all experiments since this anion will be dominant in a DGR.

4.5 Galvanostatic Charging Experiments

4.5.1 1000 µA CC Experiments

A CC of 1000 µA was applied for 1.89 h. Figure 4.2 shows that the experiment lasted approximately 20 min before the potential approached values beyond those achievable in a DGR (i.e., ≥ 0 V(SCE)). The accelerated increase in potential, occurred around -60 mV(SCE), with the value subsequently increasing to ~ 9 V(SCE) suggesting the formation of a resistive film, since minimal dissolution occurred. This is confirmed by the 3D reconstructed images, Figure 4.3, which show that preferential grain dissolution had just begun as indicated by the undefined, sharp grain edges/structures. The differences between the pre- and post-experimental averaged S-values in Table 4.1 are 0.3 µm, 0.4 µm and 0.6 µm for S_a, S_q, and S_z respectively. The S_a and S_q values, primarily used to determine roughness, are considered low since a freshly ground surface (up to p1200) results in S_a and S_q values around 0.2 µm. Similarly, for S_z, the total height of the sample, a change of 0.6 µm, indicates almost no dissolution has occurred.

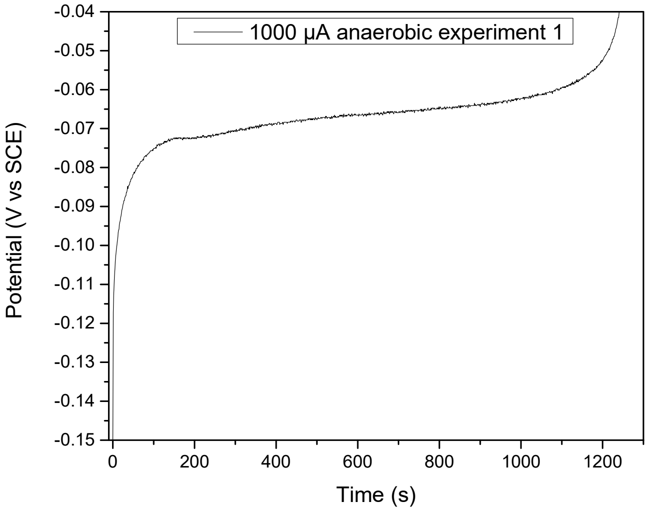

Figure 4.2. Potential vs time profile recorded for CC = 1000 µA in 1 M NaCl in the anaerobic chamber.

In an attempt to achieve the required level of charging, a CC of 1000 µA was applied five more times, with 2-3 minute pauses on open circuit, in between each application. Over the course of these six charging sessions, 46% of the targeted total charge was achieved but the change in the

S_z value was still much less than the intended 10 μm. This suggests that charging at this value of CC did not significantly roughen the surface.

At high applied currents the potential rises to the value that is needed to sustain the current. Therefore, if the rate of the initial reaction is not fast enough to consume all of the applied current then the potential rises to a value where another reaction can be supported.

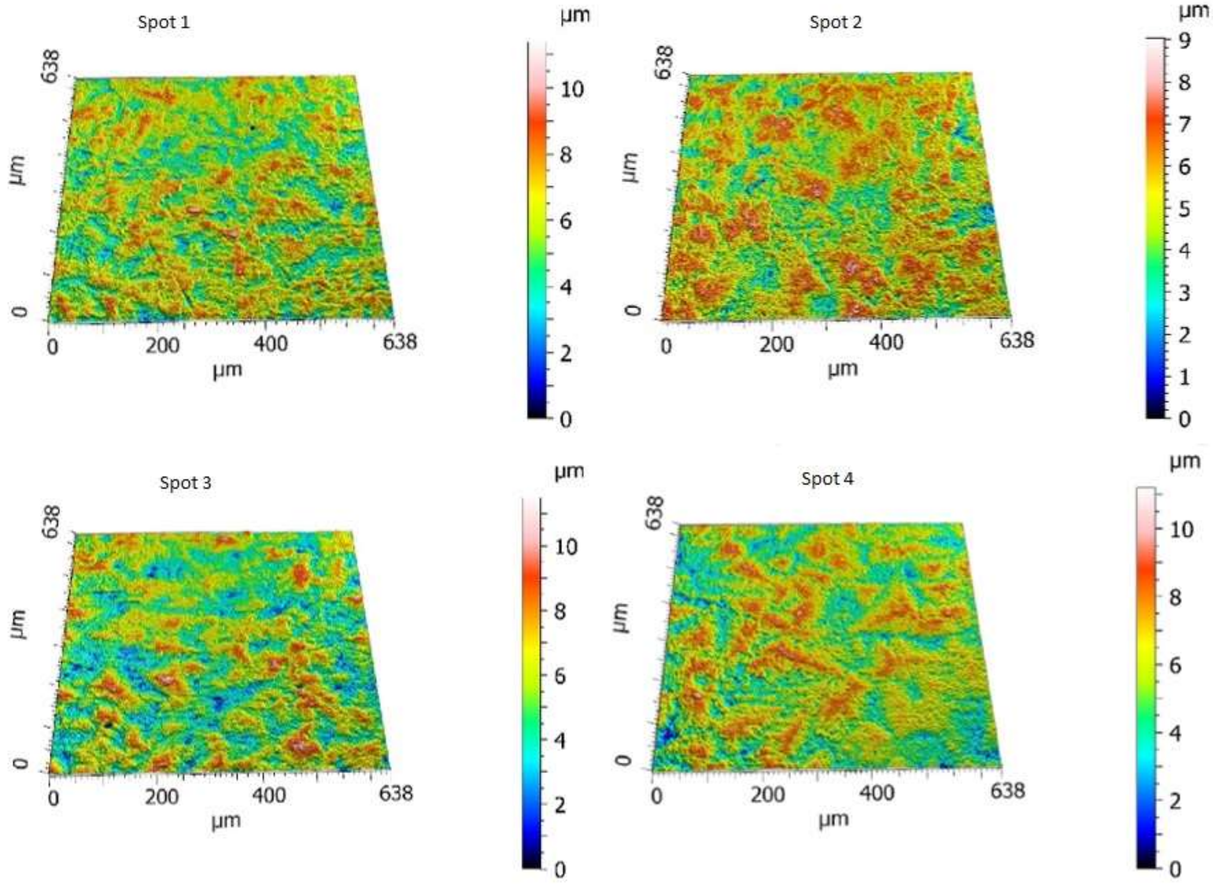

Figure 4.3. 3D reconstructed images of four spots analyzed with CLSM after CC = 1000 μA in 1 M NaCl in the anaerobic chamber

$CuCl_{ads}$ formation is expected in Cl^- solutions >1 mM, especially at potentials from 0 mV(SCE) to -200 mV(SCE).[11,13] However, CuCl is soluble in Cl^- solutions as $CuCl_2^-$ and is transported to the bulk solution. CuCl can also be consumed by OH^- to form $Cu(OH)_{ads}$ and Cl^-.[11] The dissolution of these adsorbed films and the transportation of the soluble products away from the surface increases the dissolution rate. However, since there was no convection in the electrochemical cell the $CuCl_{ads}$ remained on the electrode surface for extended periods of time. In this scenario the formation of $CuCl_{ads}$ would have been rapid because of the high applied current, while the diffusion of dissolved Cu species would have been slow since the solution was stagnant.

At CC = 1000 μA the overall reaction is the dissolution of Cu^+ as $CuCl_x^{(x-1)-}$, which proceeds through the $CuCl_{ads}$ surface intermediate. Since the rate of $CuCl_{ads}$ formation is faster than its subsequent dissolution, it thickens with time. The region in which the potential increases slowly suggests that the film is resistive rather than conductive and the slow increase occurs to maintain the film dissolution process. The potential begins to rapidly increase once the surface layer is too thick to sustain the current (since it is resistive it requires a very large potential gradient to force the current through the electrical field in the CuCl layer). Therefore, the increase in potential up to 9 V(SCE) is required to support H_2O oxidation to O_2.

Figure 4.4 shows that restarting the charging experiment resulted in the brief period of stable potential before the rapid increase occurred again. Subsequent charging attempts, after waiting 2-3 minutes on open circuit, yielded even shorter periods of stable potential before the increase occurred. At open circuit the CuCl layer can dissolve into the Cl^- solution. On reapplying the current the film would be thin or completely dissolved but the formation/dissolution cycle would begin again. Since the solution would contain a large amount of dissolved Cu^+ from the previous CC period, the rate of dissolution would be slower when current is re-applied with film formation occurring more rapidly and thickening faster leading to an earlier potential increase to support H_2O oxidation.

It also could have been possible that a gas bubble formed on the electrode surface from the H_2O oxidation. Without any convection any bubbles produced and adhered to the reactive surface could have taken a long time to detach. Both the formation of a CuCl or the formation of gas bubbles supports the idea that the reactive surface was temporarily occluded and insulated during these experiments.

Table 4.1. Roughness values recorded on a Cu electrode before and after applying CC = 1000 µA in 1 M NaCl for 0.93 h for a total of 3.1 C. Associated averages and differences are listed, values in red are pre-experimental (pe)

Location on the surface (Spot)	1	2	3	4	5	Average	Difference Between Average Values
S_a (µm) pe	0.7	0.68	0.66	0.66	0.62	0.7	0.3
S_a (µm)	1.0	0.91	1.2	1.1	0.97	1.0	
S_q (µm) pe	0.9	0.87	0.85	0.86	0.8	0.9	0.4
S_q (µm)	1.3	1.1	1.5	1.4	1.2	1.3	
S_z (µm) pe	11.1	9.5	11.6	10.1	9.9	10.4	0.6
S_z (µm)	11.4	9.1	11.5	11.2	11.9	11.0	

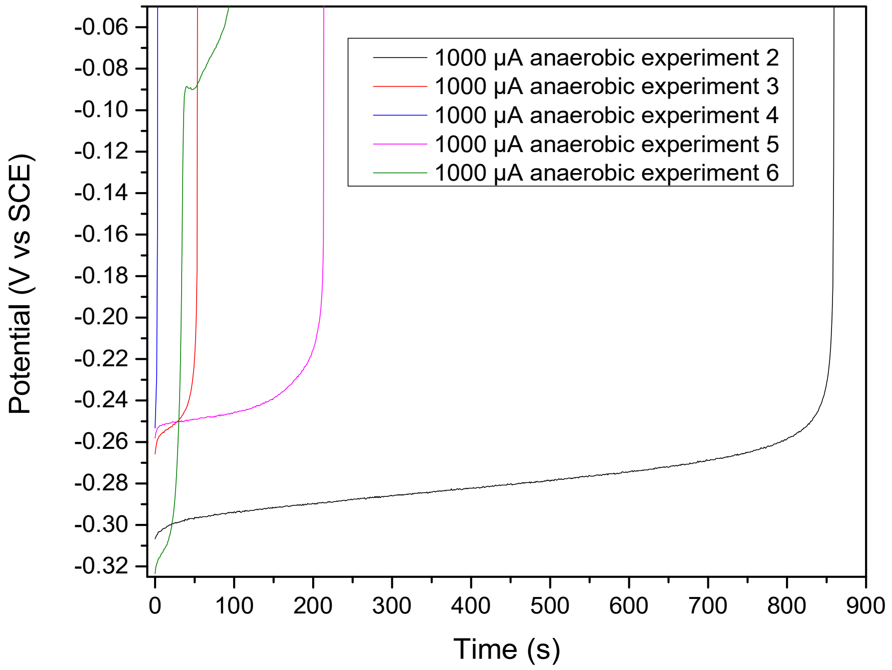

Figure 4.4. Potential vs time profiles recorded in the anaerobic chamber for a sequence of applications of CC = 1000 µA in 1 M NaCl with a 2-3 minute break on open circuit between each application.

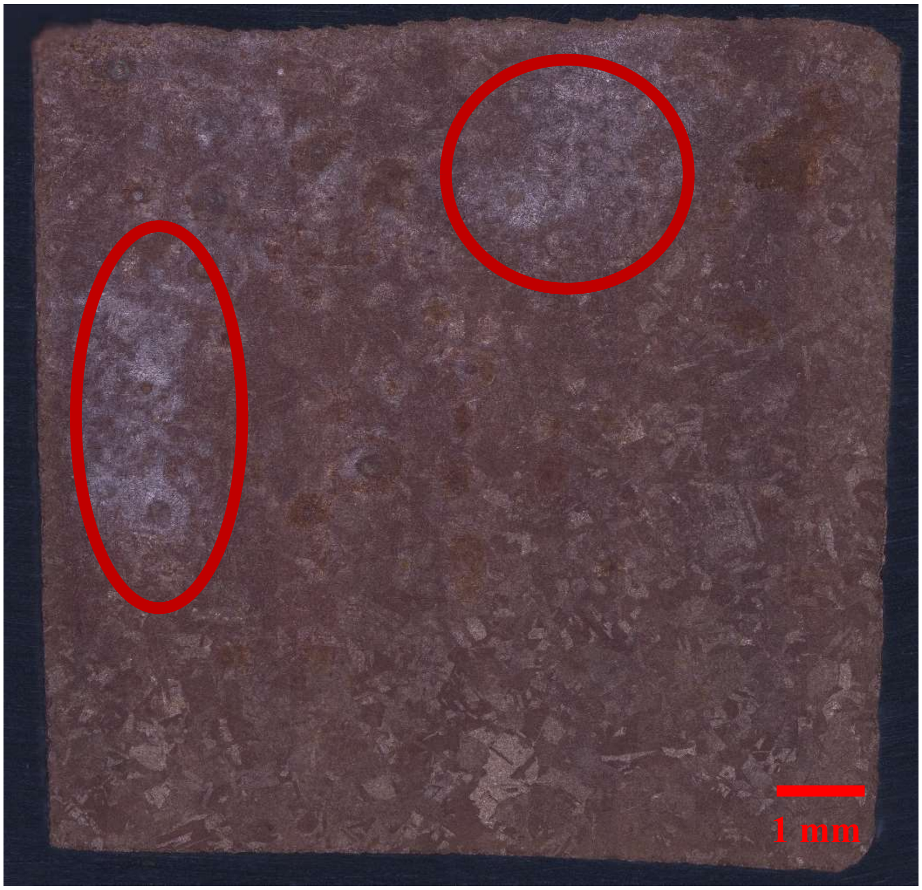

Figure 4.5. An optical image of a Cu coupon surface after applying CC = 1000 µA in 1 M NaCl in the anaerobic chamber. Spots showing an unidentified white film are circled in red

The circled areas in Figure 4.5 indicate a white film was present on the Cu coupon after the experiment was complete. This supports the idea that a film was temporarily insulating the reactive surface which led to a large increase in resistance as indicated by the potential rise, and suggests the film was not fully dissolved between experiments.

Since the surface is not fully covered in white film, it is also possible that both a film and oxygen bubbles occluded the surface. Areas with no residual film after experimentation could have been covered by a film that dissolved or a gas bubble that dissipated. Based on the electrochemical data and the optical images of the Cu surface after experimentation it cannot be verified if gas bubbles were present in conjunction with CuCl to occlude the electrode surface. For 1000 µA to be a viable CC the cell design would have to be improved to include convection to determine if improved mass transport could help increase the dissolution rate of Cu^+ and avoid the thickening of the CuCl layer.

4.5.2 500 μA and 250 μA CC Experiments

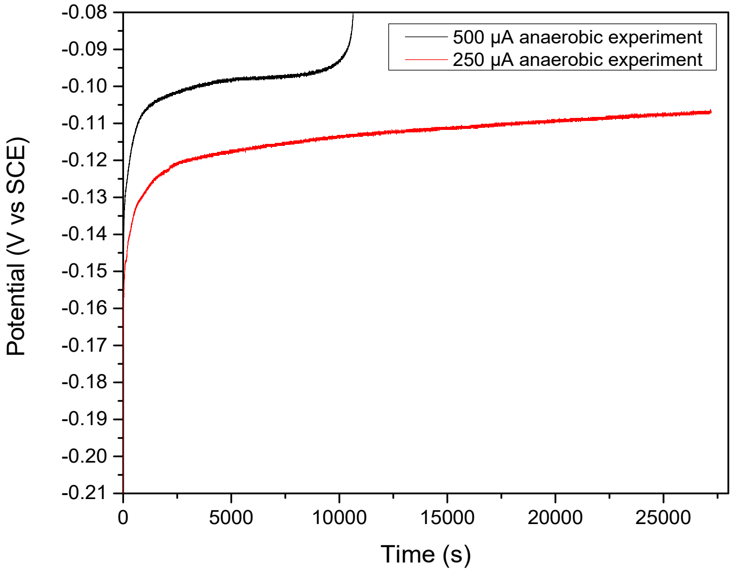

Figure 4.6. Potential vs time profiles recorded for CC = 500 μA and CC = 250 μA in 1 M NaCl in the anaerobic chamber

Figure 4.6 shows the potential versus time profiles recorded for CC = 500 μA and CC = 250 μA in 1 M NaCl in the anaerobic chamber. The most notable feature of these plots is that at a CC of 500 μA, the potential exhibits a plateau and later an increase similar to that observed at a CC of 1000 μA indicating the Cu surface became insulated by CuCl. However, the potential increase happened after a charge of 5.5 C (81% of the targeted charge) rather than 3.1 C (46% of the targeted charge) had passed. This indicates that the CuCl film formed on the surface did not thicken as quickly at the lower CC of 500 μA. On switching to open circuit, the potential was between -100 mV(SCE) and -70 mV(SCE) in this O_2-free environment with no convection. Similar behaviour has been observed when Cu is polarized to ~ -100mV(SCE) in NaCl solutions, when CuCl formation is the dominant reaction based on [Cl^-] and current density.[14] Figure 4.7 shows the grains are well-defined indicating the preferential dissolution of grains with different crystallographic orientations. This is supported by the 3D reconstructed images in Figure 4.8, which confirm the more extensive etching of some grains with a number of visible well-defined twins (spots 3 and 4).

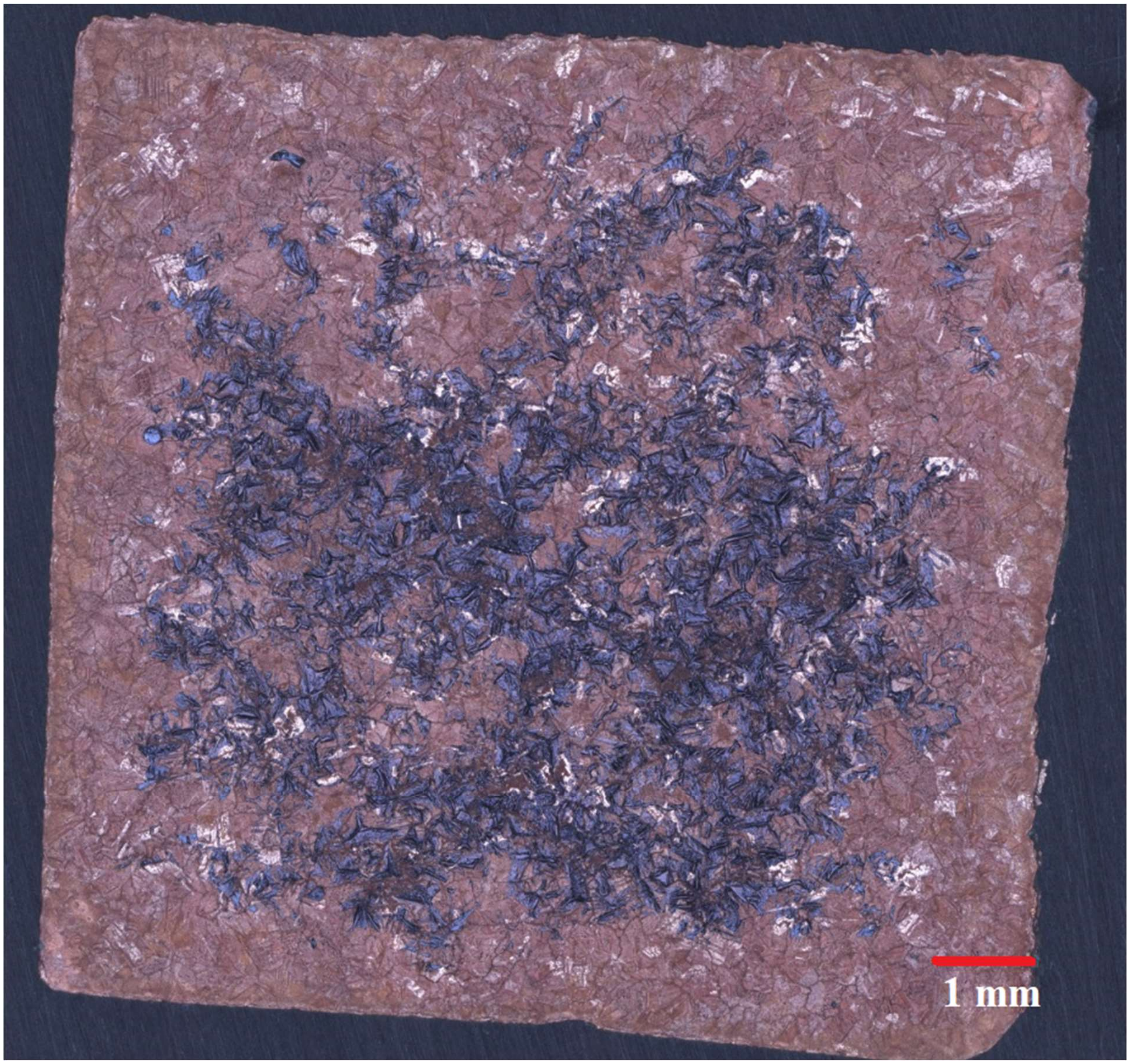

Figure 4.7. Optical image of the entire Cu coupon after exposure to a total charge of 5.5 C in 1 M NaCl in the anaerobic chamber

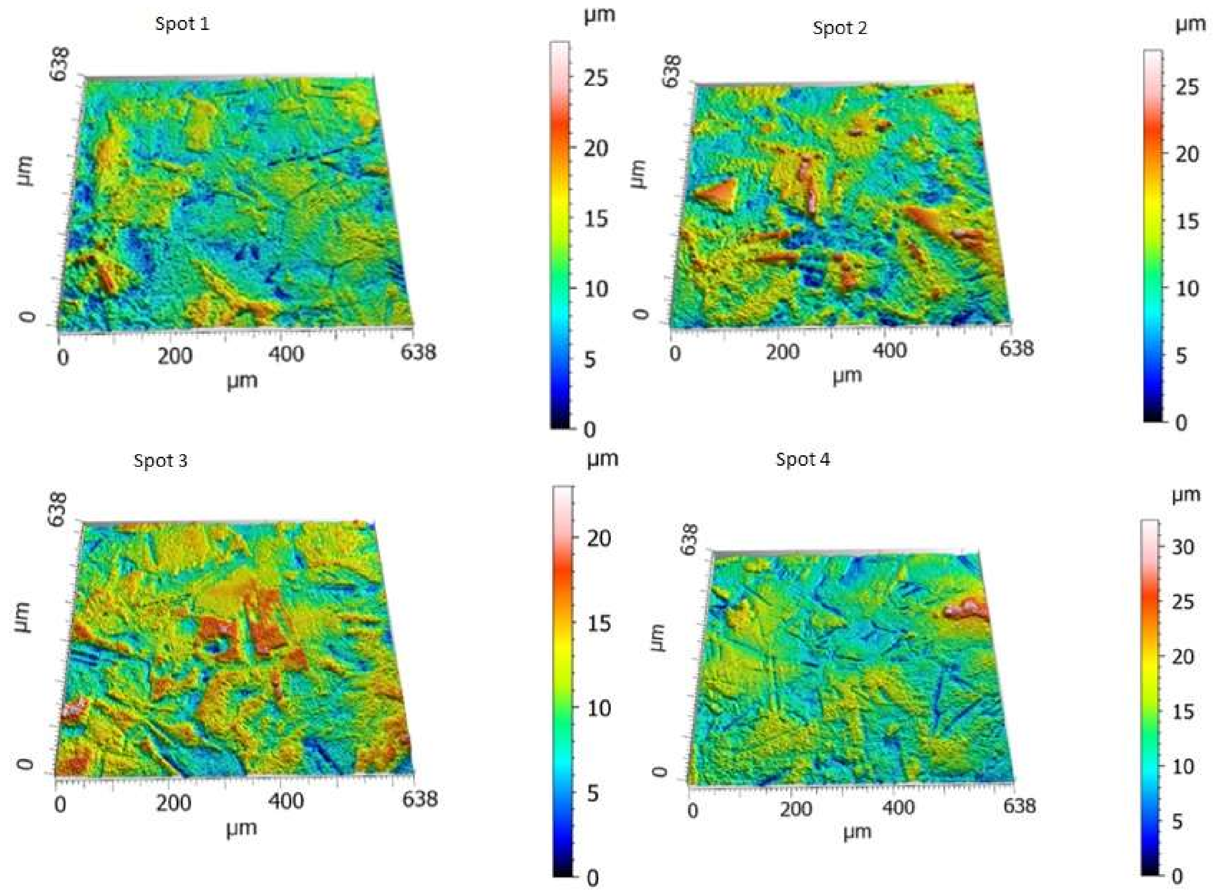

Figure 4.8. 3D reconstructed images of four spots analyzed with CLSM after applying CC = 500 µA Cu in 1 M NaCl in the anaerobic chamber

The blue-black deposit in the centre of the optical image shown in Figure 4.7 is most likely $CuCl_2$, based on its colour. The $CuCl_2$ was probably a product of CuCl oxidation on the surface. The oxidation could have occurred electrochemically during the experiment or by reaction with O_2 during transportation of the coupon to the microscope. The deposit appears to be very thin, as the grains are still visibly outlined in the optical image and the 3D reconstructed images. The extent of dissolution (determined by S_z) and roughening (determined by S_a and S_q) produced by the application of 500 µA CC is greater than on the coupon subjected to 1000 µA CC. This is shown by the results in Table 4.2, which show a ~400% increase in averaged S-values. The notable increase in roughness combined with preferential grain etching suggests that the influence of the film was not major.

Table 4.2. Roughness values recorded before and after applying CC = 500 µA in 1 M NaCl for 3.04 h for a total of 5.5 C. Associated averages and differences are listed, values in red are pre-experimental (pe)

Location on the surface (Spot)	1	2	3	4	5	Average	Difference Between Average Values
S_a (µm) pe	0.46	0.45	0.40	0.43	0.44	0.4	2.0
S_a (µm)	2.2	2.7	2.3	2.3	2.6	2.4	
S_q (µm) pe	0.58	0.57	0.52	0.55	0.57	0.6	2.6
S_q (µm)	2.7	3.5	2.9	3.1	3.4	3.1	
S_z (µm) pe	8.2	6.3	8	5.9	6.4	7.0	21.6
S_z (µm)	28	28	23	33	31	28.6	

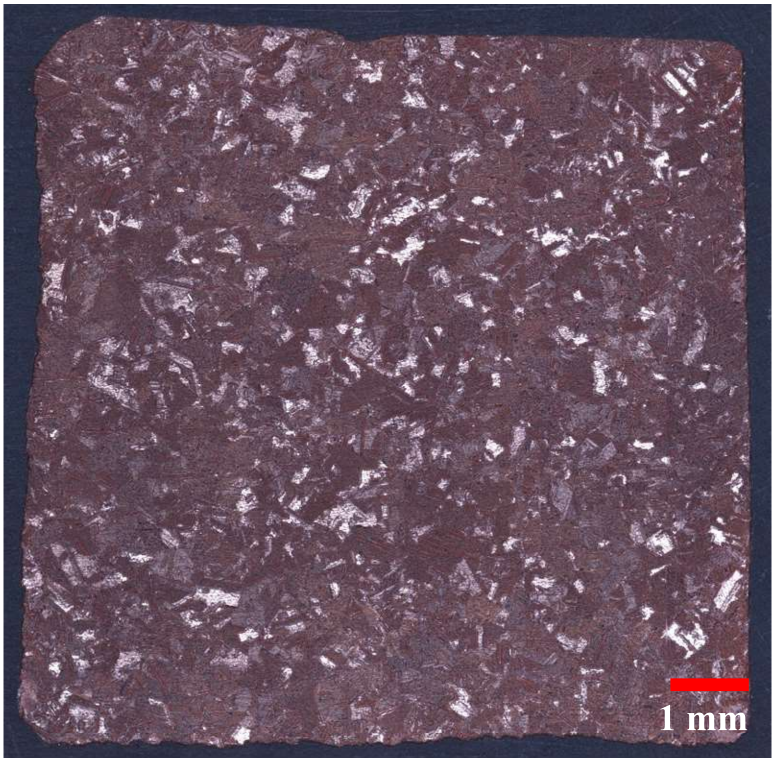

Figure 4.9. Optical image of the entire Cu coupon surface after applying CC = 250 µA in 1 M NaCl in the anaerobic chamber

Based on these results, both 1000 µA and 500 µA were too high values of CC to examine the corrosion morphology of Cu in O_2-free, Cl^--based solutions because the formation of a resistive $CuCl_x$ layer forced the potential to a value at which H_2O oxidation prevailed. If the solution could be stirred leading to convective transport, the dissolution of the CuCl layer would be accelerated and a CC of 1000 μA or 500 μA could then be viable.[11,14] However, when the CC was reduced to 250 μA, the potential remained below -100 mV(SCE), Figure 4.6, and the formation of resistive layer was avoided. The surface, Figure 4.9, shows preferential grain dissolution as seen at the higher CC values but with no visible film formation on the surface. This similarity suggests that the corrosion morphology is independent of the CC.

When the S-values measured at CC values of 1000 μA, 500 μA and 250 μA are compared, it is apparent that the roughness and dissolution depths are dependent on the applied CC. The "Average Difference" values from Table 4.1, Table 4.2, and Table 4.3 provide some insight into this behaviour. After reaching 46% of the targeted charge the average difference in S-values produced by the application of 1000 μA CC are very small which suggest the surface has barely changed. The difference in the S_a and S_q averages for experiments conducted at the two lower CCs are negligible (0.1 μm and 0.3 μm), while the difference in S_z is much larger (5.1 μm). Based on the % of targeted charge achieved if the application of 500 μA CC had reached 100% instead of only 81%, the average differences of the S-values would be higher than those observed at 250 μA CC, which did reach the targeted charge. This projected trend suggests that the roughness and dissolution depth are dependent on the CC.

The CC also appears to control the dissolution rate and the steady-state potential based on the E vs t plots shown in Figure 4.2 and Figure 4.6. Figure 4.2 shows that if 1000 μA CC is applied the potential will exceed -100 mV(SCE). This also occurs for CC = 500 μA, Figure 4.6. However for 250 μA CC, Figure 4.6 remains below -100 mV(SCE) and appears to eventually reach a steady-state. Figure 4.9, which shows the optical image of the coupon after the application of 250 μA CC, shows no film formation on the surface. This indicates that, at this lower CC, dissolution as $CuCl_2^-$ is sufficiently rapid to prevent the build up of a resistive CuCl layer.

To test the influence of low amounts of O_2 on the corrosion morphology, an experiment with a CC of 250 μA was conducted on the benchtop with Ar sparging to limit the availability of O_2 in solution and provide a small amount of convection. Figure 4.10 shows a comparison of optical images recorded on the coupons in the benchtop and anaerobic chamber experiments. Both images show the coupon has undergone preferential grain dissolution, but the coupon used in the benchtop experiment has a distinct black colour which is usually indicative of a Cu oxide.

However, the surface features suggest this layer is extremely thin and unlikely to have influenced the overall behaviour.

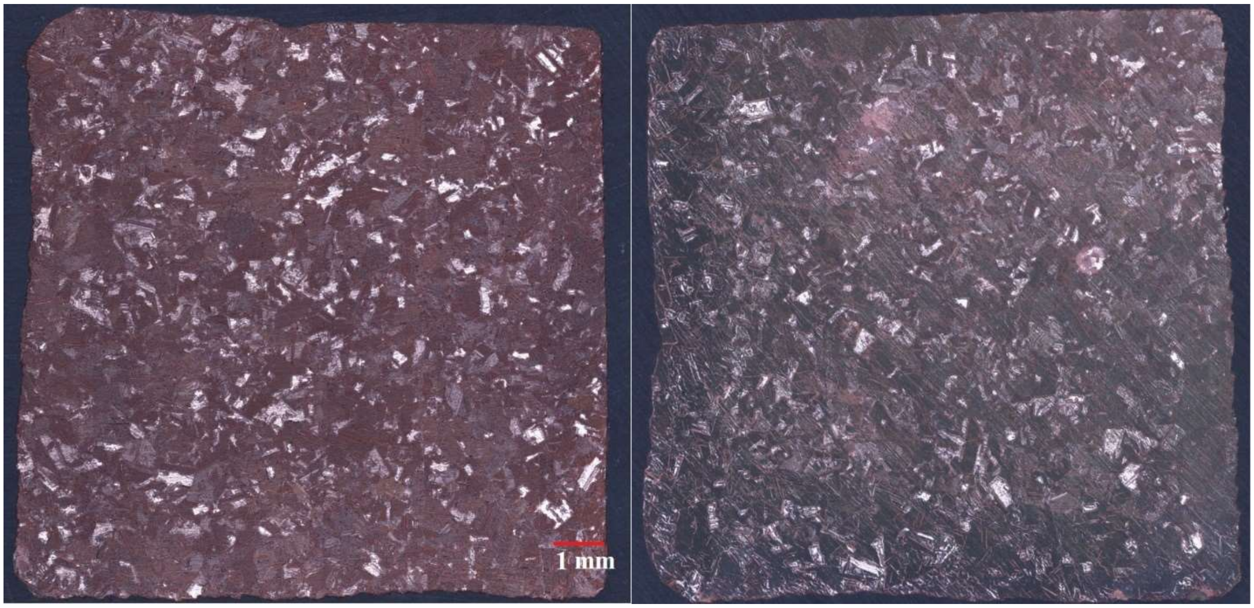

Figure 4.10. Optical images of the entire Cu coupon surface after applying CC = 250 µA in 1 M NaCl in the anaerobic chamber (left) and on the benchtop (right)

Table 4.3. Roughness values recorded before and after applying CC = 250 µA in 1 M NaCl in the anaerobic chamber for 7.56 h for a total of 6.8 C. Associated averages and differences are listed, values in red are pre-experimental (pe)

Location on the surface (Spot)	1	2	3	4	5	Average	Difference Between Average Values
S_a (µm) pe	0.50	0.5	0.50	0.46	0.48	0.5	
S_a (µm)	2.7	2.8	2.7	2.4	2.4	2.6	
S_q (µm) pe	0.63	0.64	0.63	0.59	0.61	0.6	2.9
S_q (µm)	3.5	3.8	3.8	3.2	3.3	3.5	
S_z (µm) pe	7.1	8.2	7	6.3	7.1	7.1	26.7
S_z (µm)	28	30	57	29	25	33.8	

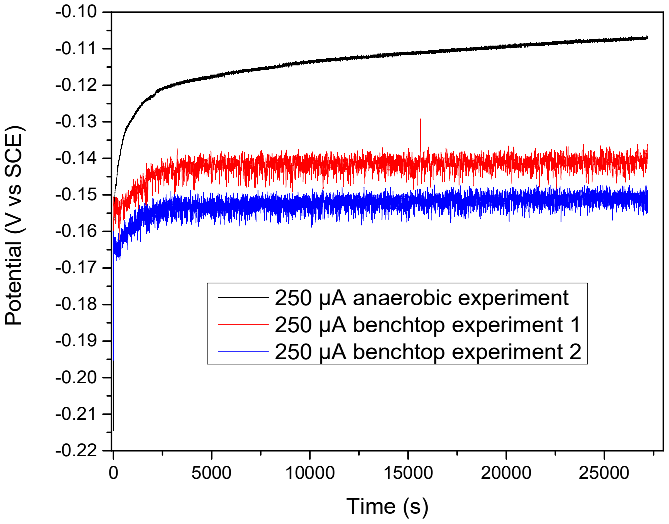

Figure 4.11. Potential vs time profiles recorded at a CC = 250 µA in 1 M NaCl in both the anaerobic chamber and on the benchtop

Figure 4.11 shows the potential versus time plots for the three different applications of 250 µA CC. Two experiments were performed with Ar sparged solutions on the benchtop and one in the anaerobic chamber. The potential responses from the benchtop experiments were similar, steady-state values around -150 mV(SCE) being achieved in both experiments. By contrast the potential measured in the anaerobic chamber was slightly higher (-110 mV(SCE)). This potential difference between the anaerobic chamber and benchtop experiments could be due to the difference in atmosphere, and the influence of the convection caused by Ar sparging. The convection from the sparging may have prevented oxidation products from blocking the surface by facilitating the transport of soluble Cu away from the surface which would increase the dissolution rate of any CuCl layer thereby lowering the potential required to sustain the applied CC for the benchtop experiments. The even damage distribution at the lower potentials is consistent with Figure 4.12 which compares the 3D reconstructed images of both the benchtop and anaerobic chamber experiments. The corrosion morphology appears to show less corrosion damage and a flatter surface for the benchtop sample compared to the anaerobic chamber sample. This is consistent with the S-value averages and their differences, shown in Table 4.3 and Table 4.4. The S-value average differences show that the roughness values and dissolution depth produced by the experiment in the anaerobic chamber are 100-200% larger than the values produced by the experiments on the benchtop. This suggests that the experiments performed on the benchtop had lower roughening rates consistent with the lower potential observed.

Since this coupon is coated in epoxy it is important to investigate the possibility of edge effects on the damage profile due to the unique geometry existing between the edges of a sample and the occluding layer formed by the coating. Edge effects can lead to increased dissolution rates due to the formation of crevices. Figure 4.13 shows that any edge effect varies from experiment to experiment, regardless of the amount of dissolution on the rest of the surface, with no reproducible edge effects. However, the dissolution depths were generally higher than on the general surface. This non-reproducibility suggests that edges should be left out of analyses.

Table 4.4. Roughness values recorded before and after the application of CC = 250 in 1 M NaCl on the benchtop for 7.56 h for a total of 6.8 C. Associated averages and differences are listed, values in red are pre-experimental (pe)

Location on the surface (Spot)	1	2	3	4	5	Average	Difference Between Average Values
S_a (µm) pe	0.64	0.33	0.48	0.34	0.52	0.5	0.8
S_a (µm)	0.89	1.2	1.4	1.3	1.3	1.2	
S_q (µm) pe	0.83	0.43	0.61	0.43	0.67	0.6	1.0
S_q (µm)	1.2	1.6	1.8	1.7	1.8	1.6	
S_z (µm) pe	9.0	4.7	8.8	4.9	8.7	7.2	7.1
S_z (µm)	12.3	11.9	14.9	17.6	15.1	14.4	

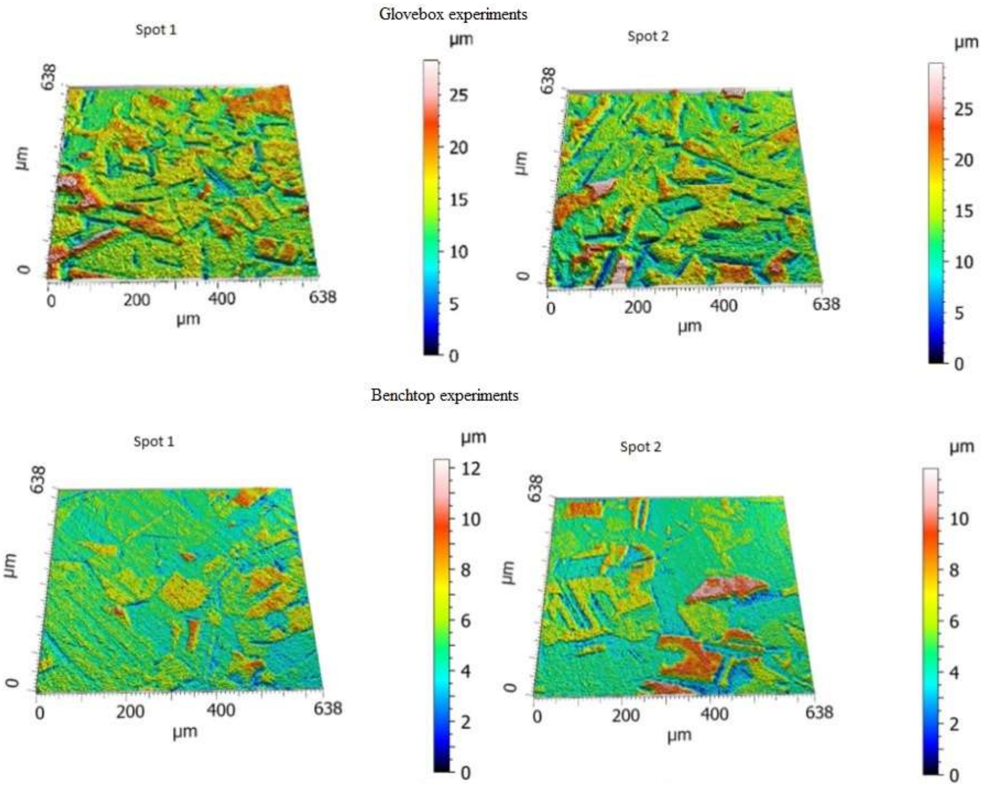

Figure 4.12. 3D reconstructed images of the first two spots analyzed using CLSM after CC = 250 µA in 1 M NaCl in the anaerobic chamber and on the benchtop

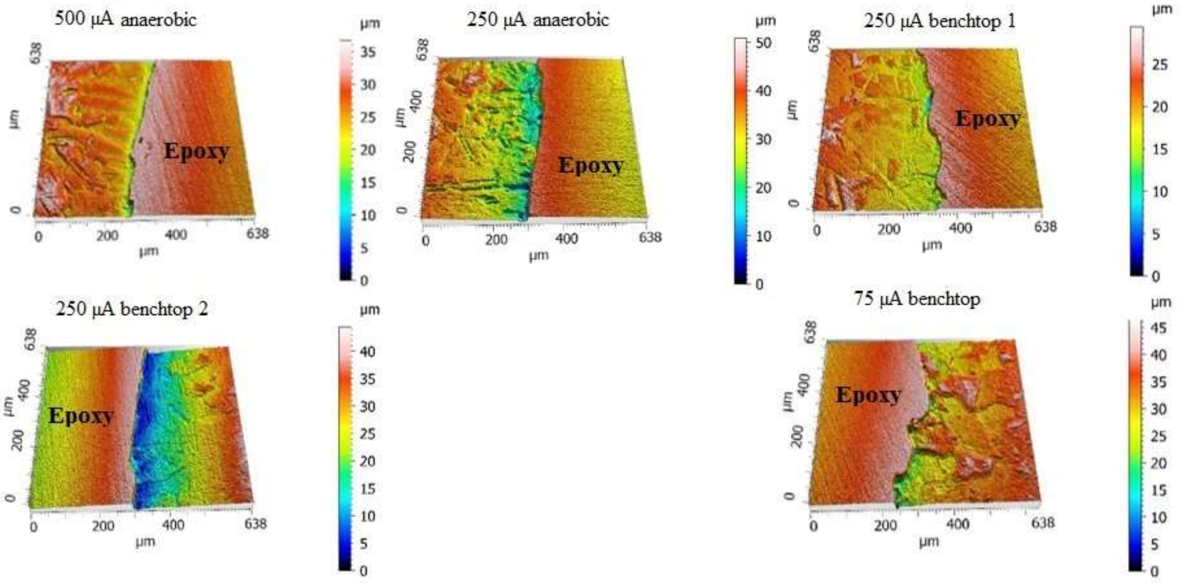

Figure 4.13. 3D reconstructed images of the Cu-epoxy interface recorded by CLSM for various applied CCs in 1 M NaCl either on the benchtop or in the anaerobic chamber

4.5.3 75 µA CC Experiment

The remaining experiment was performed on the benchtop at a CC of 75 µA for 25.1 hours. A smaller cell was used for this experiment due to a leak in the 1 L glass cell. In this experiment, the potential reached a steady state value around -100 mV(SCE), Figure 4.14. When the experiment was finished, the surface was covered in $CuCl_2$, identifiable by its blue colour, but this deposit was promptly removed using type-1 water.

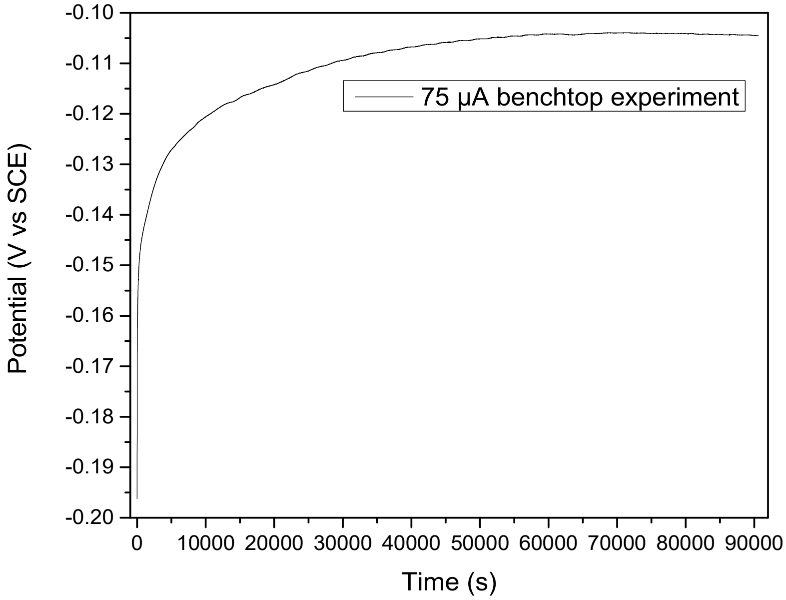

Figure 4.14. Potential vs time profile recorded at a CC = 75 µA in 1 M NaCl on the benchtop

At this CC value the S_a, S_q, and S_z values were significantly higher than those measured at higher CC values. The S_z values recorded at a number of locations on the surface have a very large range, indicating less uniform dissolution, Table 5.

Table 4.5. Roughness parameters and average values from the application of CC = 75 μA in 1 M NaCl on the benchtop with Ar-sparging for 25.1 hours

Location on the surface (Spot)	1	2	3	4	5	6	Average	Difference from the average pre-experimental values
S_a (μm)	2.9	2.8	2.9	2.3	2.1	3.5	2.6	2.1
S_q (μm)	4.0	3.7	4.4	5.1	2.9	4.5	4.0	3.4
S_z (μm)	28	30	65	69	68	46	52.0	44.8

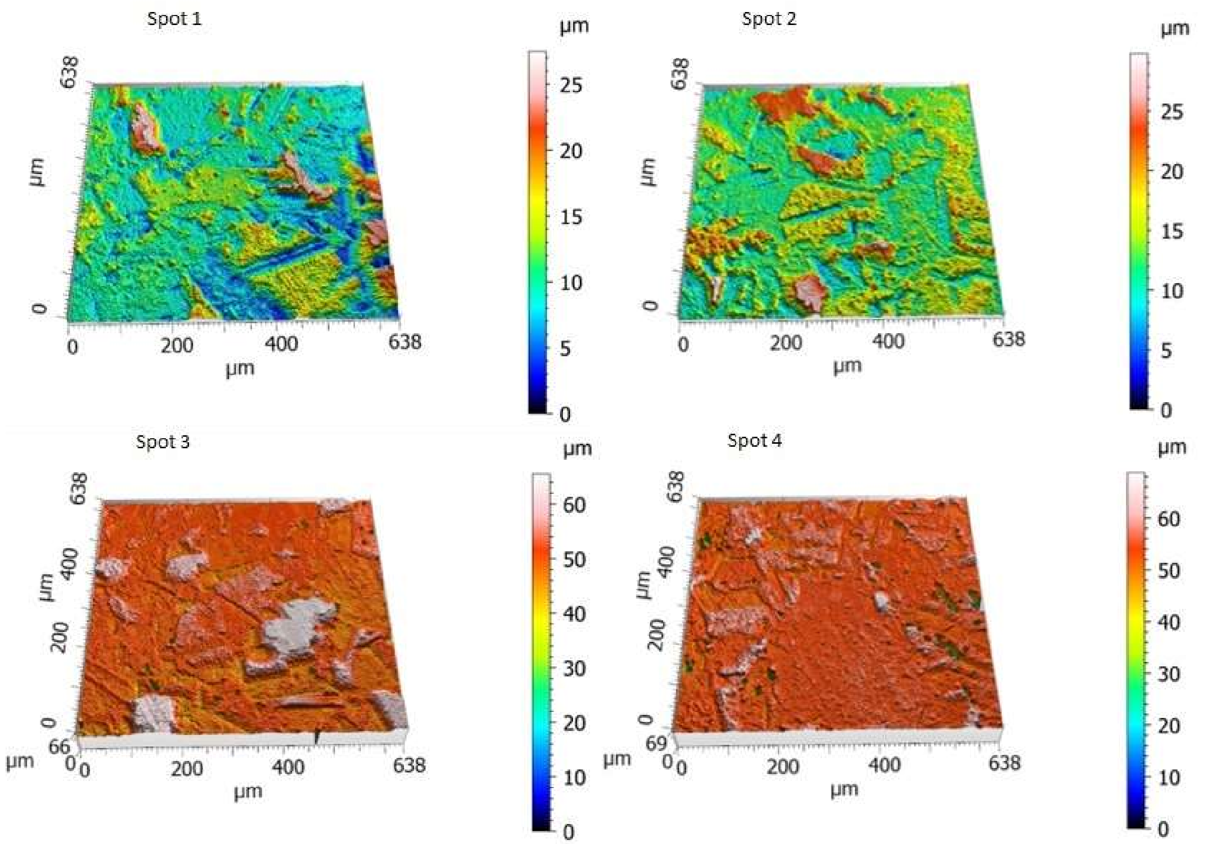

Figure 4.15. 3D reconstructed images recorded on four spots using CLSM after the second CC = 75 μA Cu in 1 M NaCl on the benchtop

Figure 4.15 and Table 5 show spots 1 and 2 exhibit large differences in S_Z values compared to spots 3, 4, and 5 (not shown in the figure) despite very similar S_a and S_q values. The 3D reconstructed images recorded at different surface locations, Figure 4.15, still show preferential etching on different grains and at grain boundaries. This could indicate that the dissolution rates at specific areas vary with time. Grains experiencing lower corrosion rates could be in the initial stages of roughening. Spots 3 and 4 highlight this initial roughening stage which has areas with deep penetration across the surface that seem to have coalesced. These corroded areas, when contrasted with the areas with the highest elevation are responsible for the large S_z values. It is possible that these areas contain grains where the formation of CuCl and its subsequent dissolution is slower compared to other spots on the surface. The apparent coalescence of corroded sites could represent lateral dissolution of a thick layer of CuCl that has not yet dissolved into $CuCl_2$ due to the slow reaction rate. The apparent coalescence of corroded locations also suggests that the corrosion reaction progressed more slowly with depth allowing more rapidly corroding adjacent sites to catch up. This suggests that roughening is limited by the reaction rate (based on grain orientation) of the formation and subsequent dissolution of CuCl making it look like corrosion was proceeding laterally.

4.6 Summary and Conclusions

Table 4.6. Average roughness parameter values recorded in all charging experiments in 1 M NaCl with associated differences from pre-experiment values (dfpe)

Charging current (µA)	1000	500	250	250	250	75
Time (h)	0.93	3.04	7.56	7.56	7.56	25.1
Q (C)	3.1	5.5	6.8	6.8	6.8	6.8
Atmosphere	Anaerobic chamber	Anaerobic chamber	Anaerobic chamber	Ar sparge	Ar sparge	Ar sparge
S_a (µm) avg dfpe	0.4	2.0	2.1	0.8	1.0	2.1
S_a (µm) avg	1.0	2.4	2.6	1.2	1.4	2.6
S_q (µm) avg dfpe	0.4	2.6	2.9	1.0	1.3	3.4
S_q (µm) avg	1.3	3.1	3.5	1.6	1.8	4.0
S_z (µm) avg dfpe	0.6	21.6	26.7	7.1	9.7	44.8
S_z (µm) avg	11.0	28.6	33.8	14.4	14.8	52.0

Table 4.6 provides the S-value averages and their associated differences for all the charging experiments in the anaerobic chamber and on the benchtop with Ar sparging. The results suggest that overall dissolution is time-dependent rather than CC dependent. However, in the anaerobic

chamber it appears that the results are slightly more CC dependent than on the benchtop. This is because the roughness values increase with total charge, and despite not getting the full charge, the S-values after applying 500 µA CC are very close to those produced after applying 250 µA CC. The benchtop experiments favor time-dependent dissolution since the application of 75 µA CC produced more dissolution than either of the experiments in which 250 µA CC was applied. This shift suggests that this change was due to the presence of O_2 in the solution or the convection caused by Ar sparging.

It is important to note that the deeply penetrated areas observed after the application of 75 µA CC are not observed at higher applied currents. Therefore, it is possible that the dissolution rate of CuCl is very close to the rate of its formation rate at this applied current. Under these conditions thickening of the CuCl layer would be limited and the differences in dissolution rates of individual grains with distinct orientations more prominent. Additional support for this type of mechanism will be presented in later sections.

Since the dissolution at maximum experimental duration, corresponding to the application of 75 µA CC, produced dissolution similar to the application of 250 µA CC in the anaerobic chamber the shorter experimental length (7.56 hours) was designated as the maximum experimental length for Chapters 5 and 6. The S_z values produced by the application of 250 µA CC seems more reasonable for smaller samples, such as the 50 µm diameter electrodes used with the G3 I3 PCBs.

Ideally these charging experiments will be performed for each groundwater anion individually and then performed with binary and ternary solutions. Based on other work, the influence SO_4^{2-} on the behaviour of Cu is important because it is considered to have the opposite effect of Cl^- in the active dissolution regime.[15] However, SO_4^{2-} is present in much smaller quantities than Cl^-, and it has been shown that when all three groundwater anions are present in solution the net effect is the promotion of dissolution of Cu.[16] HCO_3^-/CO_3^{2-} is well known pH buffer that can promote passive film formation, therefore it is not necessary to include it in further experiments as long as the pH can be controlled.[17] However, a separate study could be performed to ensure HCO_3^-/CO_3^{2-} does not have a specific influence on corrosion behaviour and to verify the impact of pH at near neutral and basic values.

4.7 References

---

1. Huttunen-Saarivirta, E.; Rajala, P.; Bomberg, M.; Carpén, L. EIS Study on Aerobic Corrosion of Copper in Ground Water: Influence of Micro-organisms. *Electrochim. Acta.* **2017,** 240, 163-174.

2. Standish, T.; Chen, J.; Jacklin, R.; Jakupi, P.; Ramamurthy, S.; Zagidulin, D.; Keech, P.; Shoesmith, D. W. Corrosion of Copper-Coated Steel High Level Nuclear Waste Containers under Permanent Disposal Conditions. *Electrochim. Acta.* **2016,** 211, 331-342.

3. Muller, H.R.; Garitte, B.; Vogt, T.; Kohler, S.; Sakaki, T.; Weber, H.; Spillmann, T.; Her- ¨ trich, M.; Becker, J.K.; Giroud, N.; Cloet, V.; Diomidis, N.; Vietor, T. Implementation of the Full-Scale Emplacement (FE) Experiment at the Mont Terri Rock Laboratory. *Swiss J. Geosci*. **2017**, 110 (1), 287–306.

4. Giroud, N.; Tomonaga, Y.; Wersin, P.; Briggs, S.; King, F.; Vogt, T.; Diomidis, N. On the Fate of Oxygen in a Spent Fuel Emplacement Drift in Opalinus Clay. *Appl. Geochem.* **2018,** 97, 270–278.

5. Tomonaga, Y.; Giroud, N.; Brennwald, M.S.; Horstmann, E.; Diomidis, N.; Kipfer, R.; Wersin, P. On-Line Monitoring of the Gas Composition in the Full-Scale Emplacement Experiment at Mont Terri (Switzerland). *Appl. Geochem.* **2019**, 100, 234–243.

6. Tomonaga, Y.; Wersin, P.; Kipfer, R. *Understanding the Evolution of the Gas Composition in the Full-scale Emplacement Experiment (Mont Terri, Switzerland)*. Technical Report NAB-19-36, Nagra, Wettingen, Switzerland, **2019**.

7. Kelly, R. G.; Scully, J. R.; Shoesmith, D. W.; Buchheit, R. G. Electrochemical Thermodynamics and Kinetics of Relevance to Corrosion. *Electrochemical Techniques in Corrosion Science and Engineering;* Marcel Dekker Inc: New York, 2002; pp 4-6.

8. *Design, Production, and Initial State of the Canister;* TR-10-14; SKB: Stockholm, Sweden, 2010; pp 55.

9. Butler, I.B.; Schoonen, M. A. A.; Rickard, D. T. Removal of Dissolved Oxygen From Water: A Comparison of Four Common Techniques. *Talanta.* **1994**, 41, 211-215.

10. Lide, D. R. *CRC Handbook of Chemistry and Physics.* 1st ed. CRC Press: Boca Raton, 2005; pp 8-24.

11. King, F.; Hall, D. S.; Keech, P. G. Nature of the Near-Field Environment in a Deep Geological Repository and the Implications for the Corrosion Behaviour of the Container. *Corros. Eng. Sci. Techn.* **2017,** 52, 25-30.

12. King, F.; Lilja, C.; Pedersen, K.; Pitkanen, P.; Vähänen, M. *An Update of the State-of-the Art Report on the Corrosion of Copper Under Expected Conditions in a Deep Geologic Repository*. Technical Report SKB-TR-10-67, Svensk Karnbränslehantering AB, **2010**.

13. Soares, D. M.; Wasle, S.; Weil, K. G.; Doblhofer, K. Copper Ion Reduction Catalyzed by Chloride Ions. *J. Electroanal. Chem.* **2002,** 532, 353-358.

14. Starosvetsky, D.; Khaselev, O.; Auniat, Y.; Ein-Eli, A. Y. Initiation of Copper Dissolution in Sodium Chloride Electrolytes. *Electrochim. Acta.* **2006,** 51, 5660-5668.

15. Cong, H.; Michels, H. T.; Scully, J. R. Passivity and Pit Stability Behaviour of Copper as a Function of Selected Water Chemistry Variables. *ECS. Transactions.* **2009,** 16 (52), 141-164.

16. Qin, Z.; Daljeet, R.; Ai, M.; Farhangi, N.; Noël, J. J.; Shoesmith D. W.; King F.; Keech, P. The Active/Passive Conditions for Copper Corrosion under Nuclear Waste Repository Environment. *Corros. Eng. Sci. Techn.* **2017,** 52, 45-49.

17. Ochoa, M.; Rodriguez, M.A.; Farina, S.B. Corrosion of High Purity Copper in Solutions Containing NaCl, Na_2SO_4, and $NAHCO_3$ at Different Temperatures. *Proc. Mat. Sci.* **2015,** 9, 460-468.

5. Determining the Roughening Pattern of Copper Coupons Immersed in Groundwater Solutions

5.1 The Rationale for Immersing Coupons in Solution to Study Roughening

Corrosion is a natural process that can occur slowly or rapidly depending on the system. When corrosion is studied using electrochemical methods, it is often artificially accelerated, which does not necessarily represent the natural process.[1] One of the biggest challenges in electrochemistry is making potential- or current-controlled experiments relatable to measurements at the corrosion potential (E_{corr}). It can be rationalized that experiments using potentiodynamic or galvanodynamic conditions are accelerated versions of measurements at E_{corr}.[1] However, the conditions prevailing in potential- or current-controlled experiments are commonly unachievable under natural conditions because they only represent unique, often worst case scenarios, which ignores the limits which constrain measurements at E_{corr}.[2] In immersion experiments, results are obtained at E_{corr}, therefore providing insights into trends in the corrosion process.

Immersion samples could also confirm the expectations based on the results from the active/passive map studies in Chapter 2 where the potential was scanned after an E_{corr} measurement, but surface analysis was not feasible due to sample design. Immersion samples would allow exploration of surface damage which is expected to be general roughening under DGR conditions. The exploration of DGR conditions includes determining whether surface roughening due to corrosion is observable on short time scales and how this is influenced by the combined or singular influences of the groundwater ions. Roughness measurements on immersed samples can also provide information on the usefulness and viability of using Cl^--based solutions to roughen the PCB MEAs to obtain useful measurements which will be discussed in Chapter 6.

Immersion samples were used to track the corrosive roughening of Cu in conditions representative of the DGR and to find an exposure solution that will corrode the PCB MEAs at a reasonable rate thereby providing samples for analysis. If it is possible to track Cu roughening, the goal is to analyze the damage pattern and geometry. During galvanostatic experiments (Chapter 4), a constant current was applied to Cu in Cl^- solutions. This caused apparent preferential etching at different grains over the course of an experiment along with the rapid establishment of steady-state potentials. Therefore, if corrosion under immersion conditions proceeds in a similar manner to that observed with galvanostatic charging (Chapter 4), the duration of experiments will be crucial to analyzing roughening trends. It is possible that preferential grain dissolution is due to higher energy edges or dislocations in the bulk of the Cu. This selective grain dissolution led to a general roughening of the whole surface which was less uniform than expected.

An additional goal of immersion experiments is to determine if it is possible to produce corrosive roughening on Cu similar to the patterns obtained from galvanostatic steady-state polarization. If the damage is the same in both accelerated and non-accelerated scenarios, then it may be possible to develop a quantitative model describing the evolution of surface damage. This model could apply to long-term scenarios with limited variance and allow the extrapolation of damage evolution over the DGR time scale. To achieve this, it is necessary to demonstrate a valid link between solution composition and damage patterns.

5.2 Experimental Procedure

All immersion experiments were conducted in a similar manner. The SKB Cu coupons were ground up to p1200 grit with SiC papers. Afterwards, each coupon was washed with type-1 water with a resistivity of 18.2 MΩ cm, quickly dried with a steady stream of Ar, and then weighed on an analytical balance. If the coupon was to be used that day it was quickly transferred into its cell: if not, it was stored in an anaerobic chamber with an Ar atmosphere with less than 0.1 ppm O_2. Once a coupon was ready for usage it was placed into its cell, which was then quickly filled with solution while Ar sparging was initiated. Coupons were placed opposite to the sparging tube to avoid the attachment of bubbles to the coupon surface. The cell was covered with parafilm for the duration of the experiment after it was filled with solution and Ar sparging was initiated. If any E_{corr} measurements were to be performed, they were initiated after the cell was covered with parafilm.

After the designated immersion time, samples were removed using Teflon-coated tweezers to avoid scratching the surface. The sample was then rinsed with type-1 water, dried with a steady stream of Ar, weighed, and measured with a caliper, if necessary. If analysis was to be done the day an experiment finished, the sample was placed in a vacuum transfer box and taken to Surface Science Western for optical microscopy. If analysis was delayed to a later day, the sample was stored in the anaerobic chamber. An additional step was added to later experiments; the placement of a Cu wire sensor in the solution to obtain E_{corr} data. The sensor was a piece of Cu wire manufactured by Goodfellow that was ground to a p1200 grit finish to remove its outer insulating coating. The wire was placed into the cell during sparging and the addition of electrolyte. A SCE reference electrode was also placed in the cell at the same time. This electrode was calibrated versus a master SCE reference electrode (+241 mV vs saturated hydrogen electrode (SHE)) maintained for this purpose and considered acceptable if it measured within ± 5 mV of the master SCE in saturated KCl solution before and after experiments lasting 20 minutes.[3]

5.3 Materials

All immersion experiments were conducted using 1 cm x 1 cm x 1 cm coupons cut from a block of Cu supplied by Svensk Kärnbränslehantering AB (SKB). The copper contains >99.99% Cu, <5 ppm O and 30-100 ppm P, and is designated as O_2-free and P-doped.[4] Coupons were ground to p1200 grit using SiC grinding paper on a polishing wheel. Solutions were made using H_2O with a resistivity of 18.2 MΩ cm. Experiments were conducted in a 250 mL electrochemical glass cell that was covered with parafilm and sparged with Ar. Sparging with N_2 creates an O_2-limited environment containing <0.5 ppm O_2 at initial sparging and down to <0.3 ppm at times of 30 minutes and onwards.[5] Ar sparging is considered to be comparable to N_2 in this respect since the atomic mass is higher and Ar is available at comparable purities. The higher atomic mass also allows for easier maintenance of the effective headspace in the event of exposure to large quantities of air.

5.4 The Phases of Immersion Experiments

Immersion experiments were performed in two phases. The first phase was performed in solutions containing the groundwater ions Cl^-, SO_4^{2-}, HCO_3^-/CO_3^{2-} in unary, binary or ternary solutions designed to promote active dissolution. Optical microscopy was performed before and after experimentation to track any potential surface changes. In the event the roughening was minimal, the dimensions of the coupon were measured using calipers before and after immersion. All immersions were performed in Ar-sparged environments to avoid oxide formation. Ar sparging also more accurately simulates DGR conditions, since it is expected that, in the DGR, all the O_2

would be consumed quickly. This phase focused on determining whether solutions containing a minimal amount of O_2 would produce observable damage.

The second phase of experiments was focused on corroding coupons using an alternative oxidant while limiting O_2, with groundwater ions such as Cl^- present for complexation. This involved simulating damage patterns similar to those produced by galvanostatic charging, while eliminating the external controlling influence of an applied current. To achieve this, E_{corr} needed to be at a value similar to the steady-state potential observed during galvanostatic experiments on Cu in 1 M NaCl solutions (Chapter 4). To ensure this, solutions were designed to contain some DGR elements such as Cl^- but with the pH and added oxidant concentration adjusted.

5.5 Phase 1 Experiments

5.5.1 The Influence of Cl^- on Mass Loss

In phase 1, specimens were exposed for various durations in 1 M NaCl solutions (at an unadjusted pH) to test the effect of time on dissolved mass. Exposure periods of 2, 4, 6, and 24 hours were performed.

Table 5.1. Mass loss measurements for 1 cm x 1 cm x 1cm coupons immersed for various lengths of time in 1 M Cl^-.

Solution	Hours of immersion	Mass Before (g) ±0.0001 g	Mass After (g) ±0.0001 g	Mass Change (g) ±0.0001 g
1 M NaCl	2	8.8865	8.8864	-0.0001
1 M NaCl	4	8.8672	8.8675	0.0003
1 M NaCl	6	8.8976	8.8976	0.0000
1 M NaCl	~24	8.8748	8.8747	-0.0001
1 M NaCl	~24	8.8713	8.8708	-0.0005

In Table 5.1 the mass losses for each coupon indicate minimal amounts of detectable corrosion with the values being close to the detection limit, regardless of exposure time. This suggests a very low corrosion rate and, hence, only minor surface roughening, as expected for Cu in neutral media.[6] No visual change was observed on the coupons after each experiment. Since minimal mass change was recorded, the duration for immersion experiments was chosen to be ~24 hours. This time was chosen to promote more damage and for experimental convenience (preparation, clean up and analysis) with minimum exposure to the outside environment. pH values of 5 and 8 were used as slightly acidic and basic environments, respectively.

Table 5.2. Mass loss measurements for 1 cm x 1 cm x 1 cm coupons immersed for various lengths of time in 1 M Cl^{-}

Solution	Immersion time (h)	pH	Mass Before (g) ±0.0001 g	Mass After (g) ±0.0001 g	Mass Change (g) ±0.0001 g
1 M NaCl	22	8	8.8223	8.8219	-0.0004
1 M NaCl	23	8	8.8146	8.8156	0.0010
1 M NaCl	24	8	8.8240	8.8237	-0.0003
1 M NaCl	23	5	8.7340	8.7340	0.0000
1 M NaCl	23	5	8.7817	8.7813	-0.0004
1 M NaCl	23	5	8.7690	8.7691	0.0001

Table 5.2, much like Table 5.1, indicates there is only minimal mass change in the samples. Visual inspection shows the coupons still appear freshly ground. Therefore, in Cl^{-} based solutions with Ar sparging, mass loss and surface roughening are both minimal. This implies the reaction occurring is slow or negligible within the timescale chosen for the experiments.

5.5.2 Multiple Groundwater Anion Solutions

Table 5.3 shows similar results are obtained in binary and ternary solutions similar to those used in the determination of active and passive regions in Chapter 2. Also, experiments conducted in 1 M Cl^- solutions at pH values of 4 and ~1.25 showed similar minimal mass losses, as illustrated in Figure 5.1.

Table 5.3. Mass loss measurements for 1 cm x 1 cm x 1 cm coupons immersed for various lengths of time in various groundwater ion solutions determined to promote active dissolution (determined in the active/passive behaviour work).

Solution	Immersion time (h)	pH	Mass Before (g) ±0.0001 g	Mass After (g) ±0.0001 g	Mass Change (g) ±0.0001 g
1 M NaCl + 0.01 M Na_2SO_4	23	9	8.8081	8.8079	-0.0002
0.01 M NaCl + 0.01 M Na_2SO_4	19	8.5	8.7926	8.7926	0.0000
0.1 M NaCl, 0.01 M Na_2SO_4, $3x10^{-4}$ M $NaHCO_3$	21	7.65	8.8626	8.8626	0.0000

Figure 5.1. Images of coupons immersed in Ar sparged pH 4, 1 M NaCl for 19 hours (left) and 1 M HCl for 21 hours (right)

Overall, these results indicate that solutions with limited O_2, acidic pH and containing groundwater ions will lose 0.0204 mm^3/year of Cu. Since the experimental Cu coupons have 5 reactive surfaces with surface areas of 1 cm^2, this amounts to a corrosion rate (assumed to be uniform) of 40 μm/year. This minimal amount of corrosion makes the study of surface roughening difficult. It is possible that with more sensitive measuring techniques the damage could be analyzed under these conditions: however due to the availability, convenience and practicality of techniques confocal laser scanning microscopy (CLSM) combined with optical microscopy was used.

5.6 Phase 2 Experiments

5.6.1 *The Potential Buffer*

In order to corrode Cu in O_2-limited environments, an alternative oxidant was used. The alternative oxidant chosen had no side reactions with the groundwater ions, corrosion products or the metal itself. The solution was also able to maintain its redox properties over the desired period of immersion. The oxidant was selected from a table of standard reduction potentials based on its reduction potential. Our criterion for a viable redox pair was that it must enforce a potential close to the steady-state potential achieved in the galvanostatic experiments on Cu in 1 M NaCl (Chapter 4). In this case the steady-state potential was determined to be -120 mV(SCE). The redox pair that fits this criterion best was Cu^{+}/Cu^{2+}.

$$Cu^{2+}_{(aq)} + e^{-} \rightarrow Cu^{+}_{(aq)} \qquad [5.1]$$

[5.1] has a standard reduction potential (E^{o}_{red}) of 160 mV(SHE).[3] This value was converted to -84 mV(SCE). This converted value is ~ 40 mV below the steady-state charging value. Using the Nernst equation[2]

$$E_{cell} = E^{o}_{cell} - \frac{0.0592V}{n} . \log Q \qquad [5.2]$$

in which n=1 and Q is given by

$$Q = \frac{a_{red}}{a_{ox}} = \frac{[Red]}{[Ox]} = \frac{[Cu^{+}]}{[Cu^{2+}]} \qquad [5.3]$$

for the overall reaction

$$Cu^{2+}_{(aq)} + Cu_{(s)} \rightarrow 2\,Cu^{+}_{(aq)} \qquad [5.4]$$

The potential of the solution containing the Cu ions can be adjusted to -120 mV(SCE), E^{o}_{cell} in [5.2] was the value from [5.1] (-84 mV(SCE)). Since the reaction has only a one electron transferred, n = 1, and Q was the ratio of $Cu^{+}:Cu^{2+}$ shown in [5.3], a $Cu^{+}:Cu^{2+}$ ratio of 4.05:1 was calculated. If the ratio were any larger than this, which was the case for many other redox couples it would be difficult to accurately prepare the solution. The accuracy is dependent on the solubility of the Cu compounds used at the desired pH. If the solubility is low, it can be made irrelevant to a degree by creating a large volume of solution, or by adjusting the pH of the solution. Therefore, the most ideal scenario is to have a ratio that is fairly close so that if either compound has low solubility it can be offset by the volume or a change in pH. Oxidants added to the solution must be Cu compounds that either contain an anion present in the groundwater or add unreactive spectator anions. Therefore, CuCl and $CuCl_2$ were used to prepare the potential buffer solutions. $CuCl_2$ is readily dissolved in water. However CuCl has limited solubility at neutral and basic pH values.[7] To circumvent this issue, HCl was added to adjust the pH of the solution to a range where CuCl is fully soluble without changing the solution volume or amount of CuCl/$CuCl_2$ needed.

Although acidic pH values were shown to have no significant impact on Cu corrosion in the absence of O_2, the effect of pH was monitored. Three main criteria were used to design a viable solution. The first criterion was that the solution must have the 4.05:1 ratio of Cu^+:Cu^{2+}. The second criterion was that the solutions used should not require a series of dilutions to achieve the desired concentration. This is because dilution will lower the amount of Cu ions available to oxidize the reactive Cu surface therefore, reducing the buffering and oxidation strength of the solution. It is also possible that the solution transfer between containers during dilutions may cause unwanted oxidation of CuCl which would cause the Cu ion ratio and potential buffer capacity to be incorrect. The third criterion was that the solution must be acidic enough to fully dissolve the CuCl. Within these criteria there are many viable CuCl/$CuCl_2$ concentration combinations. Therefore, following the three main criteria the values of 0.03 M CuCl and 0.0074 M $CuCl_2$ (0.0374 M total [Cu] ions) were arbitrarily chosen from the range of viable concentrations. The solutions prepared were supplemented with 1 M or 2 M HCl spikes of 1-10 mL for adjusting pH and the remaining volume was filled with 1 M NaCl. The [Cl^-] of the solution was determined to be ~1 M.

5.6.2 pH 0 Immersion Experiments

The first solution made was the most acidic, substituting 1 M NaCl with 1 M HCl, resulting in a pH of ~ 0. Immersions were performed for 3 h, 8 h, and 25.1 h to approximately replicate the timescale of the 500 µA, 250 µA, and 75 µA galvanostatic charging experiments (Chapter 4), respectively. The main roughness parameters monitored were S_z, S_a, and S_q. S_z denotes the height difference between the highest and lowest points in the analyzed area. S_a is typically the parameter used to describe surface roughness, as it determines the difference in height for each point from the mean plane of reference in absolute terms. S_q is typically used to describe the standard deviation of S_a values.

Table 5.4. The roughness parameters measured at different locations and average values obtained by CLSM on a sample that was immersed in a pH 0 potential buffered solution for a time designed to replicate 500 μA galvanostatic charging experiments in 1 M NaCl

Immersion in pH 0, 0.0374 M [Cu] for 3 h						Average
Spot	1	2	3	4	5	
S_a (μm)	1.1	0.9	0.8	1.3	0.9	1.0
S_q (μm)	1.4	1.1	1.1	1.6	1.2	1.3
S_z (μm)	13.7	11.2	9.2	12.2	9.2	11.1

Table 5.4 shows that at pH 0, 3 hours of immersion of a Cu coupon in the potential buffered solution yields an average value of 1.0 μm for S_a, 1.3 μm for S_q and 11.1 μm for S_z. Figure 5.2 shows the 3D reconstructed images obtained by CLSM with the colours indicating the surface elevation at each point. Corrosion occurs at different rates on individual grains, with the red grains having the highest elevation. Large areas of the surface appear flat with features similar to polishing lines.

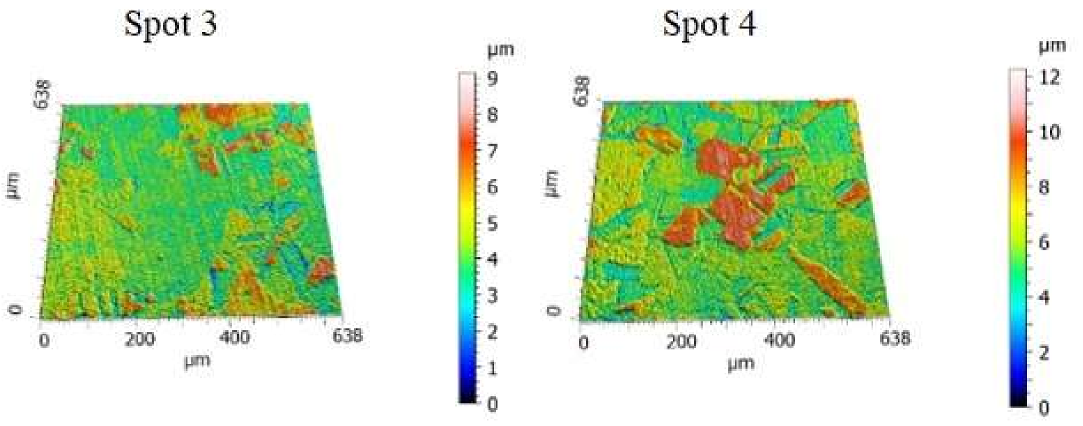

Figure 5.2. 3D reconstructed images of spots 3 and 4 on the Cu coupon after immersion in the pH 0 potential buffer for 3 hours

Table 5.5. The roughness parameters measured at different locations on a sample that was immersed in a pH 0 potential buffer for a time designed to replicate 250 μA galvanostatic charging experiments in 1 M NaCl

Immersion in pH 0, 0.0374 M [Cu] for 8 h						Average
Spot	1	2	3	4	5	
S_a (μm)	3.0	3.6	2.0	2.0	2.4	2.6
S_q (μm)	3.9	4.8	3.0	2.9	3.1	3.5
S_z (μm)	30.0	32.0	25.0	25.0	22.7	26.9

Table 5.5 shows that at pH 0, 8 hours of immersion in the potential buffer solution yields average values of 2.6 μm for S_a, 3.5 μm for S_q and 27.0 μm for S_z. Compared to the average S_z value from the 3-hour immersion, the height is increased by ~2.5 times. Figure 5.3 shows more distinct differences in corrosion between grains. Twins, grains common to SKB material, have become more distinct, while the features resembling polishing lines have disappeared.[8] However, the highest (least corroded) grains, which were mostly untouched after 3 hours of immersion, seem to be forming their own internal height differences. These are denoted by the red and white colour combinations indicating a possible sloping shape which could mean the surface is smoothing out or roughening further in these areas. It is likely that these higher regions have lower surface energies and less strain, which would lead to them corroding (roughening) more slowly, while the highly corroded grains possess higher energies or more stress.[9] It is possible that the different corroded areas possess similar surface energies at the end of the exposure period.

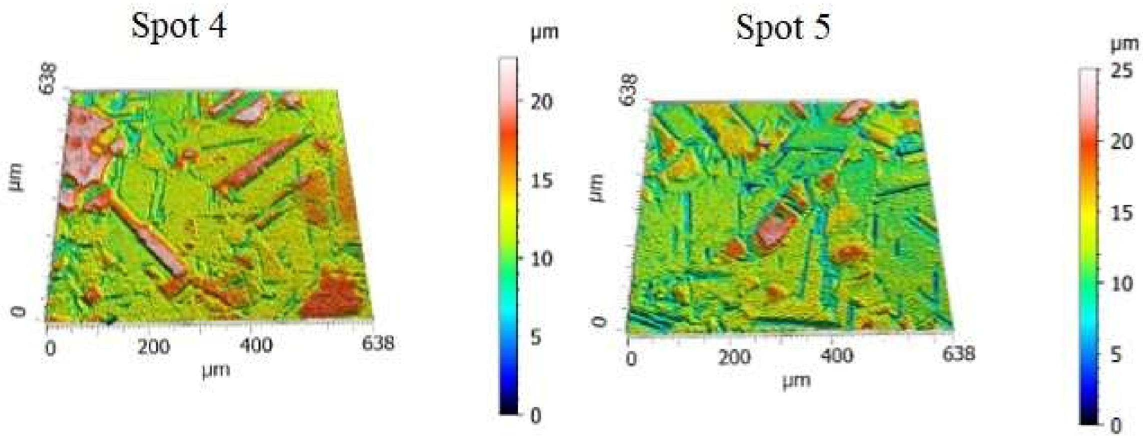

Figure 5.3. 3D reconstructed images of spots 4 and 5 on the Cu coupon after immersion in the pH 0 potential buffer for 8 hours

Table 5.6. The roughness parameters measured at different locations and average values obtained by CLSM on a sample that was immersed in a pH 0 potential buffered solution for a time designed to replicate 75 μA galvanostatic charging experiments in 1 M NaCl

Immersion in pH 0, 0.0374 M [Cu] for 25.1 h						Average
Spot	1	2	3	4	5	
S_a (μm)	4.3	4.5	5.2	4.8	5.3	4.8
S_q (μm)	5.5	5.7	7.0	6.1	6.9	6.2
S_z (μm)	44.0	47.0	57.0	44.0	58.0	50.0

Table 5.6 indicates that at pH 0, 25.1 hours of immersion in the potential buffer solution yields average values 4.8 μm for S_a, 6.2 μm for S_q and 49.8 μm for S_z. The roughness parameters indicate that the differences in corrosion rates across the surface have not increased to the degree expected. While the immersion time was nearly tripled from the 8-hour immersion, the S values have increased by only 75-85%. Comparatively, the difference in S-values measured between the 3 and 8 hour experiments yielded an average increase of 260% which is almost equivalent to the increase of immersion time (266%).

In Figure 5.4, the increase in height differences between grains is observable and consistent with more extensive corrosion. However, the higher, less corroded, grains are beginning to roughen, as indicated by the height differences of surrounding areas decreasing. Also, the more corroded grains have developed some contour. This suggests that after this exposure period when significant corrosion has occurred, the grains are beginning to corrode more evenly suggesting they may have become closer in surface energy. Despite these areas being possibly more uniform, there are still areas which have large height contrasts, which indicates that roughening is not as uniform as expected.

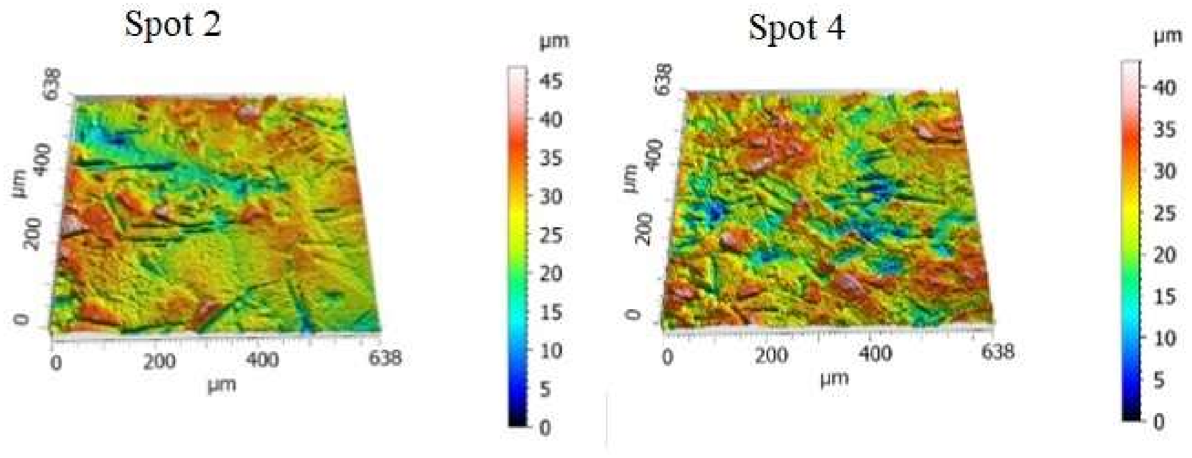

Figure 5.4. 3D reconstructed images of spots 2 and 4 on the Cu coupon after immersion in the pH 0 potential buffer for 25.1 hours

5.6.3 pH 1 Immersion Experiments

Table 5.7. The roughness parameters and average values obtained by CLSM on a sample that was immersed in a pH 1 potential buffered solution for a time designed to replicate 500 µA galvanostatic charging experiments in 1 M NaCl

Immersion in pH 1, 0.0374 M [Cu] for 3.77 h						Average
Spot	1	2	3	4	5	
S_a (µm)	0.71	0.94	1.0	1.2	0.95	0.96
S_q (µm)	0.88	1.3	1.4	1.5	1.2	1.3
S_z (µm)	8.0	11.8	12.7	15.0	10.3	11.6

To determine the influence of pH on the S-values, measurements were also performed in potential buffer solutions with pH values of 1 and 2. In these acidic environments, CuCl is still very soluble, which added the advantage of solution stability and integrity compared to near-neutral pH values. The length of experiment was adjusted to replicate the lengths of galvanostatic experiments used in Chapter 4. Table 5.7 shows S-values after 3.77 hours of immersion in the pH

1 potential buffer solution. The average roughness values were 0.96 µm for S_a, 1.3 µm for S_q and 11.6 µm for S_z. These values are very similar to those obtained in the 3-hour immersion in the pH 0 potential buffer, with the largest difference being 0.5 µm in S_z. Figure 5.5 shows the metal corrosion pattern after the 3.77 hour immersion, which is comparable to that obtained after the 3 hour immersion in the pH 0 potential buffer. The most notable difference is that the higher elevation (least corroded) grains were smaller in size and sparse in number. The low height (most corroded) areas remain flat and appeared much smoother which is confirmed by the low S_a values.

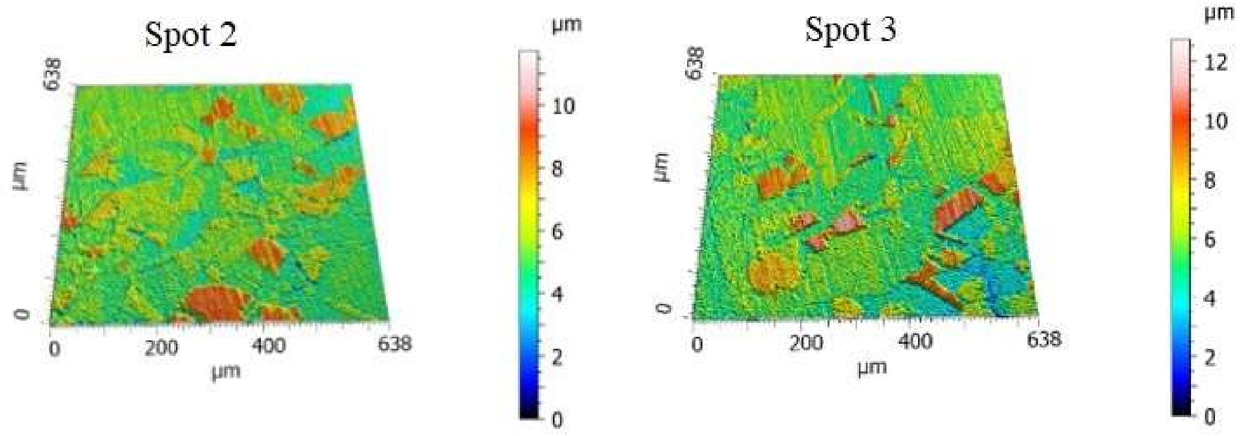

Figure 5.5. 3D reconstructed images of spots 2 and 3 on the Cu coupon after immersion in the pH 1 potential buffer for 3.77 hours

Table 5.8. The roughness parameters measured at different locations and average values obtained by CLSM on a sample that was immersed in a pH 1 potential buffered solution for a time designed to replicate 250 µA galvanostatic charging experiments in 1 M NaCl

Immersion in pH 1, 0.0374 M [Cu] for 7.56 h						Average
Spot	1	2	3	4	5	
S_a (µm)	1.8	2.1	3.1	2.0	1.9	2.2
S_q (µm)	2.4	2.9	4.2	2.8	2.7	3.0
S_z (µm)	19.0	26.0	31.0	23.0	24.0	24.6

Immersion in the pH 1 potential buffer solution for 7.56 hours yields slightly different results than immersion for 3.77 hours. Table 5.8 shows that the average values were 2.2 µm for S_a, 3.0 µm for S_q and 24.6 µm for S_z. The average values are slightly reduced compared to the pH

0 experiment of similar duration (8-hour immersion). This may reflect the lower solubility of Cu ions in pH 1 solution. However, spot 3 has corroded more than the other spots, as indicated by the S-values. Both of the 3D reconstructed images in Figure 5.6 display a similar corrosion trend seen after 8 hours of immersion in the pH 0 potential buffer, with the twins more apparent and the polishing-like features reduced. A feature of these images is that the lower height grains are split by areas that have dissolved faster, creating channel-like features across the surface. There are fewer minimally corroded (higher) grains which are, on average, much smaller than those seen after 3.77 hours of immersion. Another important feature of these reconstructions is that some of the higher elevation (slowly corroding) grains, which are coloured red and white, are corroding predominantly around the edge. However, if the grains are coloured only white it is possible they are corroding evenly.

The microstructure produced by corrosion in the potential buffer solution is similar to that produced by annealing after a few cycles of multidirectional forging (MDF). MDF annealing leads to the breakdown of high angle grain boundaries due to their high energy, causing the grain size to be reduced and reducing the surface energy.[10] The similarity in microstructure suggests that corrosion in the potential buffer solution also preferentially dissolves high energy grains to reduce the overall surface energy. Thus, the green or blue locations in the 3D reconstructed images were once higher energy grains that were preferentially corroded over the immersion period in the potential buffer.

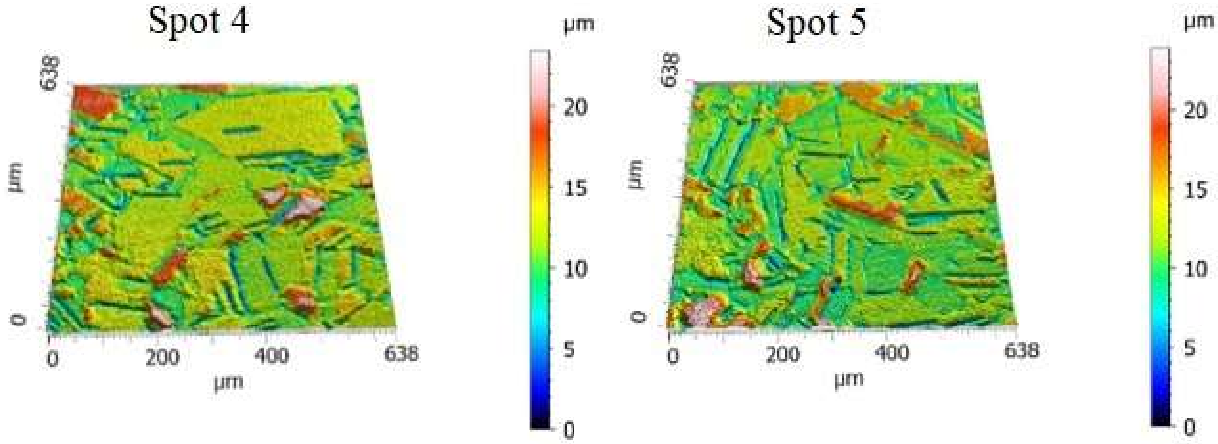

Figure 5.6. 3D reconstructed images of spots 4 and 5 on the Cu coupon after immersion in the pH 1 potential buffer for 7.56 hours

Table 5.9. The roughness parameters measured at different locations and average values obtained by CLSM on a sample that was immersed in a pH 1 potential buffered solution for a time designed to replicate 75 µA galvanostatic charging experiments in 1 M NaCl

Immersion in pH 1, 0.0374 M [Cu] for 25.1 h						Average
Spot	1	2	3	4	5	
S_a (µm)	4.3	3.2	5.1	3.8	4.0	4.1
S_q (µm)	5.7	4.3	6.7	5.1	5.6	5.5
S_z (µm)	43.0	41.0	49.0	45.0	47.0	44.6

After 25.1 hours of immersion in the pH 1 solution, the damage and average roughness parameters of the Cu are slightly reduced compared to the damage produced after 25.1 hours of immersion in the pH 0 solution. Table 5.9 shows average values of 4.1 µm for S_a, 5.5 µm for S_q and 44.6 µm for S_z. The 3D reconstructed images in Figure 5.7 show trends similar to the previous results produced after immersion in the pH 0 potential buffer solution for 25.1 hours. There are no longer any polish line-like features, the low height flat areas are separated by lower height channel features and the range of height values has increased drastically. The highest points are still dissolving, indicated by the presence of small patches of metal at maximum height (white areas) on top of high grains (red areas). This would suggest that by 25.1 hours of immersion the corrosion rate is decreased, due to either a local depletion of oxidant near the reactive surface, adsorbed surface species, or reaching the Cu ion buffer capacity which would distort the Cu ion ratio and change the buffer potential. The slight difference between the roughness parameters could be due to the decreased solubility of CuCl at pH 1, which could lead to precipitation of the solid that is easily oxidized or converted to $CuCl_2^-$/$CuCl_3^{2-}$ on the electrode surface.[11]

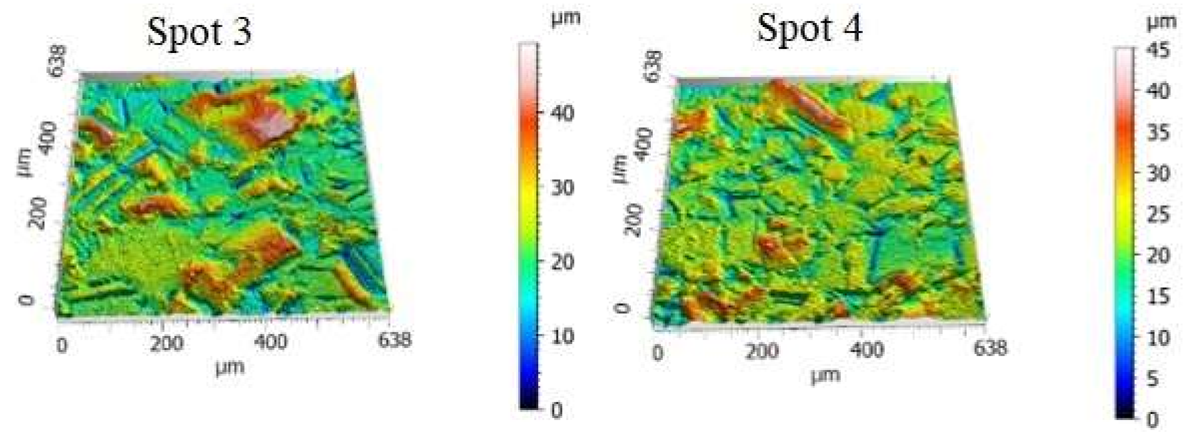

Figure 5.7. 3D reconstructed images of spots 3 and 4 on the Cu coupon after immersion in the pH 1 potential buffer for 25.1 hours

5.6.4 pH 2 Immersion Experiments

Table 5.10. The average roughness parameter values obtained by CLSM after immersion in a pH 2 potential buffered solution for times designed to replicate 75 µA, 250 µA and 500 µA galvanostatic charging experiments in 1 M NaCl

[Cu] (M)	0.0374	0.0374	0.0374
Time (h)	3.77	7.56	25.1
pH	2	2	2
S_a average(µm)	1.7	2.1	3.2
S_q average(µm)	2.1	2.7	4.2
S_z average (µm)	12.5	19.6	29.0

The aggregate S-values for immersions in pH 2 potential buffer solution are listed in Table 5.10. Compared to the values from the experiments at pH 1 and 0, immersion in the pH 2 potential buffer solution for 3.77-hour produced slightly higher values, while after 7.56 and 25.1-hours of immersion the values were significantly reduced. The S_a and S_q values from the 3.77-hour immersion are ~70% larger than their pH 1 and 0 counterparts, while the S_z value is only increased by ~10%. The 7.56-hour immersion produced S_a and S_q values similar to those of the pH 1 counterpart. However, the S_z values show a large decrease, about 5-7 µm, indicating that sample penetration depth can be independent of roughness. This conclusion also highlights that S_z, on its own, does not reflect general roughness but demonstrates the worst case scenarios on the surface regardless of the size of the feature that the value corresponds to.[12] With regard to a DGR, the S_z parameter is the most important since it identifies areas where the Cu coating would be most deeply corroded. If S_z is used as a rate indicator, then immersion in the pH 2 potential buffer for 7.56 hours has a corrosion rate that is ~30% lower than those measured at pH 0 and 1 for 7.56 hours.

The 3D reconstructed images in Figure 5.8 are similar to those obtained in the pH 1 experiments, and the damage does not indicate any slower or inhibited processes. The largest S-value discrepancy is highlighted by comparing all the 25.1-hour immersion values. In Table 5.10, the average values from the immersion in pH 2 potential buffer after 25.1 hours can be seen. These values are 3.2 μm for S_a, 4.2 μm for S_q and 29.0 μm for S_z, which are much lower than their lower pH counterparts. The S_a values produced by the immersion in pH 2 potential buffer for 25.1 hours were 1-2 μm lower than the S-values produced from similar immersions in pH 1 and 0 solutions, while the S_q values are ~2 μm lower. The S_z value produced from the longest pH 2 immersion shows the largest average difference of ~20 μm compared to S_z values produced from the longest pH 1 and 0 immersions. This is further highlighted when looking at the S_z difference between the longest pH 1 and 0 immersions, which is only 5.2 μm. This suggests that the corrosion rate during the immersion in the pH 2 potential buffer is lower than, or plateaus at a rate lower than, those measured in pH 1 and 0 immersions. This difference in rate could be attributed to the change in solubility of CuCl which would distort the Cu ion ratio of the buffer (and therefore change the potential), or enough of the Cu ions were consumed in the reaction which would also distort the Cu ion ratio (also changing the potential). It is also possible that the faster roughening rates lead to a local depletion of Cu ions at the reactive surface which is not easily replenished because the solution is stagnant. This idea is confirmed by the 3D reconstructions in Figure 5.8, which contain numerous grains with well-defined edges and many high grains that are slowly dissolving.

After evaluation of the results from immersion experiments performed with pH 0, 1 and 2 solutions a pH value range was chosen for potential buffer solutions prepared to be used in experiments using PCBs (to be described in Chapter 6). This range was between pH 1 and 2 which is due to the lower dissolution rate at longer immersion lengths compared to pH 0. This allowed for more controlled dissolution and subsequent analysis of corrosion over extended immersion periods.

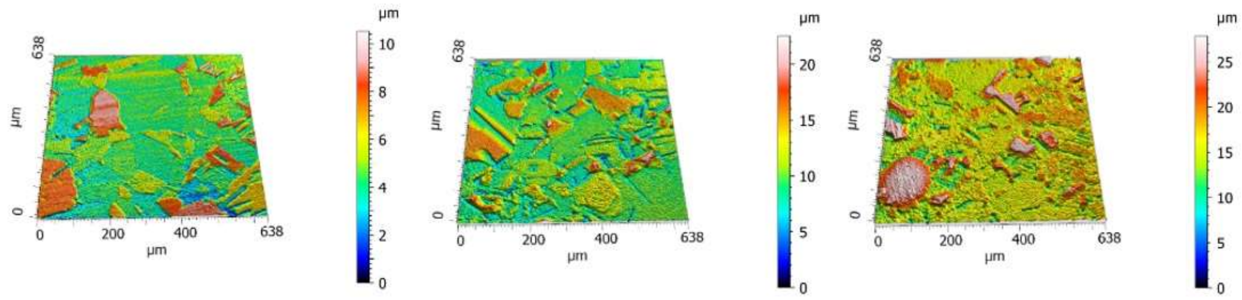

Figure 5.8. 3D reconstructed images of spots from the Cu coupon immersed in the pH 2 potential buffer for 3.77 hours (left image), 7.56 hours (middle image), 25.1 hours (right image)

5.6.5 As-made (AM) pH Experiments

Table 5.11. The roughness parameters measured at different locations and average values obtained by CLSM on a sample that was immersed in a pH AM potential buffered solution for a time designed to replicate 500 μA galvanostatic charging experiments in 1 M NaCl

Immersion in pH AM, 0.0062 M [Cu] for 3.77 h						Average
Spot	1	2	3	4	5	
Sa (μm)	0.43	0.48	0.40	0.42	0.39	0.42
Sq (μm)	0.55	0.60	0.52	0.54	0.49	0.54
Sz (μm)	9.7	8.2	6.7	6.7	6.0	7.5

This set of immersion experiments was performed at the as-made (AM) pH. No HCl was used to spike the solution. In this pH range the solubility of CuCl is greatly decreased, therefore the overall concentration of the buffer compounds was decreased accordingly These experiments were primarily performed to test how much corrosion occurs at reduced potential buffer concentrations. The first solution tested had a CuCl concentration of 0.005 M, a total [Cu] of 0.0062 M and the sample was immersed for 3.77 hours. This solution will be referred to as the 0.0062 M [Cu] potential buffer. Table 5.11 shows the roughness parameter values measured on this sample. It is evident from these values that minimal damage has occurred on the surface. The S_a and S_q values are 0.42 μm and 0.54 μm, respectively, which are values close to those measured on a freshly polished surface, as shown in the galvanostatic charging experiments (Chapter 4, Table 4.2). The optical image shown in Figure 5.9 shows some light damage on the coupon, especially in certain regions where it looks like the corrosion is just beginning however, it is very faint. This would indicate a low rate of corrosion, either due to the buffering potential, or a limit imposed by the decreased oxidant concentration, which lowers the concentration of available Cu ions in solution near the reactive surface.[13] Looking at the left image in Figure 5.10 it is hard to see significant height differences; therefore the S_z value is likely generated from extremely small surface features . However, the image on the right side a distinct corrosion pattern is emerging which indicates the early stages of the preferential corrosion of some grains. The presence of polishing lines across the surface gives the grains a fragmented appearance. Due to the low solubility of CuCl at neutral pH, it is possible that the CuCl is at or near saturation making the buffer ratio lower than its intended value. Such a change in the buffering potential would greatly reduce the damage done.

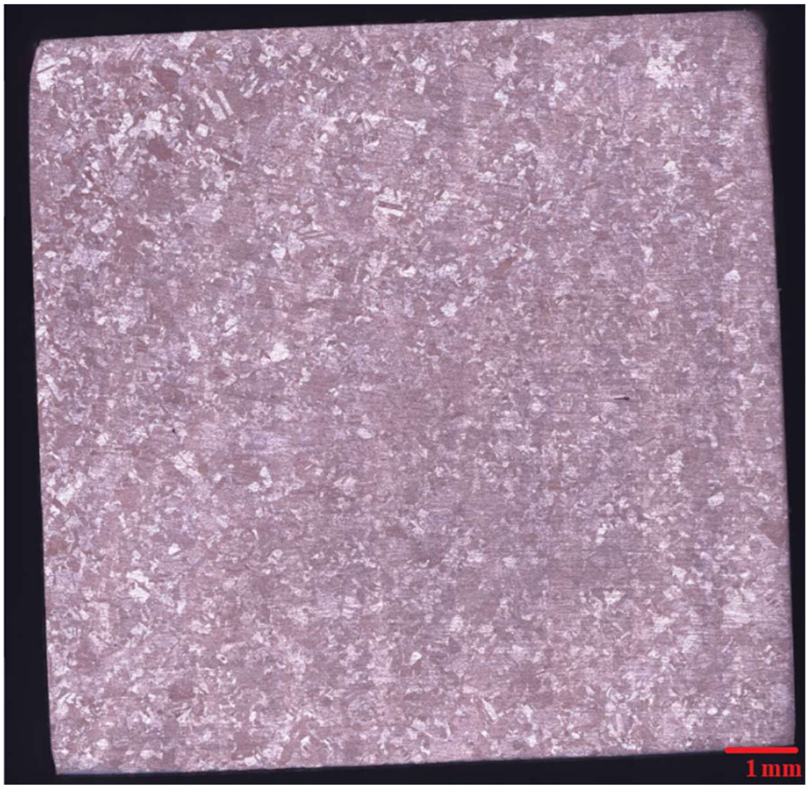

Figure 5.9. The optical image of side 1 of a 1 cm x 1 cm x 1 cm coupon after immersion in an AM pH 0.0062 M [Cu] potential buffer solution for 3.77 hours

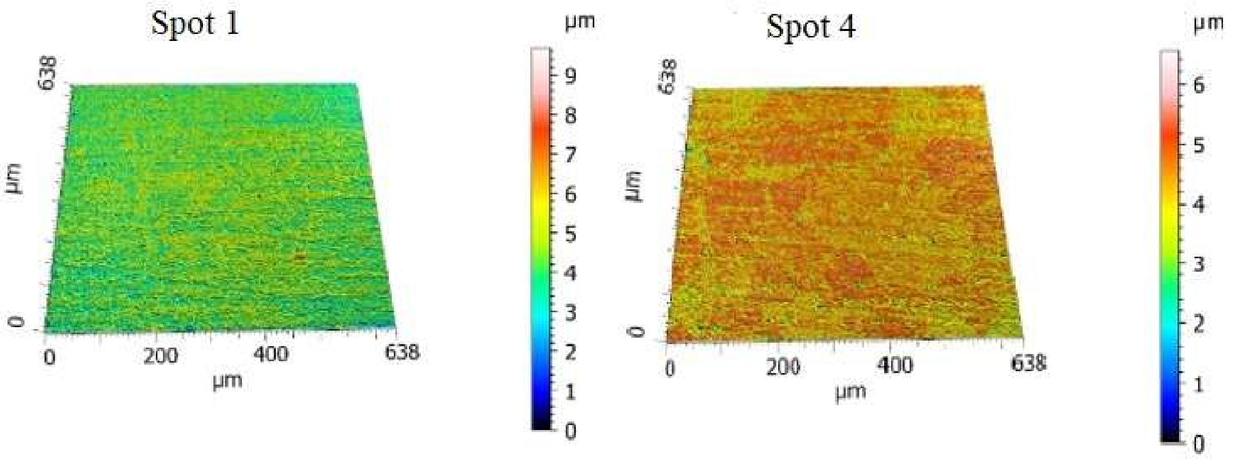

Figure 5.10. 3D reconstructed images of spots 1 and 4 on the Cu coupon after immersion in the 0.0062 M [Cu] pH AM potential buffer for 3.77 hours

Table 5.12. The roughness parameters measured at different locations and average values obtained by CLSM on a sample that was immersed in a second pH AM potential buffered solution for a time designed to replicate 500 µA galvanostatic charging experiments in 1 M NaCl

Immersion in pH AM, 0.0037 M [Cu] for 3.77 h						Average
Spot	1	2	3	4	5	
Sa (µm)	0.28	0.25	0.25	0.27	0.23	0.26
Sq (µm)	0.34	0.31	0.32	0.34	0.29	0.32
Sz (µm)	5.6	3.4	3.5	5.6	3.8	4.4

Another experiment at the AM pH was conducted for 3.77 hours with a concentration of 0.003 M CuCl and a total [Cu] of 0.0037 M. This solution will be referred to as the 0.0037 M [Cu] potential buffer. The total [Cu] was reduced to see if the buffer ratio could be maintained if there was less solid to dissolve. In the optical image in Figure 5.11, the beginning of preferential grain corrosion is suggested by the brightened areas to the left and right sides of the coupon. Table 5.12 shows that the decrease in oxidant concentration also decreases the extent of surface roughening. The presence of undissolved CuCl suggests saturation with Cu^+, and a decreased ratio of Cu^+:Cu^{2+}. This could lead to the precipitation of CuCl onto the Cu surface as corrosion progresses at a decreased corrosion rate.

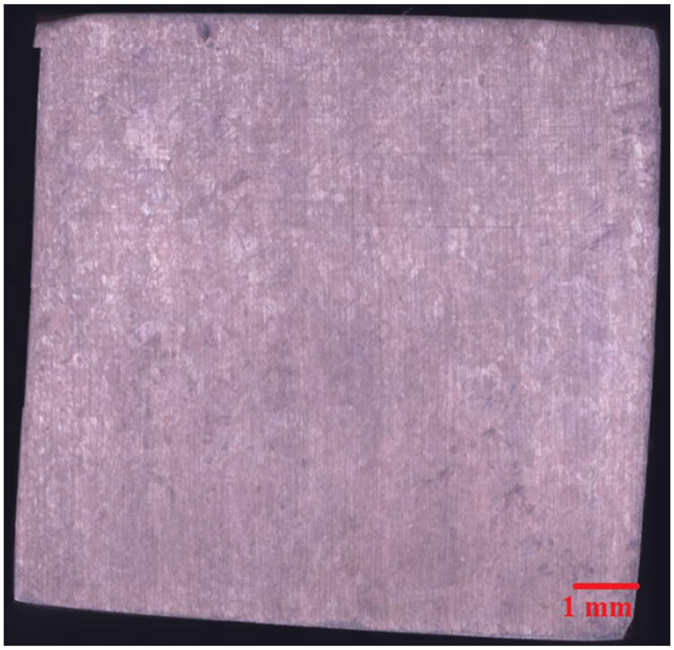

Figure 5.11. An optical image of side 1 of a 1 cm x 1 cm x 1 cm coupon immersed in 0.0037 M [Cu] potential buffer solution at AM pH for 3.77 hours. There was an issue with the image processing in the top left corner causing the corner frame image to be offset slightly, this could not be amended but it is insignificant with regards to analysis since it still displays the data but in a shifted position.

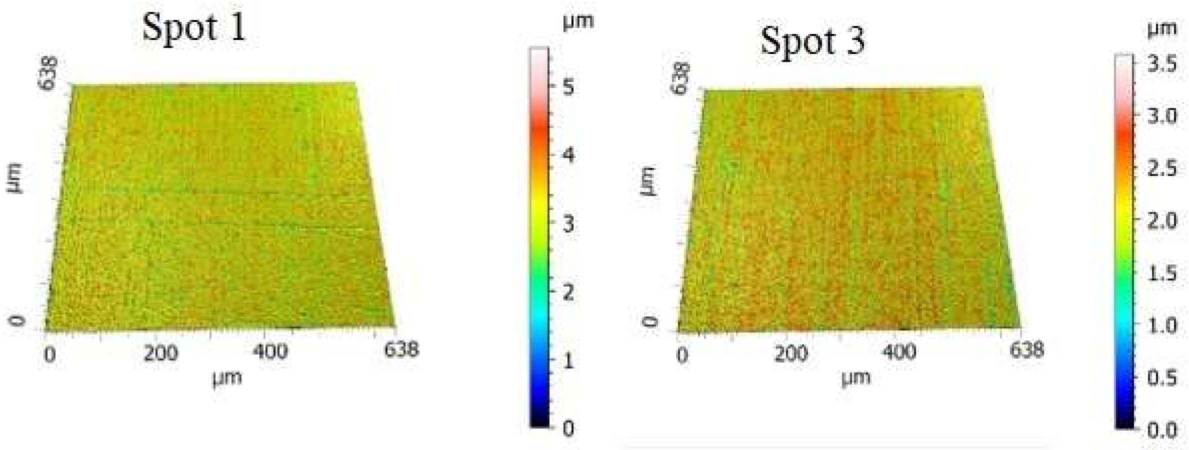

Figure 5.12. 3D reconstructed images of spots 1 and 3 on the Cu coupon after immersion in the AM pH 0.0037 M [Cu] potential buffer for 3.77 hours

A notable feature of this immersion experiment is that the average S_z, S_a and S_q values, 4.4 µm, 0.25 µm and 0.32 µm, respectively, show a 60% reduction compared to the sample immersed in the 0.0062 M [Cu] solution. The minimal corrosion is confirmed by confocal analyses which show a lack of visible preferentially dissolved grains and nearly uniform colour across the 3D reconstructed image surfaces in Figure 5.12. This indicates a slower corrosion rate compared to that produced by the experiment with the immersion in the 0.0062 M [Cu], which suggests this sample has roughened even less and could display the initial step in the roughening. The lack of preferential corrosion in these AM immersion experiments indicates that the corrosion rate is reliant on the oxidant concentration. A possible method for obtaining higher corrosion rates would be solution stirring or multiple immersions to avoid local concentration depletion.

Table 5.13. Corrosion rates for each immersion experiment using the 0.0374 M [Cu] potential buffer calculated from average S_Z values from each sample

Corrosion rates for 0.0374 M [Cu] immersion experiments (µm/year)			
Immersion time (h)	pH 0	pH 1	pH 2
3	32,300	34,000	36,800
8	29,600	27,000	21,700
25.1	17,400	15,600	10,100

The corrosion rates in Table 5.13 were calculated by taking the average S_Z value for each experiment and multiplying it by the exposure period. These rates are calculated irrespective of local oxidation depletion and do not factor in any change in rate over the course of time.

It is clear from the previous experiments in this chapter that pH influences the amount of damage on the Cu by affecting the ability of the solution to maintain the 4.05:1 ratio of Cu^{+}:Cu^{2+} needed to buffer the potential. As such, any damage occurring in neutral pH solution will also require more time, due to the decreased solubility of the oxidant. This is indicated by the corrosion rates shown in Table 5.13 as increasing the pH significantly lowers the corrosion rate especially at longer immersions compared to shorter immersions. Therefore, picking a higher concentration of the buffering compounds at a lower pH is more time efficient because of the increase in ability to maintain the buffering ratio, available oxidant and subsequently higher dissolution volumes. However, it should be noted that at the shorter immersion times the corrosion rates produced are anywhere from 2-3 times larger than a longer immersion will produce. This implies that the corrosion rate changes significantly over time as the oxidation reaction proceeds and the oxidant is depleted. These results emphasize and validate the first and third criteria used to design the initial solution which stated that the solution should have a Cu ion ratio of 4.05:1 of Cu^+:Cu^{2+} and that the solution should be acidic enough to easily dissolve CuCl. The buffering ratio of Cu ions is dependent on the pH of the solution; if either criterion is not met the corrosion rate will be reduced greatly. If a longer exposure is desired, the pH can be increased slightly to lower the corrosion rate. The pH could be increased up to neutral values (~7) but the Cu roughening rate would then be very slow and the amount of oxidant available will also be limited making it viable only for experiments where minimal dissolution is desired.

5.6.6 Buffering Potential Stability and Values

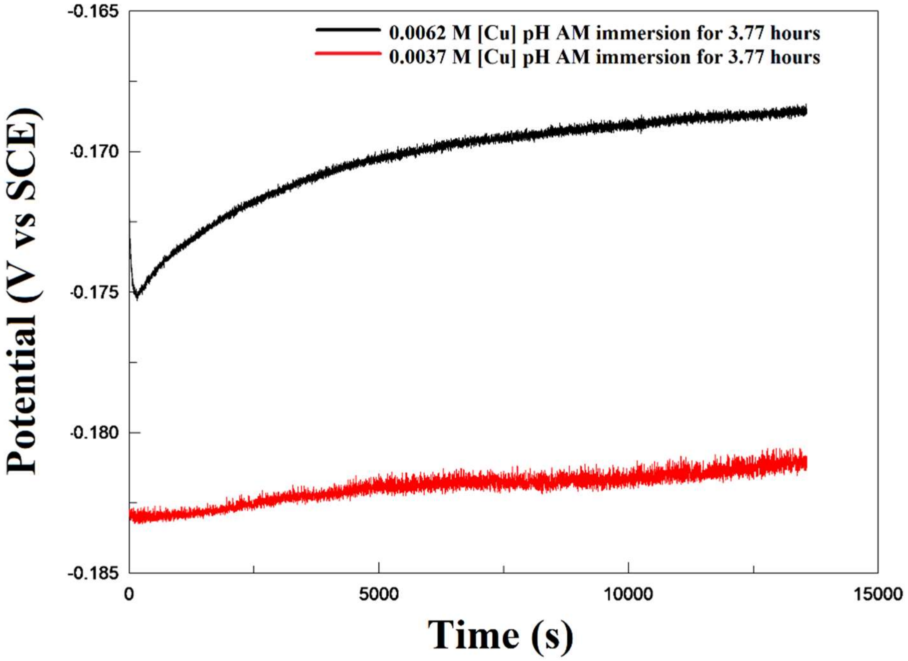

Figure 5.13. E_{corr} versus time measured on coupons immersed in either 0.0062 M or 0.0037 M [Cu] potential buffer solutions at AM pH

To demonstrate that the potential buffer solution functioned as desired, its buffering potential and stability over the course of an experiment was checked. The target buffering potential derived from the galvanostatic charging experiments (Chapter 4) used to design the potential buffer was -120 mV(SCE). A polished Cu wire and SCE reference electrode were placed in the immersion cell during experiments to measure the E_{corr}. Figure 5.13 shows that the AM pH solutions did not have the correct Cu ion ratio because the buffering potential was ~ -167 mV(SCE) and ~ -180 mV(SCE) for the 0.0062 M and 0.0037 M [Cu] solutions, respectively, almost 50-60 mV from the intended value. This supports the previous conclusion in 5.6.5 that the ratio of Cu ion concentrations was more accurate in the 0.0062 M [Cu] potential buffer than in the 0.0037 M [Cu] potential buffer. A series of dilutions would likely provide more accurate results for these solutions.

The E_{corr} values measured for the pH 1 and 2 solutions in Figure 5.14A show that the potential buffer is initially within +/- 10 mV of the intended range and remains there for all lengths of immersion. Both 25.1-hour immersion experiments, Figure 14C, have a region in which the potential plateaus at 65,000 seconds and then decreases slightly beyond 75,000 seconds, indicating that the corrosion rate decreases with exposure time. A decrease in corrosion rate would most likely be prompted by reaching the buffer capacity, or the saturation limit for Cu which would cause precipitation of Cu chlorides or oxides. These compounds could then either block the reactive surface (decreasing the reaction rate) or dissociate to replenish the Cu^{2+} concentration.

The potential response from the pH 1 potential buffer experiment in Figure 5.14C differs from the rest of the responses in Figure 5.14, showing a series of slow sequential potential decreases and no plateau as opposed to a rise in potential followed by a plateau. This indicates that the solution becomes less reliable over longer immersions, bolstering the case for using lower immersion times with the PCB MEAs. The fluctuation in potential cannot be attributed to a change in corrosion damage since the pH 1 7.56 hour and 25.1 hour experiments reach similar buffering potentials but the damage patterns and S-values are different. This implies that the duration of exposure is the main factor determining the amount of corrosion damage and the buffering potential does not have an impact on the damage within the potential range at which the Cu ion ratio is maintained. This is also confirmed by the potential response for the immersion in the pH 2 potential buffer solution for 7.56 hours, which reaches a steady state potential 12 mV lower than the rest of steady-state potentials in Figure 5.14 but the damage is not drastically different. Therefore, if the buffering potential remains within +/- 10 mV of the intended range, the difference in Cu corrosion rates is nearly negligible. In this range of potentials, time is the dominating factor for the degree of damage due to the similarity in corrosion rates which is indicated by the similar S-values. This is especially true for the shorter experiments where the potentials remain close to each other. The buffering potential can be used to determine the accuracy of the solution preparation and if the Cu ion ratio is maintained throughout an experiment.

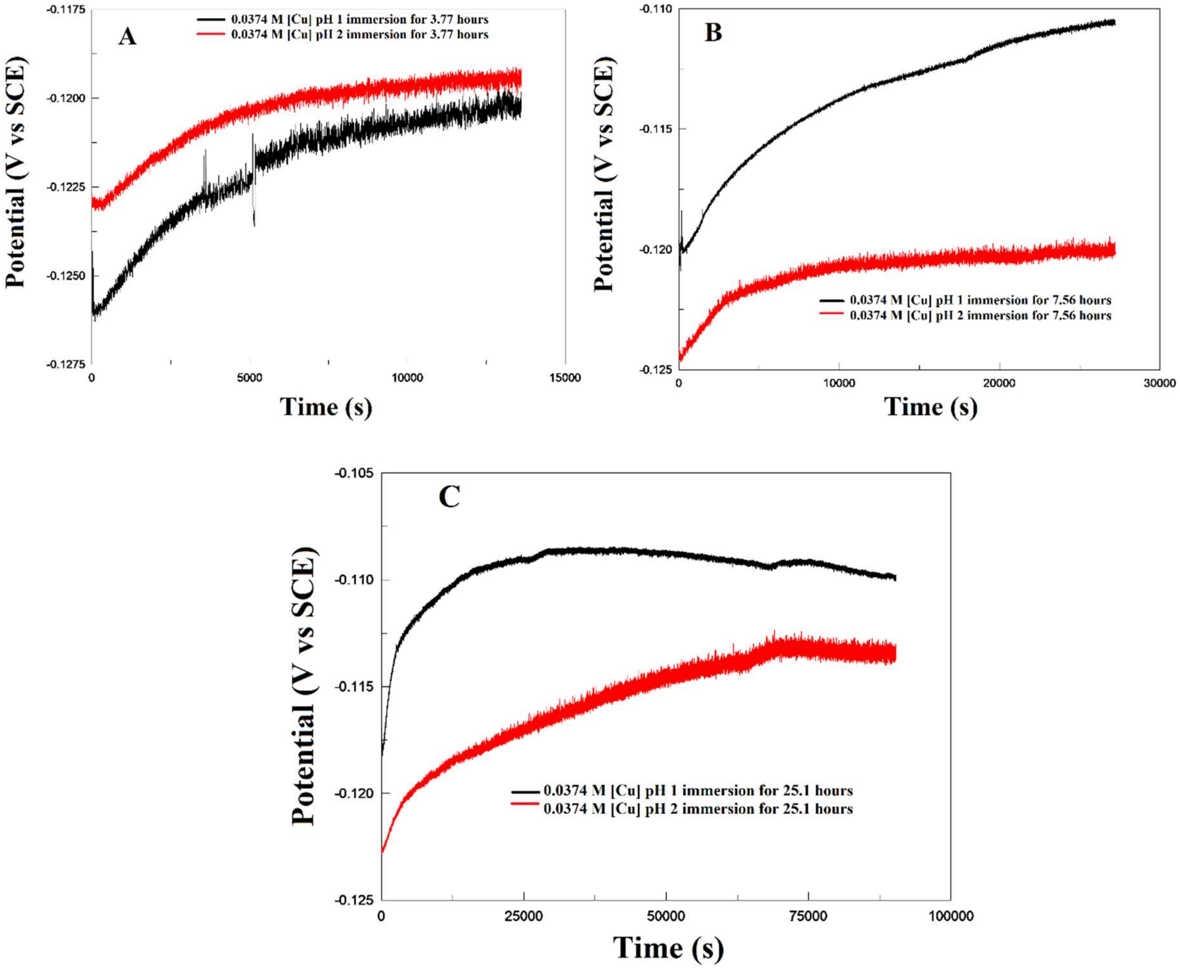

Figure 5.14. E_{corr} versus time on coupons immersed in the potential buffer solutions at pH 1 and 2 for various times to replicate 500 µA, 250 µA and 75 µA galvanostatic charging experiments

5.7 Summary and Conclusions

Analysis of O_2-limited groundwater ion solutions verifies that corrosion of SKB Cu proceeds at an extremely low rate, especially at neutral pH (40-200 µm /year) but in the acidic potential buffer solution the corrosion rates are much more severe since the calculation uses S_z values creating worst case scenario values that reach as high as ~36,800 µm/year. Reasonable damage rates can be obtained using alternative oxidants in an acidic solution designed to buffer the E_{corr}. The potential buffer, at open circuit, was validated by replicating damage from the galvanostatic charging experiments. Therefore, a valid link between accelerated and non-accelerated experiments has been created through the design of the potential buffer, opening the possibility for verifying accelerated experiment trends. The potential buffer uses Cu^{2+} as an oxidant and Cl^{-} as a groundwater ion component, allowing for analysis of Cl^{-}-dominant solutions. The potential buffer, based on E_{corr} measurements, remains at a stable potential value for approximately up to one day, but it does favour shorter experiments. It was found that roughening at E_{corr} using the potential buffer also proceeds through preferential grain dissolution that is limited by available oxidant at the sample surface.

A specific roughening rate cannot be obtained, due to the number of experimental trials and the large variance in rates indicated by Table 5.13 (between ~10,000 – 36,800 µm/year), which changes drastically based on immersion time. These conditions while designed to simulate the damage from the galvanostatic experiments in Chapter 4 cannot be fully correlated to DGR conditions due to the absence of bentonite clay, the presence of significant concentrations of oxidant, and the absence of additional groundwater ions. pH was found to affect the potential buffer ability since it affects the solubility of the oxidant, therefore affecting the buffering potential and the ratio of oxidant to reductant.

In order to more accurately replicate DGR conditions, the potential buffer would have to be modified to include SO_4^{2-} and HCO_3^{-}/CO_2^{2-} anions, which could be achieved by adding sodium- or Cu-based compounds (Na_2SO_4, $CuSO_4$, $Cu_2(OH)_2CO_3$ and $NaHCO_3$) to maintain the integrity of the single oxidant solution. Low pH has been found to be beneficial because it promotes full dissolution of the Cu-based compounds, however the concentration of HCO_3^{-}/CO_2^{2-} used for simulating the DGR may have enough buffer capacity to neutralize the low pH and cause CuCl to precipitate. To analyze the individual effect of SO_4^{2-} the steady-state potential achieved by galvanostatic charging in a SO_4^{2-} solution must be determined. Then a new ratio of cupric/cuprous sulfate must be calculated using the steady-state potential to create a new potential buffer. The potential buffer could be used with the PCB samples if it does not damage the solder mask. Further work with the potential buffer requires optimization of experimental length, concentration of the potential buffer and the chosen pH for new types of samples, especially those with organic epoxy layers, to avoid delamination or fragmentation.

5.8 References

---

1. Marcus, P.; Mansfeld, F. *Analytical Methods in Corrosion Science and Engineering.* 1st ed. CRC Press: Boca Raton, 2006; pp 437-438.

2. Kelly, R. G.; Scully, J. R.; Shoesmith, D. W.; Buchheit, R. G. Electrochemical Thermodynamics and Kinetics of Relevance to Corrosion. *Electrochemical Techniques in Corrosion Science and Engineering;* Marcel Dekker Inc: New York, 2002; p 9.

3. Lide, D. R. *CRC Handbook of Chemistry and Physics.* 1st ed. CRC Press: Boca Raton, 2005; pp 8-24.

4. *Design, Production, and Initial State of the Canister;* TR-10-14; SKB: Stockholm, Sweden, 2010; pp 32.

5. Butler, I.B.; Schoonen, M. A. A.; Rickard, D. T. Removal of Dissolved Oxygen From Water: A Comparison of Four Common Techniques. *Talanta.* **1994**, 41, 211-215.

6. Kreizer, I. V.; Marshakov, I. K.; Tutukina, N. M.; Zartsyn, I. D. Partial Reactions of Copper Dissolution under Cathodic Polarization in Acidic Media. *Prot. Met.* +. **2004,** 40, 28-30.

7. Jianu, O. A.; Wang, Z.; Naterer, G. F.; Rosen, M. A. Constitiuent Solubility and Dissolution in a CuCl-HCl-H2O Ternary System. *Chem. Eng. Sci.* **2018,** 184, 209-215.

8. Andersson-Östling, H. C. M.; Hagström, J.; Danielsson, M. *Phosphorus in Copper Intended for Spent Nuclear Fuel Disposal;* SKB R-17-19; SKB: Solna, Sweden, 2018; pp 38.

9. Kuznetsov, P. V.; Rakhmatulina, T. V.; Belyaeva, I. V,; Korznikov, A. V. Energy of Internal Interfaces as a Characteristic of the Structural Evolution of Ultrafine-Grained Copper and Nickel after Annealing. *Phys. Met. Metallogr.* **2017,** 118, 255-262.

10. Flausino, P. C. A.; Nassif, M. E. L.; Bubani, F. C.; Pereira, P. H. R.; Aguilar, M. T. P.; Cetlin, P. R. Microstructural Evolution and Mechanical Behaviour of Copper Processed by Low Strain Amplitude Multi-Directional Forging. *Mat. Sci. Eng. A-Struct.* **2019,** 765, 474-483.

11. Faita, G.; Fiori, G.; Salvadore, D. Copper Behaviour in Acid and Alkaline Brines- I Kinetics of Anodic Dissolution in 0.5M NaCl and Free-Corrosion Rates in the Presence of Oxygen. *Corros. Sci.* **1975,** 15, 383-392.

12. Leach, R. K. *Good Practice Guide No.37: The Measurement of Surface Texture using Stylus Instruments.* 1st ed. National Physical Laboratory: Middlesex; pp 16-25.

---

13. Warraky, A. E.; Shayeb, H. A. E.; Sherif, E. M. Pitting Corrosion of Copper in Chloride Solutions. *Anti-Corros. Method. M.* **2004,** 51, 52-61.

6. Mapping Individual Anodes and Cathodes using the Multichannel Microelectrode Analyzer and Su8 coated PCBs

6.1 Method Development

6.1.1 Developing a Method for Mapping Arrays

As previously mentioned in Chapter 3, CLSM and optical microscopy were used to analyze the PCB MEAs. The procedure that utilized both of these techniques was designed around the trade-off between speed and detail. Both optical microscopy and CLSM can collect detailed data at the cost of increased analysis times. A rapid analysis was important due to the presence of O_2, which could alter the composition of corrosion products. This was made worse if any residual moisture remained on the MEA which would damage the electrodes by staining or salt deposition. These types of damage could not be accurately captured by CLSM analysis. Therefore, the analysis procedure was designed to reduce their likelihood.

Optical mapping of the PCB MEAs was performed by selecting the entire area containing the electrodes and splitting it into smaller areas which were imaged and subsequently stitched together. First the highest and lowest points were determined on a chosen area. These values were chosen at the points where the image began to blur and lose focus at both ends of the focal range. Each section was then imaged in designated z-interval slices, which were then compiled into a single file and stitched together. The resulting image was a completely in-focus image. The file was then split into sections which were labelled and saved individually.

Image magnification had the most influence on quality versus time for optical analysis. The magnification chosen for the optical imaging was 10×. Imaging at magnifications of 20× and 50× required too many subsections and CPU processing power, leading to large files and long analysis times. At 10× magnification, these issues were negated, with the large z-intervals providing an accurate representation of the general appearance of each electrode, with small file sizes and could be completed in less than 10 minutes. Optical imaging was used for preliminary analysis to create a basic overview of the MEA to identify any obvious flaws on the surface. Shorter optical scans also reduced exposure of the MEA to air.

CLSM imaging required the optimization of many parameters, starting with magnification. The electrodes on the MEAs were ~132-174 μm × ~145-172 μm when uncoated and 50 μm diameter circles when coated with Su8. The 50× magnification lens was used for analysis. Consequently, each electrode was imaged individually. The z-interval chosen for image collection was the recommended value by the Zeiss software. At 50× magnification the recommended z-interval was 0.54 µm per slice, which was large with respect to the electrodes which had 5-10 µm tall features. The lowest the z-interval that could have been accurately set was 1/5th of the recommended value, according to the manufacturer. Therefore, a z-interval of 0.33 µm per slice was arbitrarily chosen to balance between detail and time. Small changes in the z-interval greatly impacted the experimental time depending on the value of the z-range, which was typically 10-50 µm.

The CLSM data was collected with each image comprised of X by Y pixels. Normally X=Y was used to create a square image. The default X and Y values were 256 pixels which could be increased up to a maximum of 4096 pixels. The pixel count directly correlated with experimental time. For these experiments it was optimal to set both X and Y to 512 or 768 pixels.

Pixel size is a physical translation of how much space is captured by a single pixel and is directly affected by the pixel count. Typically, when X and Y were both set to 768 pixels the pixel size was approximately 0.19 µm (this created a 146 µm × 146 µm image) which was used to image both the coated and uncoated electrodes since it offered a good compromise between detail and time. A z-interval of 0.33 µm and X and Y dimensions of 768 pixels yielded an experimental time of 6-7 hours.

Each electrode in the MEA was fully imaged, including the coating, during CLSM and optical analyses. This was because the Su8 coating away from the opening was very flat, whereas the area just outside the electrode opening tended to have a slight decline. Therefore, during CLSM data analysis the outer edges of the electrode (which were coated) were used as reference points for electrode height changes since the Su8 was flat and unreactive in test solutions. It was important when analyzing roughness data to exclude the sections of the electrode near the Su8 walls. The edges of the Su8 opening could not be accurately analyzed by CLSM. The likely explanation for this limitation was that the laser light could be trapped at the Su8 edges which were then registered as non-measured points (NMPs). A more complete version of the CLSM analysis would have involved tilting the sample but due to the sample size and the stage setup it was not feasible to perform this step. Therefore, an inner section of the electrode was analyzed by excluding 2-3 µm thick circles or squares, depending on the electrode shape, from the outer section of the electrode to create a smaller shape that was used for roughness analysis (this was referred to as inner roughness analysis). It was possible to guarantee that the same areas were analyzed each time by selecting the same pixels for pre- and post-experimentation analysis.

Before the roughness analysis was performed, the raw CLSM data was processed. The CLSM software could have pre-filtered the noise before importing the data. However, the pre-filtering was not used because it lacked fine control compared to the analysis software (Confomap) which offered more accurate controls.

Confomap data analysis was conducted in steps. All of the data was thoroughly checked at each step to avoid over-processing. Since the electrodes were small, little noise and few analytical artifacts were present from data collection. Roughness changes were tracked by generating tables of roughness values at each step: the raw data, the levelled data and the outlier-corrected data. Data were levelled by subtracting an uneven background height if there was a noticeable slant to the surface. Slants were found to prominently impact the data due to the small z-range. At these z-ranges small height differences yielded large angle changes. After levelling, outliers were removed with a soft or medium smoothing method to avoid altering the data significantly. The strength of the method (soft, medium, or hard) was chosen by how smoothed the data look in the output screen, if the data were oversmoothed then the strength was reduced. After levelling and outlier correction the data were considered fully processed. Lastly the inner area for roughness analysis was selected and had its own roughness values table generated to demonstrate the difference in perceived roughness that is attributed to the Su8 wall height versus the electrode-only height.

6.1.2 PCB Longevity and Storage

A single G3 I3 PCB MEA would take a day to fabricate. G3 I3 MEAs could be made in batches of four. The pre-experimental MEA analysis was performed 6-12 hours prior to test solution exposure (the $CuCl/CuCl_2$ buffer). After analysis or experiment the MEAs were stored to minimize O_2 exposure. Three storage methods were tested to determine their efficacy.

The first storage method involved placing the MEAs in an anaerobic chamber. The anaerobic chamber uses an Ar environment that contains less than 4 ppm of O_2. The disadvantage of the anaerobic chamber was that vacuum effects (during transfer into the anaerobic chamber) on fully developed Su8-coated MEAs were unknown, though considering the stability of fully cured Su8 delamination this was determined not to be an issue. However, any lightly adhered or partially cured Su8 sections or Cu oxides could have been disrupted by negative pressure during transport into the anaerobic chamber. The other disadvantage to using the anaerobic chamber was that the time required to remove the samples and transport them to analytical instruments could take up to one hour.

The second storage method tested was placing the MEAs in a desiccator sealed with vacuum grease. This was much faster than storing the MEA in the anaerobic chamber, but the speed of the desiccation was limited by the desiccant, and moisture was removed at a slower rate than in the anaerobic chamber. Therefore, desiccating allowed some O_2 to reach the MEA during placement, removal and transport.

The last method tested was storing the MEAs in the boxes used to transport them from the nanofabrication facility. This was the fastest method but allowed O_2 to continually reach the electrode surfaces. To limit O_2 access to the MEAs they were stored in the nanofabrication facility where the air was constantly filtered. It was possible that the electrodes barely corroded in the presence of O_2 with no moisture. Native oxide films are known to grow slowly and were not considered a threat for 1-2 years of storage.[1] Small amounts of Cu oxide were found to grow on the MEA electrodes after a year of storage, but this was considered beneficial since it replicated the UFCs emplacement state more accurately. The UFCs cannot be placed in a N_2 atmosphere prior to sealing and disposal and air-formed oxides will be present. Comparison of storage methods indicated storage in transfer boxes was the best solution. Almost no oxides were formed in short term storage (1 month) as a consequence of this method which was comparable to storage in the anaerobic chamber. This indicated that native oxide formation is very slow and negligible in short term storage.

Another aspect of storage that influenced oxide formation was heat. It was important to avoid exposing the MEAs to unnecessary heat sources to avoid increasing the rate of oxide formation. Therefore, to avoid unnecessary damage to the MEAs they were stored in a closed container in a cool environment to limit airflow and moisture.

Determining PCB MEA reusability was also a high priority. Two main methods to determine reusability were considered. The first method was to etch the electrodes in a strong acid and track any optical changes over many etching cycles. The second method was to perform CLSM imaging before and after to track the changes in electrode roughness and height.

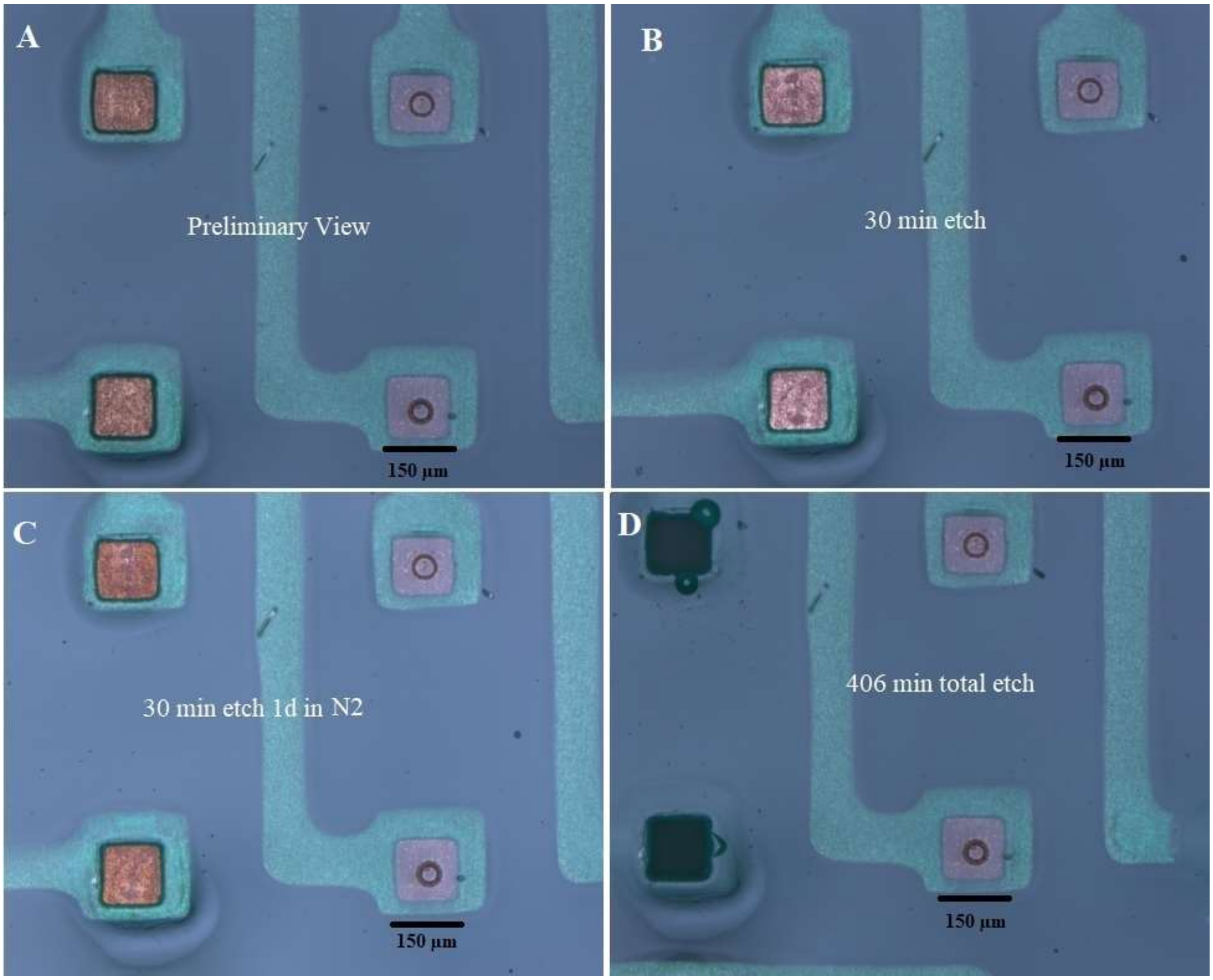

Figure 6.1. Images of the upper left quadrant of CB35A after different lengths of etching in 25% HNO_3

G3 I3 PCBs were identified using a naming system following the format of "CBxxY" where CB denotes these MEAs were contained on a PCB. "xx" was the number of seconds used to cure the Su8 layer on the surface, if this value was 0 then the PCB did not have a Su8 coating. Y was a letter of the alphabet used to indicate the order in which samples were made for the cure time (xx value) with A being the first sample.

The first sample, CB35A was etched to determine its reusability. Images of the electrodes from the upper left quadrant of CB35A, are shown in Figure 6.1. CB35A was etched in 25% HNO_3 for 30 minutes then washed, dried and placed into a N_2 desiccator overnight. Figure 6.1B shows minor etching occurred. When it was subsequently exposed to a N_2 atmosphere for a day the damage worsened, as indicated by the discolouration seen in Figure 6.1C. The sample was then etched the next day for 376 minutes in 25% HNO_3 for a total of 406 minutes. After this etch the uncoated electrodes were completely dissolved while the Su8-coated electrodes were completely protected despite having smaller than intended openings, Figure 1D.

The next etched sample was CB40A, which had 5 additional seconds of UV curing during fabrication and was only etched once for a longer period of time than CB35A. Figure 6.2 shows the comparison of the PCB before and after the etching. The etching was conducted for 10 hours in 25% HNO_3. As Figure 6.2 shows there was minimal damage, indicated by the change in colour of the electrodes. This figure demonstrates that, when Su8 properly coated the surface, the electrodes were well protected.

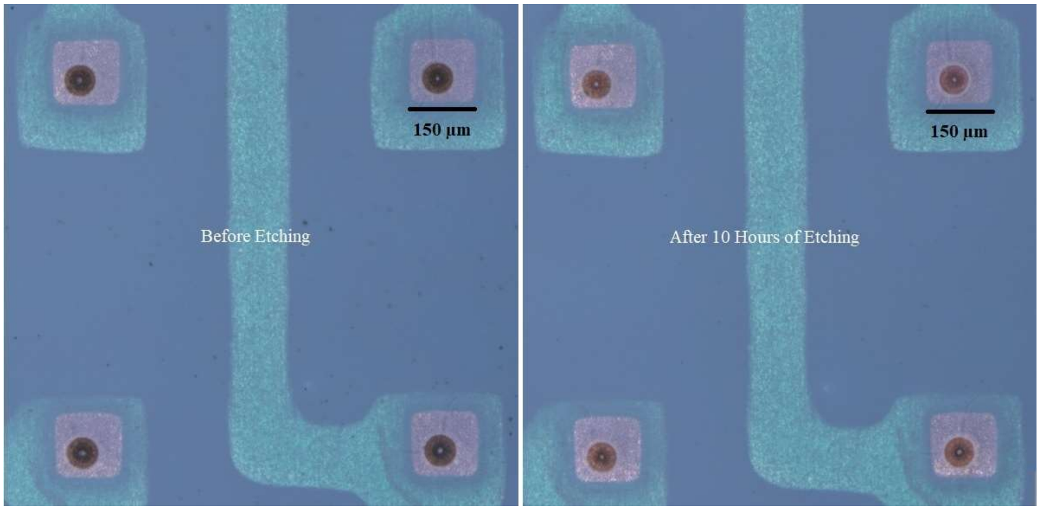

Figure 6.2. Optical images taken of Su8-coated electrodes before and after 10 hours of etching in 25% HNO_3

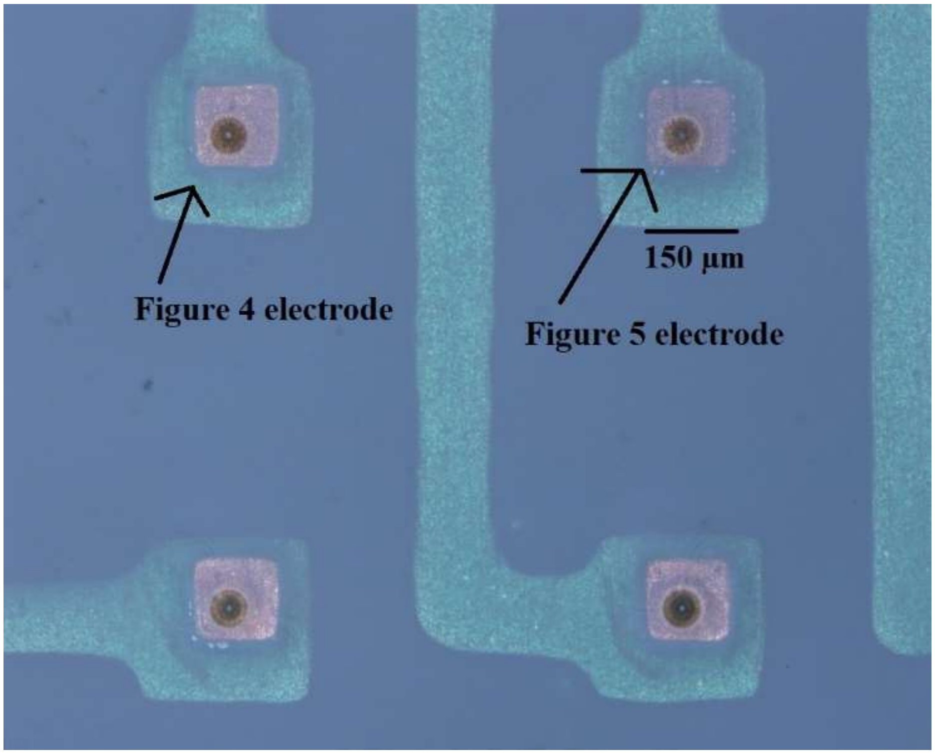

Figure 6.3. An optical image highlighting discolouration of pads and electrode openings after 24 hours of immersion in Ar-sparged 1 M NaCl

Next, CB40A was immersed in Ar-sparged 1 M NaCl for 24 hours. After this immersion minimal damage to the electrodes was observed. The damage is identifiable by the minor discolouration of electrodes, especially in the coated portions, Figure 6.3. The roughness profile and the 3D reconstructed images (shown in Figure 6.4 and Figure 6.5) of the two labelled electrodes in Figure 6.3 demonstrate the difficulty in determining how much corrosion had occurred. Figure 6.4 and Figure 6.5 compare the profiles and 3D reconstructed images of two adjacent electrodes. The first electrode, Figure 6.4, had a Su8 pillar on the surface. The second electrode, Figure 6.5, despite its appearance, either had Su8 on the surface or had a very small opening in the Su8, though the slight hump in the profile favours Su8 on the surface. Based on these results, it was judged that PCB reusability was much easier to study with uncoated electrodes. It was expected that the uncoated electrodes, similar to the samples used in Chapter 5, would be moderately damaged after each experiment, allowing samples to be re-used a small number of times. Based on the results of CB35A and CB40A it was likely that Su8-coated PCBs would not be reusable unless corrosion was limited to a few µm per experiment.

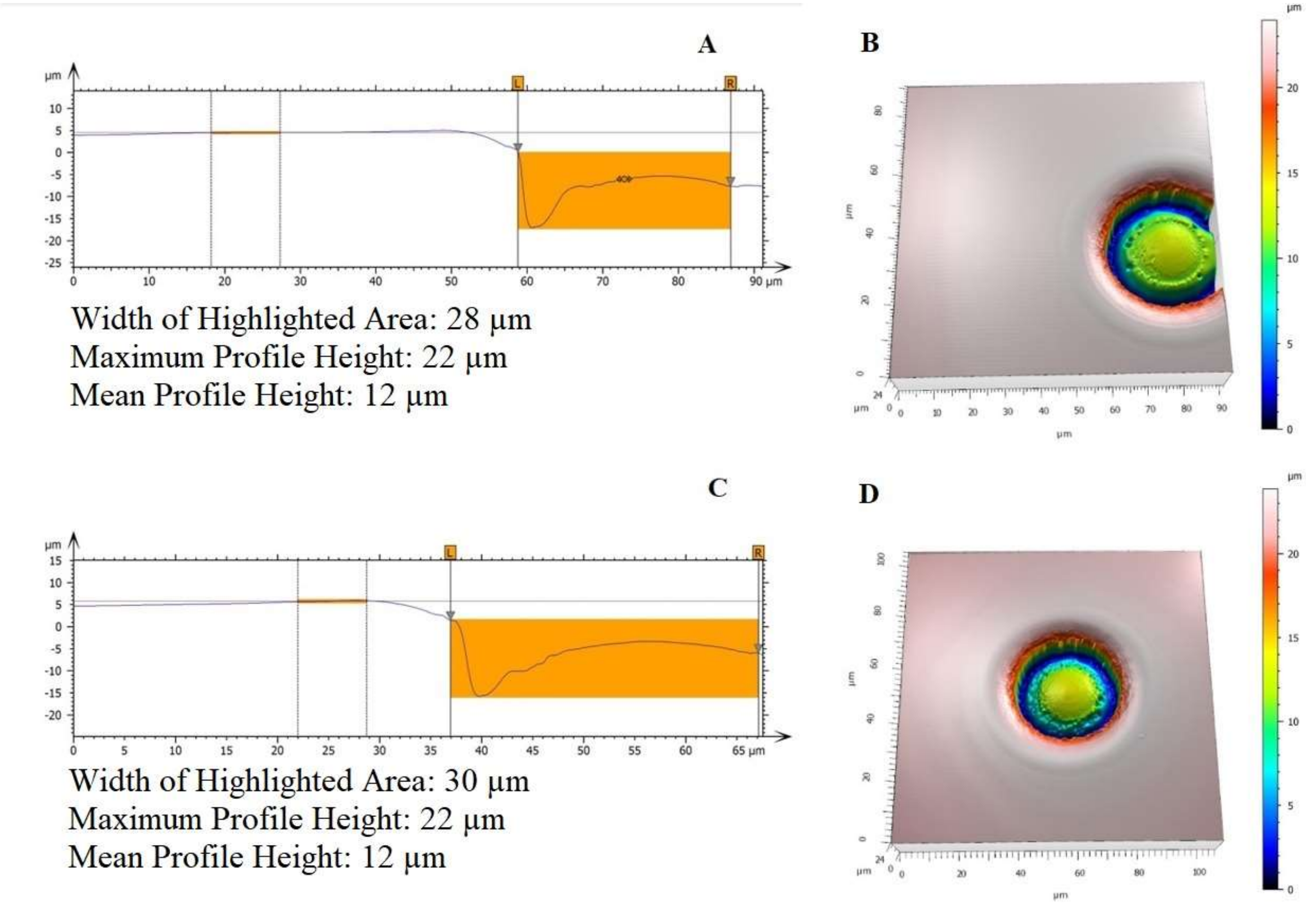

Figure 6.4. 3D reconstructed images and the associated profiles of a Su8 coated electrode on CB40A before (A and B) and after (C and D) immersion in Ar-sparged 1 M NaCl for 24 hours

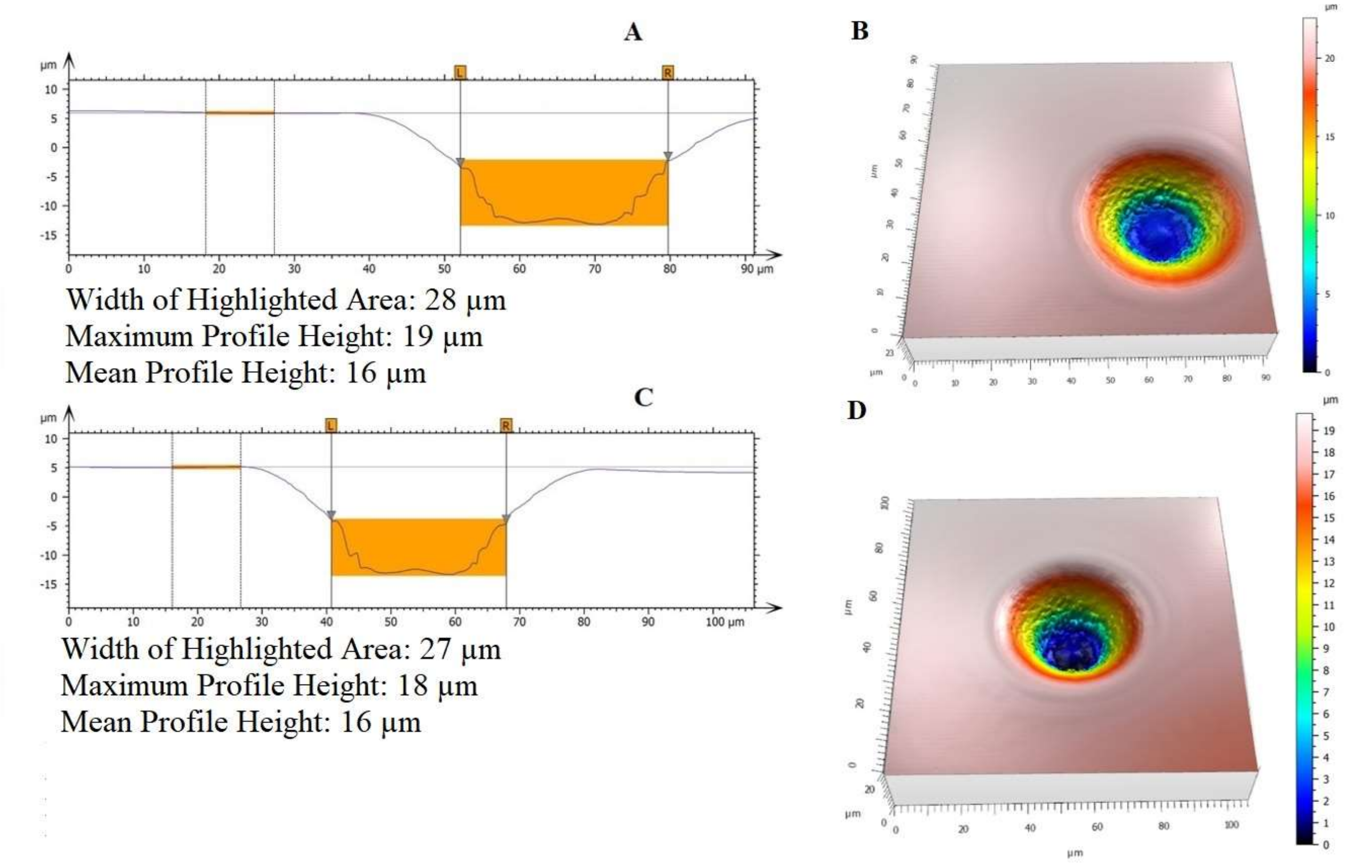

Figure 6.5. 3D reconstructed images and the associated profiles of a second Su8 coated electrode on CB40A before (A and B) and after (C and D) immersion in Ar-sparged 1 M NaCl for 24 hours

6.1.3 Ideal Experimental Conditions

Based on the data from Chapters 4 and 5, along with the preliminary observations of PCB MEA longevity and Su8 stability, ideal experimental conditions were determined. Important factors considered were the thickness of the Cu electrodes, and experimental times and environments. Previous experiments (CB35A experiments) indicated that mildly aggressive acidic solutions could fully dissolve the Cu electrode. Based on the results in Chapter 5 the $CuCl/CuCl_2$ potential buffer did not corrode Cu quickly within the experimental time frame and therefore it was used with the MEAs. The potential buffer was also an appropriate solution choice because the DGR will be Cl^{-} dominated.

The experimental method used with the potential buffer was modified to promote less corrosion during MEA experiments than in the experiments described in Chapter 5. The potential buffer was modified to have a pH of 1.5, chosen as a compromise because the damage produced in the short corrosion experiments using pH 1 and 2 was either too much or too little, respectively. The modified solution was tested on an uncoated MEA to ensure the solder mask did not degrade or dissolve. The main modification to the experimental method was the length of the experiment. The shortest immersion experiments were 3.77 hours long and designed to remove 10 µm of Cu from a large surface area. The combined surface area of all the electrodes in MEAs have much less surface area than the Cu coupons used in the experiments described in Chapter 5 so it was possible that less time in the potential buffer is needed to produce moderate amounts of corrosion. However, since the solution pH was adjusted to promote less corrosion, immersions under 4 hours were tested to see if the MEA electrodes were too corroded. The last consideration was the experimental environment. The environment was designed to mimic experiments described in Chapter 5 as closely as possible. Therefore, Ar sparging was employed to limit the availability of O_2 in solution and ensure Cu^{2+} was the main oxidant.

6.1.4 Setting up an Experiment with the MMA

The MMA has 5 main ribbon cables. Each main ribbon cable connected to the MMA has 20 connections which are split into two smaller ribbon cables of 10 connections. Each smaller ribbon cable can be configured to measure current or voltage. In order to accurately track and measure the current or potential response from an electrode it was important to know which electrodes were wired to which portion of the ribbon cable. It was possible to omit specific connections for each cable, but it is important to note that during measurement the software uses the maximum current value as a placeholder. This placeholder value did not contribute to the average data values.

"Nulling" was an important function that was used prior to conducting an experiment with the MMA. There were three possible options for nulling with the MMA: On, Off and Null. Nulling is the baseline function of the MMA software; all currents are zeroed when the null option is selected. On and off applied the baseline created by the null setting. If a new baseline is required "null" is selected at the appropriate time which deletes the old baseline and creates a new one based on the measurements at the time of selection. Selecting a good null was crucial to performing a proper experiment as a poorly timed null could have biased the current totals to positive or negative values. Depending on the sensitivity of the measurement, this bias could have had a large influence on measurements.

Prior to each MEA experiment, the null function was selected. A null was considered successful when the total current (the leakage current otherwise classified as noise) measured by the MMA fluctuated between a positive and negative value in the 0.1 nA range. Nulling is primarily affected by the filtering and interval parameters. The filtering and interval values have a significant impact on how data was collected during an experiment. Interval is the measurement interval at which data is recorded. The interval for the MEA experiments was always set to the fastest possible value of 0.0001s to allow for more accurate filtering and nulling. A fast filter value created a low-pass filter which more effectively eliminated noise. However, the filter setting had some complexities to consider. The filter averaged the data at specific points in time to reduce noise, but this value needed to be offset with the measurement interval to prevent aliasing. To avoid under sampling, the measurement interval in the experiment screen was set to half of the chosen filter value.[2]

It is important to note that the current measured by the MMA on one electrode is influenced by the currents measured on adjacent electrodes, therefore all electrodes experience some neighbouring effects depending on their position within the array. The electrodes near the centre of the MEA experience the largest effect while the electrodes located at the edges of the MEA experience the smallest effect. This effect could not be confirmed because the currents observed were not consistently or vastly different based on their location within the MEA.

The "Cell Status" function which has two options, "on" and "off", which controlled if potential was applied to the working electrodes. "On" allowed potential to be applied and "off" prevented potential from being applied even if values were input into the software. Therefore, for E_{corr} measurements the cell status was set to "off". A reference electrode value modifier, listed as "Base Potential", was also available in the experimental setup. This modifier could have controlled the potential with a counter electrode or set the baseline value for measuring potential. To set a baseline value the other potential-controlling options were set to "0 vs base". There were three options that controlled the measured cell potential value in this menu "0 vs OCP" (OCP is commonly referred to as E_{corr}), "0 vs ref", and "0 vs previous". "0 vs OCP" set the measured potential as 0 during open circuit measurements, making it impossible to determine the true E_{corr} value during an experiment. "0 vs ref" set the reference electrode base value as 0, allowing for the determination of the E_{corr} value versus the reference electrode. "0 vs previous" was used when there were two measurement steps in order. This modifier set the most recent potential measured as 0, which is helpful in systems where stabilization of the E_{corr} value is required prior to polarization. For all experiments “0 vs OCP” was selected.

6.1.5 The Final Experimental Procedure for G3 I3 PCB MEAs

Selecting an experimental procedure for the G3 I3 PCB MEAs was performed after the software interface components were selected. The only remaining parameter that needed to be determined was the detection limit of the ZRAs. To determine the lower detection limit (also referred to as resolution) a shortened E_{corr} measurement was performed. The interval on the analysis screen was set to 0.0001s and the filter to 1s. The experimental interval was set to 0.5s (half of the filter value), the cell status was set to “off” and the base potential value set to “0 vs ref”. The experimental interval was chosen to limit the dataset size and still produce enough points per second to maintain a fast scan. Once the MEA was connected to the MMA the experiment was started. The lower detection limit range was dependent on the effect of the null. Therefore, multiple nulls were performed to ensure any bias towards positive or negative currents was eliminated. After the nulls were completed the solution was added to elucidate the different types of electrode responses.

Figure 6.6 shows the three main types of electrode response to solution addition after nulling. Electrode 1,4’s response shows a typical large current response, electrode 1,6 shows a typical minimal current response and electrode 2,2 shows either no response or an undetectable response. Each plot has five regions highlighted. The first region (black) represents the typical unfiltered leakage current for 1 μA ZRAs with values near -40 nA for each electrode. These are regarded as high and noisy values. The second range is coloured red which corresponds to the first null, which immediately sets the current on each electrode near 0 in the 0.1 nA range. The second and third nulls, which correspond to the blue and purple lines, show that any subsequent nulling on each electrode has a minor but unpredictable impact on the measured noise while remaining in the 0.1 nA range. The second null created the unpredictable change since each electrode shows a different response corresponding to an increase, decrease or unchanged current response compared to the first null. The third null seems to return the noise response to values closer to those produced by the first null. The current recorded when 1 M NaCl is added to the cell and Ar-sparging initiated is indicated by the green line. Comparing the green line to the noise responses produced by the nulls allows identification of the electrode's response.

The lower detection limit was determined by analyzing the noise response and determining the total range of the noise values during each null. Based on the noise analysis from these three electrodes the range of noise varies from as low as ±0.076 nA to as high as ±0.138 nA, which would make the lower detection limit ±0.138 nA. Solution addition to the MEA led to current responses with ranges of ±0.198 nA, ±0.336 nA and ±1.36 nA from electrodes 2,2; 1,6; and 1,4 respectively. When looking at the third type of response (non-responsive or undetectable) from electrode 2,2, its range is just slightly above the lower detection limit which suggests the electrode may have registered a small response at some point during the measurement. However, due to the proximity of the electrode response values to the lower detection limit it cannot be verified and the electrode should be considered unresponsive.

The potential buffer solution generated a comparatively large amount of corrosion compared to 1 M NaCl as described in Chapter 5, leading to higher current responses above the lower detection limit except on unresponsive electrodes. Subsequent nulls were used to establish a reliable background, similar to the lower detection limit determination, to differentiate leakage current from low signal response. The determination of the detection limit was performed prior to each experiment to aid in the identification of non-responsive/undetectable electrodes.

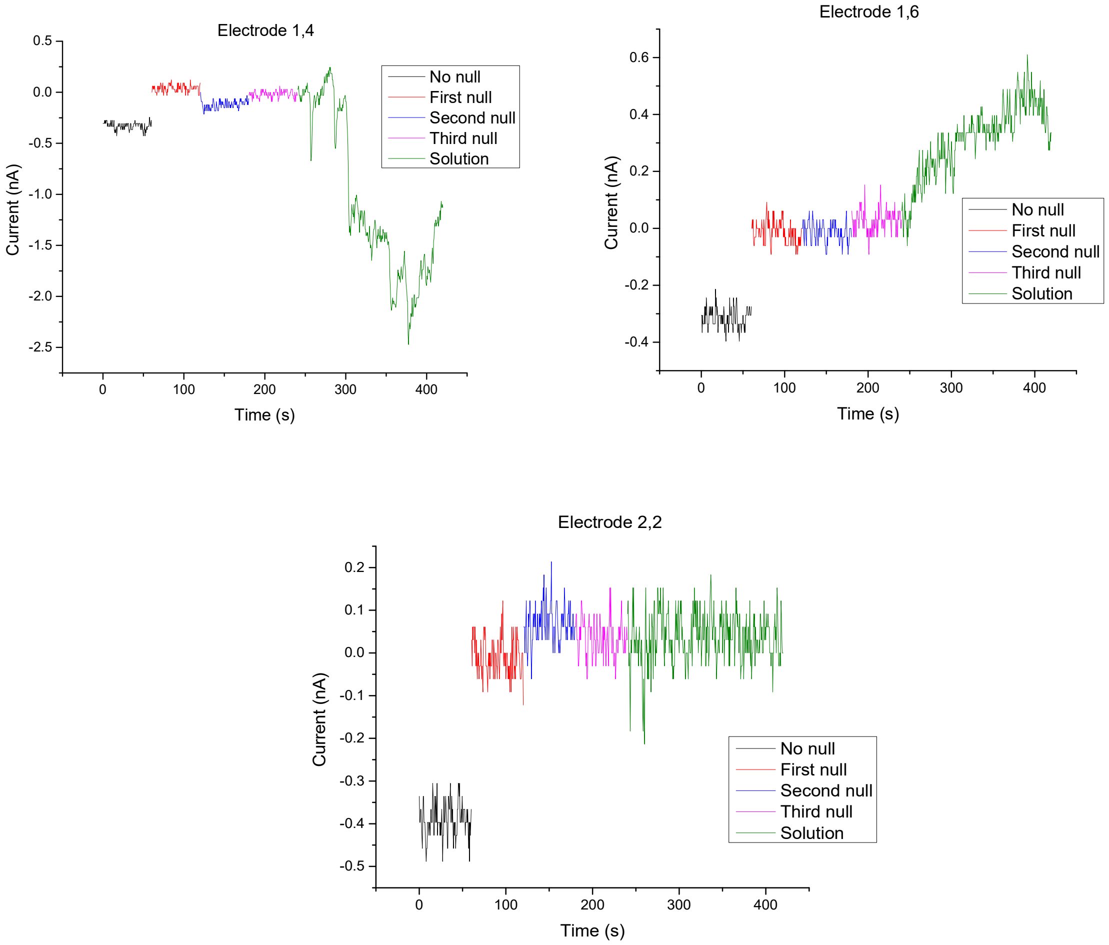

Figure 6.6. Three current versus time plots for electrodes used to determine the lower detection limit based on the variations in noise due to the MMA nulling procedure compared to the subsequent response after addition of 1 M NaCl and the initiation of Ar sparging

6.1.6 Data Treatment for MMA Experiments

Data collected from the PCB MEAs was modified by the nulling and filtering according to the parameters selected during the experimental setup.

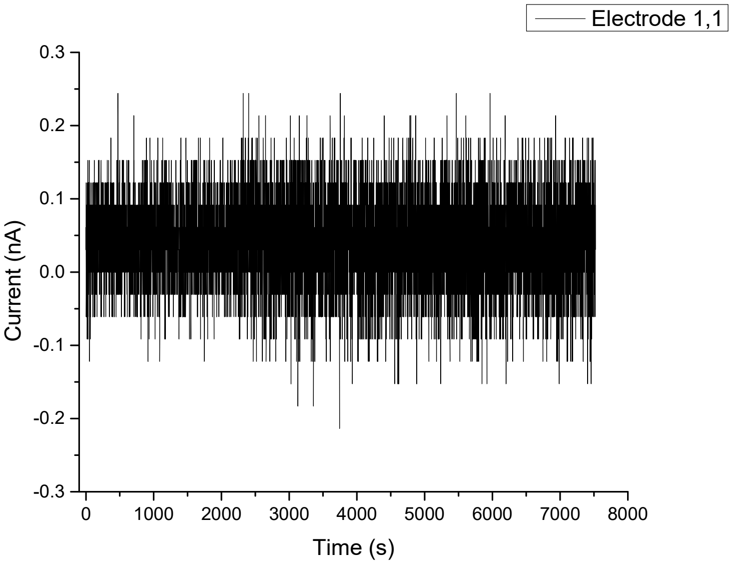

Figure 6.7. A current versus time plot for an electrode in a MEA immersed in Ar-sparged 1 M NaCl.

Despite these methods, the data for electrodes with low current responses, was extremely noisy and very close to the detection limit, as shown in Figure 6.7. Therefore, without further data treatment many electrodes had similar curve shapes and their behaviour was difficult to ascertain. The most effective method of noise treatment was to calculate a moving average. Moving averaging is performed by re-calculating each point in a time series as an average of a specific number of points forward and backward from the recalculated point. The window of points used in the average is known as the forecast, this value can be large or small. Choosing a forecast that is too extreme can cause major artifacts or smoothing in the data.

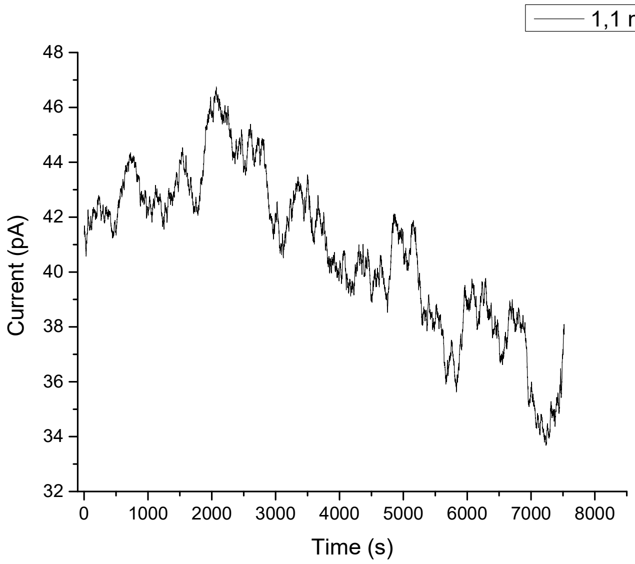

Figure 6.8. The data from Figure 6.7 after processing using the moving average method with 1000 points forward and backward for the forecast

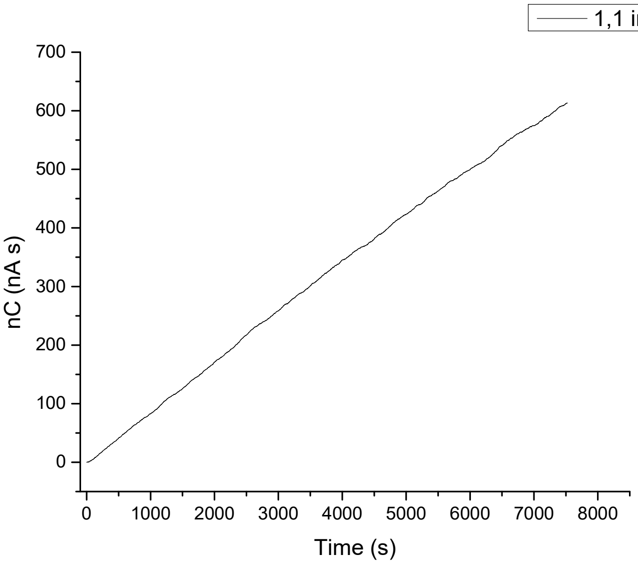

Figure 6.9. Integration of the current response shown in Figure 6.7

An example of data processed using the moving average method is shown in Figure 6.8. This image shows the noisy flat current response is transformed into an electrochemical response with far less noise and an identifiable trend. The trend was confirmed by integrating the current-time response. This produces a charge vs time plot, Figure 6.9, with increases and decreases in slope matched to positive and negative changes in current of the moving average. Figure 6.9 shows a linear increase in current since the values in Figure 6.8 are positive. The slope in Figure 6.9 has small decreases when the moving average current tends towards 0. To increase the accuracy of the analysis, a baseline can be determined from the nulling procedure. The baseline, which was either an average value or the most recent value from the null prior to solution addition, had an axis line drawn to show the new 0 line. An example of this is shown in Figure 6.10. With this baseline procedure established Figure 6.8 and Figure 6.9 could be used to more accurately identify electrode behaviour.

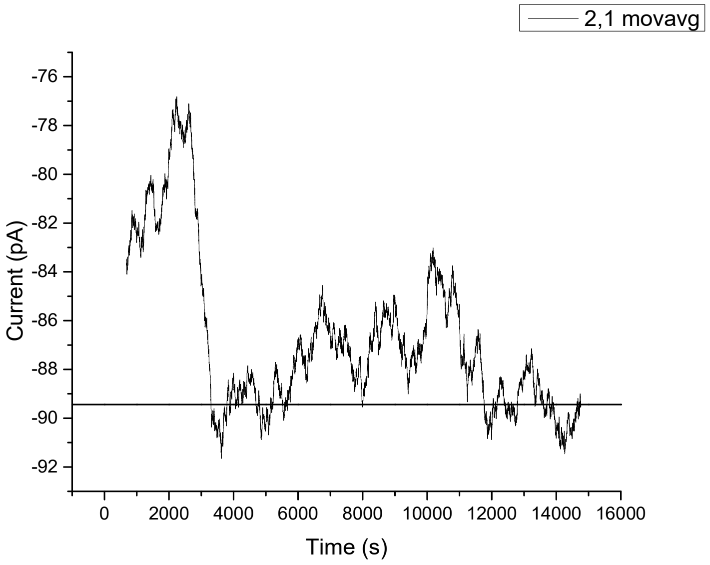

Figure 6.10. A moving average plot with a modified baseline (as described in the text) to help identify anodic and cathodic current regions

6.2 Su8-coated PCB Experiments

6.2.1 MMA Experiments on Su8-coated PCBs in Solutions with a Limited O_2 Concentration

As seen in previous experiments in Chapter 3, especially during Su8 optimization and PCB MEA design, O_2 in solution has a major influence on electrode damage. While damage sustained in air is negligible over short exposure periods, exposure to aerated solutions leads to oxide formation on the MEA electrodes which could have assisted in photoresist delamination, causing a higher failure rate.

Near the end of Su8 optimization, with the addition of the thinner in the spin coating step, two ideal G3 I3 MEAs were fabricated: CB40J and CB40K. CB40J was used to demonstrate MEA longevity in air and was the first G3 I3 MEA used in an Ar-sparged test solution. Two experiments were performed with two different solutions. The first experiment was conducted for 2 hours in Ar-sparged 1 M NaCl + 0.1 M Na_2SO_4 to test if additional groundwater ions promoted more corrosion in O_2-limited environments. After this experiment, the MEA was exposed to air for one day and then analyzed by CLSM which showed this exposure led to no additional meaningful corrosion. The second experiment was conducted almost 20 days later for 4 hours in Ar-sparged 0.01 M NaCl + 0.01 M Na_2SO_4. The focus of CB40J was on the second experiment.

Figure 6.11 shows the optical images of CB40J's upper left quadrant of electrodes after storage in air for 16 days, 18 days and then post-experimentation. There is no major visual difference between any of these electrodes other than some minor darkening. This is confirmed by the roughness analysis of some of the electrodes in the second row. The S_a and S_q values (the arithmetical mean deviation of the absolute surface profile values and the root mean square deviation of the surface profile values, both used to determine roughness) in Table 6.1 change by ≤ 0.1 µm, even for uncoated electrodes like 2,6. There is a singular data spike which increases the S_z values for electrode 2,2 shown in Table 6.1. In order to verify if any corrosion had occurred the 3D reconstructed images can be inspected, Figure 6.12. It is difficult to compare the pre- and post-experimental 3D reconstructed images for the uncoated electrode (2,6) in Figure 6.12 because there are only minor differences in its surface morphology. However, the main feature that skews its roughness values is circled in orange, while the feature that skews the roughness values recorded on electrode 2,2 is circled in pink in its post-experimentation image. Despite these features the pre- and post-experiment 3D reconstructed images are very similar.

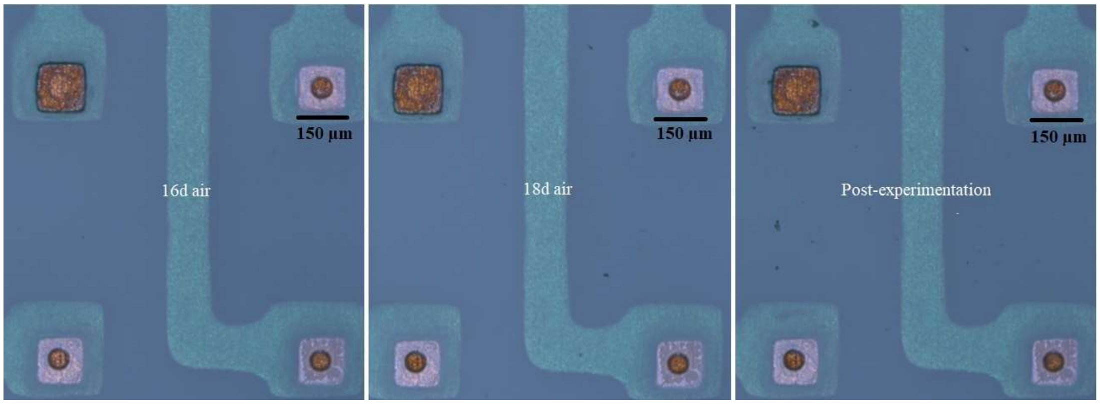

Figure 6.11. Optical images of the upper left quadrant of CB40J after sitting on the benchtop for 16 days, 18 days and after 4 hours of immersion in Ar-sparged 0.01 M NaCl + 0.01 M Na_2SO_4 featuring one uncoated electrode and three Su8-coated electrodes

Table 6.1. Roughness values and the associated differences for 5 of CB40J's second row electrodes before and after both immersions in Ar-sparged 0.01 M NaCl + 0.01 M Na_2SO_4, values in red were not used to calculate average values due to data artifacts or peaks skewing the data

Electrode	2,1	2,2	2,3	2,4	2,6	Average
Pre-experiment 1						
S_a (µm)	0.15	0.13	0.13	0.13	0.16	0.14
S_q (µm)	0.19	0.17	0.17	0.16	0.20	0.18
S_z (µm)	1.72	1.35	1.34	1.24	1.49	1.43
Pre-experiment 2						
S_a (µm)	0.14	0.14	0.14	0.12	0.15	0.14
S_q (µm)	0.18	0.18	0.17	0.16	0.19	0.18
S_z (µm)	1.53	1.47	1.26	1.19	1.44	1.38
Pre-experiment 1->2 Differences						
S_a (µm)	-0.01	0.01	0.01	-0.01	-0.01	0.01
S_q (µm)	-0.01	0.01	0.00	0.00	-0.01	0.01
S_z (µm)	-0.19	0.12	-0.08	-0.05	-0.05	0.10
Post-experiment						
S_a (µm)	0.14	1.50	0.14	0.12	0.16	0.14
S_q (µm)	0.17	3.10	0.17	0.16	0.21	0.18
S_z (µm)	1.56	14.50	1.31	1.13	3.95	1.33
Pre-experiment 2->Post-experiment Differences						
S_a (µm)	0.00	1.36	0.00	0.00	0.01	0.00
S_q (µm)	-0.01	2.92	0.00	0.00	0.02	0.01
S_z (µm)	0.03	13.03	0.05	-0.06	2.51	0.05

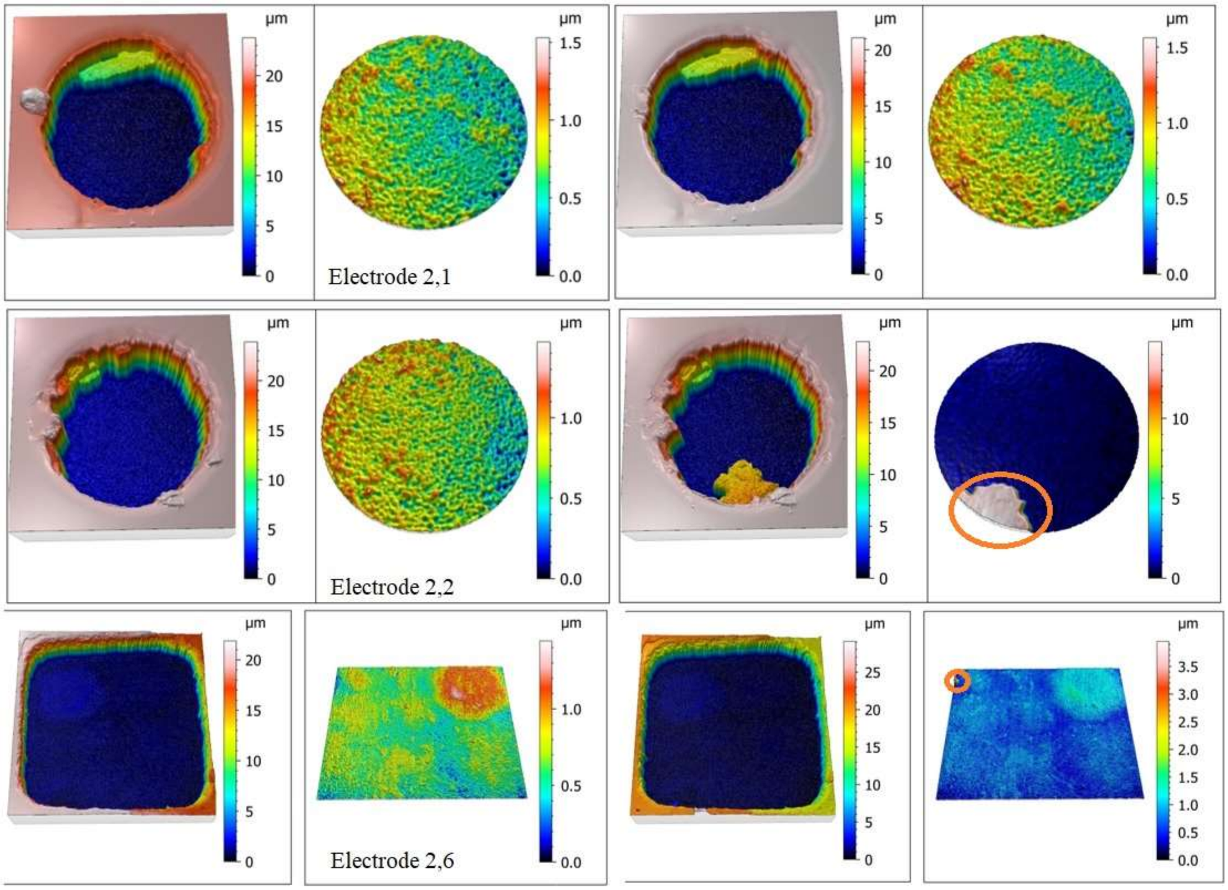

Figure 6.12. 3D reconstructed images of various electrodes in the second row of CB40J before (left side) and after 4 hours of immersion in Ar-sparged 0.01 M NaCl + 0.01 M Na_2SO_4 (right side) including both full and inner electrode images with important outlier features circled in the after images

To verify the results from the second experiment with CB40J, a similar experiment was performed with CB40K, the only difference being a 0.1 M NaCl solution was used to confirm that SO_4^{2-} was not preventing Cl^- from complexing Cu^+ and increasing the corrosion rate. Figure 6.13 shows the optical images of the upper left quadrant of the CB40K pre- and post-experimentation. Notable brightening and darkening of the electrodes is observable in Figure 6.13. The red-circled electrode is brightened while the white circled electrode is darkened. Brightened electrodes have reacted slowly or are unreactive and darkened electrodes have reacted faster and may have corrosion product deposits. This trend cannot be reaffirmed using the electrochemical data, due to noise and possible crevice formation due to Su8 delamination. Similarly, the roughness parameters do not indicate a clear roughening trend. The roughness parameters in Table 6.2 reveal there are minimal changes in both S_a and S_q for this sample. To distinguish between cathodic and anodic behaviour, the S_z values from full electrode analysis (including Su8 walls) were used. The 3D reconstructed images of the inner section of electrode 1,1 before and after experimentation, shown in Figure 6.14 (with Su8 excluded) have no fixed reference point to which changes in surface height features can be compared. This lack of a reference point means that a detailed height comparison between the inner sections cannot be made and that the S_z value from this 3D reconstruction is unreliable. However, the 3D reconstructed images still provide detailed topography which was useful for studying the morphology that resulted from roughening. These 3D reconstructed images show no major colour changes but have slightly differing colour patterns and height scales, indicating that the surfaces may have dissolved slightly becoming more uniform in height, but the topography and roughness patterns are generally similar between the pre- and post-experimental surface. As expected in Ar-sparged 0.1 M NaCl, minimal corrosion was observed.

In these experiments an increase in S_z values with a fixed reference point was initially attributed to anodic behaviour (metal dissolution, therefore removal of material) and a decrease or no change was initially attributed to overall cathodic behaviour (trace O_2 reduction or reduction of Cu^{2+} corresponding to no surface changes). Electrodes 2,1 and 2,2 both exhibit an increase in S_z as shown in Table 6.2. However, in Figure 6.13 they both exhibit different optical changes which indicates that the association between electrode colour and its anodic/cathodic behaviour needed further verification. This dataset indicates that any exposure to Cl^- and SO_4^{2-} species in O_2-limited solutions results in low corrosion rates due to the lack of an oxidant (O_2).

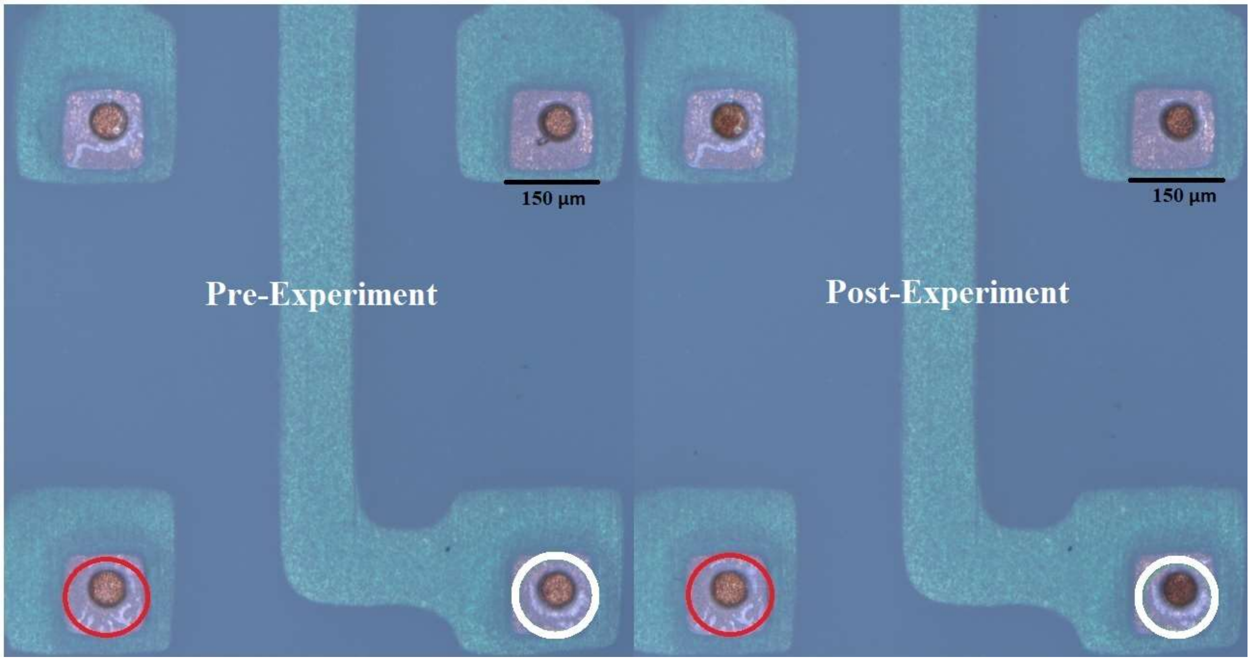

Figure 6.13. Optical images of Su8-coated electrodes on CB40K before (left) and after (right) immersion in Ar-sparged 0.1 M NaCl for 24 hours; notable electrode pairs are circled in red or white

Table 6.2. Roughness values and the associated differences from before and after immersion in Ar-sparged 0.1 M NaCl for 24 hrs for the top left quadrant of electrodes on CB40K

Electrode	1,1	1,2	2,1	2,2	Average
Pre-experiment					
S_a (µm)	0.13	0.15	0.16	0.15	0.15
S_q (µm)	0.17	0.20	0.21	0.20	0.20
S_z (µm)	24.20	32.00	25.00	24.00	26.30
Post-experiment					
S_a (µm)	0.14	0.17	0.18	0.18	0.17
S_q (µm)	0.18	0.21	0.23	0.23	0.21
S_z (µm)	26.20	28.00	26.00	26.00	26.55
Pre-experiment -> Post-experiment Differences					
S_a (µm)	0.01	0.02	0.02	0.03	0.02
S_q (µm)	0.01	0.01	0.02	0.03	0.02
S_z (µm)	2.00	-4.00	1.00	2.00	2.25

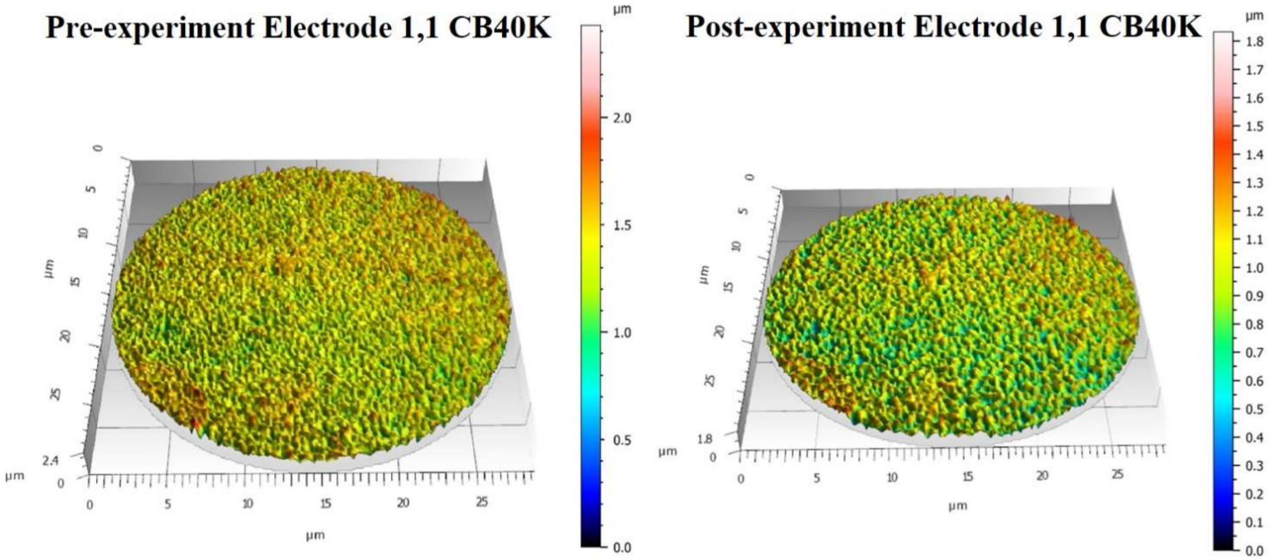
Pre-experiment Electrode 1,1 CB40K

Post-experiment Electrode 1,1 CB40K

Figure 6.14. A comparison of 3D reconstructed images of a single electrode before and after 4 hours of immersion in Ar-sparged 0.1 M NaCl for 24 hrs using inner data with no complimentary full electrode data for reference

6.2.2 MMA Experiments in Solutions Containing an Alternative Oxidant

Since solutions containing groundwater anions did not promote enough corrosion within the experimental duration a modified version of the potential buffer solution described in Chapter 5 (a solution containing 4.05:1 of [CuCl]:[$CuCl_2$] in 1 M NaCl with HCl used to adjust the pH) was used to accelerate corrosion. Several G3 I3 and G3 I2 MEAs were used in these experiments. The MEAs were split into two main categories: Su8-coated and Su8-free. Only one Su8-coated G3 I3 MEA, CB40K, was used due to a limited amount of remaining fresh MEAs. There were many Su8-free MEAs which were split into subcategories of iteration 2 (I2) and iteration 3 (I3) G3 MEAs, with the main difference between these MEAs being the electrode openings: I2 had larger openings than I3. The G3 I2 MEAs were CB0C and CB0E. The G3 I3 MEAs were CB0A, CB0B, CB0D and CB0F.

The MEA, CB0A was used to determine the stability of the solder mask in the low pH potential buffer solution (CuCl/$CuCl_2$). CB0A was previously exposed to Ar-sparged 1 M NaCl and 0.1 M Na_2SO_4 for 2 hours and then stored for a couple months prior to the stability tests. Negligible corrosion occurred in these previous tests; however, a small amount of oxide had formed on the electrodes during storage based on the optical appearance of the electrodes. The first stability test with CB0A was performed in an Ar-sparged as-made (AM) pH, 0.0037 M [Cu] solution (4.05:1 CuCl:$CuCl_2$) for 2 hours. No CLSM analysis was performed since no optical changes that indicated significant corrosion were observed.

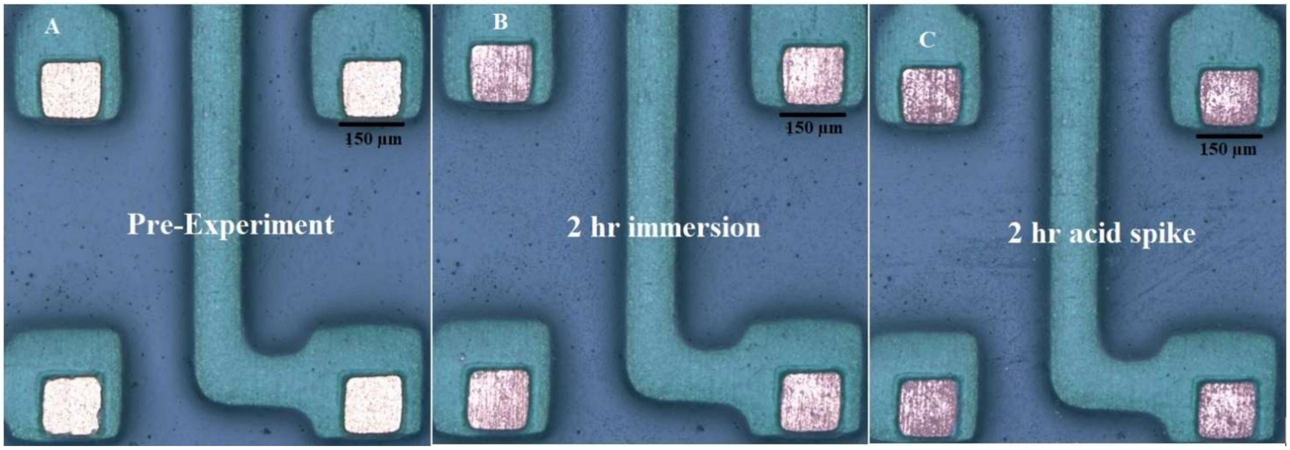

Figure 6.15. Optical images of the upper left quadrant of CB0A from before experimentation, after 2 hours of immersion in the Ar-sparged 0.0037 M [Cu] potential buffer at AM pH and after 2 hours of immersion in the Ar-sparged 0.0037 M [Cu] potential buffer spiked with 1 M HCl

Figure 6.15 shows the optical images of the upper left quadrant of CB0A at each important experiment timepoint. The first notable comparison is between the pre-experiment image and the image after 2 hours of immersion. The pre-experimental image, Figure 6.15A, shows some dark areas on the Cu electrodes which could indicate a slightly corroded surface. Overall, the Cu appears very shiny and reflective, indicating that the dark areas have a minimal effect on the optical quality of the surface. The electrodes after 2 hours of immersion, Figure 6.15B, have darkened notably but remain slightly shiny. These electrodes have identifiable damage on the surface but are not uniformly damaged, suggesting a possible separation of anodic and cathodic activity on the same surface. The formation of only small amounts of corrosion product also indicates that the reaction rates in the neutral pH solution are low, consistent with the results in Chapter 5. By contrast to the results in Chapter 4 or Chapter 5, no preferential grain dissolution was observed. This is surprising since preferential grain dissolution would be expected[3,4] It is possible that the fabrication process led to small grains since the Cu is often electrodeposited on the FR4 substrate and then sprayed with HCl spray to etch and roughen to Cu so it adheres better to the solder mask.[5]

The damage produced in this solution was too low to determine a roughness trend, which would also be partly obscured by the presence of deposits. In order to verify the influence of pH on the corrosion rate the potential buffer was spiked with HCl to see if more damage was observable. CB0A was immersed for two additional hours and the resulting surfaces are shown in Figure 6.15C.

The damage increased notably after the acid spike. This behaviour was verified by a follow up experiment with CB0A in a low pH potential buffer. The potential buffer concentration was increased by a factor of 10 (from 0.0037 M [Cu] to 0.0374 M [Cu] (4.05:1 $CuCl:CuCl_2$)) and its pH was adjusted to 1.5. The experimental duration was also doubled to 4 hours to more accurately replicate the shortest immersion experiment in Chapter 5. At the halfway point, the experiment was stopped to analyze the MEA and then resumed. This interruption was performed to determine the difference in damage after 2 and 4 hours of immersion. This procedure differs notably from the previous experiment since the same solution is used for both parts of the experiment.

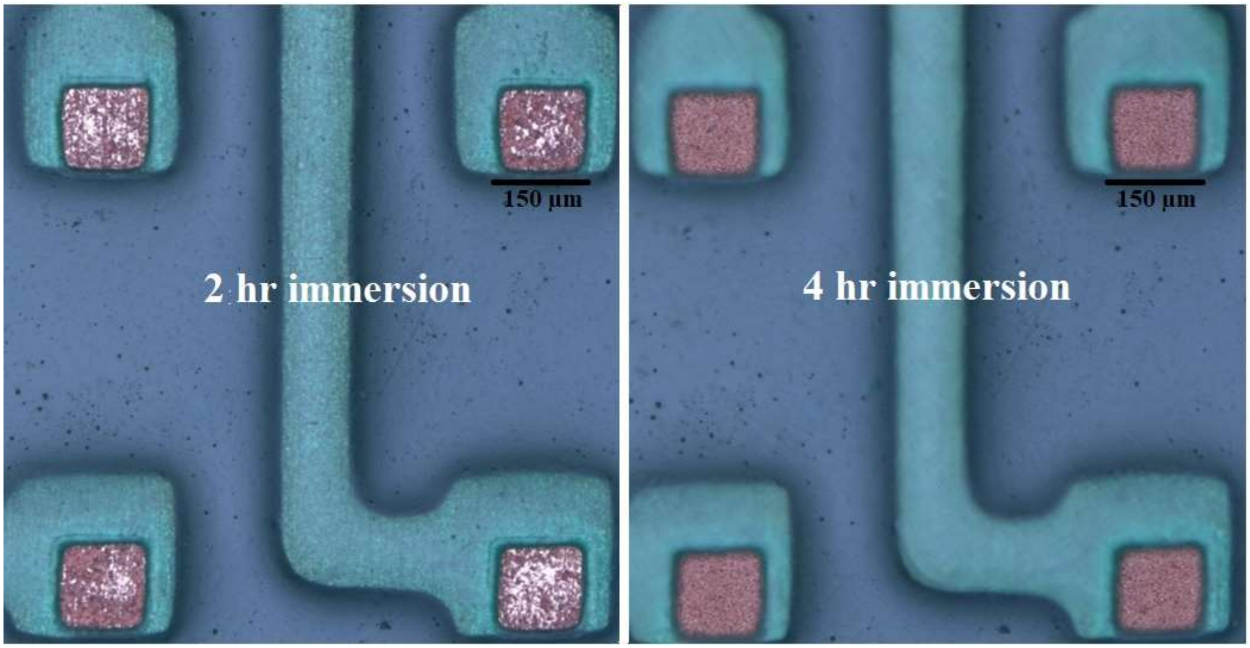

Figure 6.16. Optical images of the upper left quadrant of CB0A after 2 hours and 4 hours of immersion in the Ar-sparged pH 1.5, 0.0374 M [Cu] potential buffer

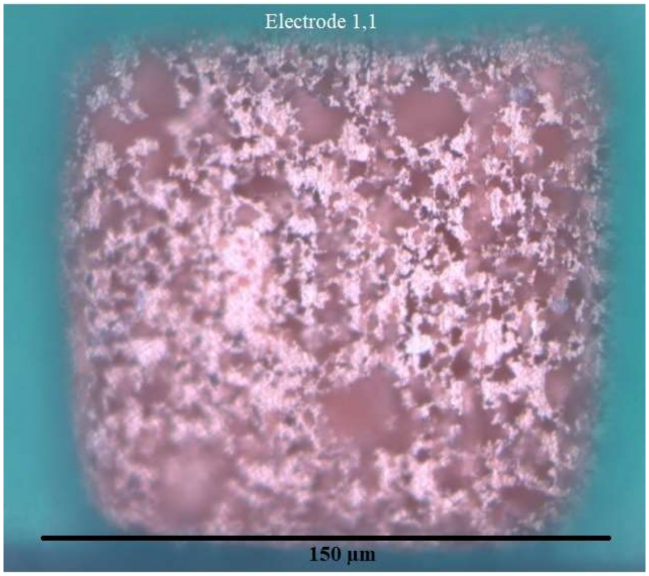

Figure 6.17. An optical image of electrode 1,1 on CB0A after 2 hours of immersion in the Ar-sparged pH 1.5, 0.0374 M [Cu] potential buffer

The corrosion produced by 2-hours of immersion in the Ar-sparged, pH 1.5 potential buffer shown in Figure 6.16 is much greater than the damage produced by the Ar-sparged HCl spiked potential buffer shown in Figure 6.15. A closer look at the damage in Figure 6.16 using optical microscopy clarified the roughening pattern produced by 2 hours of immersion in the potential buffer, Figure 6.17. In this image the brighter spots of copper are either unreacted or marginally reacted locations while the darker areas indicate areas where more extensive corrosion has occurred. These depressed locations look darker because the reflected light is decreased in intensity due to a longer travel path or dispersed due to increased roughness. Based on the results in Chapter 5 the less corroded areas likely have a lower surface energy.

The second 2 hour immersion clarifies the electrode behaviour and gives insight into the corrosion pattern. All of the electrodes after 4 hours of immersion have reached a similar optical state as shown in Figure 6.16. The electrodes are all darkened, implying significant uniform corrosion leading to deeper penetrations, suggesting the pock-marked surface produced after 2 hours of immersion in the potential buffer is an intermediate step in the corrosion process. While the majority of the electrodes are uniformly corroded (darkened) there are a few outliers shown in Figure 6.18 which created new avenues to explore.

The first notable electrode in Figure 6.18 is circled in red. This electrode is much brighter than the rest and retained its pockmarked surface though it has darkened slightly compared to after 2 hours of immersion. There are two possible explanations for this behaviour. The first is that this electrode sustained more cathodic activity than the others and supported trace O_2 reduction or the reduction of Cu^{2+} to Cu^{+} (which could form a deposit). The second is that the slight darkening indicates these electrodes reacted slower than most of the MEA due to a surface feature or grain orientation.

The second type of electrode, shown in Figure 6.18 and circled in orange, has very dark spots on the surface. It is assumed that more corrosion has occurred in these areas although it is not clear why. The last type of electrode in Figure 6.18 has a distinct feature circled in pink. This electrode has a small section of bright material, but the rest of the surface has corroded at a similar rate and then roughened, suggesting very little separation between anodic and cathodic reaction sites. This re-instates the question of whether the brighter material is simply unreacted, is slower to react or Cu^{+} is reduced to Cu and deposited onto the surface. A study by Lee et al suggests that bright spots are larger grains with different orientations compared to the rest of the surface produced during electrodeposition when the PCB is fabricated.[5] This would further support the idea that grains are preferentially corroded based on orientation. CLSM analyses would clarify these questions. However, the damage needed to be replicated to determine if this behaviour was unique to this sample or a recurring trend.

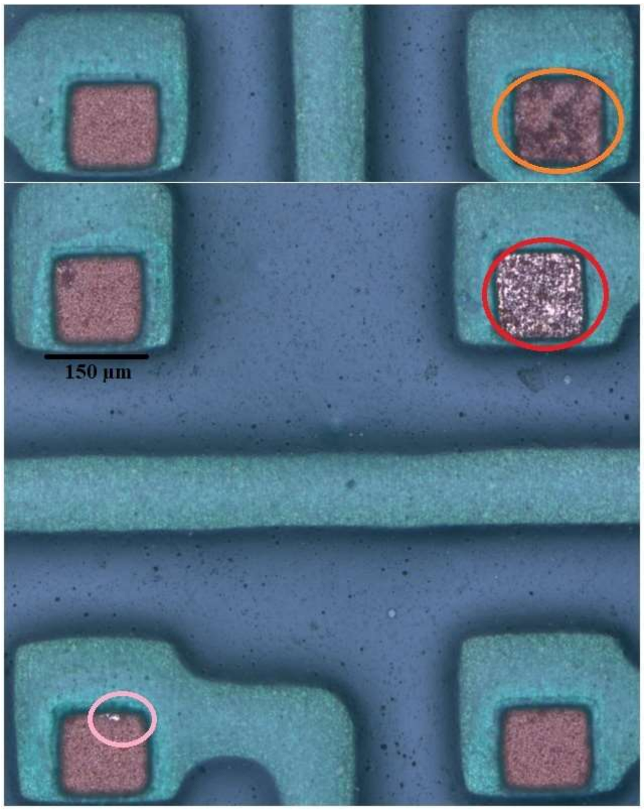

Figure 6.18. Notable outlier electrodes from CB0A after a total of 4 hours of immersion in the Ar-sparged pH 1.5, 0.0374 M [Cu] potential buffer; notable features are circled with various colours

Another MEA, designated CB0B, was investigated in an to attempt to replicate the results from the CB0A MEA exposed to the Ar-sparged, 0.0374 M [Cu] (pH = 1.5) potential buffer. The experiment was performed with two similar immersion periods of 2 hours each using an identical solution. However, unlike CB0A, CB0B had no experimental history meaning it had a cleaner starting surface. After each period of immersion, optical and CLSM analyses were performed. Figure 6.19 shows the pre- and post-experimental images for both immersion periods in the experiment. The first pre-experimental image, Figure 6.19A, shows the electrodes are very reflective with some dark spots indicating either debris on, or grooves in, the surface where the reflected light is trapped and not reflected. Figure 6.19B, the image recorded after 2 hours of immersion shows that the majority of the electrode surfaces darkened suggesting they corroded at a similar rate and therefore have smaller S_z values compared to surfaces with bright material. Reinspection of the surface prior to the second period of immersion, Figure 6.19C, showed air exposure had no noticeable effect on the surface. Figure 6.19D shows that after 4 hours of immersion (2 hours + 2 hours) similar corrosion damage to that observed on CB0A was observed.

All the electrode surfaces are almost completely darkened indicating roughening. There are some darker and lighter areas compared to the rest of the surface which is probably due to varying corrosion rates on the same surface and a separation in anodic and cathodic activity.

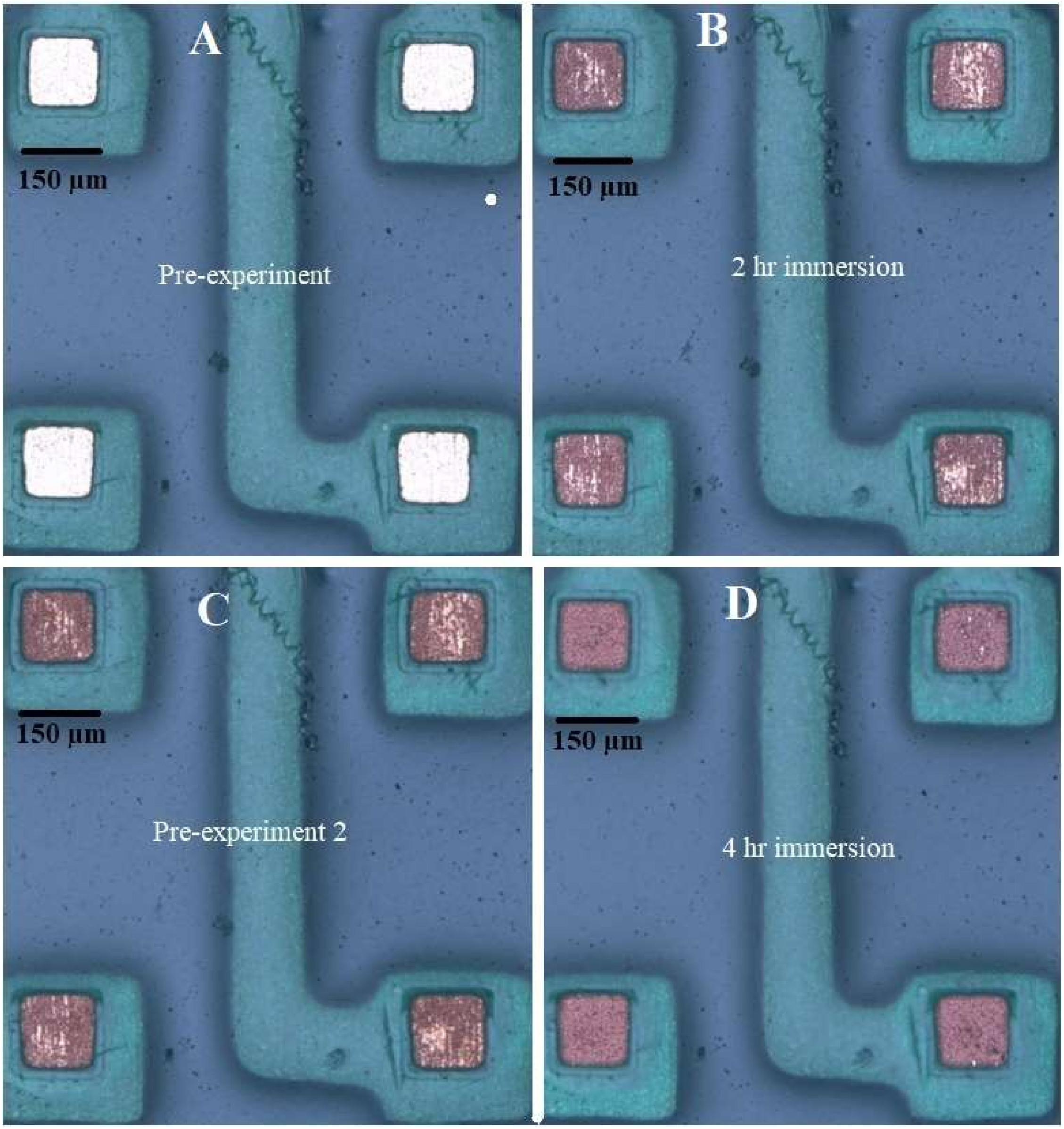

Figure 6.19. Optical images of the upper left quadrant of CB0B before and after both 2 hour immersions in the Ar-sparged pH 1.5, 0.0374 [M] potential buffer, pre-experiment 2 was taken after storage in air following the first 2 hour immersion analysis

Table 6.3. Roughness values and the associated differences for the first row of electrodes on CB0B before and after both immersions in the Ar-sparged pH 1.5, 0.0374 M [Cu] potential buffer

Electrode	1,1	1,2	1,3	1,4	1,5	Average
Pre-experiment 1						
S_a (µm)	0.12	0.08	0.10	0.10	0.13	0.11
S_q (µm)	0.16	0.10	0.13	0.14	0.16	0.14
S_z (µm)	21.50	21.60	21.40	22.40	22.30	21.84
2 hr immersion						
S_a (µm)	1.80	1.10	1.80	1.10	1.70	1.50
S_q (µm)	2.00	1.40	1.90	1.40	1.90	1.72
S_z (µm)	28.20	27.90	28.20	28.00	27.50	27.96
Pre-experiment 1->2 hr immersion Differences						
S_a (µm)	1.68	1.02	1.70	1.00	1.57	1.39
S_q (µm)	1.84	1.30	1.77	1.26	1.74	1.58
S_z (µm)	6.70	6.30	6.80	5.60	5.20	6.12
Pre-experiment 2						
S_a (µm)	1.70	1.10	1.80	1.10	1.70	1.48
S_q (µm)	1.90	1.40	1.90	1.40	1.80	1.68
S_z (µm)	27.20	27.70	27.20	27.60	27.50	27.44
(2+2) 4 hr immersion						
S_a (µm)	1.40	1.60	1.70	1.20	1.30	1.44
S_q (µm)	1.80	2.50	2.70	1.80	2.00	2.16
S_z (µm)	37.50	35.70	35.40	35.50	36.80	36.18
Pre-experiment 2->4 hr immersion Differences						
S_a (µm)	-0.30	0.50	-0.10	0.10	-0.40	0.28
S_q (µm)	-0.10	1.10	0.80	0.40	0.20	0.52
S_z (µm)	10.30	8.00	8.20	7.90	9.30	8.74

Table 6.3 shows S-values for the first five electrodes in the first row of CB0B. This table contains the roughness values and the differences for each part of the experiment as well as the total difference between both immersions. The S_z values change uniformly with each electrode starting at ~22 µm of depth, then progressing to ~28 µm and ending at ~36 µm indicating that all these electrodes contain locations that support the anodic reaction to similar degrees and possibly have similar roughening rates. The uniformity of the S_z changes is reinforced by the difference values comparing each stage of analysis. The S_z average values also have a low variance. The S_a values, however, change depending on the experimental phase; samples are typically at their roughest during the intermediate phase after 2 hours of immersion when the surface is pockmarked, which creates stark height differences. The final S_a values decrease compared to the intermediate phase due to the more uniformly distributed corrosion on the surfaces. This change in S_a indicates that the anodic and cathodic reactivity is more evenly spread across all electrodes during the second immersion compared to the first immersion. Some electrodes, such as 1,1, contain unreacted material which skews the final S_a to a higher value despite the surface being almost uniformly corroded.

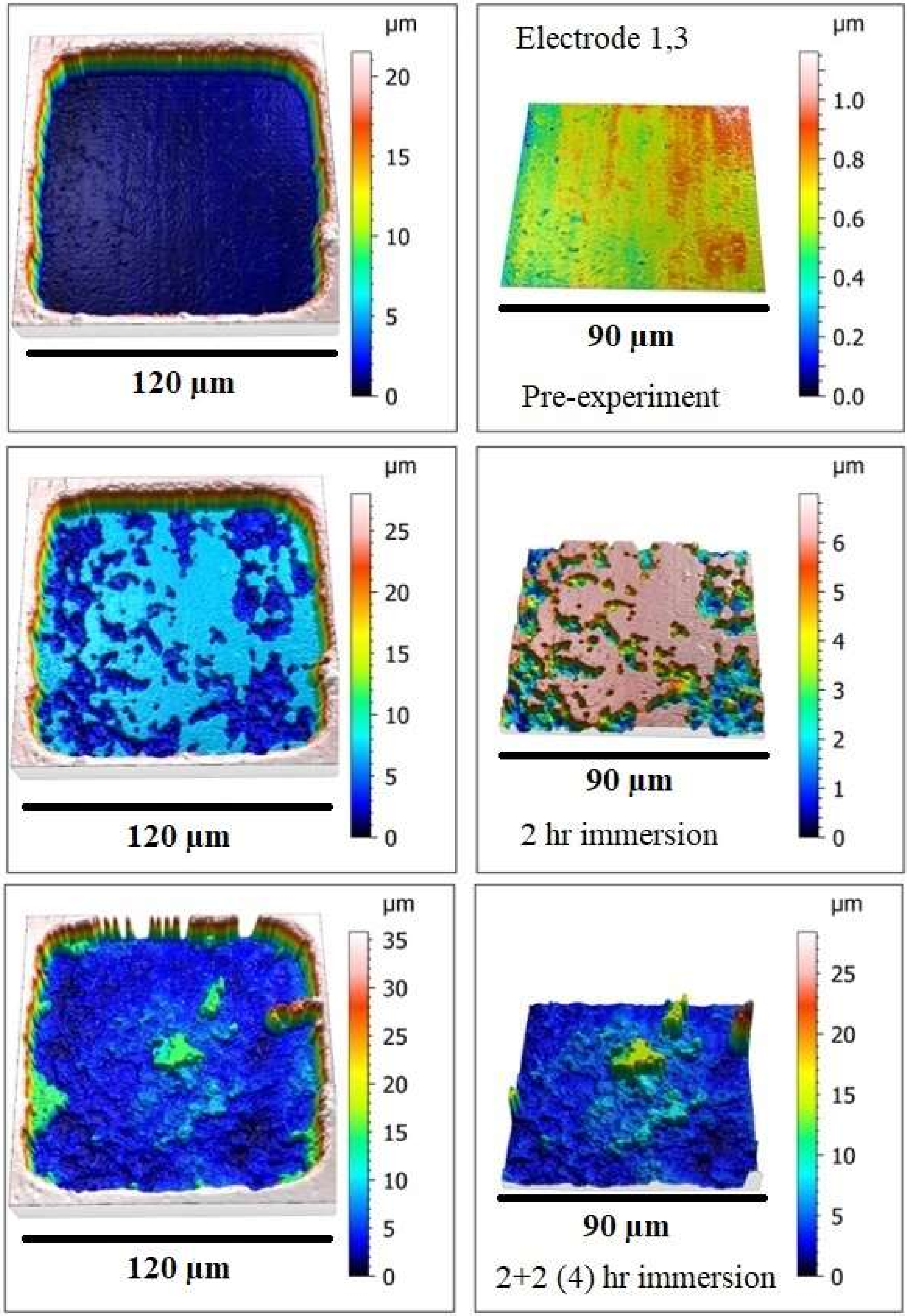

Figure 6.20. 3D reconstructed images of electrode 1,3 on CB0B before, and after 2 and 4 hours of immersion in the Ar-sparged pH 1.5, 0.0374 [M] potential buffer including full electrode analysis (left) and inner electrode analysis (right)

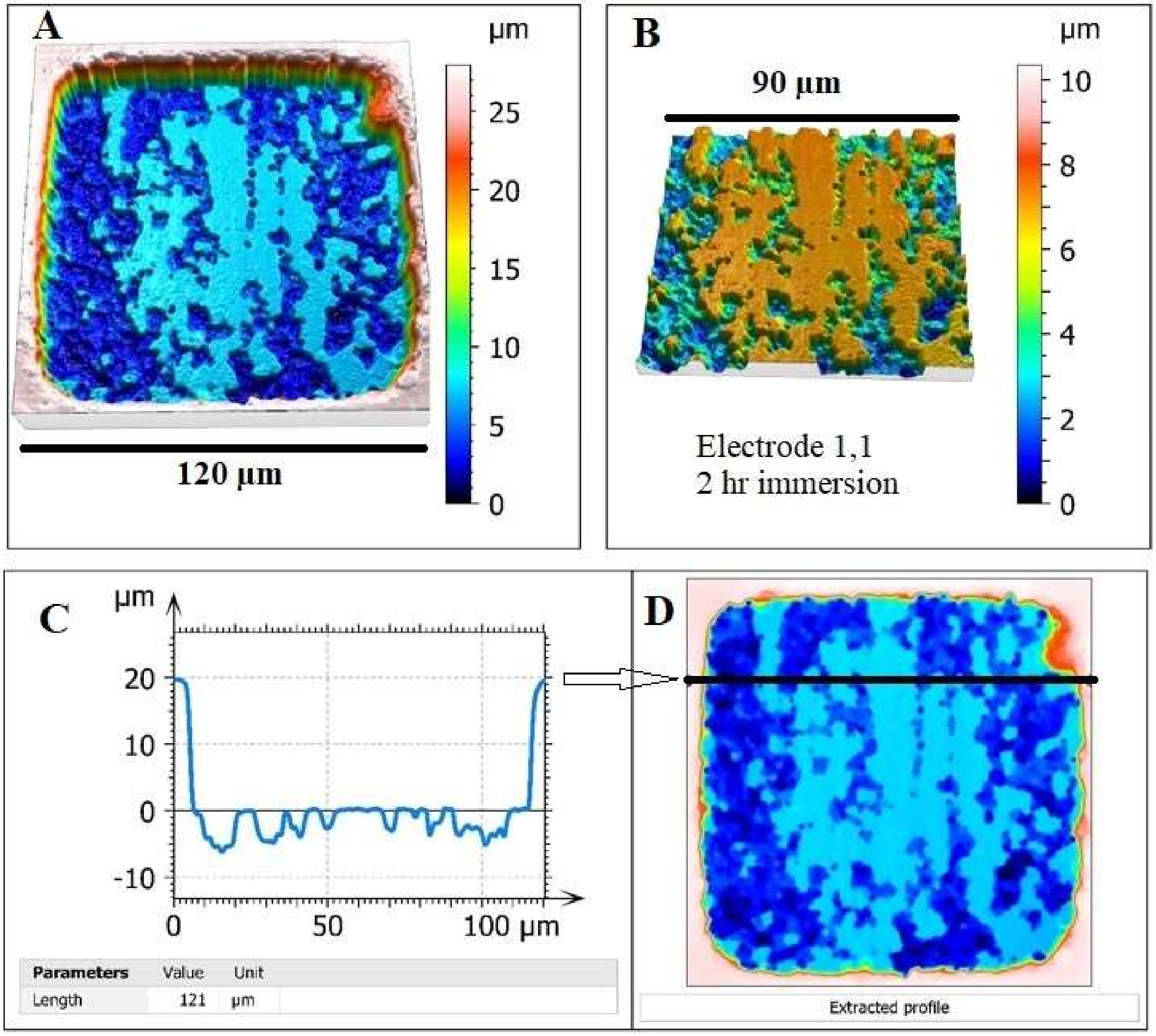

Figure 6.21. Full and inner electrode 3D reconstructed images of electrode 1,1 on CB0B after 2 hours of immersion in the Ar-sparged pH 1.5, 0.0374 M [Cu] potential buffer with an accompanied line profile taken from the area indicated by the black line and arrow

The peaks and troughs of pock-marked surfaces are shown in the 3D reconstructed images of electrode 1,3 in Figure 6.20 and the line profile of electrode 1,1 in Figure 6.21C produced from the region indicated by the black line in Figure 6.21D.

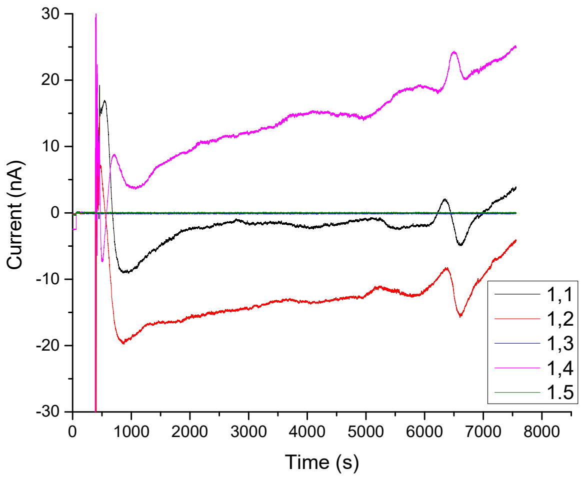

Figure 6.22. Current vs time plots for the first five electrodes in row 1 of CB0B during the 2 hours of immersion in the Ar-sparged pH 1.5, 0.0374 M [Cu] potential buffer solution. Two of the lines are not visible due to their low current response. Solution was added at 360s after the detection limit test

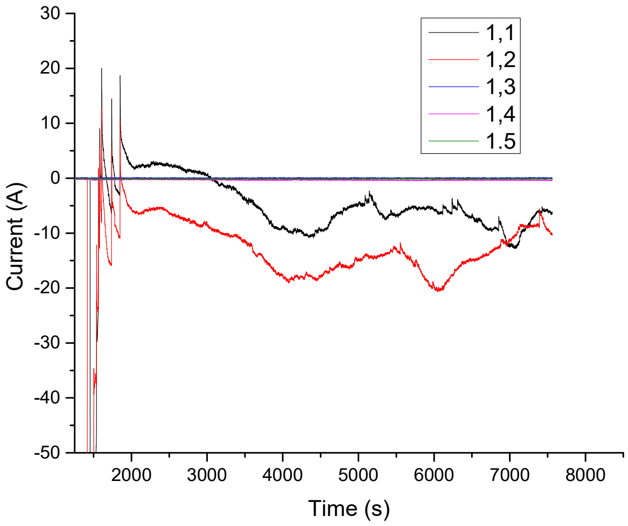

Figure 6,23. Current vs time plots for the first five electrodes in row 1 of CB0B during the (2+2) 4 hours of immersion in the Ar-sparged pH 1.5, 0.0374 M [Cu] potential buffer solution. Three of the lines are not visible due to their low current response. Current responses were not observed prior to 1500s due to an electrical contact error.

The current vs time plots in Figure 6.22 show that during the intermediate roughening phase it is difficult to correlate anodic/cathodic behaviour to the electrochemical data. Electrodes 1,1 and 1,2 initially switch between anodic and cathodic behaviour and then settle on cathodic behaviour after ~800 seconds. However, electrode 1,1 switches back to anodic behaviour near the end of the experiment, ~7000s. Electrodes 1,3 and 1,5 both have unreactive current responses which cannot be seen relative to the other three electrodes. In Figure 6,23, electrodes 1,1 and 1,2 initially switch between anodic and cathodic behaviour multiple times before settling on cathodic behaviour around 3000s. This suggests a high corrosion rate at the start of the experiment followed a low cathodic reaction rate of Cu^{2+}. Due to the current responses gathered in the intermediate phase it is difficult to make a definitive statement about the surface morphology related to the current. It important to note that the current response is the net current and electrodes can experience both anodic and cathodic behaviour on the same surface which would mean that behaviour and current are not well related. This MEA led to the testing of whether the electrode size affects the roughening pattern, if current becomes a better identifier of behaviour on larger reactive surfaces, and if more corrosion occurs if exposure times are increased.

A G3 I2 MEA, designated as CB0C, was used to test the effect of electrode size and exposure time. The G3 I2 MEA electrodes are ~30 μm x ~30 μm larger than the G3 I3 MEAs (CB0A and CB0B). The G3 I2 MEAs were exposed to air during storage for about a year, consequently some electrodes have visible oxides on them. The native oxide formation was more prominent in the scuff marks on the electrodes created by other MEAs during shipping and transport from the manufacturer's facility. The second pre-experimental image was eliminated from this procedure since the roughness parameters and optical appearance in the CB0B dataset were nearly identical to those in the first post-experimental dataset. The CB0C experiment was performed for twice the experimental length as the CB0B experiment, therefore both immersions were conducted in the same Ar-sparged, 0.0374 M [Cu] solution (pH = 1.5) for 4 hours, for a total of 8 hours.

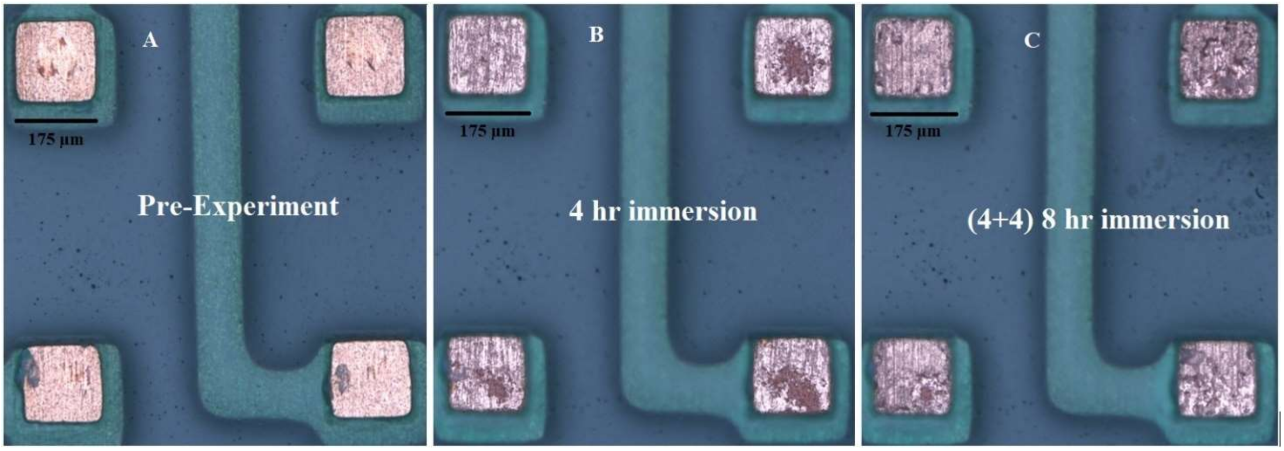

Figure 6.24. Optical images of the upper left quadrant of CB0C before, and after 4 and 8 hours of immersion in the Ar-sparged pH 1.5, 0.0374 M [Cu] potential buffer.

The optical images in Figure 6.24 show that after both 4 hour immersions CB0C has a completely different roughness pattern compared to the G3 I3 MEAs (CB0A or CB0B), Figure 6.19. Figure 6.24A shows that initially the electrodes are not as clean as the G3 I3 MEAs however, the surface is still moderately reflective. Figure 6.24B shows that after the first 4 hours of immersion there is noticeable corrosion, but unlike the G3 I3 MEAs, there electrodes have hardly darkened. Figure 6.24C shows that even after 8 hours of immersion it looks as if the electrodes have just reached the intermediate surface morphology that was observed halfway through the G3 I3 MEA experiments. The 3D reconstructed images in Figure 6.25 show that, contrary to the G3 I3 MEAs, the dark areas observed after the first 4 hours of immersion are elevated rather than depressed. These elevated areas appear to be corrosion product deposits, suggesting these areas have mainly supported the cathodic reaction, leading to the deposition of either Cu or Cu_2O by the reduction of Cu^{2+}. These features are most apparent in electrodes 1,2; 1,3; and 1,4. Table 6.4 contains the roughness parameters and their associated differences for the first row of electrodes. The S_z values all start around 18 µm then increase to ~39 µm and end at 45 µm. This uniform increase in S_z is similar to that observed on CB0B. The initial rapid S_z increase during the first immersion indicates that some locations corrode faster than others, likely anodic reactivity is better supported by particular grains. Therefore, it is possible that less corroded areas after the first immersion are primarily cathodes. The smaller increase in S_z produced by the second immersion indicates there is less of a distinct separation between the anodic and cathodic reactivity of grains compared to the first immersion. Unlike on CB0B (a G3 I3 MEA), Table 6.3, the S_a values for

CB0C are highest at the end of the experiment rather than the middle, which is supported by the 3D reconstructed images in Figure 6.25 which shows that the rougher surface topography, which has a multitude of locations with large S_z differences across the surface, is the result of the second immersion rather than the first immersion. This trend was observed by Hu et al., who stated that a rougher starting surface will lead to a less uniformly corroded surface, which seems to be the case for CB0C (a G3 I2 MEA), Table 6.4 and Figure 6.25.[6] However, for CB0B (a G3 I3 MEA) this trend is found to be the opposite, Table 6.3 and Figure 6.20, suggesting that the condition of the starting surface, and perhaps the electrode size affects the surface morphology.

The S_a average after the first immersion is 0.41 µm compared to 1.98 µm after the second immersion indicates that the anodic reactivity is more generally distributed during the first immersion as opposed to the second, this is reminiscent of the results in Chapter 4 where corrosion could be highly localized and then become gradually distributed leading to more lateral corrosion across the surface. This was also reported by Miyamoto et al and Martinez-Lombardia et al. who noted that anodic and cathodic activity could be separated.[7,8] Miyamoto et al. showed that this separation of anodic and cathodic activity between grains was based on the overall grain structure with larger grains making this separation more evident while finer grains did not display a large separation of these behaviours.[7] Also, Martinez-Lombardia et al. stated that the separation of anodic and cathodic behaviour was more pronounced for a specific grain depending on the grain orientation of its neighbours.[8]

The rough intermediate surface morphology is notably different between G3 I2, Figure 6.24B, and G3 I3 MEAs, Figure 6.19B. Instead of a pock-marked surface like on the G3 I3 MEAs, the G3 I2 MEAs have large valleys that are interconnected, which could grow further to interconnect. These results imply that electrode size makes a considerable difference on the resulting corrosion morphology and that immersion time must be changed appropriately as electrode size changes. It could be that the different iterations of the G3 MEAs also have differing grain structures since they were fabricated in different batches at the manufacturer. It is possible that the increased reactive surface size changes the damage pattern by spreading out the anodic/cathodic events or having more grains available for preferential corrosion therefore reducing the corrosion depth. Another possible explanation is that the Cu physical properties are different between MEA iterations. The grains could be different sizes, or the reduced electrode opening could restrict the amount the available grains that have higher surface energy.

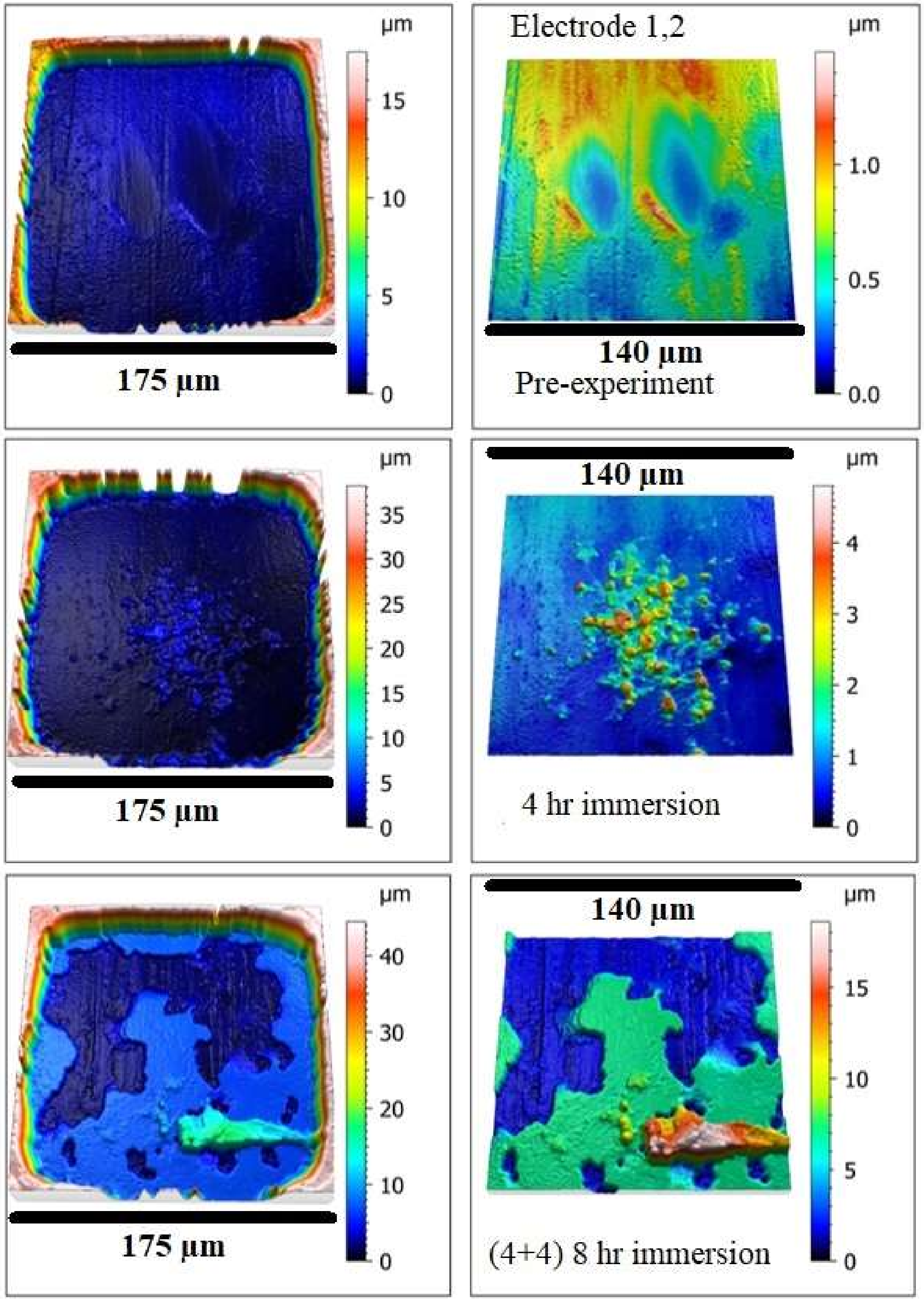

Figure 6.25. 3D reconstructed images of electrode 1,2 on CB0C before, and after 4 and 8 hours of immersion in the Ar-sparged pH 1.5, 0.0374 M [Cu] potential buffer showing a full electrode analysis (left) and an inner electrode analysis (right)

Table 6.4. Roughness values and the associated differences for the first row of electrodes on CB0C before and after both immersions in the Ar-sparged pH 1.5, 0.0374 M [Cu] potential buffer

Electrode	1,1	1,2	1,3	1,4	1,5	Average
Pre-experiment						
S_a (µm)	0.20	0.20	0.25	0.19	0.19	0.21
S_q (µm)	0.24	0.23	0.30	0.23	0.24	0.25
S_z (µm)	17.20	17.10	18.50	18.20	20.00	18.20
4 hr immersion						
S_a (µm)	0.20	0.37	0.62	0.64	0.21	0.41
S_q (µm)	0.24	0.57	0.90	0.89	0.37	0.59
S_z (µm)	38.50	38.20	39.10	38.80	39.10	38.74
Pre-experiment ->4 hr immersion Differences						
S_a (µm)	0.00	0.17	0.37	0.45	0.02	0.20
S_q (µm)	0.00	0.34	0.60	0.66	0.13	0.35
S_z (µm)	21.30	21.10	20.60	20.60	19.10	20.54
(4+4) 8 hr immersion						
S_a (µm)	0.60	2.90	2.50	2.30	1.60	1.98
S_q (µm)	1.20	3.40	2.60	2.40	2.10	2.34
S_z (µm)	44.10	44.50	44.80	44.70	44.90	44.60
4 hr immersion->8 hr immersion Differences						
S_a (µm)	0.40	2.53	1.88	1.66	1.39	1.57
S_q (µm)	0.96	2.83	1.70	1.51	1.73	1.75
S_z (µm)	5.60	6.30	5.70	5.90	5.80	5.86

A G3 I3 MEA, designated as CB0D, was used to test the effect of a longer total immersion time on smaller electrodes to determine whether the final surface morphology would be similar to that observed on larger electrodes from the G3 I2 MEA, CB0C. CB0D was immersed twice in Ar- sparged, 0.0374 M [Cu] solution (pH = 1.5), first for 4 hours, and then for a further 4 hrs for a total of 8 hours.

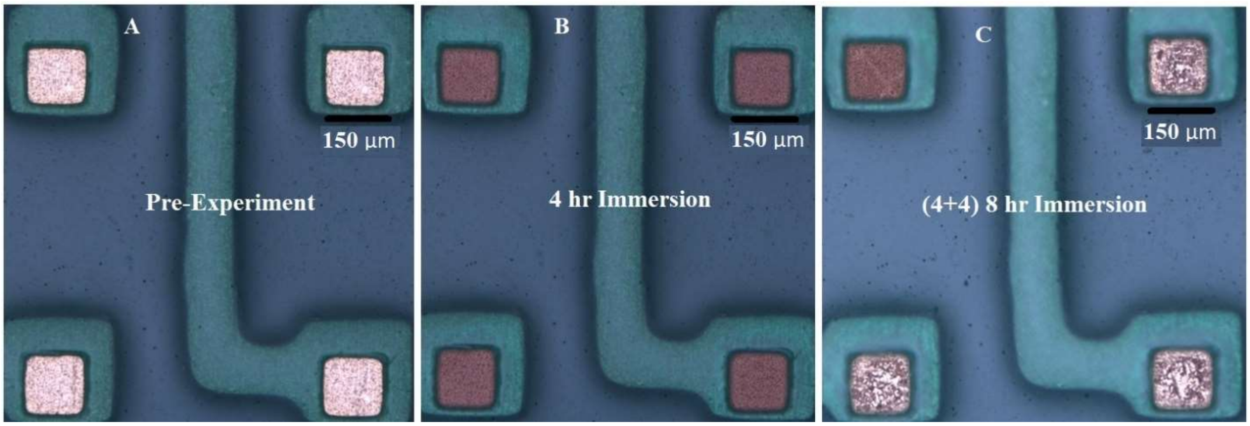

Figure 6.26. Optical images of the upper left quadrant of CB0D before, and after 4 and 8 hours of immersion in the Ar-sparged pH 1.5, 0.0374 M [Cu] potential buffer. These images start with electrode 1,3 in the top left

Differences between the smaller G3 I3 electrodes and larger G3 I2 electrodes are immediately noticeable when examining the optical images collected from CB0D, Figure 6.26. Figure 6.26B shows that after 4 hours of immersion the electrodes have reached the same uniformly corroded surface state experienced by the other G3 I3 MEAs, Figure 6.19D. However, Figure 6.26C shows that after 8 hours of immersion most of the electrodes have the same corrosion damage pattern experienced by CB0C, a G3 I2 MEA, Figure 6.24C. Electrode 1,3 is an outlier shown in the top left section of Figure 6.26C. This electrode barely corroded during the second immersion, similar to the some of the outlier electrodes seen on CB0A.

Table 6.5 shows the roughness values and the associated differences from electrodes 1,1 to 1,5 on CB0D before and after each period of immersion. The S_z values measured on the uncorroded surface are around 20 µm and increase to ~41 µm and 56 µm after the first and second immersion periods, respectively. These values indicate the largest amount of corrosion so far. The second immersion produces a smaller change in S_z compared to the first immersion. Based on the small change in S_a and S_q values (0.04 µm for both values) and the lower change in S_z (20 µm compared to 35-37 µm) between the two immersions, this electrode is supporting less of the anodic reaction compared to the rest of the electrodes. The rest of the 3D reconstructed images indicate an even distribution of the anodic and cathodic reactions across the surface after 4 hours of immersion, indicated by low S_a values (~0.6-0.8 µm). The change in S_a values between immersions is similar to the CB0C, Table 6.4, where the surface is the roughest at the end of the experiment. This is confirmed by the 1,1 electrode 3D reconstructed image in Figure 6.27 which has large interconnected channels on an otherwise flat surface. The most interesting feature of the 3D reconstructed images after the second immersion period is that the lower areas and the upper areas are both extremely flat. This suggests that a longer period of immersion would lead to a more uniformly corroded surface with a more even distribution of the anodic and cathodic reactions across the surface indicated by a low S_a value. The progression in surface morphology observed raises the question of whether this surface morphology is achievable by one long immersion or if it is the product of re-immersion in solution with the oxidant replenished.

Table 6.5. Roughness values and the associated differences for the first row of electrodes on CB0D before and after both immersions in the Ar-sparged pH 1.5, 0.0374 M [Cu] potential buffer. The values highlighted in red indicate an accidental duplicate measurement

Electrode	1,1	1,2	1,3	1,4	1,5	Average
Pre-experiment						
S_a (µm)	0.17	0.22	0.20	0.13	0.24	0.19
S_q (µm)	0.21	0.27	0.24	0.17	0.29	0.24
S_z (µm)	19.80	20.90	20.30	20.20	21.50	20.54
4 hr immersion						
S_a (µm)	0.74	0.64	0.64	0.73	0.79	0.71
S_q (µm)	1.10	0.82	0.82	0.94	1.10	0.96
S_z (µm)	40.30	40.40	40.40	42.20	40.70	40.80
Pre-experiment ->4 hr immersion Differences						
S_a (µm)	0.57	0.42	0.44	0.60	0.55	0.52
S_q (µm)	0.89	0.55	0.58	0.77	0.81	0.72
S_z (µm)	20.50	19.50	20.10	22.00	19.20	20.26
(4+4) 8 hr immersion						
S_a (µm)	2.40	2.40	0.68	2.30	2.10	1.98
S_q (µm)	2.50	2.50	0.86	2.80	2.40	2.21
S_z (µm)	56.00	55.70	40.60	56.00	57.00	56.18
4 hr immersion->8 hr immersion Differences						
S_a (µm)	1.66	1.76	0.04	1.57	1.31	1.27
S_q (µm)	1.40	1.68	0.04	1.86	1.30	1.26
S_z (µm)	15.70	15.30	0.20	13.80	16.30	15.28

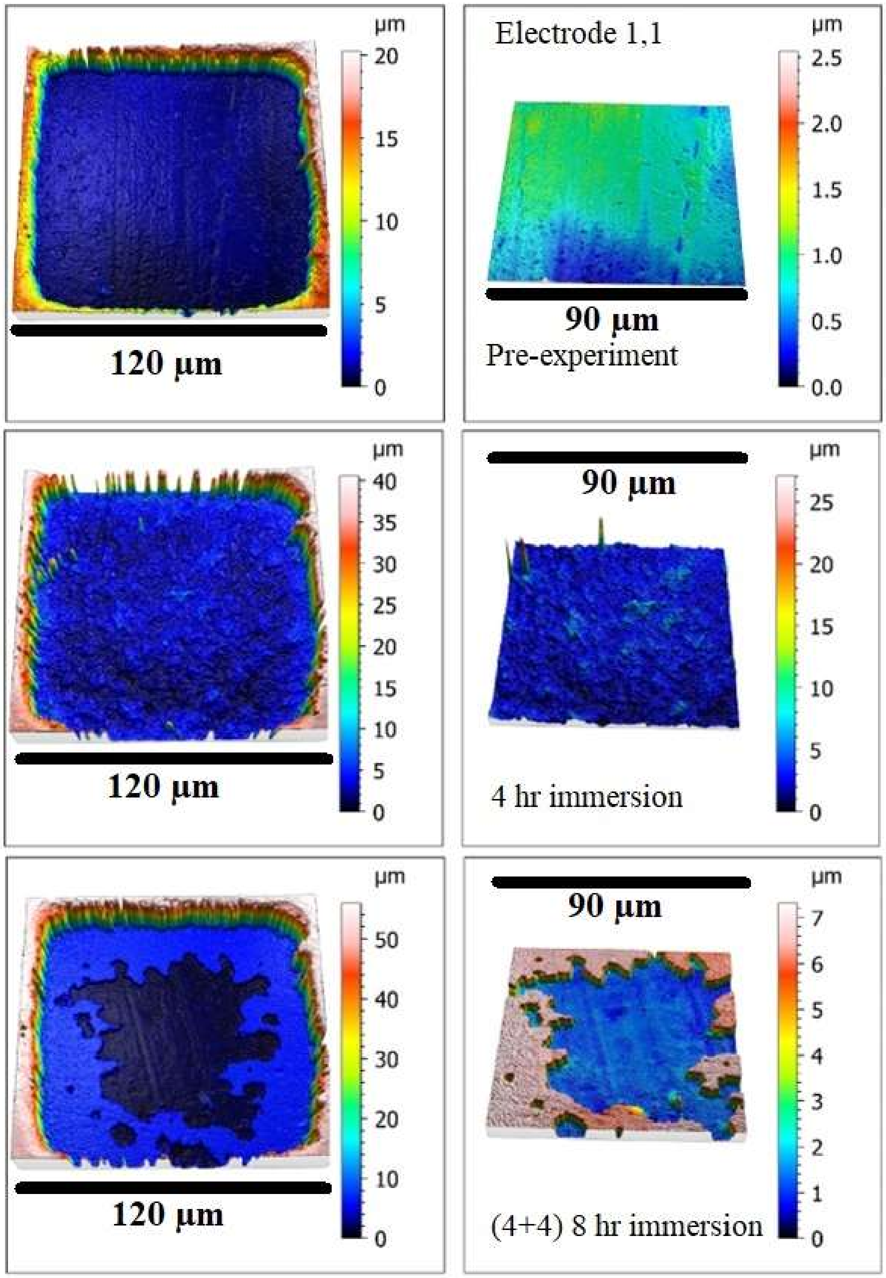

Figure 6.27. 3D reconstructed images of electrode 1,1 on CB0D before, and after 4 and 8 hours of immersion in the Ar-sparged pH 1.5, 0.0374 M [Cu] potential buffer showing a full electrode analysis (left) and an inner electrode analysis (right)

Two MEAs, designated CB0E and CB0F, were used to test the effect of one long immersion on the damage pattern rather than two sequential immersions. These MEAs represent both G3 I2 and G3 I3 MEAs. They were both immersed separately in Ar-sparged, 0.0374 M [Cu] solution (pH = 1.5) for 8 hours.

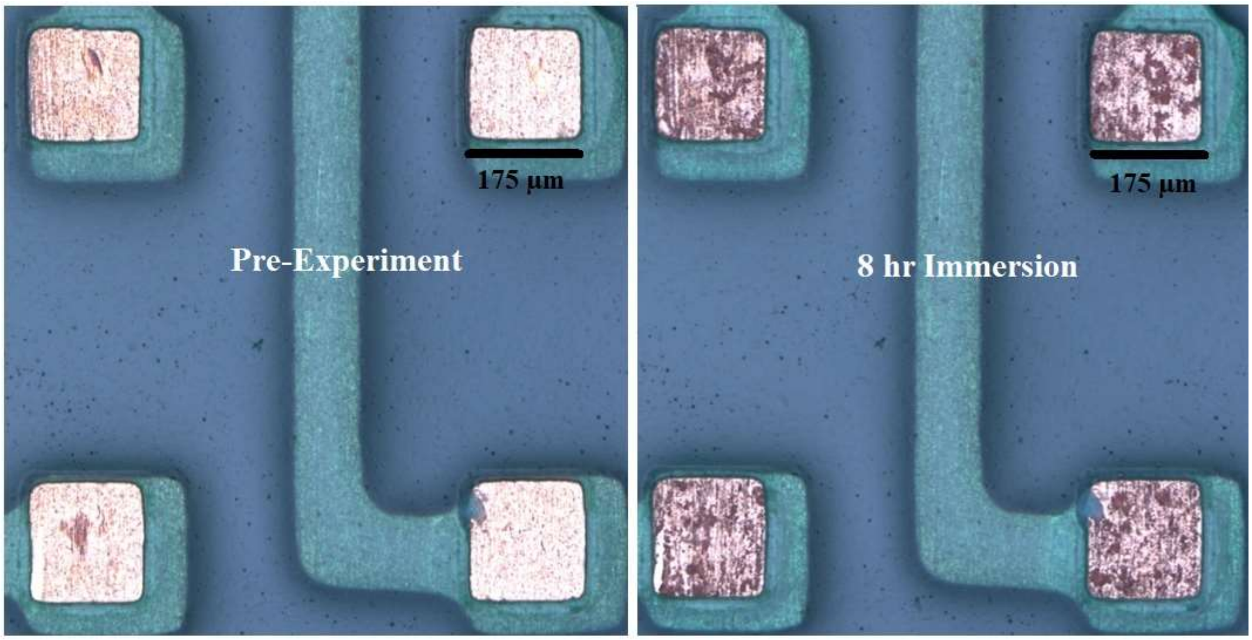

Figure 6.28. Optical images of the upper left quadrant of CB0E before and after 8 hours of immersion in the Ar-sparged pH 1.5, 0.0374 M [Cu] potential buffer

Optical analysis of CB0E reveals that after 8 hours of immersion the surface morphology is different compared to CB0C, the other G3 I2 MEA, Figure 6.24B. Figure 6.28 shows the optical image of 4 electrodes before and after 8 hours of immersion in the Ar-sparged, pH 1.5 potential buffer. The surface looks slightly more corroded compared to the surface topography produced by immersing CB0C for 4 hours in the Ar-sparged, pH 1.5 potential buffer, but not as corroded as the surface topography produced by immersing CB0C for 8 hours in the Ar-sparged, pH 1.5 potential buffer, Figure 6.24C. The roughness parameters for this experiment are listed in Table 6.6. The initial S_z values are between 18 and 20 µm and change by ~20 µm after immersion. The exception is electrode 1,3 which changes by 32 µm. The S_a values are also not as consistent as seen on previous samples, exhibiting a wide range of values (1.0-4.6 µm).

These changes in S-values are different compared to those observed on other G3 I3 MEAs and G3 I2 MEAs. The 3D reconstructed images in Figure 6.29 do not match up correctly to the optical images in Figure 6.28 which shows large holes on a mostly flat surface. This creates the large discrepancy in the S_z and S_a values. When looking at the data used to build the 3D reconstructed images, the greyscale image from electrode 1,3 shown in Figure 6.30, appears normal, Figure 6.31. However, a SEM image of electrode 1,3 clarifies the real surface morphology. The SEM shows the electrode surface is pockmarked and uneven with multiple small perforations, indicating that more corrosion occurred on the surface than is apparent in the 3D reconstructed image. These optical and SEM images indicate that when the surface is pockmarked (with many small holes with little distance between) then a 3D image cannot be accurately analyzed and reconstructed using CLSM. The surface morphology seen in Figure 6.31 implies this electrode exhibits corrosion between the intermediate and final surface morphologies seen on CB0B. However, this sample has exposed a flaw in the CLSM analysis that should be avoided.

Table 6.6. Roughness values and the associated differences for the first row of electrodes on CB0E before and after immersion in the Ar-sparged pH 1.5, 0.0374 [M] potential buffer

Electrode	1,1	1,2	1,3	1,4	1,5	Average
Pre-experiment						■
S_a (μm)	0.40	0.31	0.41	0.39	0.34	0.37
S_q (μm)	0.49	0.37	0.50	0.46	0.42	0.45
S_z (μm)	20.10	18.70	18.40	19.50	18.10	18.96
8 hr immersion						■
S_a (μm)	2.10	0.98	1.90	4.60	3.50	2.62
S_q (μm)	4.20	2.50	3.70	6.60	5.60	4.52
S_z (μm)	38.00	38.00	52.00	39.00	39.00	41.20
Pre-experiment -> 8 hr immersion Differences						■
S_a (μm)	1.70	0.67	1.49	4.21	3.16	2.25
S_q (μm)	3.71	2.13	3.20	6.14	5.18	4.07
S_z (μm)	17.90	19.30	33.60	19.50	20.90	22.24

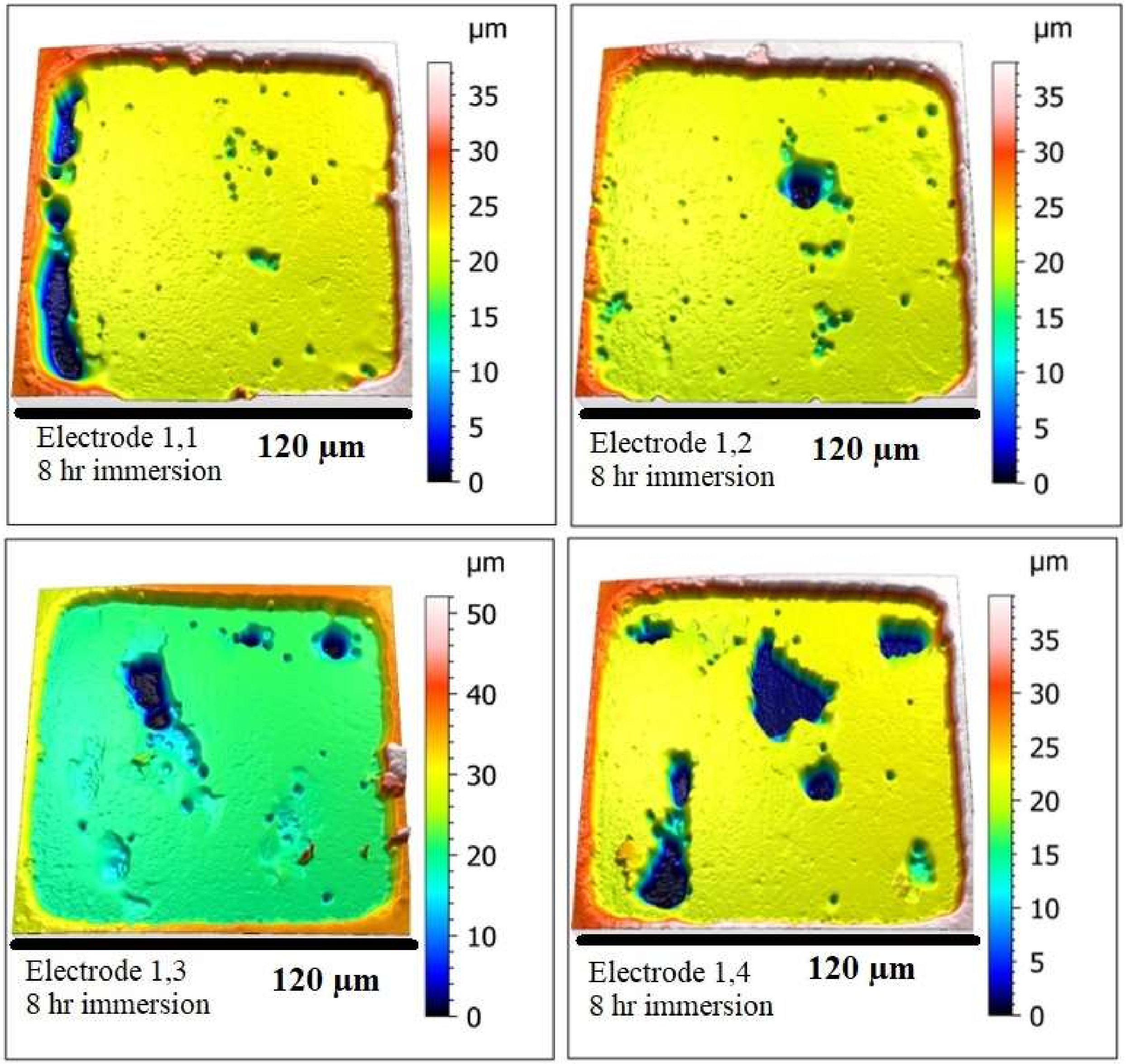

Figure 6.29. Full electrode 3D reconstructed images of four electrodes on CB0E after 8 hours of immersion in the Ar-sparged pH 1.5, 0.0374 M [Cu] potential buffer

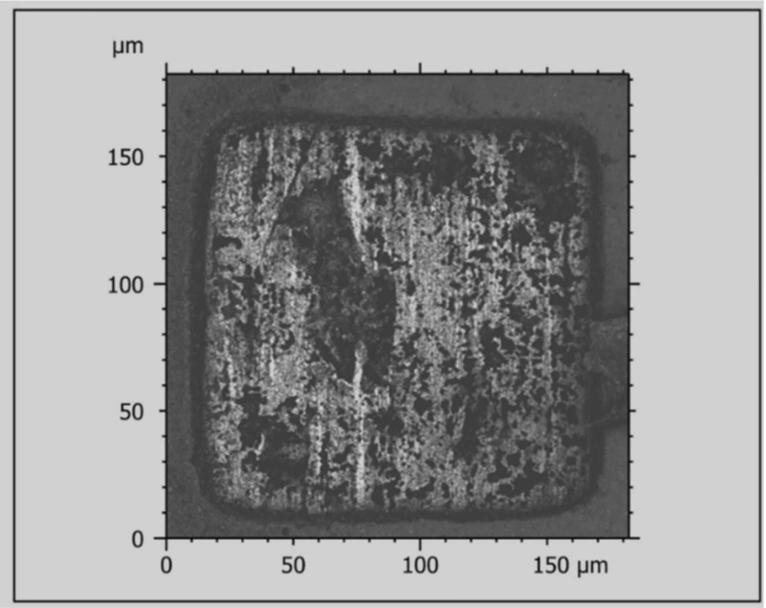

Figure 6.30. The greyscale image of electrode 1,3 on CB0E after 8 hours of immersion in the Ar-sparged pH 1.5, 0.0374 M [Cu] potential buffer used to create the 3D reconstructed image

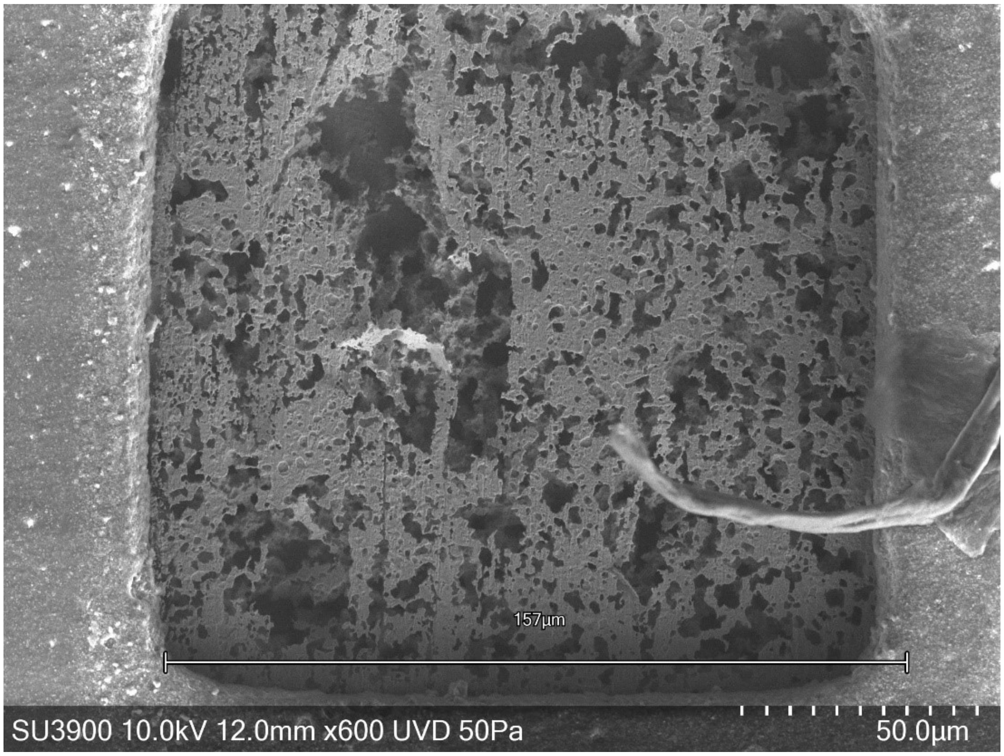

Figure 6.31. A SEM image of electrode 1,3 on CB0E after 8 hours of immersion in the Ar-sparged pH 1.5, 0.0374 M [Cu] potential buffer

The final G3 I3 MEA analyzed, designated CB0F, was used to study the impact of a single long immersion on smaller electrodes. Similar to CB0E, the surface morphology produced on the CB0F electrodes after 8 hrs of immersion seems to be in between the intermediate and final surface morphologies observed on G3 I3 MEAs, Figure 6.19 and Figure 6.26. The optical images, Figure 6.32 show darkened electrodes with a few bright spots. Based on previous results, the bright spots are material with higher elevation compared to the dark material. Based on the results, these higher elevation areas have a lower corrosion rate than the majority of the surface, likely due to grain orientation, Chapter 4. Figure 6.33 confirms that corrosion is general but unevenly distributed on the darkened areas of the electrode surface. Table 6.7 shows the roughness values for the first five electrodes on CB0F. All electrodes exhibit a similar trend with electrodes from other MEAs. The initial S_z values are in the range of 19 to 22 μm and, after immersion are 38 to 41.4 μm. These results show the extent of corrosion after one long or two short immersions is similar across the G3 I3 and G3 I2 MEAs, Tables 4-7. The similarity in S_z values confirms that the extent of corrosion and the surface roughness are dependent on the initial surface and the surface concentration of oxidant not whether the experiment is conducted over two short periods or one long period. The large variance in S_a values for CB0F produced by 8 hours of immersion in the Ar-sparged, pH 1.5 0.0374 M [Cu] potential buffer solution are due to the small areas containing slow-reacting material on some of the electrodes, seen as bright spots in Figure 6.32 which are thought to be low surface energy grains. The remaining elevated material and resulting surface topography suggest that these electrodes are proceeding towards the final corrosion pattern seen on G3 I3 MEAs like CB0B, Figure 6.19. This is supported by electrode 1,1 which has the lowest measured S_a value of 1.2 μm and is the most uniformly corroded according to the 3D reconstructed images.

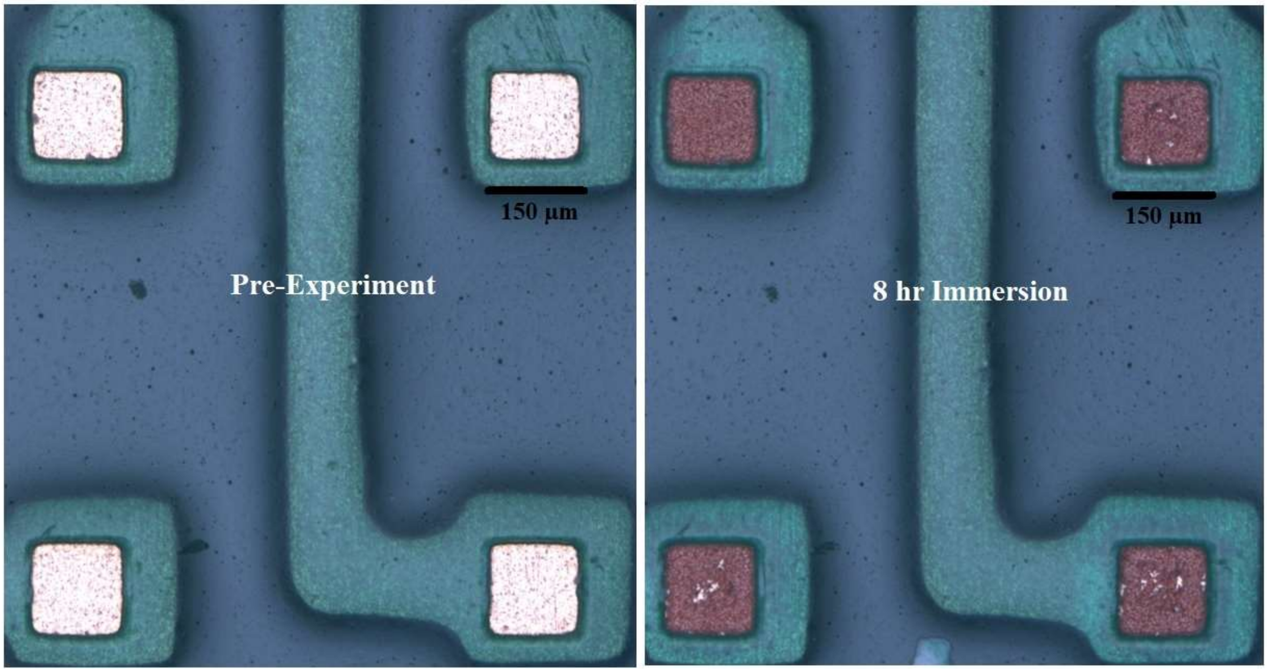

Figure 6.32. Optical images of the upper left quadrant of CB0F before and after immersion in the Ar-sparged pH 1.5, 0.0374 M [Cu] potential buffer

Table 6.7. Roughness values and the associated differences for the first row of electrodes on CB0F before and after immersion in the Ar-sparged pH 1.5, 0.0374 M [Cu] potential buffer

Electrode	1,1	1,2	1,3	1,4	1,5	Average
Pre-experiment						
S_a (µm)	0.28	0.19	0.26	0.24	0.31	0.26
S_q (µm)	0.34	0.24	0.30	0.31	0.36	0.31
S_z (µm)	19.10	20.60	22.10	20.70	20.50	20.60
8 hr immersion						
S_a (µm)	1.20	2.40	3.70	4.60	2.80	2.94
S_q (µm)	1.50	3.30	4.60	5.40	3.80	3.72
S_z (µm)	41.40	38.00	38.00	39.00	38.00	38.88
Pre-experiment -> 8 hr immersion Differences						
S_a (µm)	0.92	2.21	3.44	4.36	2.49	2.68
S_q (µm)	1.16	3.06	4.30	5.09	3.44	3.41
S_z (µm)	22.30	17.40	15.90	18.30	17.50	18.28

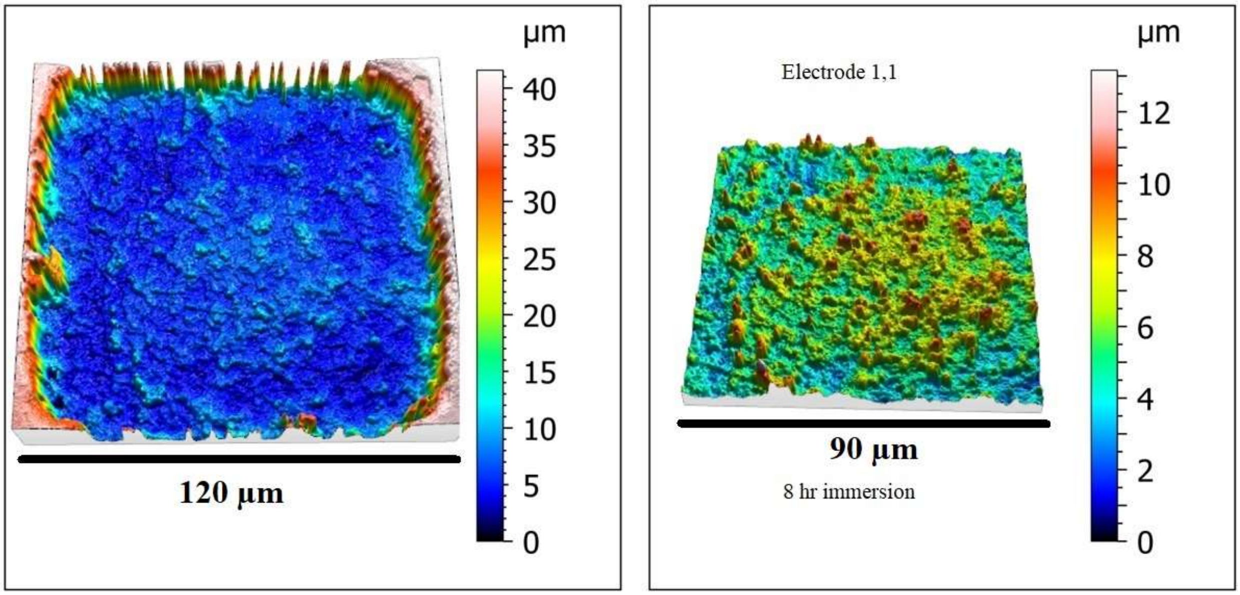

Figure 6.33. 3D reconstructed images of electrode 1,1 on CB0F after 8 hours of immersion in the Ar-sparged pH 1.5, 0.0374 M [Cu] potential buffer including full electrode analysis (left) and inner electrode analysis (right)

The results from CB0E and CB0F support the idea that over the course of the immersion in the potential buffer solution the local concentration of oxidant is depleted or its transport to the reactive surface is slow in the stagnant solution. Local concentration depletion of oxidant at the reactive surface would explain the continued corrosion that occurs after a second immersion, though the more even distribution of anodes and cathodes cannot be attributed to the surface replenishment of the oxidant. The corrosion seen on CB0B, Figure 6.19, is similar to that on CB0F; however, the total immersion time of CB0B is half that of CB0F, yet CB0B is more uniformly corroded than CB0Fs. Therefore, it is probable that as the surface preferentially corrodes, likely based on grain orientation, a point is reached where the more corroded (lower height) grains, which predominantly supported the anodic reaction, are lower in energy compared to the less corroded (higher height) grains that predominantly supported the cathodic reaction. Eventually, as the higher energy surfaces are destroyed, the surface would become more uniformly susceptible to corrosion, which would lead to a more even distribution of the cathodic and anodic reaction across the surface. This could be correlated to the section in the individual current vs time plots where most electrodes undergo a significant current spike when first immersed (when the surface energies of the different grains are at their highest), followed by a flattening of the current response to a more stable value (when the grains become closer in energy and the anodic/cathodic reaction separation decreased), as seen in Figure 6.34. It is possible that, on re-immersion, when the local oxidant would initially not be depleted at the Cu surface, this process could recur leading to a more exaggerated corrosion pattern compared to that observed after a single long immersion.

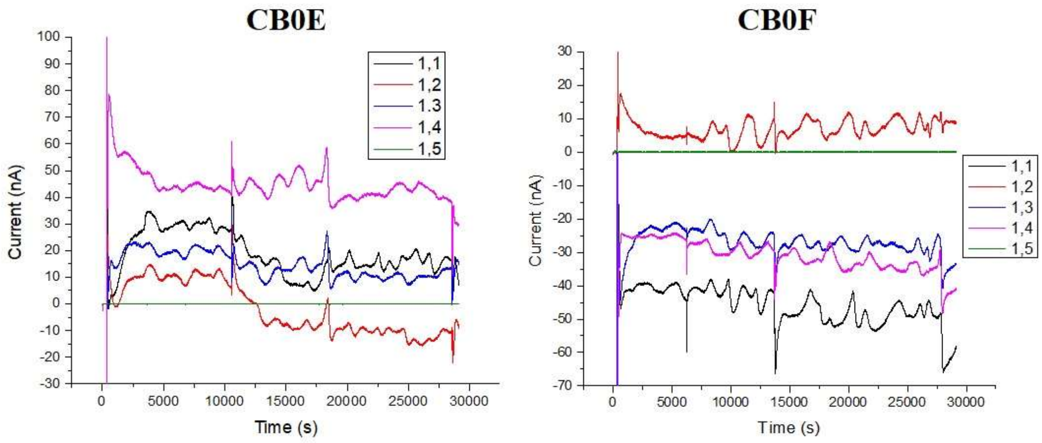

Figure 6.34. Current versus time plots for the first five electrodes in the first row on CB0E (left) and CB0F (right) during 8 hours of immersion in the Ar-sparged pH 1.5, 0.0374 M [Cu] potential buffer

Based on the results from CB0B, CB0C, CB0D, CB0E and CB0F, it is likely that if the isolation of individual anodes/cathodes was possible during roughening at E_{corr} it would be on a much smaller scale. The size at which isolation of a single anodic/cathodic event is possible could be estimated by determining the reactive surface area of the slowly reacting (higher region material) material seen on some G3 I3 MEA, like CB0F, Figure 6.32. Therefore, a reliable method for isolating anodic and cathodic events may not be possible with these MEAs. However, the preferential corrosion seen on the G3 MEAs and SKB Cu (from Chapter 4) suggests that the corrosion process is dependent on grain orientation or grain boundary angles. Based on previous studies mentioned in section 1.5.2 by Vitos, Setty and Mayanna, Mayanna and Vvedenskii the grains that are preferentially dissolving can be predicted.[9,10,11,12] From these studies it is clear that the (110) grain orientation will dissolve the fastest while the (100) and (111) orientations will dissolve at slower and similar rates. If surface adsorption plays a role, in the dissolution process, as seen in the studies performed by Huang et al, then the grain size must be considered as well.[13] The smaller grain sizes could reduce the difference between the grain orientation dissolution rates such that they are more even since the adsorption of reactive species such as Cl^- and O_2 is not distinctly selective for specific grain orientations. The limited depth penetration could also suggest that uncorroded material with multiple exposed faces is more reactive than the uniformly corroded regions after re-immersion in fresh solution. It is also possible that the length of the experiment matches a point at which the dissolution rates of all the grain orientations have normalized due to the adsorption and local depletion of the reactive species. Smaller immersion intervals could help elucidate the process and clarify which grains dissolve preferentially. Using smaller intervals, the surface could be imaged while initially roughening before the surface becomes more uniformly corroded.

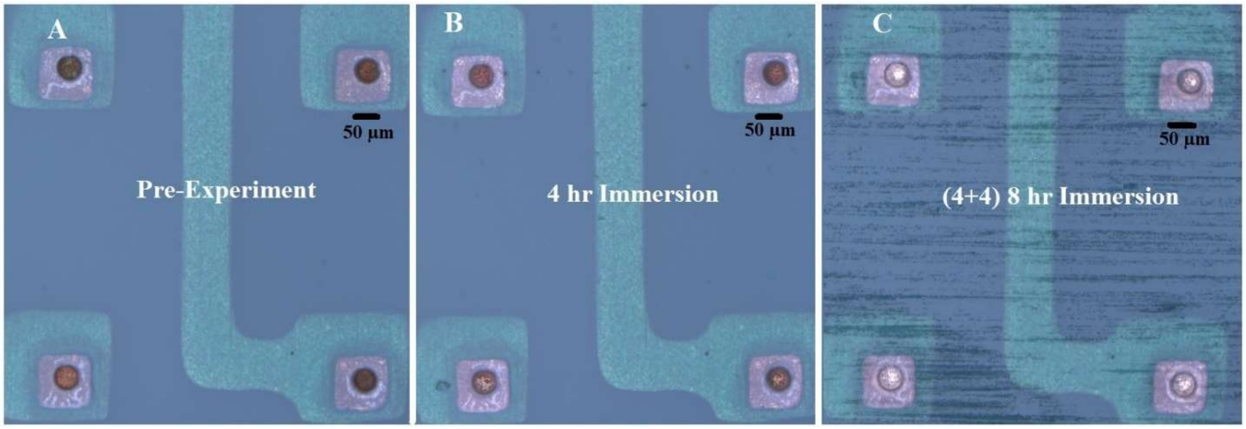

Figure 6.35. Optical images of the upper left quadrant of CB40K before, and after 4 and 8 hours of immersion in the Ar-sparged pH 1.5, 0.0374 M [Cu] potential buffer

The last attempt to distinguish individual anodes and cathodes was performed with CB40K, a G3 I3 Su8-coated MEA. The exposed electrode area was a 50 µm diameter circle for each electrode. It is important to note that CB40K had already been used twice in Ar-sparged Cl^- and SO_4^{2-} solutions and was stored in a transfer container for months prior to this experiment. Therefore, the MEA had a small amount of native oxide on the electrodes as indicated by the dark colour of the electrodes in Figure 6.35A.

Figure 6.35 shows a time series of optical images of CB40K. Initially, the electrodes were quite dark, Figure 6.35A, and after 4 hours of immersion in the Ar-sparged, pH 1.5 0.0374 M [Cu] potential buffer were slightly brightened, Figure 6.35B. Figure 6.35C shows that after 8 hours of immersion the electrodes are much brighter than the unexposed surface. The optical image after the first 4 hours of immersion in the Ar-sparged, pH 1.5 potential buffer is similar to that of the

CB0F electrodes after 8 hours of immersion in the Ar-sparged, pH 1.5 potential buffer, Figure 6.32. After 8 hours of immersion in the Ar-sparged, pH 1.5 potential buffer the final surface morphology resembles that observed on the CB0C electrodes after 8 hours of immersion in the Ar-sparged, pH 1.5 potential buffer, Figure 6.24C. While the optical analysis shows some resemblance to already observed corrosion patterns, such as those on CB0B, Figure 6.19, the 3D reconstructed images in Figure 6.36 indicate that the patterns do not actually bear any resemblance to any previous corrosion patterns in this thesis. The surface morphologies resemble those seen in a study conducted by Arjmand and Adriaens in which a microcapillary cell (100 μm diameter) was filled with 1 M NaCl and potentiostatically polarized to corrode Cu and investigate the surface morphology.[14] After 4 hours of immersion in the pH 1.5 potential buffer the electrodes show some very rough areas, indicating the available grains have significant surface energy differences. However, after a total of 8 hours of immersion in the Ar-sparged, pH 1.5 potential buffer solution the electrodes appear uniformly corroded with little roughness, similar to the ultra-fine grained Cu studied by Miyamoto et al.[7]

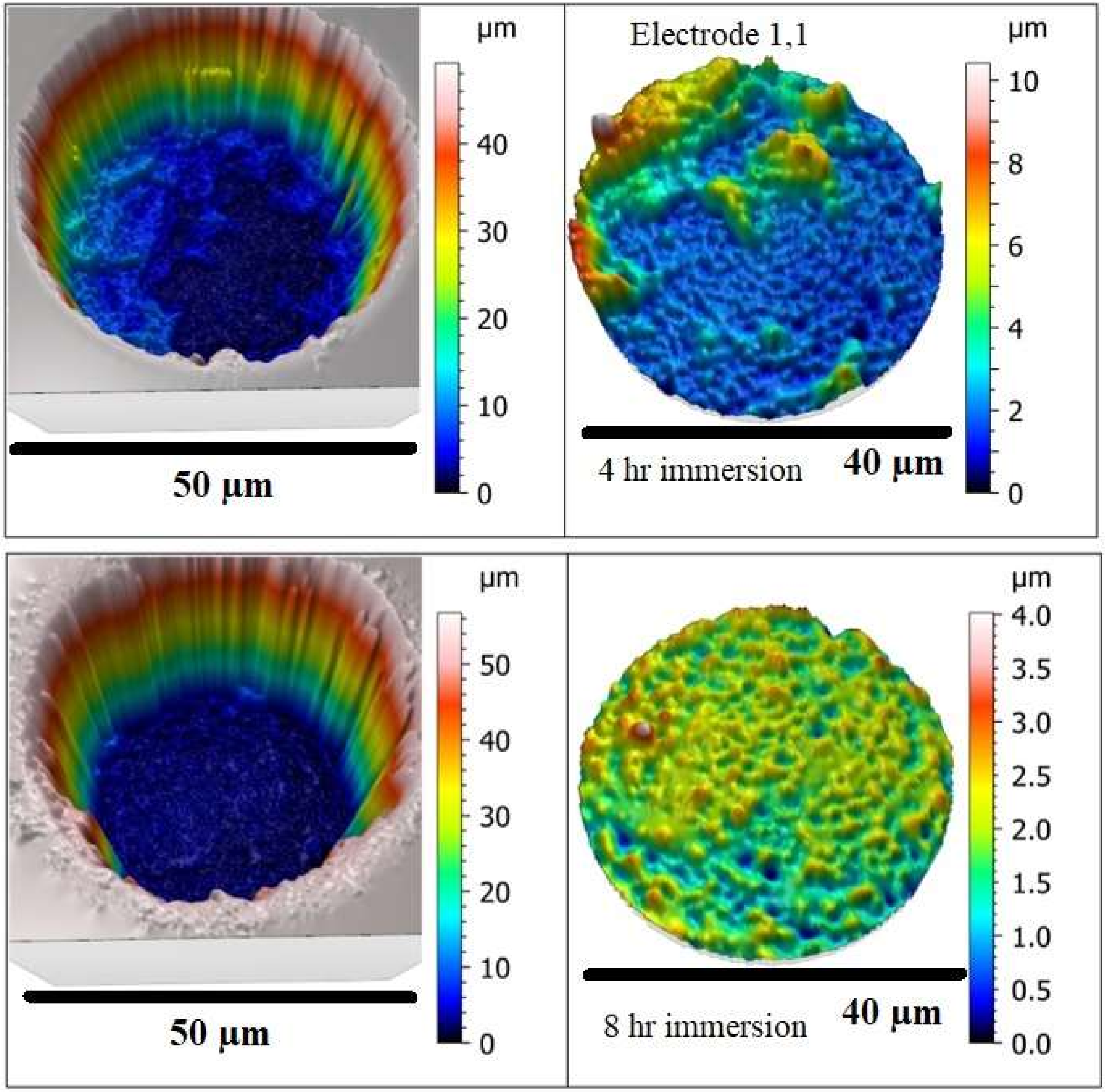

Figure 6.36. 3D reconstructed images of electrode 1,1 on CB40K after both 4 hour immersions in the Ar-sparged pH 1.5, 0.0374 M [Cu] potential buffer including full electrode analysis (left) and inner electrode analysis (right)

Table 6.8. Roughness values and the associated differences for the second row of electrodes on CB40K before and after both immersions in the Ar-sparged 1.5, 0.0374 M [Cu] potential buffer, outlier values are highlighted in red

Electrode	2,1	2,2	2,3	2,4	2,5	2,6	Average
Pre-experiment							
S_a (µm)	0.13	0.13	0.09	0.11	0.17	0.10	0.12
S_q (µm)	0.15	0.17	0.11	0.14	0.33	0.12	0.17
S_z (µm)	23.00	22.00	20.90	22.00	26.00	23.00	22.82
4 hr immersion							
S_a (µm)	1.20	0.78	0.09	1.30	1.20	0.45	0.99
S_q (µm)	1.60	1.00	0.11	1.60	1.50	0.74	1.29
S_z (µm)	49.00	48.00	21.00	48.00	51.00	48.00	48.80
Pre-experiment ->4 hr immersion Differences							
S_a (µm)	1.07	0.65	0.00	1.19	1.03	0.36	0.86
S_q (µm)	1.45	0.83	0.00	1.46	1.17	0.62	1.11
S_z (µm)	26.00	26.00	0.10	26.00	25.00	25.00	25.60
(4+4) 8 hr immersion							
S_a (µm)	0.31	0.32	0.19	0.29	0.31	0.42	0.33
S_q (µm)	0.40	0.41	0.25	0.38	0.42	0.53	0.43
S_z (µm)	57.00	55.00	46.00	56.00	59.00	55.00	56.40
4 hr immersion->8 hr immersion Differences							
S_a (µm)	-0.89	-0.46	0.10	-1.01	-0.89	-0.03	0.66
S_q (µm)	-1.20	-0.59	0.14	-1.22	-1.08	-0.21	0.86
S_z (µm)	8.00	7.00	25.00	8.00	8.00	7.00	7.60

Table 6.8 shows the roughness values of the electrodes in the second row on CB40K before and after both 4 hour immersions in the Ar-sparged, pH 1.5 0.0374 M [Cu] potential buffer. As observed on other G3 I3 and G3 I2 MEAs, the relative S_z changes are similar across all electrodes starting at ~23 µm and increasing to ~49 µm and then ~56 µm, indicating the separation of anodes

and cathodes on different grains is greater over the first immersion period, as observed on all other G3 MEAs, Tables 6.4-6.7. The S_z values also confirm that the Su8 coating is only ~1-7 μm thick since the uncoated MEAs typically have initial S_z values of ~19-20 μm while this sample has values ranging between 21-26 μm. The S_a values for this sample are the highest after the first immersion, while the second immersion leads to values closer to the pre-immersion values, indicating a more uniformly corroded surface with very little roughness.

The current responses do not elucidate any clear trends regarding anodic and cathodic behaviour isolation on CB40K, however electrode 2,3 presents an interesting case, Figure 6.37. After the first immersion, the roughness parameters associated with electrode 2,3 change negligibly and the current vs time plot, shown in Figure 6.37A, indicates the cathodic reaction predominantly occurred on this electrode. During the second immersion electrode 2,3 behaves differently, as shown in Figure 6.37B. The current response shows some initial anodic spikes followed by a long cathodic region. The current versus time plots for other electrodes in the same row, such as electrode 2,2, show conflicting trends, Figure 6.38. Electrode 2,2 has a strong anodic current response, as shown in Figure 6.38A, but does not have different S_a or S_z values compared to other electrodes in its row after 8 hours of immersion in the Ar-sparged, pH 1.5 potential buffer, indicating its corrosion is likely not any deeper or rougher than the other electrodes in the row, Table 6.8. Therefore, the magnitude of the current cannot be associated directly with S_a or S_z. While the predominance of the cathodic or anodic reaction during the immersion in the Ar-sparged, pH 1.5 potential buffer can be correlated to the current response, a direct correlation to the roughness values and surface morphology cannot be made, making this process inconclusive for E_{corr} measurements. It is possible that the separation between anodic and cathodic activity is not great enough at E_{corr} to be accurately detected by the MMA. Thus, in order to confirm that the MMA is accurately detecting the separation between anodic and cathodic activity on a G3 MEA, a system was chosen for which the separation should be more obvious. The chosen system was polarized growth of Cu_2S films.

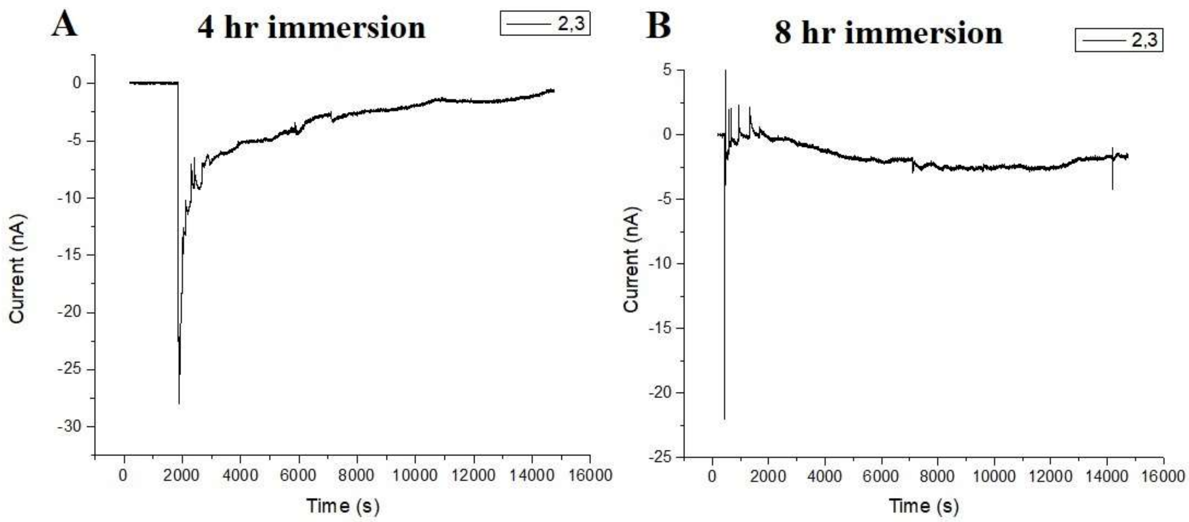

Figure 6.37. The current versus time plots for electrode 2,3 on CB40K during both of its immersions in the Ar-sparged pH 1.5, 0.0374 M [Cu] potential buffer

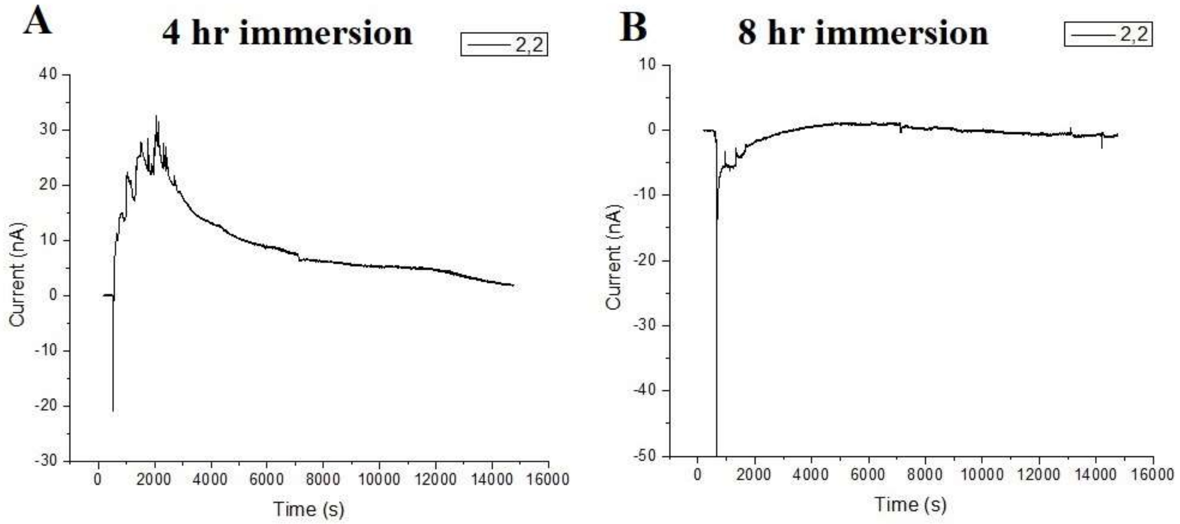

Figure 6.38.The current versus time plots for electrode 2,2 on CB40K during both of its immersions in the Ar-sparged pH 1.5, 0.0374 M [Cu] potential buffer

6.2.3 Observing the Separation of Anodes and Cathodes using Cu_2S Films

The polarized growth of Cu_2S films was performed as a standardization experiment to prove that the currents measured during immersions in the Ar-sparged, pH 1.5 potential buffer solution are accurate and that anodic/cathodic isolation is not possible with electrode surface areas of 7854-30726 μm^2. The G3 I2 MEA used in this experiment was designated as CBS0A, with the S0 indicating there was no Su8 film and SH^- was used in the experiment. This experiment was conducted by growing a very thin Cu_2S film on approximately half the electrodes by placing the cell over half of the MEA and polarizing the covered electrodes at -0.4 V vs SCE for 30 min in a 10^{-3} M SH^- solution.[15] After film growth the MEA was immersed in a 10^{-3} M SH solution for a day and the currents observed on individual electrodes at E_{corr} were measured to determine if the existing sulfide film would couple to the fresh Cu electrodes and cause the electrodes with the pre-grown film to predominantly support the cathodic reaction and the fresh Cu to predominantly support the anodic reaction. No analysis was performed on the pre-grown film. The structure and appearance of the films are well-documented in the study performed by Guo et al.[15]

Time sequences of the colour current display given by the MMA are shown in Figure 6.39 and Figure 6.40, these rectangular grids are created to replicate the shape of the MEA and the position of electrodes within the MEA boundaries. Each square represents a single electrode in the MEA while the colour of the electrode dictates the magnitude and sign of the current the electrode is experiencing based on the relative scale chosen within the MMA software. The square below the time sequence of the colour current displays indicate the colour representation used within these displays. If the square is red or purple then large, positive current was measured on that electrode. If the square is yellow or green then small currents were measured on that electrode, yellow indicating positive current and green indicating negative current. If the square is white then zero current was measured on that electrode. If the square is light or dark blue then large, negative currents were measured on that electrode. Black squares were omitted from the measurement. Nulling was performed from 0-300s after which the solution was added to the cell. The initial current measured on the electrodes in Figure 6.39, is opposite of the expected behaviour for the electrodes. In the first 200s of the experiment after solution is added the electrodes with the pre-grown Cu_2S film (the left half of the colour display) are anodes (purple squares), whereas experiments performed by Chen et al indicate that they should be cathodes.[16] However, by 520s the electrodes have developed the expected behaviour with the left half of the board which has pre-grown Cu_2S films acting as cathodes (dark blue and light blue squares). After this separation of cathodes (left) and anodes (right) has been established (between 300 and 520s), Figure 6.39, the current pattern remained relatively unchanged for the remaining exposure period, Figure 6.40.

The individual current vs time plots, Figure 6.41, indicate different types of current responses. Each type of response has an initial anodic or cathodic current spike when solution is added. After this spike, two main types of current responses occur. The first response is that the current remains weakly anodic or cathodic, while the second trend is that the current starts anodic or cathodic before switching sign multiple times. Figure 6.41A shows the first type of current response. The second current response can be seen in Figure 6.41B, Figure 6.41C, and Figure 6.41D. Based on these responses, combined with the optical images of each electrode, it is possible that anodic and fluctuating current responses can be associated with the formation of thin Cu_2S films on the clean electrodes, and the formation of the high locations where Cu_2S has deposited and low locations which are more corroded but not covered by deposits or uncorroded on the electrodes that were already covered by a Cu_2S film. It appears that a cathodic current response has no major impact on the surface morphology of the electrodes.

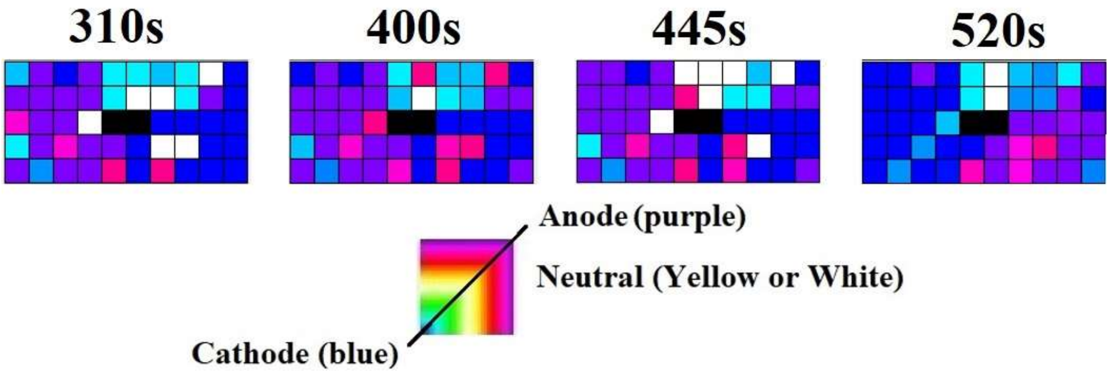

Figure 6.39. A time sequence of the MMA current colour display used to indicate anodic or cathodic behaviour for electrodes during the first 220s of CBS0A's immersion in 10^{-3} M SH^- solution

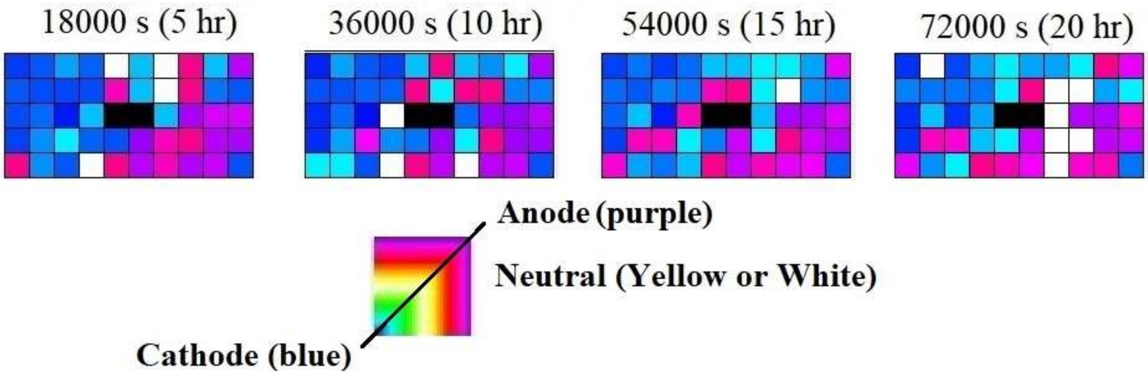

Figure 6.40. A time sequence of the MMA current colour display used to indicate anodic or cathodic behaviour for electrodes over the course of CBS0As immersion in 10^{-3} M SH^- solution for a day

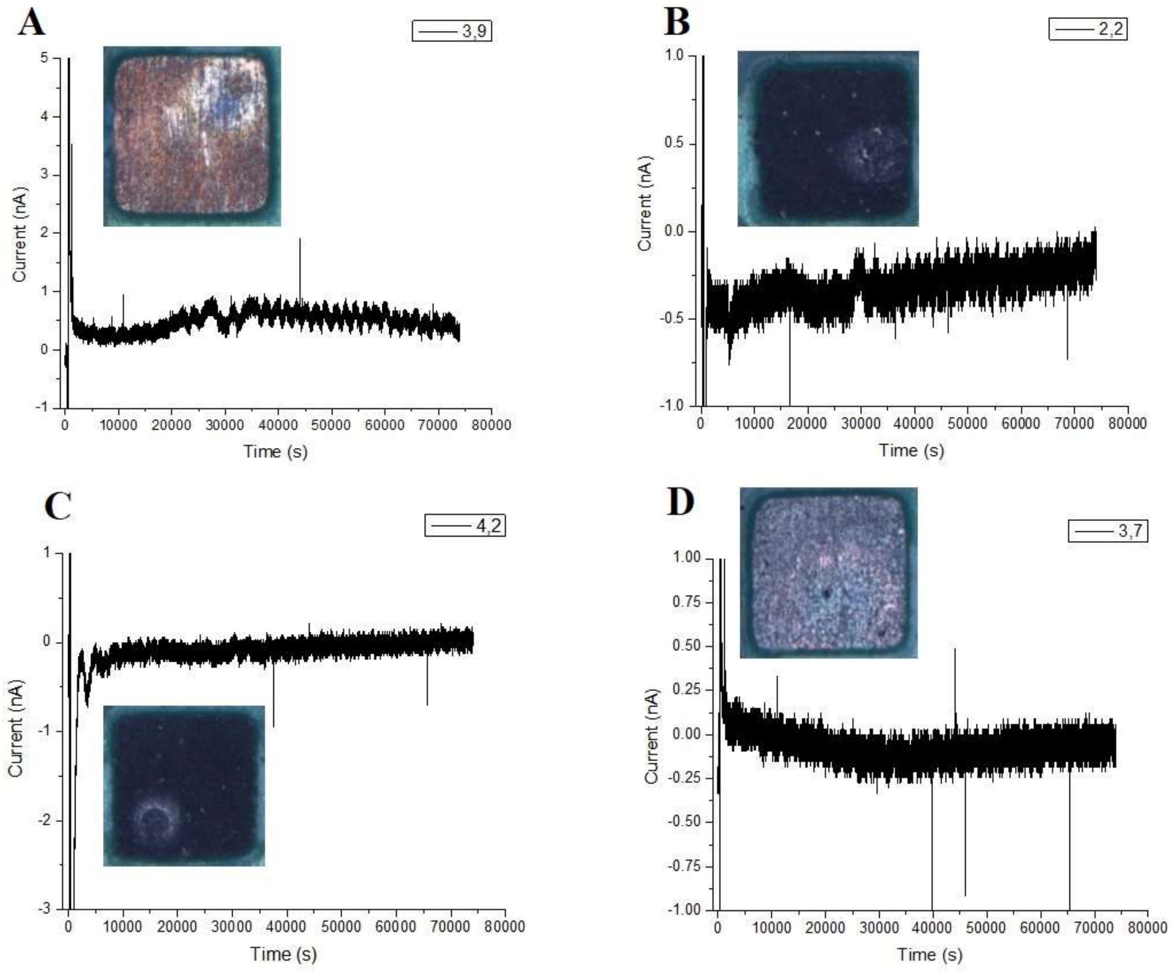

Figure 6.41. Current versus time plots for individual electrodes after immersion in 10^{-3} M SH^- solution for a day with accompanying optical images

The 3D reconstructed images of electrodes 3,1; 3,2; 3,8 and 3,9, Figure 6.42, show a noticeable difference in surface morphology between the electrodes with pre-grown Cu_2S films and the initially clean electrodes. Most of the electrodes that had the pre-grown Cu_2S film have a large difference between high and low features on their surfaces. These images show high areas indicate the presence of Cu_2S corrosion product deposits and low areas which are either not corroded or corroded only slightly. These features from Figure 6.42A and Figure 6.42B were analyzed using a line profile in Figure 6.43A and Figure 6.43C (recorded along the black lines shown in Figure 6.43B and Figure 6.43D, respectively). The line profiles in Figure 6.42A and Figure 6.42B confirm these differences in behaviour suggesting locations where anodes and cathodes may be distinctly separated. Conversely, Figure 6.42C and Figure 6.42D show no significant differences in surface topography, a scuff mark originally present on the electrode being clearly visible (indicated by the red circle) in Figure 6.42C.

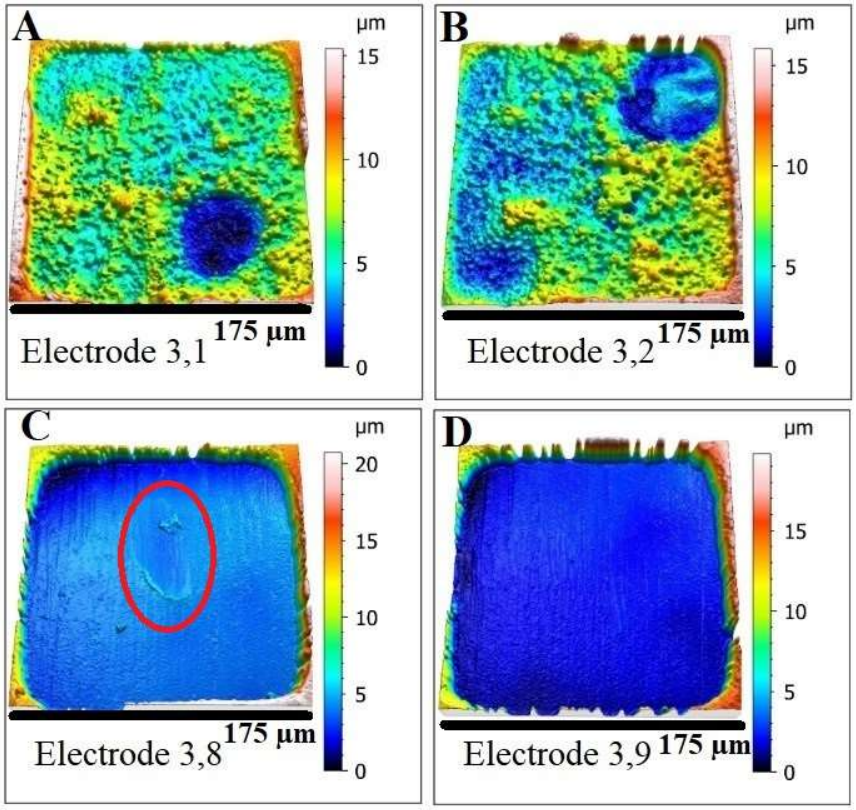

Figure 6.42. 3D reconstructed images of electrodes after a day of immersion in 10^{-3} M SH^{-} solution. The top row of electrodes were covered with a pre-grown Cu_2S film while the bottom row were initially clean electrodes

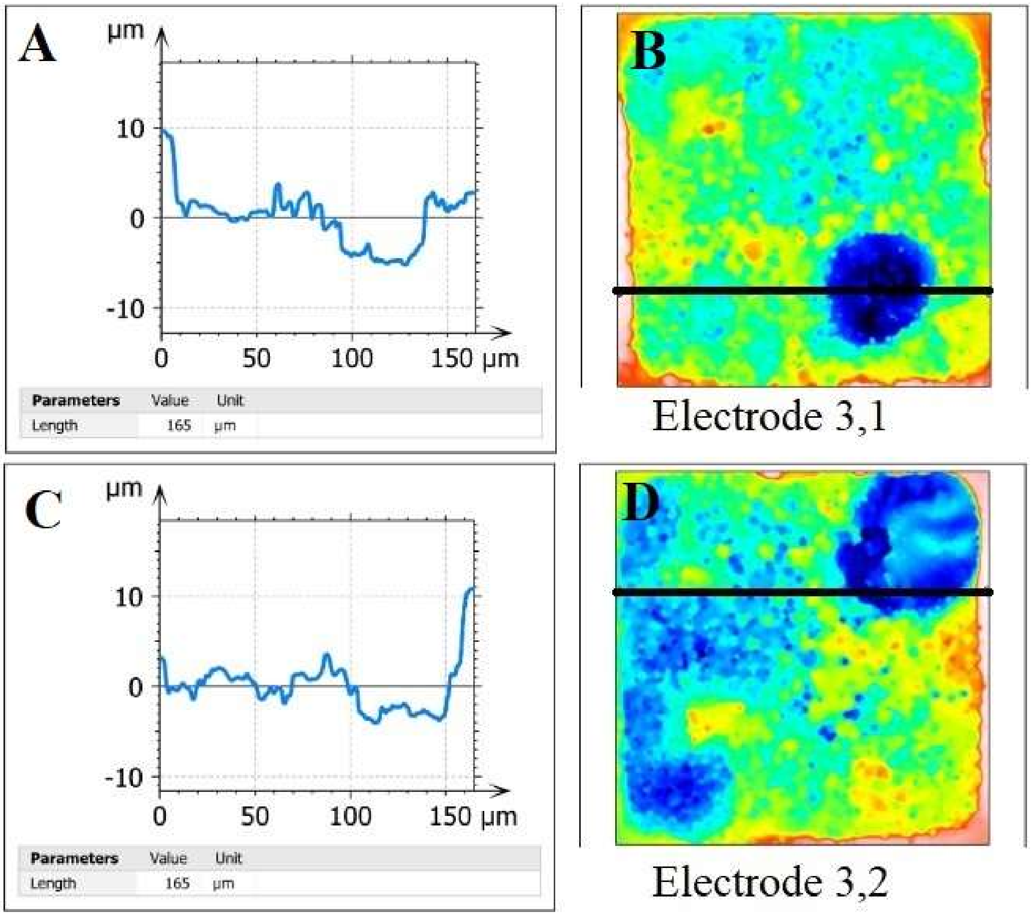

Figure 6.43. Profile scans from low and high areas on electrodes that had pre-grown Cu_2S films after 1 day of immersion in 10^{-3} M SH^- solution. The black line in the right images indicates where the profiles were located on the surface

Figure 6.44. Optical images of electrodes 3,3-3,6 after 1 day of immersion in 10^{-3}M SH^-, highlighting the difference in film grown between the pre-grown Cu_2S films and the previously clean Cu

The separation of high and low areas due to local anode and cathode separation on a single electrode surface indicate that individual anodes and cathodes cannot be isolated on the G3 MEA electrodes. However, weak current responses from the electrodes could be correlated to the overall anodic or cathodic behaviour of single electrodes, which was not always possible using the pH 1.5, Ar-sparged 0.000374 M [Cu] potential buffer and clean Cu electrodes. The ability to correlate the electrode response to its overall behaviour is further confirmed by the optical images shown in Figure 6.44 which indicate that electrodes A/B which have the pre-grown Cu_2S film look as expected while electrodes C/D, formerly clean electrodes, have grown a very thin Cu_2S film. Therefore, it is possible to distinguish between electrodes that display overall anodic or cathodic behaviour using the surface topography correlated with the current responses recorded at E_{corr} on the MMA.

6.3 Summary and Conclusions

Using a combination of optical imaging and CLSM a viable method was developed to analyze PCB MEAs. MEAs were first optically imaged at low magnification and then imaged using CLSM at high magnification with a low z-interval. The Su8 coating or solder mask were used as reference points for CLSM analysis to obtain S_z values (total height measurements). If S_a or S_q values were skewed by the coating or solder mask then the data collected from these areas were omitted after S_z analysis was performed to obtain an accurate roughness values.

PCB MEAs were found to be reusable depending on the S_z value measured after each experiment given that they were tested in the determined ideal experimental conditions. The ideal experiment was performed with a pH 1.5, Ar-sparged 0.0374 M [Cu] potential buffer for up to 8 hours with a nulling procedure performed for the first 300s of the experiment prior to solution addition. The lower detection limit for current response was found to be approximately ±0.138 nA, in the potential buffer solution. It was possible to measure current responses below the detection limit on individual electrodes which were then classified as unresponsive rather than exhibiting anodic or cathodic behaviour. Unresponsive electrode responses were treated using the moving average method, which also involved establishing a new baseline using the nulling data for each unresponsive electrode.

The majority of the PCB MEAs tested using the pH 1.5, Ar-sparged 0.0374 M [Cu] potential buffer were uncoated, while one MEA was coated with Su8. It was confirmed through CLSM analysis that Cu that appeared bright or shiny in the optical images after immersion in the potential buffer was often unreacted or only slightly corroded while darker areas in the optical images were generally corroded and, hence, slightly roughened. The most probable explanation for this distinction is that darker areas indicated higher energy grains at the start of the immersion while the bright areas were low energy grains at the start of the immersion. The darker areas typically have lower S_a values due to a more even distribution of anodes and cathodes across the surface. When both dark and bright areas were present on the electrode surface, S_a values were higher than if the electrode surface was composed of only dark areas. If an immersion was performed in 2 steps the S_z values were found to be increased due to the replenishment of the oxidant in the second immersion. A single long immersion often produced rougher samples due to the increased presence of both corroding (dark) and slowly corroding (bright) material whereas two shorter consecutive immersions often resulted in surfaces with only dark areas (corroding material). Over the course of an experiment, regardless if it was performed in one or two immersions, the grains likely became closer in energy which resulted in a decreased separation between the anodic and cathodic reactions on an individual electrode surface.

The data collected from the Su8-coated PCB, CB40K, showed that when electrodes which have surface areas of 7854-30726 μm^2 are immersed in the pH 1.5, Ar-sparged 0.0374 M [Cu] potential buffer the current responses cannot accurately be matched to the overall electrode behaviour or surface roughness. To confirm that the current responses could be matched to overall electrode behaviour Cu_2S films were grown on half of an MEA, which was then immersed in a solution containing a low concentration of SH^-. Coupling between the originally clean electrodes and the electrodes with a pre-grown film was observed. However, isolation of individual anodes and cathodes could not be achieved with this system. This demonstrates that the electrode sizes were too large with respect to the size of individual anodes and cathodes. This system also confirmed that the current responses and anodic/cathodic behaviour on the electrodes in the potential buffer solution are weaker and less distinct compared to the Cu_2S system analyzed. Therefore, a current analysis with a MMA will only be helpful for systems in which the current measured at each electrode is large and persistent enough to definitively label the behaviour as anodic or cathodic.

6.4 References

---

1. Schweitzer, P.A. *Fundamentals of Corrosion: Mechanisms, causes, and preventative methods*. CRC Press, Boca Raton, FL, 2010, pp65-66.

2. Shannon, C.E. Communication in the Presence of Noise. *P. IEEE.* **1998,** 86, 447-457.

3. Tawancy, H.M.; Mohammed, A.I.; Alhems, L.M. Microstructural Analysis of Corroded Copper Pipes Used in Water Distribution Network. *Metallogr. Microstruct. Anal.* **2019,** 8, 307-313.

4. Tzevelekou, T.; Flampouri, A.; Rikos, A.; Vazdirvanidis, A.; Pantazopolous, G.; Skarmoutsos, D. Hot-water Corrosion Failure of a Hard-drawn Copper Tube. *Eng. Fail. Anal.* **2013,** 33, 176-183.

5. Lee, C.; Lin, P.; Yang, C.; Ho, C. Significantly Improving the Etching Characteristics of Electroplated Cu Films Through Microstructure Modification. *Surf. Coat. Tech.* **2020,** 386, 125471.

6. Hu, M.; Zhang, W.; Shang, X.; Wen, J.; Zhao, Z.; Qiao, B.; Kong, D.; Dong, C. Effect of Surfaec Roughness on Copper Corrosion in Simulated Beishan Groundwater, China. *Int. J. Electrochem. Sci.* **2020,** 15, 2691-2972.

7. Miyamoto, H.; Harada, K.; Mimaki, T.; Vinogradov, A.; Hashimoto, S. Corrosion of Ultra Fine-grained Cu Fabricated by Equal-channel Angular Pressing. *Corros. Sci.* **2008,** 50, 1215-1220.

8. Martinez-Lombardia, E.; Gonzalez-Garcia, Y.; Lapiere, L.; De Graewe, I.; Verbeken, K.; Kesten, L.; Marcuse, P.; Terryn, H. Scanning Electrochemical Microscopy to Study the Effect of Crystallographic Orientation on the Electrochemical Activity of Pure Copper. *Electrochim. Acta.* **2014,** 116, 89-96.

9. Vitos, L; Ruban, A.V.; Skriver, H.L.; Kollár, J. The Surface Energy of Metals. *Surf. Sci.* **1998,** 411, 186-202.

10. Mayanna, S.M.; Setty, T.H.V. Effect of Halide Ions on the Dissolution of Copper Single Crystal Planes in Dilute Sulphuric Acid. *Corros. Sci.* **1974,** 14, 691-699.

11. Mayanna, S.M. Adsorption Isotherm of Iodide Ions on Copper Single Crystal Planes in Sulfuric Acid. *J. Electrochem. Soc.* **1975,** 122, 251-252.

---

12. Vvedenskii, A.; Grushevskaya, S.; Ganzha, S.; Eliseev, D.; Abakumova, L.I. Copper Oxides: Kinetics of Formation and Semiconducting Properties. Part II. Copper Single Crystals. *J. Solid. State. Electr.* **2014,** 18, 3437-3451.

13. Huang, Y.; Handoko, A.D.; Hirunsit, P.; Yeo, B.S. Electrochemical Reduction of CO_2 using Copper Single-Crystal Surfaces: Effects of CO^* Coverage on the Selective Formation of Ethylene. *ACS. Catal.* **2017,** 7, 1749-1756.

14. Arjmand, F.; Adriaens, A. Influence of pH and Chloride Concentration on the Corrosion Behavior of Unalloyed Copper in NaCl Solution: A Comparative Study Between the Micro and Macro Scales. *Materials.* **2012,** 5, 2439-2464.

15. Guo, M.; Chen, J.; Lilja, C.; Behazin, M.; Noël, J.J.; Shoesmith, D.W. The Anodic Formation of Sulfide and Oxide Films on Copper in Borate-Buffered Aqueous Chloride Solutions Containing Sulfide. *Electrochim. Acta.* **2020,** 362, 137087-137096.

16. Chen, J.; Qin, Z.; Martino, T.; Shoesmith, D.W. Non-uniform Film Growth and Micro/macro-galvanic Corrosion of Copper in Aqueous Sulphide Solutions Containing Chloride. *Corros. Sci.* **2017,** 114, 72-78.

7. Conclusions, Summary and Future Work

7.1 Conclusions and Summary

At the beginning of this thesis, CV scans were performed using a bare Cu rod electrode submerged in a range of solutions containing Cl^-, SO_4^{2-} and carbonate. The pH and temperature of these solutions were varied to determine whether Cu would passivate or undergo active dissolution. The CVs were used to determine whether the current response from the Cu electrode indicated active or passive behaviour in the solution, based on the presence of an active-to-passive transition peak on the forward scan or a hysteresis loop on the return scan. A series of active/passive (A/P) maps were generated based on solution composition, temperature and pH. The expected solution composition in a DGR environment was overlaid onto each A/P map to determine which behaviour would prevail under each set of conditions. These maps showed that active conditions were promoted by low pH values (< 7.5), temperatures of 40-80ºC and $[Cl^-] \geq 1$. Passive conditions were promoted by high $[(CO_3)_{tot}]$ and $[SO_4^{2-}]$ if there was no Cl^- in the solution. Compared to the expected DGR conditions, binary solutions containing SO_4^{2-} and low $[(CO_3)_{tot}]$ would promote passive film formation. However, the DGR is expected to contain all three groundwater ions, with Cl^- more abundant than the other two anions. In the only ternary solution tested, which was deemed closest to the expected DGR conditions, active dissolution of Cu was observed at all temperatures. The conclusions drawn from Chapter 2 directly influenced the remainder of this thesis, creating an emphasis on studying active dissolution and the roughening process for Cu in high to moderate $[Cl^-]$ solutions.

Chapter 3 involved the study of the best method to fabricate MEAs. It was determined that the best method to study active dissolution and roughening of Cu was through using MEAs. MEAs were chosen due to their ability to simulate a surface or perform high throughput testing based on the electrode size to inter-electrode distance ratio. MEAs were also chosen because they can be fabricated with MEs or UMEs which could be used to attempt to isolate single anodes/cathodes on an electrode surface. After three different generations of MEAs were tested, the best option for MEA fabrication was found to be PCB MEAs which could be fabricated with up to 48 electrodes. The application of PMMA coatings was tested on PCB MEAs followed by analysis in SEM. Due to the charging of the PMMA coatings SEM could not capture an accurate image of the electrodes and was deemed an unsuitable analysis technique for coated PCB MEAs. PMMA was also deemed an unsuitable coating due to its fabrication process involving Cr coating the MEA prior to imaging.

Su8-3005 was found to be a suitable alternative coating that did not require another base layer like Cr. The application of the Su8 coating was a multi-step process involving spin coating, soft baking, UV curing, post-exposure baking and developer washing, all of which were optimized. The ideal spin coating process involved depositing 1-2 drops of the Su8 thinner compound over the MEA and then spinning the PCB for 5 s at 500 rpm, then at 800 rpm for 40 s. After spinning, the PCB was soft baked for 20 minutes at 95°C followed by UV curing in 10 s intervals with 90 s rest periods between intervals for a total cure time of 40 s. The sample was then left to cool to room temperature. After curing, the PCB was baked (post-exposure bake) again for <20 min at 95°C. A longer bake at this step resulted in a more stable coating. After the final bake, the ideal developer wash procedure was determined to be 210 s in the MIBK/iPa developing solution, followed by a 30 s dip in fresh developing solution. After this optimization that the main problem preventing the MEAs from being used successfully was that the 1 M NaCl solutions did not promote enough corrosive damage to enable analysis by optical microscopy and CLSM. Therefore, it was deemed necessary to study the active dissolution of Cu in Cl^--based solutions with a non-O_2 oxidant.

To successfully create a Cl^--based, O_2-free solution, the corrosion damage and roughening patterns produced in O_2-free or O_2-limited 1 M NaCl had to be understood and verified. To achieve this, experiments using galvanostatic charging, an accelerated testing method, were reported in Chapter 4. Experiments were performed in an anaerobic chamber or on the benchtop with Ar-sparging. Constant currents (CCs) of 1000 μA, 500 μA, 250 μA, and 75 μA were applied to a Cu coupon to achieve a total charge of 6.8 C. At high CCs, such as 1000 μA and 500 μA, the formation of a resistive $CuCl_{ads}$ layer was faster than its dissolution, leading to the development of very high potentials (~9 V(SCE)) that resulted in the oxidation of H_2O. At lower CCs, such as 250 μA and 75 μA, the $CuCl_{ads}$ layer was dissolved fast enough that it was not found on the surface after the experiments, therefore the corrosion damage could be studied. The roughening patterns produced by the application of 250 μA and 75 μA CC were found to be very similar. The maximum dissolution depth, S_z, was found to be time-dependent rather than CC dependent when Ar-sparging was employed. In the anaerobic chamber the CC had slightly more impact on the S_z value than it did in experiments performed on the benchtop. At a CC of 75 μA the rate of CuCl formation was likely very close to its dissolution rate due to corrosion reaching a finite depth before laterally spreading on the surface. This also indicated that as corrosion proceeds depthwise it slowed down the deeper it penetrated into the resistive CuCl layer or bulk Cu and allowed other nearby sites to reach the same corrosion rate which resulted in lateral dissolution. The surface topography produced in these experiments suggested that active dissolution proceeds through preferential grain dissolution and that over the course of time it is possible to have a rough surface with height differences of up to 30 μm in surface features due to the inherent energy differences between different grain orientations.

After determining that preferential grain dissolution was the main roughening mechanism in the active dissolution of Cu in 1 M NaCl a valid link to compare accelerated testing and non-accelerated testing was sought. The immersion experiments reported in Chapter 5 were used to achieve this goal. First, immersions of Cu coupons in Ar-sparged 1 M NaCl solutions with varying pH were performed to confirm that the corrosion rate was too low in all scenarios to be analyzed by optical microscopy and CLSM. A solution containing 1 M Cl^- that could be used to study the active dissolution of Cu was found. This solution, called the potential buffer, was designed to buffer the potential between -125 mV(SCE) – -105 mV(SCE) and used Cu^{2+}/Cu^+ as the oxidant-reductant couple. The solution was made using a ratio of 4.05:1 of CuCl:$CuCl_2$ with a total of 0.0374 M [Cu], 1 M NaCl and 1 M HCl to adjust the pH. It was found that for the potential buffer to produce corrosion depths and roughening similar to those seen in the galvanostatic experiments in Chapter 4, the pH of the solution had to be adjusted to a value between 1 and 2. The corrosion rates of the Cu in these solutions were drastically tied to the immersion time. This was reflected by the estimated corrosion rates which decreased by up to 66% over the course of a day. However, over these immersion times the buffering potential remained stable for up to 8 hours, after which the potential began to fluctuate. It is likely that this fluctuation was due to the solution reaching the solubility limit of Cu^+, which would decrease the rate of corrosion over time despite the potential remaining in the desired region. Therefore, to obtain the highest corrosion rates for studying the roughening patterns, experiments were set to between 3.77 hours and 7.56 hours. These values were rounded to 4 hours and 8 hours for the experiments using the PCB MEAs.

Chapter 6 reports the development of a valid method for analyzing roughness and corrosion depth for PCB MEAs. This method involved taking a preliminary optical image of the entire MEA followed by CLSM analysis of each electrode before and after experimentation. The procedure for measuring current passed by the electrodes PCB MEAs at E_{corr} using the MMA was also optimized, which involved performing a series of nulls for the first 300s of each experiment to establish a baseline current in the event electrodes displayed unresponsive behaviour. Unresponsive electrodes were those with current responses below the approximate detection limit, which was determined to be ±0.138 nA, though this value can vary slightly depending on the connection. Unresponsive electrodes were treated with the moving average method to help elucidate their anodic/cathodic behaviour.

The PCB MEAs were found to undergo preferential grain dissolution similar to the Cu coupons used in Chapters 4 and 5. However, it appeared that the grains of the Cu used in the fabrication of the PCB MEAs were much smaller than those seen on the SKB Cu used in Chapters 4 and 5. Additionally, the PCB MEAs could be reused and immersed in the potential buffer as long as the corrosion depth (S_z) was monitored.

Su8-coated PCBs were used to test smaller electrode sizes and attempt to isolate individual anodes/cathodes. The ideal experiment involved immersing the MEA for a total of 8 hours in the pH 1.5, Ar-sparged 0.0374 M [Cu] potential buffer. The immersions were either performed in one 8-hour interval or two 4-hour intervals. Optical microscopy allowed the relative heights of different features (bright areas and dark areas) on the Cu surface to be determined. Bright areas of Cu were either unreacted or slowly corroding pieces while darker, brown areas were generally corroded and slightly roughened. The darker areas were found to have low S_a values, likely due to a more even distribution of anodic and cathodic events on the surface. If a surface had both dark and bright areas present, then the S_a values were much higher than those of a surface comprised of only dark areas. A single immersion often produced samples with high S_a values which corresponded to surfaces with the presence of both dark and bright areas, whereas two 4-hour immersions produced a surface with mostly dark areas, indicating a lower S_a value.

Individual anodes and cathodes could not be isolated on electrodes with reactive surface areas of 7854-30726 μm^2 when they were immersed in the pH 1.5, Ar-sparged 0.0374 M [Cu] potential buffer for up to 8 hours. This is because the surfaces in this area range simultaneously supported the anodic and cathodic reactions across the entire surface. On a similar note, the current responses measured at E_{corr} could not accurately be matched to the surface roughness or the electrode behaviour. This was confirmed by the final surface topographies, which were similar across all the analyzed PCB MEA electrodes. To confirm that current responses could be matched to overall electrode behaviour, Cu_2S films were grown on half of a PCB MEA and then the entire PCB MEA was immersed in a low [SH^-] solution for a day. Galvanic coupling between the initially clean electrodes and the electrodes with the pre-grown Cu_2S film was observed. The observed galvanic coupling allowed for the identifications of overall electrode behaviour indicating net anodes and net cathodes, however individual anodic and cathodic events were not able to be isolated on these surfaces. These results indicate that the electrode sizes in this thesis were too large with respect to the size of individual anodes and cathodes on the Cu electrodes. The Cu_2S film study also confirmed that the anodic/cathodic behaviour in the potential buffer solution is less distinct and elicits weaker current responses than in other systems like the Cu_2S experiment. This led to the conclusion that current analysis using a MMA is best if the current measured at each electrode is large and persistent enough to definitively label its behaviour as anodic or cathodic.

7.2 Future Work

Further work could aim to explore the roughening process for Cu with a more statistical approach using the potential buffered Cl^- solution. Additionally, analysis of specimens in a SO_4^{2-} solution would allow the differentiation of corrosion patterns between solutions dominated by different groundwater anions. A study by Pradhan et al suggests that SO_4^{2-}-dominated, acidic solutions will promote roughened surfaces due to etching which leaves behind a high number of microfeatures or nanopillars, rather than preferential grain dissolution.[1] Vargas et al., studied the effect of HCO_3^- and solution flow on Cu corrosion. They found that colloidal malachite ($Cu_2CO_3(OH)_2$) formation occurs in the presence of high [HCO_3^-].[2] A simulated groundwater potential buffer may also allow the development of a statistical roughening model for Cu under active dissolution conditions. A potential-buffered Cl^- solution in neutral to slightly basic pH solutions would also expand the viability of these solutions. It would also allow simulation of conditions closer to the DGR environment and the creation of a more comprehensive roughening model.

The PCB MEA design could be improved by searching for manufacturers that create smaller openings in solder masks which may then allow the separation of individual anodes/cathodes on smaller electrodes. However, the possibility exists that anodic and cathodic events are completely mixed, and separation is not possible based on electrode size. If this is the case then it would be more feasible to pick a Cu material with medium-sized, well-defined grains and map the grains use electron backscatter diffraction. After the surface is mapped then a coating could be applied to limit the number of grains exposed to solution. Then a series of immersion experiments could be performed in a short time scale to track the grain dissolution process and measure the corresponding current from the dissolving grains. To help support these experiments more work could be performed to refine the Su8 coating application and optimize parameters such as thickness. This would help elucidate the results produced by CB40K, the only Su8-coated PCB MEA immersed in the potential buffer, which were contrary to the results from the other PCB MEAs. In these results, the bright areas indicated a low S_a value with a more even distribution of anodes and cathodes across the surface while dark areas indicated high S_a surfaces with multiple topographical features, none of which resembled preferential grain dissolution. Fabrication of more Su8-coated PCB MEAs can be used for further Cu corrosion experiments. These new Su8-coated PCB MEAs could be corroded using the potential buffer to determine an expected range of roughening patterns and extent of corrosion for 50 μm diameter electrodes. This would greatly improve upon CB40K's dataset, which was useful, despite it being gathered from a previously used MEA. Eventually the goal with MEA experiments is to develop a database similar to the A/P maps (Chapter 2), that compares the effects of different groundwater ions on the roughness of Cu under active conditions. The deposition of a thin layer of bentonite on the MEA electrodes, followed by immersion in the potential buffer, would help characterize differences in surface roughening and the current responses under conditions more closely approaching those anticipated in a DGR. The G3 MEAs can also potentially be designed to incorporate other metals instead of Cu to either analyze another metal or to have local reference electrodes within the MEA to obtain more potential, pH or ion-selective data for the individual electrodes. These additional metals could be electrodeposited onto the Cu electrodes provided adhesion is good or there is a conducting adhesive layer that can be applied to aid this process.

7.3 References

---

1. Pradhan, S. K.; Balaji, U.; Mishra, S.; Jeevitha, M., Swain, S. Surface-Enhanced Raman Scattering on Chemically Etched Copper Surface: An Upper-Level Spectroscopic Measurement and Analysis. *J. Chem. Educ.* **2020,** 97, 557-564.

2. Vargas, I.T.; Pavissich, J.P.; Olivares, T.E.; Jeria, G.A.; Cienfuegos, R.A.; Pastén, P.A.; Pizarro, G.E. Increase of the Concentration of Dissolved Copper in Drinking Water Systems Due to Flow-induced Nanoparticle Release from Surface Corrosion By-products. *Corros. Sci.* **2010,** 52, 3492-3503.

Curriculum Vitae

Name:	Roshan Daljeet
Post-secondary Education and Degrees:	The University of Western Ontario London, Ontario, Canada 2010-2015 B.Sc. The University of Western Ontario London, Ontario, Canada 2015-Present Ph.D.
Honours and Awards:	Western's Nanofabrication Lab Supported Project 2017-2018
Related Work Experience	Lab and Resource Room Teaching Assistant The University of Western Ontario 2015-2019 1st Year Lab Technician The University of Western Ontario 2021

Publications:

Qin, Z; Daljeet, R; Ai, M; Farhangi, N; Noel, J.J.; Ramamurthy, S; Shoesmith, D; King, F; Keech, P. The active/passive conditions for copper corrosion under nuclear waste repository environment. *Corros. Eng. Sci. Techn.* **2017,** *52*, 45-49.

Poster Presentations:

Daljeet, R.; Ai, M.; Farhangi, N.; Qin, Z.; Zagidulin, D.; Noël, J.J.; Ramamurthy, S.; King, F.; Shoesmith, D.W.; "**Determination of the Active/Passive Behaviour of Copper under Nuclear Waste Disposal Conditions**", *UNENE-Waterloo*. University of Western Ontario, 2016

Daljeet, R.; Ai, M.; Farhangi, N.; Qin, Z.; Zagidulin, D.; Noël, J.J.; Ramamurthy, S.; King, F.; Shoesmith, D.W.; "**Determination of the Active/Passive Behaviour of Copper under Nuclear Waste Disposal Conditions**", *ECS Oshawa*. University of Western Ontario, 2016.

Daljeet, R.; Ai, M.; Farhangi, N.; Qin, Z.; Zagidulin, D.; Noël, J.J.; Ramamurthy, S.; King, F.; Shoesmith, D.W.; "**Determination of the Active/Passive Behaviour of Copper under Nuclear Waste Disposal Conditions**", *NACE NAE*. University of Western Ontario, 2016.

Daljeet, R.; Ai, M.; Farhangi, N.; Qin, Z.; Zagidulin, D.; Noël, J.J.; Ramamurthy, S.; King, F.; Shoesmith, D.W.; "**Determination of the Active/Passive Behaviour of Copper under Nuclear Waste Disposal Conditions**", *Corrosion 2017- New Orleans*. University of Western Ontario, 2017.

Daljeet, R.; Qin, Z.; Zagidulin, D.; Ramamurthy, S.; King, F.; Shoesmith, D.W.; and Noël, J.J.; "**Analyzing the Behaviour of Anodes and Cathodes on Corroding Copper Surfaces**", *Unene 2017*. Toronto, 2017.

Daljeet, R.; Qin, Z.; Zagidulin, D.; Ramamurthy, S.; King, F.; Shoesmith, D.W.; and Noël, J.J.; "**Analyzing the Behaviour of Anodes and Cathodes on Corroding Copper Surfaces**", *CSC 2017- Toronto*. University of Western Ontario, 2017.

Daljeet, R.; Zagidulin, D.; Ramamurthy, S.; Shoesmith, D.W.; Noël, J.J.; "**Exploring Anode/Cathode Sizing, Strength, Persistence and Distribution on Corroding Copper Surfaces**", *Gordon Research Conferences/ Gordon Research Seminar*. New London, New Hampshire, 2018.